UNIVERSITY OF SOUTHAMPTON

Investigation into the Vertical Motions of High Speed Planing Craft in Calm Water and in Waves

J.I.R.Blake

Doctor of Philosophy

FACULTY OF APPLIED SCIENCE AND ENGINEERING
SCHOOL OF ENGINEERING SCIENCES
SHIP SCIENCE

MAY 2000

UNIVERSITY OF SOUTHAMPTON

ABSTRACT

Doctor of Philosophy

FACULTY OF APPLIED SCIENCE AND ENGINEERING

SCHOOL OF ENGINEERING SCIENCES

SHIP SCIENCE

INVESTIGATION INTO THE VERTICAL MOTIONS OF HIGH SPEED PLANING CRAFT IN CALM WATER AND IN WAVES

by JAMES IAN RICHARD BLAKE

An analysis of the dynamics of a series of hard-chine constant deadrise planing craft, operating in calm water and in waves, is investigated through the development and application of two numerical models. The basic equation for hydrodynamic lift is derived from the consideration of an unsteady perturbed potential flow associated with the motion of a rigid body moving without circulation in an infinite fluid. Through a slender body strip theory analogy, the total vertical body forces and moments are derived. The solution to these equations of motion are solved within the frequency domain for the linear problem of time-invariant hydrodynamic coefficients, and within the time domain for the non-linear hydrodynamic coefficients.

Both the linear frequency domain model and the non-linear time domain model are validated against previous experimental and theoretical research. Both models are used to investigate the effect of parametric variation on craft stability in calm water. The non-linear model is applied to predict vertical craft response in regular and irregular waves and to investigate the effect of varying design parameters. Frequency dependence of added mass and damping is accounted for, and the consequences of this inclusion investigated.

Experimental tests were carried out to provide confidence in the application of previous experimental work to validate the numerical models. Furthermore, these tests provided insight into the difficult quantification of dynamic phenomena experienced by so many experimenters in the past. A new technique in instrumentation is demonstrated which aids repeatability of tests and the archiving of important planing phenomena, thereby reducing the possibility of misinterpretation and disagreement amongst different experimenters results.

It is concluded that a non-linear strip-theory approach allows accurate quantification of planing craft responses in the vertical plane. The inclusion of frequency dependent added mass and damping coefficients is important in the areas where the added mass and damping curves are removed from their asymptotic behaviour. The linear frequency domain approach is useful in quantifying stability boundaries.

Acknowledgments

This is my opportunity to be able to write a few untechnical words that my friends and family might actually understand, and keep them looking at this thesis for longer than a couple of seconds!

I would like to thank my friends and colleagues, past and present, at the Department of Ship Science, all of whom have at sometime provided individual contributions bordering on genius...only next time enlighten me before I write the conclusions!

In particular I would like to thank Phil Wilson who has been cracking the whip tirelessly and allowing red ink manufacturers the enjoyment of his valuable custom. Thankyou Phil ...and just one more questionmark for you ?

I could not forget my 'cell-mate', Noel, who tutored me, and obviously many others, in the not-so-subtle use of profanity in circumventing software problems. Seems like his legacy continues...

A big thankyou to my flatmates and brothers-in-arms, too many to mention without the need for an extra chapter. However, Tom and Daisy have to get a mention or they'll never buy me a drink again. So thankyou both for keeping me sane ...despite your best efforts!

Also a large thanks to the Salisbury crowd who provided the frequent opportunity for me to escape... only to look a complete fool on a dancefloor somewhere. Cheers.

Finally, and for me most importantly, I must thank my family who have stood together through so much and Lucy for her unending supply of smiles and patience. These few words do little to convey their ceaseless encouragement and support, without which none of this would have been possible.

To my greatest teacher and friend, who was there at the start and with me in spirit at the end, this is written in memory of my dad.

Nomenclature

$(1+\psi)$	Splash-up factor
β	deadrise angle
Δ	displacement
η	peak acceleration
λ	wavelength
λ_{ik}	added mass of a body in an infinite fluid (i and k represent body modes)
λ_m	mean wetted length to beam ratio (λ in Appendix B)
λ_c	critical mean wetted length to beam ratio (inception of porpoising)
μ_{ik}, m_a	added mass of a floating body
Ω	Angular velocity of the body in the xy-plane
ω	wave frequency
ω_e	wave encounter frequency
$\overline{\eta}$	average peak acceleration
$\overline{q_0}$	conjugate of q_0
Φ	Total velocity potential
ϕ	Velocity potential due to body motion with unit velocity in heave
ϕ_I	Velocity potential due to incident wave field
Ψ, ψ	stream function
ρ	density
τR_0	zero speed transom immersion
τ	calm water running trim
τ_0	zero speed trim
τ_c	critical trim angle (inception of porpoising)
θ	Overall trim angle ($\theta_s + \theta_w$)
θ_s	Calm water steady-state trim angle
θ_w	Pertubation of trim due to waves
ε	spectral width
ζ	Pertubation of sinkage
ζ_s	Calm water steady-state sinkage

A	Aspect ratio
b	half beam
B	full beam, $2b$
C_Δ	Load coefficient, $W/\rho g B^3$
$C_{D,c}$	Crossflow drag coefficient
c_{ij} $i, j = 3$ or 5	stiffness coefficient for heave (3) and pitch (5) modes
C_{Lb}	lift coefficient, $L/\frac{1}{2}\rho\dot{x}_{cg}^2 B^2$
C_{Lk}	lift coefficient, $L/\frac{1}{2}\rho\dot{x}_{cg}^2 L_k^2$
C_{m0}	Added mass coefficient up to level of chine immersion (point of separation)
C_L	lift coefficient, $L/\frac{1}{2}\rho\dot{x}_{cg}^2 S$
C_m	Added mass coefficient
C_V	velocity coefficient, $\dot{x}_{cg}/\sqrt{gB}$
D	Frictional drag
$f(A)$	aspect ratio function to evaluate the added mass for $0 < A < \infty$
F_B	Buoyancy force
g	acceleration due to gravity
H	waveheight, $2r_0$
I	Pitch moment of inertia
k	wavenumber
k_y	radius of gyration
L	overall craft length
l_c	wetted chine length measured from transom (body fixed)
LCG_c	critical longitudinal postion of CG (inception of porpoising)
L_k	craft wetted keel length measured from transom (body fixed)
L_m	craft mean wetted length, $\frac{1}{2}(L_k + l_c)$
M	Craft mass
m_{ij} $i, j = 3$ or 5	added mass coefficient for heave (3) and pitch (5) modes
$m_a\|_{\text{stern}}$	added mass of the craft at the stern
$M_{\ddot{z},\ddot{\theta}}$, $M_{\dot{z},\dot{\theta}}$, $M_{z,\theta}$	Linearised rate of increase of pitch moment with increase in variable acceleration, velocity and displacement respectively
n	unit normal
n_{ij} $i, j = 3$ or 5	damping coefficient for heave (3) and pitch (5) modes
o	Origin of the body fixed axes (at the craft's CG)
O_0	Origin of spaced fixed coordinate system
P	Pressure relative to atmospheric pressure
q_0	translational velocity
R	Hydrodynamic lift
r	ratio of positive minima to total minima, or negative maxima to total maxima, in an irregular signal history (Chapter 7)
r, ζ	wave elevation
R_{AW}	added resistance
r_0	wave amplitude
R_c	calm water resistance
R_w	resistance in waves

s	arbitrary length of body contour C
S	plan area
$S(\omega)$	spectral energy associated with frequency ω
t	time
T_0	modal period
T_X	X-component of thrust
T_Z	Z-component of thrust
U	Velocity of craft parallel to keel
U_0	Velocity component in the x-direction of the translational velocity q_0
V	Velocity of craft perpendicular to keel
V_0	Velocity component in the y-direction of the translational velocity q_0
v_n	component of fluid velocity normal to body boundary
W	Craft weight
$w(z)$	complex fluid potential, $\Phi + \imath\Psi$
w_z	vertical component of wave orbital velocity
x	Longitudinal coordinate of a point on the body relative to CG (positive forwards)
X_0	Translation in the direction of the free surface with respect to O_0 (positive in the direction of craft forward motion)
x_C	Centre of pressure moment arm about CG
x_D	Frictional drag moment arm about CG
x_P	Thrust moment arm about CG
z	Vertical coordinate of a point on the body relative to CG (positive towards keel)
Z_0	Translation in the direction perpendicular to the free surface with respect to O_0 (positive downwards)
z_c	chine submergence at the transom (space fixed)
z_{cg}	Vertical position of CG with respect to $O_0X_0Z_0$ $(\zeta + \zeta_s)$
$Z_{\ddot{z},\ddot{\theta}}$, $Z_{\dot{z},\dot{\theta}}$, $Z_{z,\theta}$	Linearised rate of increase of heave force with increase in variable acceleration, velocity and displacement respectively

Contents

List of Figures

Chapter 1

Introduction

Seakeeping is of major interest and importance to a naval architect. The ability of a ship to perform well in the adverse and confused environment of the sea is the crux of a good design. The naval architect has the responsibility to consider structural, dynamic and personnel effects when producing that design.

Over the last hundred years or so, theoretical and experimental methods for the evaluation of the seakeeping ability of displacement ships have been developed. To date, most of the associated dynamic effects can be quantified and qualified to an accuracy useful enough for a naval architect's design methodology. Over time, however, advanced marine vehicles have been developed, such as hydrofoils, planing craft, SWATH and SES craft and hybrid combinations of these. They each have their own general characteristic in form and different methods of seakeeping prediction need to be developed. This thesis will be focus on the study of planing craft.

Planing craft are used in diverse fields. Their use can be seen in military roles, as fast attack craft, patrol vessels and rapid response craft. Commercially, they maybe used as pilot craft, tenders and inshore lifeboats. Planing craft are also prevalent in offshore powerboat racing, and semi-planing hulls are found in private boating. As this specialised form of transport develops, further studies in seakeeping are needed to achieve the maximum results that they can offer.

Theories where planing is the predominant physical effect is not solely of modern interest. In the early 1930's, seaplane designers were aware of the importance of the floats and the main hull on drag and aircraft takeoff speed and subsequent landing operations. They used a theory developed by Munk (1924) for airship hulls. In the 1950's, designers were able to quantify the lifting forces acting on a planing craft. From the 1970's onward, the advancement in computer technology has seen diverse solutions to the planing problem and further understanding of the dynamics involved.

Planing craft impose their own complications in the sense that the free surface has a pronounced effect on the craft's motions in this state. The dynamically supported planing hull generates complex surface flows, including spray jets and reentrant breaking waves. The effect of wave rise and impingement of the spray sheet on the hull cause changes in wetted length and trim angles. The stability offered by hydrostatic forces are negligible and the craft is almost fully supported by hydrodynamic forces, sensitive to perturbations in wetted length and trim.

At present much high-speed craft design is based on heavy empiricism, trial and error and past experience. Although this approach has generally provided satisfactory designs it is usually offset against high cost and time, for example producing prototypes for testing and the subsequent modifications necessary to improve the design. The power of modern computers allows more cost effective solutions to planing simulation, reducing the need for heavy empiricism.

This thesis is presented and written to create a better understanding of the dynamic effects involved with high speed planing hull design and the influence of parametric variation on subsequent performance in calm water and in waves.

1.1 Performance of Planing Craft in Calm Water

Calm water performance is dominated by two areas of interest; resistance and stability. The resistance characteristics of planing craft are the fundamental reason that these type of craft are developed and utilised. The resistance advantage over round bilge forms does not come from reduced residuary resistance. Residuary resistance is primarily made up of wavemaking resistance and induced drag from the dynamic lift. As the planing craft speed increases, the amount of wavemaking resistance falls. However, more lift is produced on the hull bottom and the amount of induced drag increases by a similar order to the drop in wavemaking resistance. Therefore, the fairly constant residuary resistance, past the inception of planing, points to the loss in total resistance stemming from the reduction in wetted surface area and skin friction. So despite the transition to planing requiring a large amount of installed power to overcome the resistance hump associated with increasing craft speed, the drop in post-hump resistance to a value less than that experienced by even the most efficient of displacement forms ensures that planing craft offer efficient performance in terms of high speed and cost.

As with all types of ship, the ability to predict the amount of resistance that a planing craft will experience at all design speeds allows a minimum of installed power. With restrictions on powering requirements, the resistance predictions can highlight improvements in hull shape and weight distributions within the hull. There has been many an experimental investigation into planing hull performance in calm water with much emphasis on resistance evaluation[1] culminating in useful design criteria for the evalution of planing resistance.

Despite the huge benefits that high speed operations afford, there are drawbacks in terms of planing craft stability. The very high speeds associated with planing craft give rise to certain phenomena that can be parasitic in nature. At speed, a planing craft is almost solely reliant on dynamic effects with little damping from the negligible hydrostatic forces. Poor design can therefore lead to instabilities in pitch and heave motions resulting in a condition known as 'porpoising', and for perturbations in roll angle, dangerous transverse instabilities. These have led to many a serious accident. The accurate prediction of these phenomena is vital. Porpoising has been treated analytically by a few authors, for example Perring and Glauert (1933), Lutowski (1973), Payne (1974), Martin (1978a). The experimental investigation of porpoising is extremely limited for planing boats although there exists many porpoising tests carried out on flying boats, Payne (1974), Martin (1978a). The dynamic roll instability has been treated recently by Lewandowski (1996) following observations by Savitsky (1995), Codega and Lewis (1987) and Blount and Codega (1995). Xu and Troesch (1999) also investigated the effect of planing assymetry on planing craft performance and the consequence upon stability.

---

[1] Savitsky (1964) cites many, for example Sottorf (1932), Shoemaker (1934), Sambraus (1938), Savitsky and Neidinger (1954), Shuford (1958), Clement and Blount (1963), and provides a useful appendix containing references to all the papers on planing published by the Stevens Institute of Technology upto 1964

1.2 Performance of Planing Craft in Waves

The seakeeping qualities of a planing craft are, in general, based on three different factors; heave and pitch motions, resistance increment and accelerations. Heave and pitch motions, along with their associated effects, are known as vertical dynamic effects. Each of these aspects is discussed below.

1.2.1 Heave and Pitch Motions

In waves, the craft will move in all six degrees of freedom but commonly the most important of these motions to be examined is the pitching motion. The behaviour of pitch has significant implications on structural design (magnitude of impact accelerations) and stability (porpoising). Figure (A.2) shows that as the planing craft increases its speed, the amplitude of pitch motion per metre of wave height increases to a maximum value. As the speed is increased still further, the amplitude drops rapidly to a near constant value.

The rough water heaving motions figure (A.1) follow essentially the same trends as the pitching motions of figure (A.2), reflecting strong coupling between these two actions. Heaving motion is at a maximum at low speed/length ratios and when the heave natural frequency of the craft is the same as the encounter frequency of the waves, demonstrated by the leftward movement in the peaks of the response with increasing speed and wavelength. After resonance, the motion reduces substantially from the peak values until the boat reaches speed:length ratios in excess of 4. At this speed and at particular wavelengths, the hull is capable of flying from wave crest to wave crest in head seas, even though the measured heaving motions are no larger than those for a speed:length ratio of 2 or 3 - a condition known as platforming.

1.2.2 Resistance Increment

Added resistance in a seaway for ships is normally observed in the need for an increase in engine power over and above that needed to propel the ship in calm-water. This increase in power is usually between 15 and 30 percent of the calm-water resistance.

For any vessel this requires a significant increase in fuel consumption and reduces the designed efficiency of that vessel.

Figure (A.5) shows the relationship between the speed/length ratio and the rough water resistance characteristics of a planing craft in regular head seas. Figure (A.6) shows the increase in resistance in the following sea condition and demonstrates that the sea direction is only significant at low speed:length ratios (less than 3).

1.2.3 Accelerations

Accelerations provide a measure of a planing craft's seaworthiness. The higher accelerations lead to possible structural damage from slamming and an intolerable working environment for the crew; visibility and comfort both being compromised.

The absolute value of the acceleration depends mainly on the hull form, trim, and sea condition. Figure (A.3) shows the impact acceleration as a function of speed and sea state for head sea conditions.

In general the accelerations are not significant up to a speed/length ratio of 2 and are linearly proportional to speed. Thereafter, the accelerations increase as the square of the speed. If one was to compare the effect of wave height then one would see that for a sea state of 5 (average wave height 1.7m) the acceleration is 5 times that of a sea state 3 (average wave height 0.7m), suggesting that the accelerations also increase as the square of wave height.

The following sea condition results in much lower accelerations overall, figure (A.4). The effect of wave height is less significant because the increase in relative wave speed due to the increase in wave height is less. In head seas, on the other hand, both wave height and wave speed increase with a larger sea state, increasing the impact acceleration.

1.3 Aims and Content

The aims of this thesis are to investigate the planing craft dynamics associated with the craft's motions in calm water and also in regular and irregular waves. Considering the large number of investigations required to achieve an understanding of the dynamic phenomena, numerical models to assess the overall performance of a planing craft will be presented. Certain simplifications can be made in order to significantly reduce the mathematical problem whilst ensuring the physical model is not compromised. In this manner, a robust and quick method for accurately evaluating planing craft performance will be ensured.

The importance of vertical dynamic effects has been demonstrated and a method for predicting these effects will be presented. This will allow an investigation into the effect of changing various planing craft parameters, such as beam, length, deadrise, trim angle and so on, resulting in an approach for the optimisation of seakeeping performance and calm water operations.

In an attempt to validate the numerical models and reduce the problem of discrepancies between different experimenters results, a new experimental technique will be presented. Furthermore, this technique aims to remotely capture information on typically hard to measure phenomena, such as wetted area and wetted lengths, spray generation and blister sheet formation.

The literature review in Chapter 2 will describe theoretical methods that have been applied to the problem of planing and some experimental analyses of particular planing phenomena. In conclusion to this chapter, a choice of theoretical procedure will be made based upon the ability to fulfill the aforementioned objectives.

Following the conclusions from Chapter 2, planing theory based upon the principles of impulsive motion is discussed in Chapter 3. The direct application of this theory to describe the generated lift of planing craft is described in the later sections.

Chapter 4 applies the planing theory in a linear frequency domain analysis to describe the stability boundaries in calm water. Chapter 5 advances the theory to a non-linear time simulation of the craft's response to a disturbance in calm water and response to regular and irregular waves.

The results of the linear and non-linear analysis of an extensive range of hard-chine constant deadrise planing craft operating in calm water will be discussed in Chapter 6. Those crafts response to regular monochromatic head seas is discussed in section 6.2. An irregular sea model is presented in Chapter 7 and the performance of those planing craft operating within this environment theoretically analysed.

The experimental investigation into planing craft dynamics in waves is described in Chapter 8, wherein is described the new experimental technique mentioned above.

The final chapters conclude the presented research and point the way forward for a continued investigation into the analysis of planing craft dynamics in calm water and in waves.

Chapter 2

Literature Review

2.1 Overview

Previous work for ship seakeeping can be characterised into two classes. The first consists of vibrations of strip and slender body theories and are two dimensional (2D) in nature.

Strip theories rely on the simplification of the three dimensional boundary conditions. The three dimensional (3D) free surface boundary condition can be reduced by assuming that the frequency of sectional oscillation is of much higher order than the forward speed, resulting in the 3D problem being solved as a summation of 2D problems. The assumption of high frequency is important and could be considered to be invalid because the maximum craft motions are considered to occur at relatively low frequencies. However, the motions in this lower frequency range are dictated by hydrostatic forces and inaccuracies in the hydrodynamic coefficients will have little effect on the predicted motions (Salvesen et al 1971). The body boundary condition can be simplified by treating the vessel as a slender-body since the transverse disturbance is of a higher order than the longitudinal disturbance. In this manner, the outward facing 3D unit normals on the hull from the fluid-vessel interaction can be approximated by their 2D equivalents.

The slender body theory assumes that the craft is again operating at a low forward speed but in this case the frequency of oscillation is low and therefore the effect of the generated waves on the craft response is not as small as that supposed by ordinary strip theory. The slenderness problem is typically treated in two domains - the near field and the far field. Neither of these problems is unique since nothing can be stated about their asymptotic behaviour either far away in the near field problem or close to the body in the far field problem. This non-uniqueness is therefore resolved by requiring the inner and outer problems to match in an intermediate region.

A unification of these two methods leads to a treatment that is quasi-3D in nature with an allowance for forward speed, for example Newman (1978) and Zhao and Faltinsen (1992). These theories have practical limitations for their application such as the inability to model interaction between multiple hulls and are limited in aspect ratio or speed.

The second class of theories is based upon a fully 3D representation of the wave flow and whilst most applications are restricted to moderate speeds, for example the wave Green function methods of Bingham et al (1993), and the Rankine methods such as the raised source desingularisation of Scorpio et al (1996), Kring et al (1996) describe a Rankine panel method (SWAN - Ship Wave Analysis) which could solve the full 3D problem over the whole speed range. Additions to the linear frequency and time-domain potential flow formulations are incorporated to model the non-linear behaviour and lift associated with high speed operation.

2.2 High Speed Planing

The theories used for predicting high-speed planing performance over the conventional theories employed for low to high speed non-planing craft are complicated by the free surface hydrodynamics. Complex flows are generated such as spray jets and reentrant breaking waves that can only be modelled accurately by fully non-linear boundary conditions. The presence of an encountered wave system complicates the mathematics even further.

Planing hydrodynamics can be described in two or three dimensions. In two dimensions, the governing theories can be categorised as high aspect ratio or low aspect ratio. Lai and Troesch (1995), give a concise summary of some of the more typical approaches employed for the mathematical modelling of 2D planing craft dynamics.

Wagner (1932) demonstrated that the lift experienced by an infinitely thin aerofoil (infinitely high aspect ratio) operating in an infinite fluid could be compared to a planing plate of equivalent profile. Payne (1982) extended the analogy by using added mass theory and showed that the acceleration terms for high frequency motions of an infinitely thin aerofoil and a planing plate are identical. Both Wagner and Payne removed the effect of gravity on the free surface by assuming that the planing plate was operating at very high Froude number. Also the agreement between the two cases was only valid at low trim angles and neither case considered a non-zero leading edge spray angle.

Green (1935), (1936a), (1936b) expanded Wagner's solution to include large trim angles and to account for a non-zero spray angle, but the solution was determinable only if the spray thickness or spray angle was known *a priori.* Shen and Ogilvie (1972), overcome this non-uniqueness by applying Green's solution in the inner problem and matching to the far field solution formed from analogy with a lifting line solution in wing theory.

Lamb (1932) established an integral equation relating pressure distribution along a 2D planing surface to its slope. The forms of planing surface were not generalised but instead were derived from two simple pressure distributions for which the integral could be evaluated. Sedov (1937) also solved linearised 2D planing by assuming an infinite series could be used to describe the pressure distribution on the planing surface. Similarly, Maruo (1951), Squire (1957) and Cumberbatch (1958) related the unknown pressure distribution on a planing surface to its geometry by an integral equation.

The low aspect ratio (slender body) planing problem was also investigated by Wagner (1932) who treated the dynamics of a planing plate as a water impact problem. The added mass momentum flux provides the lift force and is based upon the sea-plane hull impact work of Munk (1924) and Von Karman (1929). This particular area forms the basis of the theory presented herein and will be discussed at length in Chapter 3.

A theory to explain the effects of the spray-root was first proposed by Pierson (1950a), (1950b), (1954), and is analogous to added mass theory and a pressure distribution method. As with added mass theory, it relies on the 2D solution to the problem of a wedge impacting on a free-surface. But in this case, the pressure distribution along the wedge is related to the stagnation line speed relative to the stationary water axes. However, while spray root theory describes all the forces developed during steady state planing and water impact problems of prismatic hulls, it does not give a complete picture of forces during transient motion and neither can it be used for non-prismatic forms without an additional added mass term, (Payne 1992).

To provide treatment of three-dimensionality, Wagner, as well as his 2D investigation, extended the theory for low-aspect ratio and infinite Froude number by using an analogous treatment with thin wing theory. Maruo (1967), found the analogy between 3D planing and thin wing theory in the form of a circulation distribution. By using the type of approximations used in the two extreme cases for thin wing theory, i.e. at low and high aspect ratios, the complicated integral expressions Maruo originally formed could be solved. Unfortunately this method broke down for low-aspect ratios unless the Froude number remained high and was not applicable to rectangular planing surfaces.

The methods described above all consider the influence of gravity on the free-surface to be neglected. The low aspect ratio problem at general Froude number was investigated by Wang and Rispin (1971), Tuck (1975), Tulin (1957) and Panchenkov and Zenovich (1989). Doctors (1974) may have been the first to consider the 3D planing problem without restriction on aspect ratio or Froude number. That approach involved finite elements of unknown pyramidal pressures combined to represent the planing surface. The unknown pressure distributions and transom immersion were evaluated in an iterative process but the predicted pressure distributions were found to be highly oscillatory. By using constant pressure elements, Wellicome and Jahangeer (1978) removed the highly oscillatory behaviour. Tong (1989) also used constant pressure elements to investigate drifted flat plates. With constant pressure element formulation, the number of transverse elements need to be restricted to remove the unrealistic oscillatory pressure distributions found by Doctors.

Lai and Troesch (1995) used a vortex-lattice technique based on Tulin (1957) to develop a three-dimensional numerical model to solve the steady planing problem. Nonlinearities were examined and special attention given to the flow off the chines and the zero pressure condition on the free surface. Furthermore a simple model to describe the effect of gravity in the near field was also examined.

In application to more realistic craft geometries in waves, Martin (1978a), (1978b), from Wagner's expressions for lift force of impacting wedges, produced a linear 2D low aspect ratio strip theory to predict high speed planing craft performance in waves. A finite aspect ratio correction was employed to account for three-dimensionality, analogous to aspect ratio corrections used in wing lifting line theory. The success of this method was followed by Zarnick (1978) who produced a quasi non-linear 2D model which, importantly, included the time variation of the wetted surface. A combination of empirical and theoretical evaluation was used for the coefficients in the equations of motion. This method allowed a more in depth analysis of planing craft dynamics and showed that the vertical accelerations at the bow and centre of gravity had favourable comparisons with experiment. The heave and pitch results also produced fair agreement with some of the experimental data produced by Fridsma (1969). Many variations on the strip theory method followed, for example Chiu and Fujino (1989), Akers et al (1999), Wu and Moan (1996), with encouraging amounts of success. Once again, the effect of gravity on the free surface is neglected.

Experimental work on planing is extensive for calm water dynamics but extremely limited for dynamics in waves. Early experimental investigations were carried out by Sottorf (1932), Shoemaker (1934) and Sambraus (1938). These researchers accumulated large amounts of information describing the hydrodynamic characteristics of constant deadrise prismatic planing surfaces operating at fixed trim, fixed mean wetted length and constant speed. The Davidson Laboratory of Stevens Institute of Technology, based upon these data and their own theoretical and experimental investigations, developed a set of empirical equations for predicting the lift, drag, wetted surface area and centre of pressure of planing surfaces at various given speeds, trim angles, loading and deadrise angles. These equations were presented in papers by Korvin-Kroukovsky et al (1949), Savitsky and Neidinger (1954) and Savitsky (1964). Many other researchers have carried out work on calm water planing dynamics and Payne cites them extensively in his papers.

Flow characteristics in calm water including spray and blister sheet formation have been investigated by Latorre and Tamiya (1975), Latorre (1982), (1983), Savitsky and Breslin (1958), Latorre and Ryan (1990) and Payne (1984), (1993). Experimental tests were also conducted by Hirano, Uchida and Himeno (1974) for the measurement of pressure distributions on two prismatic planing hulls.

Only a few of the calm water systematic series of planing hull forms have been published:

1. **Series EMB 50**; Davidson and Suarez (1949)
2. **Series TMB 62**; Clement and Blount (1963)
3. **Series NSRDC 65**; Holling and Hubble (1974), Hadler and Hubble (1974)
4. **Series BK and MBK**; Ergorov and Bunkov (1978)

In waves, there is much more limited work available in the published domain. Fridsma (1969), (1971) carried out extensive tests on a variety of constant deadrise hard chine prismatic planing hulls and used the results to form a parametric investigation into the effect of loading, deadrise, speed, trim, inertia, length and beam on the seakeeping performance. Recently, there has been a series of tests to evaluate seakeeping characteristics of more applicable hull forms but these are still incomplete, Grigoropoulos and Loukakis (1998). Rosen and Garme (1999) carried out full-scale trials on a high speed combat craft in order to investigate slam events and developed a simulation model based upon wedge impact theory. Akers et al (1999) produced experimental results for a full-scale high speed craft in artificially contrived seas by examining the response of the test vessel moving through another vessel's wake.

2.3 Choice of Model

The above literature review points out the diversity in tackling the planing problem and the assumptions which are made in order to simplify the mathematics. Basically, there are two approaches, 2D and fully 3D solutions which may be linear or non-linear in nature. The full 3D solutions are mathematically complex and at present limited in application because of the demand in computation time. The inclusion of the free-surface and memory effect allows the problem to be modelled in a more rigorous mathematical way, but as yet the improvement in accuracy of the results over 2D or quasi-3D methods still do not justify the large increase in computation power. As a practical design tool and in order to fulfill the requirements set out in Chapter 1, section 1.3, the planing problem cannot be solved in full dimensionality. The focus then is on 2D or quasi-3D methods which can still fulfil the aims summarised in section 1.3.

Two dimensional or a quasi-3D theory is based upon a strip theory with slender body approximations and simplifications to the free surface boundary condition. For high speed or planing applications, a provision for forward speed is required.

Munk (1924) used a slender body strip theory to evaluate the motions of airships. Jones (1946) used a similar method for investigating the lift on low-aspect ratio wings. Martin (1978a) extended Munk's theory with a very high speed simplification of the free-surface boundary condition that allowed the effect of gravity to be neglected. The linearised planing problem was solved in the frequency domain and the results for the determination of stability boundaries were good. Payne (1974) had used a similar method of formulation in the frequency domain but did not solve the equations of motion explicitly. However, non-linearities typically associated with planing craft dynamics are missed when the solution is formed in the frequency domain.

Troesch (1992) showed that non-linearities are not as small as originally identified. He proved that wetted length was strongly time dependent, the restoring force matrix is strongly amplitude dependent and the added mass and damping matrices are frequency dependent. Therefore the use of a theory is required that accounts for the non-linear dependency of dynamic effects, associated with high speed planing, upon the amplitude of the forcing functions.

Solution in the time-domain provides a more in depth study of planing craft dynamics by allowing for the inclusion of non-linearities. The solution of a fully non-linear problem is difficult and so quasi non-linear theories are generally employed. Quasi non-linear theory combines linearised boundary conditions together with non-linear dynamics or linear two-dimensional dynamic calculations with a non-linear free surface boundary condition. An example of the former is Zarnick's (1978) method which evolved Martin's (1978a), (1978b) linear hydrodynamic coefficients into the time-domain to develop a non-linear code for motions in regular head seas. Chiu and Fujino (1989) included a hydroelastic response to Zarnick's theory. In essence, their final formulation was identical but the equations of motion had their second and higher order terms in body motions removed and they ignored the cross-flow drag associated with three-dimensional effects acting on low-aspect ratio bodies. By considering the inertial effects, they included an elastic parameter. The sectional hydrodynamic coefficients were evaluated in the frequency domain for the oscillatory motion and at infinite frequency for the steady forward motion. Their results produced good agreement with experimental data.

Akers et al (1999) included a wake model in their application of Zarnick's theory in order that their experimental tests (a full scale powerboat passing through the diverging wake created by another vessel) could be investigated. They concluded that in real terms, Zarnick's theory predicts transient behaviour well.

In another approach, Troesch et al (1995) developed Zarnick's non-linear integro-differential equations using a multi-variable Taylor series. This produced a highly coupled set of ordinary differential equations with constant coefficients which were valid through third order. The result was the ability to investigate the entire system response, identifying areas of critical dynamic response for further verification through the use of the simulator. Wu and Moan (1996) decomposed the total craft response into a linear and non-linear part to obtain a hydroelastic version of high-speed strip theory. Their linear part was solved using potential flow theory and the non-linear part from the convolution of the impulse response functions of the linear ship-fluid interaction and non-linear hydrodynamic forces, thereby keeping an allowance for free-surface memory effects. In this way, not only was the final solution quasi-non-linear but also quasi-3D.

In spite of the limitations of solving the equations of motion in the frequency domain, behaviour of planing craft motion in calm water can be modelled at little computational expense. Furthermore, the importance of including non-linear effects in a time-domain solution can be investigated by direct comparison with the frequency domain solution. Therefore two approaches are employed: a linear small perturbation analysis in the frequency domain based upon Martin's modified slender body strip theory and a non-linear low aspect ratio strip theory in the time-domain. These two methods should provide an ability to model the entire system response in calm water and in waves, allowing a parametric investigation to identify important planing characteristics, thereby fulfilling the numerical modelling requirements of section 1.3.

It is necessary to be able to validate the numerical models and this requires the use of available experimental data. Whilst this has been shown to be abundant for calm water planing, the volume of data in waves is scarce. Furthermore, Payne (1994), (1995) demonstrated clear anomalies between various experimenter's results given identical test conditions, and the effect of these discrepancies on their empirical formulations. In order to provide some validation for the numerical model results in waves, a series of experiments will be performed using a new data acquisition system that will give an inarguable and comprehensive set of experimental results.

Chapter 3

Problem Definition

3.1 Coordinate System

Consider the co-ordinate system of Figure(A.7). $O_0X_0Z_0$ is fixed in space. X_0 is positive forwards (direction of craft motion) and Z_0 is positive downwards. The X_0 plane coincides with the undisturbed free surface. The body fixed axis system, oxz, originates at the craft centre of gravity. x is parallel to the keel and positive forwards and z is normal to keel and positive downwards. The overall trim angle θ is given as the sum of a perturbation trim angle in waves, θ_w, and a steady state value reached in calm water of θ_s. All angles are positive anti-clockwise. The overall heave, z_{cg} is given as the sum of a perturbation in waves of ζ and a steady state sinkage in calm water of ζ_s.

The relationship between the body fixed co-ordinate system and the space fixed co-ordinate system is

$$X_0 = x' \cos\theta + z' \sin\theta + x_{cg} \tag{3.1}$$

$$Z_0 = z' \cos\theta - x' \sin\theta + z_{cg} \tag{3.2}$$

The velocities parallel and normal to the keel, U and V respectively, are therefore written as

$$U = \dot{X}_0 \cos\theta - \dot{Z}_0 \sin\theta = \dot{x}_{cg} \cos\theta - \dot{z}_{cg} \sin\theta \tag{3.3}$$

$$V = -\dot{X}_0 \sin\theta + \dot{Z}_0 \cos\theta = \dot{z}_{cg} \cos\theta - x\dot{\theta} + \dot{x}_{cg} \sin\theta \tag{3.4}$$

3.2 Equations of Motion

Figure(A.8) shows the longitudinal forces and the moment arms acting on a typical planing hull, i.e. the degrees of freedom associated with surge, heave and pitch.

Resolution of these forces and moments with respect to the fixed coordinate system, $O_0X_0Z_0$, yields, respectively, the heave force, Z, the surge force, X and the pitch moment, M,

$$\begin{aligned} X &= m\ddot{x}_{cg} = T_x - R\sin\theta - D\cos\theta - N\sin\theta \\ Z &= m\ddot{z}_{cg} = T_z - R\cos\theta + D\sin\theta - N\cos\theta + W - F_B \\ M &= I\ddot{\theta} = Rx_C - Dx_D + Nx_N + Tx_P + F_Bx_B \end{aligned} \tag{3.5}$$

m = craft mass
I = pitch moment of inertia
R = hydrodynamic lift force
D = friction drag
N = damping force
W = craft weight
F_B= buoyancy force

T_x = Thrust in X-direction
T_z = Thrust in Z-direction
x_D = moment arm of CG to centre of friction
x_P = moment arm of CG to centre of thrust
x_N = moment arm of CG to centre of damping
x_C = moment arm of CG to centre of pressure
x_B = moment arm of CG to centre of buoyancy

These equations are exact, but their accurate solution depends upon the correct derivation of the separate contributions, in particular the hydrodynamic normal force (encompassing both hydrodynamic lift and buoyancy).

3.3 Hydrodynamic Lift

The literature review of Chapter 2 describes the two dimensional (2D) solution of the planing problem, the derivation of hydrodynamic lift, from two directions. Firstly, the planing surface can be considered low aspect ratio, or a slender body, where the length is much greater than the beam. In this case, the 2D problem is formed by a strip theory synthesis. The fluid flow in each individual transverse strip of fluid is affected only by the section of fluid in that strip.

Alternativley, the 2D solution maybe derived by considering that the planing surface has a very high aspect ratio. In this case, the solution has strong analogies with thin wing theory and is readily derived.

Each of these approaches ideally describe the planing problem at the limiting conditions of infinitely low or infinitely high aspect ratio. Practically speaking, the condition of planing will involve moderate aspect ratio.

The approach used herein follows the 2D solution for the case of low aspect ratio planing. The dynamics of the planing craft in waves generally precludes the use of high efficiency (high aspect ratio) planing because of the large variation in wetted length. Furthermore, the low aspect ratio approach has strong analogies with strip theory which itself has provided very good answers to the seakeeping problem of displacement craft.

If the problem of 2D planing is approached from the low aspect ratio direction then over each interval of time for a trimmed planing surface, for example a planing prism, an individual transverse slice in the fluid will experience a continuously immersing prism, or an impacting prism or wedge. Therefore the 2D low aspect ratio planing problem can be reduced to that of a 2D impacting problem, Payne(1988).

3.3.1 2D Impulsive Motion

From Sedov(1965), the two-dimensional impulsive motion of an inviscid, incompressible and irrotational fluid initially at a state of rest and induced into motion by a rigid body motion, is a potential flow. The coordinate system defined by Sedov follows a right-handed sytem with x reflecting the beam-wise position and y reflecting the draft-wise position and is positive downwards. The velocity potential, Φ, must satisfy the two-dimensional Laplace equation throughout the fluid domain,

$$\frac{\partial^2 \Phi}{\partial x^2} + \frac{\partial^2 \Phi}{\partial y^2} = 0 \tag{3.6}$$

and the kinematic and dynamic boundary conditions on the free surface and body.

The linearised kinematic and dynamic boundary condition can be written, from Newman(1977) and neglecting forward motion, as,

$$\begin{aligned} \frac{\partial^2\Phi}{\partial t^2} - g\frac{\partial\Phi}{\partial y} &= -\frac{1}{\rho}\frac{\partial P}{\partial t} && \text{on the body} \\ &= 0 && \text{on the free surface} \end{aligned} \qquad (3.7)$$

where P is the impulsive pressure and is measured relative to atmospheric pressure.

At the free surface $P = 0$, therefore,

$$\Phi = 0 \qquad \text{at the free surface.} \qquad (3.8)$$

On the submerged portion of the body, provided there is no separation, the kinematic boundary condition is,

$$\frac{\partial\Phi}{\partial n} = v_n \qquad \text{on the body boundary,} \qquad (3.9)$$

where v_n is the normal component of velocity at a point on the body boundary, and the derivative $\frac{\partial}{\partial n}$ denotes the derivative in the direction of the unit normal n directed out of the fluid.

3.3.1.1 2D Impulsive Motion of a Floating Rigid Body

Consider a rigid body vertically impacting onto a fluid surface, figure (A.9). The fluid occupies the lower half space and is at rest at infinity. Since $\Phi = 0$ on the free surface then the velocity potential, Φ, can be continued into the upper half plane by the reflection principle of Schwarz (Spiegel 1964). If the boundary of the free surface is considered as a plane of symmetry or reflectance, the vertical derivatives of Φ in the upper half plane are equal in magnitude and sign whilst the horizontal derivatives are equal in magnitude but opposite in sign.

To emphasize this principle, if two points, P_1 and P_2, lie symmetrically about the free surface, defined by $\Phi = 0$, and on the body Σ_1 and its image Σ_2 respectively, then,

$$\left(\frac{\partial\Phi}{\partial n}\right)_{P_1} = -\left(\frac{\partial\Phi}{\partial n}\right)_{P_2} \qquad (3.10)$$

The derivative $\frac{\partial\Phi}{\partial n}$ on Σ_1 is given by,

$$\left(\frac{\partial\Phi}{\partial n}\right) = v_n \qquad (3.11)$$

and on Σ_2 is given by,

$$\left(\frac{\partial \Phi}{\partial n}\right) = -v_n \tag{3.12}$$

If the body, as a result of impact, has a vertical translation or a rotation about the horizontal axis of the free surface, the resulting fluid motion defined by the potential Φ in the region D, external to the body boundary, is represented by the absolute potential flow of the incompressible fluid around a rigid body bounded by the surface $\Sigma_1 + \Sigma_2$ $(= C)$ and moving in the same manner.

Consequently, the 2D problem of impulsive motion without separation for vertical translation or for rotation about a horizontal axis lying on the free surface is reduced to the problem of the motion of a rigid double body in an infinite fluid without circulation.

Sedov(1965) succinctly describes the solution to this problem in pages 20-31 of that reference. Without questioning the validity of that described solution, the basic assumptions will be described forthwith in order to provide insight into the mathematical basis behind the two dimensional impact problem presented herein.

The complex potential of the unsteady perturbed fluid flow generated by a body moving in an infinite fluid without circulation, $\Gamma = 0$, is denoted by $w(z) = \Phi + \imath\Psi$, where the complex variable $z = x + \imath y$ and x and y are the coordinates describing the body in the physical plane (x direction along the body's 'beam', and the y direction along the body's 'draft'). U_0 and V_0 denote the components of the translational velocity (U_0 along x and V_0 along y) and Ω the angular velocity of the system of rectangular coordinates fixed to the moving body. s describes a length of the body contour, C.

Decomposition of the normal velocity, v_n acting on the body leads to,

$$v_n = U_0\frac{dy}{ds} - V_0\frac{dx}{ds} - \Omega\left(x\frac{dx}{ds} + y\frac{dy}{ds}\right) \tag{3.13}$$

Since $v_n = d\Psi/ds$ then,

$$\Psi = U_0 y - V_0 x - \frac{\Omega}{2}(x^2 + y^2) \tag{3.14}$$

The complex fluid potential, $w(z)$, is linearly decomposed into three individual complex velocity components, weighted by component velocities, U_0, V_0 and angular velocity,

Ω, i.e.,

$$w(z) = \Phi + \imath\Psi = U_0 w_1(z) + V_0 w_2(z) + \Omega w_3(z) \tag{3.15}$$

where,

$$w_k(z) = \phi_k + \imath\psi_k \qquad k = 1, 2, 3 \tag{3.16}$$

On the body boundary, from the above expressions, it can be shown that the stream functions ψ_k $(k = 1, 2, 3)$ are,

$$\psi_1 = y \qquad \psi_2 = -x \qquad \psi_3 = -\frac{1}{2}(x^2 + y^2) \tag{3.17}$$

In real terms, the complex potentials of w_k $(k = 1, 2, 3)$ are therefore determined by the geometrical properties of the body boundary. $w_1(z)$ is the complex potential of the perturbed potential flow of the fluid when the body moves with unit velocity in the x-direction, $w_2(z)$ is the complex potential of the perturbed potential flow of the fluid when the body moves with unit velocity in the vertical or y-direction, and $w_3(z)$ provides the perturbed potential flow of the fluid when the body rotates about its origin with unit angular velocity.

Sedov derives the force acting on a rigid body in the abscence of circulation as,

$$X_0 + \imath Y_0 = \frac{dI}{dt} = \frac{\delta I}{\delta t} + \imath\Omega I \tag{3.18}$$

where X_0 is the component of force in the x-direction and Y_0 is the component of force in the y-direction and,

$$I = \imath\rho \oint_C z d\Phi \tag{3.19}$$

The corresponding moment,

$$M_0 = \Re(-\imath\overline{q_0} I) + \frac{\delta N}{\delta t} \tag{3.20}$$

where,

$$q_0 = U_0 + \imath V_0 \qquad \overline{q_0} = U_0 - \imath V_0 \tag{3.21}$$

and,

$$N = \frac{\rho}{2} \oint_C z\bar{z} d\Phi \tag{3.22}$$

and,

$$\overline{z} = x - \imath y \tag{3.23}$$

If the absolute perturbed potential flow of the fluid results from an impact due to a system of impulsive pressures, $P = -\rho\Phi$, suddenly applied along the body boundary contour C, then from equations (3.19) and (3.22), $-I$ and $-N$ can be rewritten through integration by parts as,

$$\begin{aligned} -I &= -\imath\rho \oint_C z d\Phi = \imath\rho \oint_C \Phi dz = -\imath \oint_C P dz & (3.24) \\ -N &= -\frac{\rho}{2} \oint_C z\overline{z} d\Phi = \rho \oint_C \Phi \frac{dz\overline{z}}{2} = \Re\, \rho \oint_C \overline{z}\Phi dz = -\Re \oint_C \overline{z} P dz & (3.25) \end{aligned}$$

The last two expressions in the above integrals are described by Sedov as equal to the momentum and angular momentum of the fluid.

Reducing the momentum, I to its component terms in x and y,

$$\begin{aligned} -I = -I_x - \imath I_y &= \imath\rho \oint_C \Phi dz = -\rho \oint_C \Phi dy + \imath\rho \oint_C \Phi dx \\ &= \rho \oint_C \Phi d\psi_1 - \imath\rho \oint_C \Phi d\psi_2 & (3.26) \end{aligned}$$

and,

$$-N = \rho \oint_C \Phi d\psi_3 \tag{3.27}$$

Letting μ_{ik} equal the added mass of the body defined by the contour Σ $(= C/2)$ and λ_{ik} the added mass defined by that of the area enclosed by the contour C, then,

$$\mu_{ik} = -\rho \oint_\Sigma \phi_i d\psi_k \text{for a floating body} \tag{3.28}$$

and,

$$\lambda_{ik} = -\rho \oint_C \phi_i d\psi_k \text{for a fully submerged body} \tag{3.29}$$

Using the above substitutions, the equations (3.26) and (3.27) become,

$$\begin{aligned} -I_x &= \mu_{11}U_0 + \mu_{12}V_0 + \mu_{13}\Omega & (3.30) \\ -I_y &= \mu_{21}U_0 + \mu_{22}V_0 + \mu_{23}\Omega & (3.31) \\ -N &= \mu_{31}U_0 + \mu_{32}V_0 + \mu_{33}\Omega & (3.32) \end{aligned}$$

for a floating body, and,

$$-I_x = \lambda_{11}U_0 + \lambda_{12}V_0 + \lambda_{13}\Omega \quad (3.33)$$

$$-I_y = \lambda_{21}U_0 + \lambda_{22}V_0 + \lambda_{23}\Omega \quad (3.34)$$

$$-N = \lambda_{31}U_0 + \lambda_{32}V_0 + \lambda_{33}\Omega \quad (3.35)$$

for a fully submerged body.

Sedov shows that the added masses for a floating body are exactly half the added masses for the equivalent body and its reflection. That is,

$$\mu_{ik} = \frac{\lambda_{ik}}{2} \quad (3.36)$$

In the case of a vertically impacting rigid body, the vertical momentum flux will provide the vertical force experienced by the body, i.e.,

$$Y_0 = -\mu_{22}\frac{dV_0}{dt} \quad (3.37)$$

The derivation of the added mass for a flat plate will not be repeated here but the pure vertical added mass of a flat plate is given as,

$$\mu_{22} = \frac{\rho\pi a^2}{2} \quad (3.38)$$

where a is the half width of the impacting flat plate.

3.3.2 Wedge Impact

So far equation (3.37) descibes the lift force on a flat plate vertically impacting into an incompressible fluid. To paraphrase Fabula(1957), the derivation is based upon the principle that the momentum given to the fluid up to any instant of impact is equal to that given if the body at rest in the fluid with penetration as of the instant considered, is impulsively set into motion with velocity as of the instant considered.

It is unreasonable to expect that many planing craft will have completely flat hull bottoms, despite the maximum developed lift, since there are other dynamic phenomena that need to be considered, such as stability and seakeeping performance, that will affect the choice of underwater hull design. Von Karman(1929) provided the first theoretical solution to forces on bodies other than impacting flat plates. He suggested that the potential flow around a 2D impacting wedge could be approximated by the flow around an expanding flat plate, of half width equivalent to the half beam at the intersection of the hull with the undisturbed fluid surface.

At this stage, it is convenient to change coordinate system to that more associated with seakeeping, i.e. the coordinates y and z (as opposed to x and y used above) lie in the plane of the paper, with the y origin passing through the plate centreline, following a right handed system with z postive downwards and y denoting the beam-wise position. If $R(t)$ now denotes the lift force Y_0 and $m_a(t)$ the added mass μ_{22}, which is also now dependent on time since the width of the plate, $2y(t)$, is a function of the immersion of the wedge, $z(t)$, then from equation (3.37),

$$R(t) = -\frac{d}{dt}\left\{m_a(t)V(t)\right\} \tag{3.39}$$

and $V(t)$ replaces V_0 as the impact velocity.

From figure (A.10), the added mass is dependent on the width of the equivalent plate, $2y(t)$, at the intersection between the undisturbed fluid surface and the wedge, given by,

$$\begin{aligned} y(t) &= z(t)/\tan\beta \\ m_a(t) &= \frac{\pi\rho y(t)^2}{2} \end{aligned} \tag{3.40}$$

where β is the deadrise angle.

Substituting equation (3.40) into (3.39) leads to an expression of dynamic lift force on an impacting wedge,

$$\begin{aligned} R(t) &= -\frac{\pi}{2}\rho z(t)^2\cot^2\beta.\dot{V}(t) - \frac{d}{dt}\left\{\frac{\pi}{2}\rho z(t)^2\cot^2\beta\right\}.V(t) \\ &= -\frac{\pi}{2}\rho z(t)^2\cot^2\beta.\dot{V}(t) - \pi\rho z\dot{z}\cot^2\beta.V(t) \\ &= -\frac{\pi\rho z}{\tan^2\beta}\left\{\frac{z\ddot{z}}{2} + (\dot{z})^2\right\} \end{aligned} \tag{3.41}$$

Returning to the analogy between planing and impact, if a planing plate is given a non-zero angle of attack then to an observer in a fixed slice of fluid transverse to the direction of the travelling plate, the passing of the inclined plate produces an impact. The same is true for any planing body provided there is some inclination to the direction of flow. The expression for the generated lift force is dependent on the transfer of momentum from the impacting body into the surrounding fluid. The amount of fluid associated with that transfer is called the added mass and, seen by the boundary conditions of equation (3.17), is dependent on the geometry of the body. Consequently, many authors use the term *added mass theory* (Payne 1992). The analogy between impacting bodies and planing will be employed in the subsequent numerical analyses.

3.3.3 Prismatic Planing

By an impacting wedge analogy a prismatic hull planing on a calm free surface at a trim angle of θ can be described. For a prismatic hull, the vertical and horizontal velocity components, normal and parallel to the keel respectively, can be written (from equation (3.4)) as,

$$V = \dot{x}_{cg}\sin\theta \tag{3.42}$$

$$U = \dot{x}_{cg}\cos\theta \tag{3.43}$$

where,
$\dot{x}_{cg}$ is the forward velocity of the planing prismatic hull,
θ is the hull trim angle,
V is the vertical velocity component (impact velocity), and
U is the velocity of the fluid flow parallel to the keel.

Munk(1924) and Jones(1946) describe equation (3.39) for steady planing (calm water; $\dot{V} = 0$) as,

$$\begin{aligned}\frac{dR}{dx} &= \dot{x}_{cg}\sin\theta\frac{dm_a}{dt}\\ &= \dot{x}_{cg}\sin\theta\frac{\partial m_a}{\partial x}\frac{dx}{dt}\\ &= \dot{x}_{cg}^2\sin\theta\cos\theta\frac{\partial m_a}{\partial x}\end{aligned} \tag{3.44}$$

where,

$$\frac{dx}{dt} = \dot{x}_{cg}\cos\theta$$

and since the impact velocity and added mass are usually functions of distance along the body, x, and time, t, the following operator is used,

$$\frac{D}{Dt} = \frac{\partial x}{\partial t}\frac{\partial}{\partial x} + \frac{\partial}{\partial t} \tag{3.45}$$

Integrating equation (3.44) over the wetted length provides the total dynamic lift force acting on a planing prismatic hull in calm water, suffering from no small perturbations (due to waves or instability) in the moving coordinate system,

$$\begin{aligned} R_{\text{steady}} &= \int_0^L \dot{x}_{cg}^2 \sin\theta\cos\theta\, dm_a \\ &= \dot{x}_{cg}^2 m_a|_{\text{stern}} \sin\theta\cos\theta \end{aligned} \qquad (3.46)$$

The above expressions are for the prediction of steady-state hydrodynamic lift in calm water. In waves, or in the presence of other small perturbations, the theory is the same but additional expressions exist due to the time dependency of the velocity components. The hydrodynamic lift equations in waves will not be enlarged upon until later.

Equation (3.46) is accurate in the description of the total hydrodynamic lift force for a planing prism in calm water provided that the boundary conditions described in section 3.3.1.1 are not compromised. In practical terms, these boundary conditions are restrictive. The planing body is not two-dimensional and will have end-flow effects that require further quantification. The impact/planing theory requires that the flow does not separate from the body, but experiments and practice show that for a planing hull with a chine this is unrealistic. These factors will influence the accuracy of equation (3.46) in predicting hydrodynamic lift.

3.3.3.1 Crossflow Drag

Consider the distribution of lift force over the prismatic craft length given by equation (3.44),

$$\frac{dR}{dx} = \dot{x}_{cg}^2 \sin\theta\cos\theta \frac{dm_a}{dx}$$

Now if the added mass of an impacting section of half beam b is given by,

$$m_a(t) = C_m \frac{\pi\rho b(t)^2}{2} \qquad (3.47)$$

where C_m is the added mass coefficient (equal to 1.0 for a flat plate), then,

$$\frac{dm_a}{dx} = C_m \pi\rho b \frac{db}{dx} \qquad (3.48)$$

and equation (3.44) becomes,

$$\frac{dR}{dx} = \frac{\pi}{2} C_m \rho b \frac{db}{dx} \dot{x}_{cg}^2 \sin 2\theta \tag{3.49}$$

When the chines are dry, the variation of wetted beam over craft length is finite, but when the chines are wet[1],

$$\frac{db}{dx} = 0, \ \frac{dm_a}{dx} = 0 \ \Rightarrow \ \frac{dR}{dx} = 0 \tag{3.50}$$

This result suggests that when the chines are wet, the lift force is zero. However, consideration of the separation of fluid flow produces a crossflow term that accounts for the incremental lift, Payne (1988).

Following from Payne (1992), the force acting on a prismatic form of beam, $2b$ and length L, held vertically in an infinite fluid with a free-stream velocity equal to $\dot{x}_{cg}$, is given as,

$$R = \frac{1}{2} \rho (2b) L \dot{x}_{cg}^2 C_D \tag{3.51}$$

which describes the drag experienced on the prism, where C_D is the drag coefficient. However inclining the prism at an angle θ to the flow direction gives,

$$R = \frac{1}{2} \rho (2b) L u_0^2 \sin^2 \theta C_{D,c} \tag{3.52}$$

and C_D becomes $C_{D,c}$ or the crossflow drag coefficient.

Now when the chines are dry, from equation (3.44),

$$\frac{dR}{dx} = \frac{1}{2} \frac{dm_a}{dx} \dot{x}_{cg}^2 \sin 2\theta \tag{3.53}$$

and when the chines are wet,

$$\frac{dR}{dx} = \frac{1}{2} \rho (2b) \dot{x}_{cg}^2 \sin^2 \theta C_{D,c} \tag{3.54}$$

The difference between equation (3.53) and equation (3.54) provides the increment in lift due to chine immersion,

$$\begin{aligned} \frac{dm_a}{dx} &= \frac{1}{2} \rho (2b) \tan \theta C_{D,c} \\ \Rightarrow \ \Delta m_a &= \frac{1}{2} \rho (2b) \cdot \Delta x \cdot \tan \theta C_{D,c} \\ &= \frac{1}{2} \rho (2b) \cdot l_c \cdot \tan \theta C_{D,c} \end{aligned}$$

---

[1] Wetted chines are defined by the calm water intersection with the hull being over the height of the chine line

and demonstrates that $C_{D,c}$ is a function of the increment of added mass with chine immersion.

Writing in non-dimensional form

$$\Delta C_m = \frac{\Delta m_a}{\frac{\pi}{2}\rho b^2} = \frac{4}{\pi}\cdot\frac{l_c}{2b}\cdot C_{D,c}\tan\theta$$

If z_c is height of waterline measured above the keel and l_c is the distance measured from point of chine immersion to the stern then $z_c = l_c \sin\theta$ and,

$$\Delta C_m = \frac{4}{\pi}\cdot\frac{z_c}{2b\cos\theta}\cdot C_{D,c} \tag{3.55}$$

From Payne(1988) analysis of experimental data, he suggested that

$$\Delta C_m = k\frac{z_c}{2b}\cdot C_{m0} \tag{3.56}$$

From equation (3.55) and equation (3.56),

$$C_{D,c} = \frac{\pi k}{4}\cdot C_{m0}\cos\theta \tag{3.57}$$

where C_{m0} is the added mass coefficient up to the level of chine immersion. Now the total added mass coefficient can be written as,

$$\begin{aligned} C_m &= C_{m0} + \Delta C_m \\ &= C_{m0}\left(1 + \frac{kz_c}{2b}\right) \end{aligned} \tag{3.58}$$

where k is a factor representing the increase of incremental added mass with increase in immersion of the chine and is given by Payne(1995) as,

$$k = 2.05\left[1 - \left(\frac{2\beta}{\pi}\right)^{\frac{9}{2}}\right] \tag{3.59}$$

where β is the deadrise angle in radians. This equation gives $k = 0$ when $\beta = \frac{\pi}{2}$ at which point $C_{m0} = \frac{4\ln 4}{\pi^2}$ as shown by Taylor (1930) and Yim (1971).

The discrepancy between theoretical and experimental lift on hull forms operating with wet chines has been treated by consideration of an additional crossflow drag term, for example Shuford (1958). If the added mass of the impacting section is considered to increase proportionally to the shape of the cavity produced by the separated free surface, the need for a crossflow term is not needed.

3.3.3.2 Aspect Ratio

The equation of lift of a planing prism is given by equation (3.46),

$$R_{\text{steady}} = \dot{x}_{cg}^2 m_a|_{\text{stern}} \sin\theta\cos\theta \tag{3.60}$$

Consider a planing prism of zero deadrise, effectively a planing plate, then $m_a|_{\text{stern}}$ is,

$$m_a|_{\text{stern}} = \frac{1}{2}\pi\rho b^2 \tag{3.61}$$

In an infinite fluid,

$$m_{a_{\text{inf}}}|_{\text{stern}} = \pi\rho b^2 \tag{3.62}$$

Substituting equation (3.62) in (3.60) gives,

$$R_{\text{steady}} = \frac{1}{2}\rho\dot{x}_{cg}^2\pi b^2 \sin 2\theta \tag{3.63}$$

Non dimensionalising,

$$C_L = \frac{R(t)\cos\theta}{\frac{1}{2}\rho\dot{x}_{cg}^2 S} = \frac{\pi}{4}\frac{(2b)^2}{S}\cos\theta\sin 2\theta \simeq \frac{\pi}{2}A\theta \tag{3.64}$$

for small trim angles and where the aspect ratio, $A = \frac{(2b)^2}{\text{plan area, } S}$.

Payne(1994) shows that this equation is accurate for low aspect ratio or slender wings in an infinite fluid. However as $A \to \infty$ then $C_L \to \infty$ which is proven incorrect (e.g.Newman(1977), pages 168-172). Newman(1977) derives the lift coefficient for very high aspect ratio lifting surfaces from vortex distributions given as $C_L = 2\pi\theta$ for $A \to \infty$.

The two extremes for the lift coefficient, C_L, of a moving plate in an infinite fluid can therefore be written as,

$$A \to 0 \qquad C_L \to \frac{\pi}{2}A\theta \tag{3.65}$$

$$A \to \infty \qquad C_L \to 2\pi\theta \tag{3.66}$$

Payne(1994) describes the development of Pabst(1931) work to determine a function which bridges the extremes of correct lift coefficient from very low aspect ratio planing surfaces to very high aspect ratio planing surfaces. The development will not be repeated here, but the bridging function is validated from analysis of Sottorf's(1929) experimental data for planing plates and Shoemaker's(1934) and Pierson et al(1954) experimental data for chines-dry planing craft. Figure A.11 shows three curves of planing flat plate lift corrections against aspect ratio. The 'planing' curve is from Payne's(1992) equation (13) derived from Pabst's corrected work[2] and is the bridging function used herein. The two other curves show the corrections to planing lift for general aspect ratio which have been commonly and incorrectly applied in the past (based upon Pabst; see footnote), namely Schnitzer(1953) and Shuford(1958).

The bridging function used by Payne (1994), (1995) to describe the variation of lift coefficient, and therefore added mass, with aspect ratio is given thus,

$$m_a = \frac{m_{a(A\to 0)}}{\sqrt{1+(\frac{A}{4})^2}} \tag{3.67}$$

where $m_{a(A\to 0)}$ is that value of added mass defined in section 3.3.2. This equation can be altenatively written as,

$$f(A) = \frac{m_{a(A\to 0)}}{m_a} \tag{3.68}$$

Despite this derivation being based upon a flat plate, the effect of deadrise was shown by Payne's(1995) extensive analysis of experimental data to have a negligible effect on the aspect ratio correction for angles less than 40°.

3.3.3.3 Splash-Up

The described impact theory relies upon the analogy of impulsive motion, without separation, within an infinite fluid. Physically, for impacting wedges there exists a phenomenom of increased free surface elevation at the wedge boundary. Sedov(1965) and Von Karman(1929) ignore the effect of this wave rise, or splash-up, on the added mass and consider that the added mass is evaluated from the geometry defined by the undisturbed calm water/wedge intersection, figure A.10. Wagner(1932) showed that in fact the splash-up height is a factor, $(1+\psi)$, of $\pi/2$ more than the undisturbed draft, but this was based upon small deadrise angles. This modification has a profound effect on the subsequently evaluated added mass. The smaller the deadrise angle the larger the effect of splash-up on the evaluation of lift force. The use of Wagner's factor for

---

[2] Pabst confused his derived added mass per unit length with total added mass

deadrise angles approaching 90° was shown by Payne(1981) to lead to over estimates of impact and planing forces. Zhao and Faltinsen(1992) showed that the splash-up factor actually varied from 1 to $\pi/2$ for deadrise angles of 90° to 0°. Payne(1994) uses Pierson's hypothesis (Band 1969) to provide a function for increasing importance of splash-up with diminishing deadrise angle, β,

$$\begin{aligned}(1+\psi) &= \frac{\pi}{2} - \beta\left(1 - \frac{2}{\pi}\right) && (3.69)\\ &= \frac{\pi}{2} \text{ for } \beta = 0^\circ && (3.70)\\ &= 1 \text{ for } \beta = 90^\circ && (3.71)\end{aligned}$$

where ψ is a fraction of splash-up height over keel immersion.

3.3.4 Effect of Added Mass Theory Corrections to Dynamic Lift

The effect of the above considerations and modifications to Munk's original equation (3.46) for dynamic lift on a prismatic hull can be seen in figure (A.12) and follows from Payne(1994). This figure demonstrates the lift coefficient upon beam squared against craft with increasing deadrise angles. The chines are unwetted; the intersection of chine with the free-surface is at the transom. The trim angle for all craft is 12° which represents the trim angle for a large quantity of chines-dry planing data (Shuford(1958); Pierson et al(1954); Shoemaker(1934)).

Clearly, the effect of the aspect ratio correction on the dynamic lift force given by Munk's equation is dramatic. Payne's one-sided flow correction also lowers the dynamic lift force but is shown to offer only a small reduction in comparison with the aspect ratio correction. The trend of corrected dynamic lift seems to contradict common-sense in that as the deadrise angle reduces, the lift reduces too. However, it is important to remember that this wetted length is subjected to the constraint of the chines just being wetted at the transom. In this case, as deadrise decreases so too does the wetted length and therefore the lift generated by the wetted surface.

In summary, the following equation for steady-state hydrodynamic lift is written which combines the individual corrections (aspect ratio, splash-up and crossflow drag) to equation (3.46),

$$R_{\text{steady}} = \frac{1}{2}\rho \dot{x}_{cg}^2 (C_{m0} + \Delta C_m)\frac{\pi}{8}(2b)^2 f(A)\sin 2\theta \tag{3.72}$$

3.3.5 Unsteady Hydrodynamic Lift

So far the evolution of hydrodynamic lift has considered only that lift generated by the steady forward velocity of the planing hull, i.e the lift developed in ignorance of small perturbations in the moving coordinate system due to dynamic instabilities and waves.

Returning to equation (3.39) and employing the operator of equation (3.45), the full equation for hydrodynamic lift consisting of both the steady-state part and the dynamic part, and acting over the whole planing body, can be written as,

$$\begin{aligned}
R(t) &= -\int_0^L \left\{ m_a \frac{\partial V}{\partial t} + V\frac{\partial m_a}{\partial t} - U\frac{\partial m_a V}{\partial x} \right\} dx \\
&= -\int_0^L \left\{ m_a \frac{\partial V}{\partial t} + V\frac{\partial m_a}{\partial t} - UV\frac{\partial m_a}{\partial x} - Um_a\frac{\partial V}{\partial x} \right\} dx \\
&= -\left\{ \int_0^L m_a \frac{\partial V}{\partial t}\, dx + \int_0^L V\frac{\partial m_a}{\partial t}\, dx + UVm_a\big|_{\text{stern}} \right. \\
&\quad \left. - \int_0^L m_a \frac{\partial UV}{\partial x}\, dx - \int_0^L Um_a\frac{\partial V}{\partial x}\, dx \right\}
\end{aligned} \tag{3.73}$$

where the velocity components, U and V, affected by perturbations in the moving coordinate system and the influence of waves, are given as,

$$U = \dot{x}_{cg}\cos\theta - (\dot{z}_{cg} - w_z)\sin\theta \tag{3.74}$$

$$V = \dot{x}_{cg}\sin\theta + (\dot{z}_{cg} - w_z)\cos\theta - \dot{\theta}x \tag{3.75}$$

The influence of incident waves is included by consideration of the vertical velocity component, w_z, of wave orbital velocity. The horizontal velocity component is considered to be small in comparison with the forward velocity of the planing craft.

Now since the steady-state contribution to the total hydrodynamic lift force is given by equation (3.46), then equation (3.73) can be rewritten as,

$$R(t) = R_{\text{steady}} + R_{\text{dynamic}} \tag{3.76}$$

where,

$$\begin{aligned} R_{\text{dynamic}} &= -\left\{ \int_0^L m_a \frac{\partial V}{\partial t}\, dx + \int_0^L V \frac{\partial m_a}{\partial t}\, dx + (UV - \dot{x}_{cg}^2 \sin\theta\cos\theta) m_a\big|_{\text{stern}} \right. \\ & \left. - \int_0^L m_a \frac{\partial UV}{\partial x}\, dx - \int_0^L U m_a \frac{\partial V}{\partial x}\, dx \right\} \qquad (3.77) \end{aligned}$$

3.4 Hydrostatic Force

Apart from the hydrodynamic lift generated by a planing hull, there must exist a hydrostatic contribution to the overall lift experienced by a planing craft, otherwise at zero speed the craft would sink. However, hydrodynamic lift increases as the square of forward velocity, whilst the hydrostatic force decreases with reduced immersed volume, so that at high forward speed the majority of lift is provided by the hydrodynamic force.

Payne(1988) used the term *dynamic suction* to describe the loss of buoyancy which occurs as a transom boat accelerates from rest. When the speed coefficient, C_V, is greater than 0.5, the flow at the transom corner and chines separates, reducing the pressure at these locations to atmospheric. To take into account this ventilation effect on the static pressure, an empirical correction factor, κ, to Archimedes buoyancy is introduced. Hsu(1967) proposed a value of 0.7 for flat plates but a value of $\kappa = 0.624$ was found by Brown(1971) to agree better with experimental data. Zarnick(1978) uses Shuford's(1954) approximation of $\kappa = 0.5$. The obvious problems with any of these empirical fit coefficients is that they are not true at zero speed. There must be some kind of transition between the fully attached flow, full Archimedes buoyancy, and the value for buoyancy when the craft is planing and the flow has separated. Payne(1995) also pointed out that Shuford's determination of 0.5 was based upon the difference between experimental lift coefficients and his theoretical predictions. However the experimental results he used were for $C_V = 3.87$ where the buoyant contribution was extremely small, in which case the comparisons between theory and experiment are likely to be imprecise.

Sedov(1939) actually presented an equation for the buoyant contribution to dynamic lift on a flat plate based upon wetted length and speed coefficient, C_V. Subsequently, Korvin-Kroukovsky et al(1949) altered this equation in order for it to fit specific experimental data more closely. However the agreement with those particular experimental results were questionable and the revised formulation also created singularities for buoyant lift when the aspect ratios reached their infinite or zero limit. Savitsky(1964) also based his equations on Korvin-Kroukovsky et al's work which makes his formulation questionable too, although his results for higher aspect ratio are in better agreement theoretically. Payne(1995) showed that the limits in aspect ratio to Sedov's formulation were close to the theoretical result. Despite his criticisms of their work, Payne showed that in most cases, their formulations reflected the decrease in κ as aspect ratio increases. The problem of the limit of zero speed where κ should equal 1.0 is also addressed by Payne(1994).

In conclusion, Payne suggested an equation for buoyant contribution to lift based upon an empirical approach derived from experiments. This approach is effectively a manometer model and assumes that there is little or no fluid motion in the transom wake. The subsequent drop in fluid level at the transom heel as the craft accelerates is then directly related to the decrease in pressure at this point. The loss in buoyancy as the craft accelerates is therefore treated as being entirely attributable to the loss of static pressure at the transom heel so that no contribution to buoyancy loss is attributable to flow separation off the chines. Payne(1995) showed from Savitsky and Neidinger(1954) experimental results for low speed planing flat plates and low speed planing models with deadrise that the separated flow off the chine did little to affect the measured buoyancy in comparison with the effect of separation of flow off the transom.

At low to zero speed, the transom is wet and the buoyant contribution is hypothesised as being affected by the factor,

$$\kappa = 1 - \frac{C_{DS} C_V^2}{2 \sin\theta} \left(\frac{b}{l}\right)^2 \tag{3.78}$$

where C_{DS} is an empirical transom drag coefficient given by,

$$\begin{aligned} C_{DS} &= \frac{\rho g \delta}{\frac{1}{2}\rho \dot{x}_{cg}^2} \\ &= \frac{2g\delta}{\dot{x}_{cg}^2} \qquad (3.79) \\ &< \frac{2}{F_{nz}^2} \qquad (3.80) \end{aligned}$$

where δ is the depression of the free surface at the transom, and F_{nz} is the transom

Froude number,

$$F_{nz} = \frac{\dot{x}_{cg}}{\sqrt{g z_T}} \tag{3.81}$$

where z_T is the submergence of the transom relative to the undisturbed free surface.

The limiting condition results from the fact that when the depression, δ, of the free surface at the transom is equal to the immersion of the transom, z_T, with respect to the undisturbed fluid surface then the fluid has fully separated from the transom corner and the transom is no longer considered wet. Consequently the empirical relation between buoyancy correction and beam/length ratio, which has proven agreement for fully separated flow, can be used. Therefore, when $C_{DS}.F_{nz}^2 = 2$ then,

$$\kappa = 1 - \frac{B}{L_m} \tag{3.82}$$

This equation represents the buoyant contribution when the flow is fully detached from the transom.

Conversely, when the speed is low enough that $C_{DS}.F_{nz}^2 < 2$, then Archimedes buoyancy is affected by the factor given by equation (3.78). At zero speed, $C_V = 0$, therefore $\kappa = 1.0$ and the full Archimedes buoyancy is realised.

The problem with this manometer model is that based upon the depression of the free surface at the transom for slow speed model tests, the values of C_{DS} are between 0.08 and 0.22 and at most between 0.5 and 0.6 for very slender deep draft craft. However the loss in buoyancy evaluated from model tests requires C_{DS} values closer to unity. The manometer model therefore does not fully describe the cause of buoyancy loss. However, since the operations for planing craft generally exceed the condition of $C_{DS}.F_{nz}^2 < 2$, equation (3.82) will be used.

The buoyancy force can therefore be written as

$$F_B = -\kappa(t).\rho g \int_0^L A(x,t)dx \tag{3.83}$$

where $A(x,t)$ is the sectional immersed area under the free surface and $\kappa(t)$ can be defined by equation (3.78), where $C_{DS} = 1.0$, and equation (3.82).

3.5 Added Mass and Damping

The importance of added mass is evident in its extensive appearance in the equations for hydrodynamic lift. The derivation of added mass of a body is based upon the unsteady perturbed fluid flow as a result of the motion of that body within an infinite fluid, section 3.3.1.1. The presence of a free surface and the associative boundary condition, modified from equation (3.7) to account for the changed coordinate system,

$$\frac{\partial^2\Phi}{\partial t^2} - g\frac{\partial\Phi}{\partial Z_0} = 0 \tag{3.84}$$

allows the added mass for vertical motions to be half that of the corresponding value in an unbounded fluid provided that the velocity potential, Φ equals zero on the free surface. The associative damping is zero due to the lack of generated damping waves of a body motion in an unbounded fluid.

Since Φ is generally a periodic function such that,

$$\Phi = \phi . e^{\imath\omega t} \tag{3.85}$$

then the boundary condition on the free surface, equation (3.84), can be rewritten as,

$$-\frac{\omega^2}{g}\phi - \frac{\partial\phi}{\partial Z_0} = 0 \tag{3.86}$$

Now the following limits apply,

$$\begin{array}{lll} \omega \to 0, & \dfrac{\partial\phi}{\partial Z_0} \to 0 & \text{on the free surface (gravitational forces dominate)} \\ \omega \to \infty, & \phi \to 0 & \text{on the free surface (inertial forces dominate)} \end{array}$$

Therefore, the considered problem of wedge impact, leading to planing theory, assumes that the frequency of motion of the body tends to infinity. In waves where the encountered wave frequency is low, the derivation of added mass will be based upon the condition that $\frac{\partial\Phi}{\partial Z_0} \to 0$, which produces altogether different values for added mass (Newman 1977). Furthermore the neglect of generated damping waves due to the condition that the frequency of oscillation tends to infintiy is no longer appropriate and a damping force component should be considered between the limiting values of $0 < \omega < \infty$ (Newman(1977); Chiu and Fujino(1989)). Appendix C describes the method adopted herein to evaluate frequency independent, and dependent, added mass and damping.

Chapter 4

Linear Model

Linear theory assumes that the motions in waves could be considered to be small perturbations from the steady state calm water condition, i.e that the contribution of the dynamic part of the hydrodynamic lift, equation (3.76), is only slight, and that higher order effects are small. This, for planing craft in head seas, would seem to be an over simplification. However, Fridsma's (1969), (1971) non-dimensional transfer functions for heave and pitch motions at moderate planing speeds($V_{\text{knots}}/\sqrt{L_{\text{ft}}} = 2$ to 4) demonstrated little variance over waveheight to beam ratios of 0.11 to 0.33 and plots of measured heave and pitch amplitude against waveheights (0.11 to 0.33 beams) showed distinct linearity. Furthermore, Troesch's (1992) experimental investigations of hydrodynamic coefficients showed some amplitude independence at low planing speeds and low forcing amplitudes.

A linear solution to planing motions was described by Milton Martin(1978a), (1978b). In the same manner as described in the previous chapter, Martin based his method for the determination of lift force on a slender-body theory derived from Munk(1924) and Wagner's(1932) wedge-impact theory. The resulting equations of motion were then solved in the frequency domain.

The main benefit of this linear analysis is not for motions in waves, although Martin's (1978b) results for moderate planing speeds were fair, but more in the evaluation of stability boundaries in calm water. The parasitic motions characterised by porpoising instability can be evaluated with success (Martin 1978a) and, for example, the introduction of a control system such as trim tabs analysed (Wang 1985).

The derivation of the linear model herein is based solely upon the approximations of Martin. For example, Martin's aspect ratio correction is based upon the work of Pabst(1931) (which , in its orginal form, has been shown by Payne(1994) to be erroneously applied, section 3.3.3.2). The crossflow drag coefficient is based upon the work of Schnitzer(1953) and the theory of Bobyleff (Lamb 1932) who correctly attribute the crossflow drag to chine immersion. The splash-up is assumed to be a factor of $\pi/2$ more than the undisturbed water surface, which is also erroneous, section 3.3.3.3. Furthermore, the correction to hydrostatic lift, κ, is based upon the work of Brown(1971). These approximations have been included in the following linear analysis in order to reproduce Martin's stability boundaries, prior to the application of a non-linear model that incorporates the appropriate assumptions derived within the previous chapter.

4.1 Construction of linear model

To construct the linear model, consider the general equations of motion for planing craft in calm water. Neglecting second and higher order effects, the equations of motion are given by,

$$\begin{aligned}(m - Z_{\ddot{z}})\ddot{z} - Z_{\dot{z}}\dot{z} - Z_z z - Z_{\ddot{\theta}}\ddot{\theta} - Z_{\dot{\theta}}\dot{\theta} - Z_\theta \theta &= 0 \\ -M_{\ddot{z}}\ddot{z} - M_{\dot{z}}\dot{z} - M_z z + (I_y - M_{\ddot{\theta}})\ddot{\theta} - M_{\dot{\theta}}\dot{\theta} - M_\theta \theta &= 0 \qquad (4.1)\end{aligned}$$

where the hydrodynamic coefficients of the motion variables are termed slow motion, or stability, derivatives and are independent of time[1]. For example, the term $Z_{\ddot{z}}$ represents the linearised rate of increase of vertical force, Z, with increase in vertical acceleration, $\ddot{z}$.

The surge degree of freedom has been uncoupled due to the insignificance of surge force in the planing state. This assumption is valid from numerous authors and experimentally verified by Fridsma. Fridsma carried out constant velocity and constant thrust tests in waves and found negligible difference in subsequent heave and pitch responses.

---

[1] For the derivation of these see Appendix B which is reproduced from Martin (1978a)

Martin's own investigation showed that the hydrodynamic coefficients for the surge degree of freedom are also negligible compared with the pitch and heave coefficients.

The solution to these coupled equations of motion can be solved in the frequency domain by writing,

$$\begin{aligned} z &= z_0 e^{\sigma t} & \theta &= \theta_0 e^{\sigma t} \\ \dot{z} &= \sigma z_0 e^{\sigma t} & \dot{\theta} &= \sigma \theta_0 e^{\sigma t} \\ \ddot{z} &= \sigma^2 z_0 e^{\sigma t} & \ddot{\theta} &= \sigma^2 \theta_0 e^{\sigma t} \end{aligned}$$

where $\sigma = -i\omega_e$

On substitution, equation (4.1) can be written as

$$\begin{aligned} z_0\left[(Z_{\ddot{z}} - m)\sigma^2 - Z_{\dot{z}}\sigma - Z_z\right] + \theta_0\left[-Z_{\ddot{\theta}}\sigma^2 - Z_{\dot{\theta}}\sigma - Z_\theta\right] &= z_0\alpha + \theta_0\beta = 0 \\ z_0\left[M_{\ddot{z}}\sigma^2 - M_{\dot{z}}\sigma - M_z\right] + \theta_0\left[(M_{\ddot{\theta}} - I_y)\sigma^2 - M_{\dot{\theta}}\sigma - M_\theta\right] &= z_0\gamma + \theta_0\delta = 0 \end{aligned} \tag{4.2}$$

where

$$\begin{aligned} \alpha &= (Z_{\ddot{z}} - m)\omega_e^2 - Z_z + iZ_{\dot{z}}\omega_e \\ \beta &= Z_{\ddot{\theta}}\omega_e^2 - Z_\theta + iZ_{\dot{\theta}}\omega_e \\ \gamma &= M_{\ddot{z}}\omega_e^2 - M_z + iM_{\dot{z}}\omega_e \\ \delta &= (M_{\ddot{\theta}} - I_y)\omega_e^2 - M_\theta + iM_{\dot{\theta}}\omega_e \end{aligned} \tag{4.3}$$

The solution of these equations of motion are such that,

$$\begin{aligned} z_0(\alpha\delta - \gamma\beta) &= 0 \\ \theta_0(\alpha\delta - \gamma\beta) &= 0 \end{aligned} \tag{4.4}$$

For the non-trivial solution,

$$\alpha\delta - \gamma\beta = 0 \tag{4.5}$$

The solution of this equation defines the stability of the system. The expansion of equation (4.5) leads to the following quartic,

$$A\sigma^4 + B\sigma^3 + C\sigma^2 + D\sigma + E = 0 \tag{4.6}$$

where

$$
\begin{aligned}
A &= (Z_{\ddot{z}} - m)\,(M_{\ddot{\theta}} - I_y) - M_{\ddot{z}} Z_{\ddot{\theta}} \\
B &= Z_{\dot{z}}\,(M_{\ddot{\theta}} - I_y) + (Z_{\ddot{z}} - m)\,M_{\ddot{\theta}} - M_{\ddot{z}} Z_{\dot{\theta}} - M_{\dot{z}} Z_{\ddot{\theta}} \\
C &= Z_z\,(M_{\ddot{\theta}} - I_y) + (Z_{\ddot{z}} - m)\,M_{\theta} - M_{\dot{\theta}} Z_{\dot{z}} - M_{\ddot{z}} Z_{\theta} - M_{\dot{z}} Z_{\dot{\theta}} - M_{\ddot{z}} Z_{\ddot{\theta}} \\
D &= Z_z M_{\dot{\theta}} + Z_{\dot{z}} M_{\theta} - M_z Z_{\dot{\theta}} \\
E &= Z_z M_{\theta} + M_z Z_{\theta} \qquad (4.7)
\end{aligned}
$$

Solving for σ will give four roots and if the sign of any of the real parts is positive then the craft's response to any perturbation will increase without limit.

It is possible upon examination of the hydrodynamic coefficients that the quartic equation may be approximated by a quadratic in σ - the high speed behaviour of a planing craft being domainated by inertial terms rather than the gravitational terms. However, for completeness, the quartic equation for stability is solved.

If there exists a complex pair of roots then the craft's response is considered oscillatory. The real part may then be used to determine how stable or unstable the craft is by looking at the time it takes for the disturbance motion to either halve itself or double itself in magnitude (Martin, 1978a). The damping, ξ, of the system can be expressed as

$$\xi = -\frac{\sigma_R}{\sqrt{\sigma_R^2 + \sigma_I^2}} \qquad (4.8)$$

where σ_R is the real part of the complex root and σ_I the imaginary part.

Chapter 5

Non-Linear Model

Planing hull operation in waves lead to strong non-linearities such as large changes in wetted surface area and the different associated flow regimes experienced by the hull. Theoretically, these conditions can be accounted for by considering the time-dependency of the hydrodynamic coefficients and the inclusion of all second and higher order terms in motion variables.

The linear model was solved within the frequency domain since the hydrodynamic coefficients were considered to be time-independent. As such, due to the presence of non-linearities in planing hull operations in waves, the application of the linear frequency domain model for predictions of planing motions in waves is questionable. For the solution to the equations of motion in waves, equations (3.5), a non-linear time-domain analysis is presented.

In waves, the forces described in equation (3.5) are continually changing as the craft goes through several different flow regimes. Wave forces are introduced into the equations of motion by considering that the wave excitation is caused by both the geometrical properties of the incident wave, altering the wetted length and draft of the craft, and by the vertical component of wave orbital velocity at the surface, altering the normal fluid velocity, V, experienced by the craft.

5.1 Wave Excitation

The incident wave, r, can be written in the space fixed system as

$$r = r_o \cos(kX_0 + \omega t) \tag{5.1}$$

defined from the velocity potential of the incident wave field, ϕ_I.

The incident wave velocity potential, ϕ_I, is represented in the equations of motion by its effect on the normal velocity, V, and the velocity component parallel to the keel, U. The vertical component of the wave orbital velocity, w_z, will affect U and V such that the normal velocity, V, and the velocity parallel to the keel, U, can be rewritten, from equation (3.4) as

$$\begin{aligned} U &= \dot{x}_{cg}\cos\theta - (\dot{z}_{cg} - w_z)\sin\theta \\ V &= (\dot{z}_{cg} - w_z)\cos\theta - x\dot{\theta} + \dot{x}_{cg}\sin\theta \end{aligned} \tag{5.2}$$

(The horizontal component of wave orbital velocity is assumed to be small compared to the forward speed. This assumption is also true in following seas.)

The relative velocity components for the craft planing in calm water are

$$\begin{aligned} U_0 &= \dot{X}_0\cos\theta_s \\ V_0 &= \dot{X}_0\sin\theta_s \end{aligned} \tag{5.3}$$

5.2 Hydrodynamic Lift, R

The hydrodynamic lift acting on a planing craft is described in Chapter 3. The flow over the craft length can be considered to occur in transverse planes which are fixed in space. The momentum of each layer of water transverse to the keel is $m_a(t).V(t)$, where $m_a(t)$ is the two-dimensional (2D) added mass per unit length and $V(t)$ is the sectional vertical relative velocity between the hull and the water plane. The added mass in the space fixed axes is considered to be equal to that in the body fixed axes (Chiu & Fujino 1989). The sectional hydrodynamic lift force, $dR(t)/dx$, can therefore be written as the time rate of change of the momentum of the water. Upon integration over the wetted length, the total lift force, $R(t)$, can be written from equation (3.73),

$$
\begin{aligned}
R(t) &= \int_0^L \frac{dR(t)}{dx}\,dx \\
&= -\int_0^L \left[m_a.\dot{V} + \dot{m}_a.V - U\frac{\partial}{\partial x}(m_a.V) \right] dx
\end{aligned} \tag{5.4}
$$

Chiu and Fujino (1989) and Chou, Chiu and Lee (1991) include the effect of frequency dependency, section 3.5, by decomposing the hydrodynamic normal force into frequency dependent and independent terms. This is achieved by reducing the momentum flux, equation (3.39), into two terms made up of the momenta,

$$m_a(x,t).(V(x,t) - V_0(x))$$

which represents the momentum due to the incremental increase in vertical relative velocity from the waves ($m_a(x,t)$ is frequency dependent), and,

$$m_a^*(x,t).V_0(x)$$

which represents the momentum due to the steady planing in waves ($m_a^*(x,t)$ is frequency independent).

Substituting these momenta into equation (5.4) leads to,

$$R = -\int_0^L \left[m_a.\dot{V} + \dot{m}_a.(V - V_0) + \dot{m}_a^*.V_0 - U\frac{\partial}{\partial x}(m_a.(V - V_0) + m_a^*.V_0) \right] dx \tag{5.5}$$

5.2.1 Damping Force, N

The sectional damping force, dN/dx, is that experienced by the section from generated radiating waves in the heaving mode and is given by Chiu and Fujino (1989) as,

$$\frac{dN}{dx} = n_z.V \tag{5.6}$$

where $n_z(x,t)$ denotes the sectional heave damping coefficient.

Integrating over the wetted length gives an expression for the total damping force,

$$N = \int_0^L [n_z.V]dx \tag{5.7}$$

Frequency dependency is included in much the same way as with the hydrodynamic force by decomposing the damping into two components relating to damping due to steady planing in waves and the increment due to oscillation in waves such that,

$$n_z(x,t).(V(x,t) - V_0(x))$$

represents the incremental sectional damping force due to the presence of waves, $n_z(x,t)$ is frequency dependent and,

$$n_z^*(x,t).V_0(x)$$

which represents the sectional damping force in steady planing in waves, $n_z^*(x,t)$ is frequency independent.

By substitution, equation (5.7) becomes,

$$N = \int_0^L [n_z.(V - V_0) + n_z^*.V_0]dx \tag{5.8}$$

5.3 Normal force resolved in Z_0-direction, Z

The total force acting in the Z_0-direction is written, from equations (3.5), (5.5), (3.83), and including the damping force contribution from (5.8), as,

$$\begin{aligned} Z &= -R\cos\theta - N\cos\theta - F_B \\ &= -\int_L \left[m_a.\dot{V} + \dot{m}_a^*.V_0 - U\frac{\partial}{\partial x}(m_a(V - V_0) + m_a^*.V_0) \right] \cos\theta dx \\ &\quad - \int_L [n_z.(V - V_0) + n_z^*.V_0] \cos\theta dx - \int_L \kappa\rho g A dx \end{aligned} \tag{5.9}$$

5.4 Normal force resolved in X_0-direction, X

The total force acting in the X_0-direction is written, from equations (3.5), (5.5), (5.8) and (3.83) as:

$$\begin{aligned} X &= -R\sin\theta - N\sin\theta \\ &= -\int_L \left[m_a.\dot{V} + \dot{m}_a.(V - V_0) + \dot{m}_a^*.V_0 - U\frac{\partial}{\partial x}(m_a.(V - V_0) + m_a^*.V_0) \right] \sin\theta dx \\ &\quad - \int_L [n_z.(V - V_0) + n_z^*.V_0] \sin\theta dx \end{aligned} \tag{5.10}$$

5.5 Hydrodynamic pitch moment, M

The total hydrodynamic pitch moment acting through the CG is written, from equations (3.5), (5.5), (3.83) and including the damping contribution from (5.8) with moment arm x_D,

$$\begin{aligned} M &= Rx_C + Nx_N + F_Bx_B \\ &= -\int_L \left[m_a.\dot{V} + \dot{m}_a.(V - V_0) + \dot{m}_a^*.V_0 - U\frac{\partial}{\partial x}(m_a.(V - V_0) + m_a^*.V_0) \right] .xdx \\ &\quad - \int_L \left[n_z.(V - V_0) + n_z^*.V_0 \right] .xdx - \int_L x.\kappa\rho g A\cos\theta dx \end{aligned} \tag{5.11}$$

5.6 The Equations of Motion

From the hydrodynamic forces and moments, the equations of motion in waves become:

$$\begin{aligned} (m + M_a\sin^2\theta)\ddot{x}_{cg} + (M_a\sin\theta\cos\theta)\ddot{z}_{cg} - (Q_a\sin\theta)\ddot{\theta} &= T_x + X' - D\cos\theta \\ (M_a\sin\theta\cos\theta)\ddot{x}_{cg} + (m + M_a\cos^2\theta)\ddot{z}_{cg} - (Q_a\cos\theta)\ddot{\theta} &= T_z + Z' + D\sin\theta + W \\ -(Q_a\sin\theta)\ddot{x}_{cg} - (Q_a\cos\theta)\ddot{z}_{cg} + (I - I_a)\ddot{\theta} &= Tx_P + M' - Dx_D \end{aligned} \tag{5.12}$$

where

$$\begin{aligned} M_a(t) &= \int_L m_a(x,t)dx \\ Q_a(t) &= \int_L m_a(x,t)xdx \end{aligned}$$

and where

$$\begin{aligned} X' &= X - \left\{ -(M_a\sin^2\theta)\ddot{x}_{cg} - (M_a\sin\theta\cos\theta)\ddot{z}_{cg} + (Q_a\sin\theta)\ddot{\theta} \right\} \\ Z' &= Z - \{\text{appropriate acceleration terms}\} \\ M' &= M - \{\text{appropriate acceleration terms}\} \end{aligned}$$

The solution to these equations, following Zarnick (1978), can be accomplished by introducing the state vector, $\vec{x}$ where,

$$\vec{x} = [\dot{x}_{cg},\ \dot{z}_{cg},\ \dot{\theta},\ x_{cg},\ z_{cg},\ \theta]$$

If matrix A represents the coefficients of the acceleration matrix $\ddot{\vec{x}}$ and matrix $\vec{g}$ represents the right-hand side of the equations of motion such that,

$$A\ddot{\vec{x}} = \vec{g}$$

then the acceleration matrix is written as,

$$\ddot{\vec{x}} = A^{-1}\vec{g}$$

Using the Runge-Kutta integration method, the state vector $\vec{x}$ can therefore be determined.

5.6.1 Equations of Motion for the Simplified Case of Constant Forward Speed

The surge degree of freedom can be uncoupled since there is little effect on the pitch and heave motions ((Blake 1993); (Fridsma 1969); (Martin 1978a)). Also for experimental testing of models where the model is towed at constant speed, the examination of the theoretical case for constant speed is necessary.

Zarnick also assumed that the thrust and drag forces are small in comparison to the hydrodynamic forces and that if their action was through the centre of gravity, the equations of motion could be simplified to,

$$\begin{aligned} \ddot{x}_{cg} &= 0 \\ (m + M_a\cos^2\theta)\ddot{z}_{cg} - (Q_a\cos\theta)\ddot{\theta} &= Z' + W \\ (Q_a\cos\theta)\ddot{z}_{cg} + (I + I_a)\ddot{\theta} &= M' \end{aligned} \tag{5.13}$$

By neglecting second order perturbation terms and assuming that the pitch angle, θ, is small, the simplified equations of motion can be written in matrix notation as,

$$\begin{bmatrix} m_{33} & m_{35} \\ m_{53} & m_{55} \end{bmatrix}\begin{bmatrix} \ddot{z}_{cg} \\ \ddot{\theta} \end{bmatrix} + \begin{bmatrix} n_{33} & n_{35} \\ n_{53} & n_{55} \end{bmatrix}\begin{bmatrix} \dot{z}_{cg} \\ \dot{\theta} \end{bmatrix} + \begin{bmatrix} c_{33} & c_{35} \\ c_{53} & c_{55} \end{bmatrix}\begin{bmatrix} z_{cg} - z_s \\ \theta - \theta_s \end{bmatrix} = \begin{bmatrix} e_3 \\ e_5 \end{bmatrix} - \begin{bmatrix} c^*_{33} & c^*_{35} \\ c^*_{53} & c^*_{55} \end{bmatrix}\begin{bmatrix} z_s \\ \theta_s \end{bmatrix}$$

The coefficients of the motion variables are given in Appendix D. The matrix notation is given in order to provide some analysis of the cross-coupling effects and frequency and amplitude dependency of the coefficients. The solution for z_{cg} and θ from the above equation will differ from the solution for z_{cg} and θ from equation (5.13) because of the neglect of the second order terms.

Chapter 6

Validation and Results

This chapter will present the validation of the linear and non-linear models and the results of a parametric investigation into the vertical dynamic effects experienced by a series of hard chine monohull forms operating in calm water and in waves. The validation of a numerical model for planing hull performance in calm water is readily achieved by comparison with a large amount of experimental data that exists for steady state calm water planing. In waves however, there is little published planing data in existence.

One published set of data for planing in waves comes from Fridsma(1969), (1971) who created a systematic series of tests on a hard chine, constant deadrise monohull form operating in regular and irregular seas. The craft lines are given in figure (A.13). Fridsma tested 16 configurations in total with changes in the following parameters:

Parameter	Variation
L/B	4, 5, 6
β	10°, 20°, 30°
C_Δ	0.608, 0.631, 0.912
LCG(%L)	52 - 68
τ	4°, 5°, 6°
k_y(%L)	20.0 - 26.5
$V_{\text{knots}}/\sqrt{L_{\text{feet}}}$	2, 4, 6

Table 6.1: Hard Chine Parameters; Fridsma(1969), (1971)

Fridsma used this simple series of constant deadrise models in order to study the effect of hull geometry, load conditions, running trim and craft speed on the craft response in calm water and in waves. The aim was to also investigate the linearity of the response in waves and the effect of the change in parameters on the rough water characteristics of resistance, heave and pitch motions and accelerations. Whilst the models are unsuitable for typical planing hull form design, their simplicity of construction allowed invaluable characterisation of the effect of systematically changing the parameters on calm and rough water performance. This provided much needed insight then as it does now; the size of his test matrix has not been repeated since, although a new semi-planing systematic series is under investigation (Grigoropoulos & Loukakis 1998).

The previously described series will be primarily used to validate the non linear numerical model, NoLiPCraMP, and in so doing supply a numerical parametric investigation that should be directly comparable with the experimental findings. From the experimental tests, there exists some calm water performance data that will also be used to validate the linear numerical model, MOTIONS. Furthermore, the test matrix will be numerically expanded to investigate parametric changes on calm water stability and to cover the effect of gyradius on planing performance in waves.

6.1 Calm Water Stability

Martin(1978a), from which the linear theory is derived, uses the experimental work of Day and Haag(1952) to validate the theoretical model. Some of those results are repeated in the same format in order to verify the author's correct numerical implementation of Martin's theory.

Day and Haag used a series of prismatic models described in Table 6.2 to explicitly investigate the porpoising phenomena. For a particular configuration at a particular speed, they moved the position of the LCG increasingly aft until the inception of porpoising. The subsequent trim angle at inception was taken to be the critical trim angle, τ_c, for the position of the critical LCG, LCG_c. Curves of critical trim angle, or critical LCG, against speed provide porpoising stability boundary information.

Numerically, the inception of porpoising can be predicted by analysis of the roots of equation (4.6). Approaching porpoising there exists a complex pair of roots which

Parameter	Variation
B	96.5mm
β	0°, 10.6°, 20.5°
C_Δ	0.36, 0.48, 0.72
k_y/B	1.2
C_V	2 to 5

Table 6.2: Hard Chine Parameters; Day and Haag (1952)

reflects the system's tendency to oscillate given a disturbance. The sign of the real part of any of the roots determines the system's stability. Hence if any of the roots have a positive real part then the system is considered unstable. A plot of the least stable real root, σ_R, against LCG is shown in figure(A.14) for $\beta = 10.6°$ and $C_\Delta = 0.48$ for three speeds $C_V = 2.33$, 2.67 and 3.17. The agreement with Martin's theoretical results is excellent for all three speeds.

The non linear numerical model, NoLiPCraMP, can also be used to assess calm water performance. This is achieved in two ways. Firstly through the response of the craft (for a given LCG) to a set of unbalanced initial conditions. Generally, for a 1.143m model craft, the convergence time to calm water steady-state planing was no more than 5 seconds. If the craft response to an unbalanced set of initial conditions, on changing the position of the LCG, fails to converge on a steady state solution after 20 seconds, the configuration is deemed unstable. The second approach is based upon the sign of the damping terms, which for all but one, n_{53}, is always negative. When all the means of the damping terms become negative for a given LCG, or more specifically as the n_{53} term just becomes negative, the craft is considered unstable.

Figure (A.15), (A.16) and figure (A.18) show the comparison between predicted porpoising boundaries, τ_c against speed, for the range of load coefficient, C_Δ, for deadrise of 0°, 10.6° and 20.5°. The difference between the author's linear prediction and Martin's results are not large and show good comparison with experiment. Martin points out the fact that at higher speeds, larger deadrise and lighter loads there is more propensity for the chine to become unwetted at the transom. This affects the dynamic lift force since there is no longer any separation and no cross-flow force. Theoretically, the cross-flow force is always considered since it is always different from zero for a non-zero trim angle, regardless of the fact that separation may have physically occurred. This is a short coming of the theoretical linear model. For unwetted chines, the lift force will be over predicted, the craft will be more dynamically supported and the stability afforded by the hydrostatic force will be less. A smaller critical trim angle is therefore predicted for lighter craft at higher speeds.

The stability boundaries for the 10.6° deadrise craft are shown in figure (A.17) for the non-linear theory. The results show much better agreement with experiment for all three load coefficients. This suggests that the distribution of lift force is much better predicted by the non-linear model without the need for such widespread empirical fits to established smooth water planing data used in the linear theory. Unlike the linear theory which considers three distinct regions of varying added mass, the non-linear theory determines added mass in a consistent manner along the hull length; evaluated based upon the actual immersion and a splash-up quantity (which is a value between Von Karman's and Wagner's approach, section 3.3.3.3). Whether the non-linear theory adopts a more realistic representation of the flow dynamics than that of the linear theory is open to question since the linear theory distribution of added mass is fundamentally based upon a physical observation and as such would be considered at first sight to be more applicable.

Martin's expressions for steady state hydrodynamic force and moment (Appendix B; equations (B.34) and (B.36)) are well founded on empirical evidence from many sources of calm water planing experiments. Payne (1994), (1995) demonstrates the difficulty experimenters have in identifying regions of wetted surface, in particular wetted keel length and wetted chine lengths. Martin's expressions for wetted lengths are based upon those of Brown (1971), but although Brown's expressions fit his own data well, there is still some scatter on comparison with other experimenters results (Payne 1994). This scatter affects Martin's prediction of lift force since the added mass distribution is dependent on wetted surface. This source of error can be seen in figure (A.19), where the predicted position of LCG_c is compared with the actual measured values from Day and Haag. The comparison forms some measure of the accuracy of the derivation of the steady-state equations and shows that because LCG_c is predicted further aft to achieve the similar critical trim angles seen in experiment, the steady-state equations must under predict the running trim angle.

As has been previously mentioned, the non-linear theory predicts the stability boundaries more accurately over the whole speed range. The predicted critical trim angle is very favourable with experiment and shown on figure (A.19), along with the linear results and experimental values, is the distribution of critical LCG with speed. Where the linear theory under predicts the trim angle for a given LCG, the non-linear theory is a great improvement. This reflects a forward shift in the predicted centre of pressure which allows for a more forward location of LCG for a given trim angle. The reason for the improved fit of stability boundaries with the non-linear theory's distribution of added mass compared to the linear theory approach is now more clear. The forward sections of the craft for the non-linear theory develop more lift for the same trim angle and LCG than the linear theory because of the generalisation of the evaluation of added mass. Subsequently the centre of pressure is more forward in the non-linear theory than the linear approach which results in an increased trim angle, countered by an appropriate forward movement in the LCG.

The lack of spread of data in figure (A.19) shows that the effect of increasing hull loading on porpoising inception is small. Martin points out that this is accounted for by Day and Haag's respective decrease in gyradius. Both of these quantities affect the critical LCG. Figure (A.20) reflects this compensatory nature between k_y/B and C_Δ since τ_c is decreased with increasing load and gyradius for all values of speed. Furthermore, the curves of the last graph in figure (A.21) tend to reach a maximum value on increasing speed and then reduce again in magnitude with increasing speed. This is more obvious for the lighter models. It would seem that increasing speed can actually extricate the craft out of the porpoising condition provided the craft is only weakly unstable.

Figure (A.21) shows the effect of increasing deadrise on critical LCG position. As deadrise increases LCG_c can become further aft (increasing the critical trim angle) before porpoising occurs. This is true for all speeds and all loads. The porpoising boundaries produced as a function of deadrise show similar trends as the boundaries produced from functions of load when plotted against speed. Provided the craft is not too far over the limit for porpoising, increasing speed can actually remove the craft from the porpoising region.

Fridsma published some calm water data on porpoising stability for the three deadrise angles of 10°, 20° and 30° and for three load coefficients $C_\Delta = 0.304$, 0.608 and 0.912. The data is limited and so Table 6.3 is constructed to show the ratio of predicted critical LCG over the measured critical LCG and predicted critical mean wetted length to measured critical mean wetted length. The last two columns show the same two quantities but with a different method of calculation of critical LCG and mean wetted length that follows directly from Savitsky (1964).

β (degs)	C_Δ	C_V	Martin		Savitsky	
			$\frac{\lambda_c \text{ calculated}}{\lambda_c \text{ measured}}$	$\frac{\lambda_{mc} \text{ calculated}}{\lambda_{mc} \text{ measured}}$	$\frac{\lambda_c \text{ calculated}}{\lambda_c \text{ measured}}$	$\frac{\lambda_{mc} \text{ calculated}}{\lambda_{mc} \text{ measured}}$
10	0.304	3.33	0.94	1.04	0.93	1.06
	0.304	2.00	0.85	0.95	0.94	1.00
	0.608	3.00	0.90	0.83	0.90	0.99
	0.912	3.83	1.06	0.90	0.86	0.94
20	0.304	2.98	0.96	0.89	1.02	1.00
	0.304	2.66	0.98	1.02	1.00	1.12
	0.608	2.73	0.82	0.95	1.03	0.97
	0.608	3.89	0.95	0.93	1.07	1.17
30	0.608	2.73	0.90	0.82	1.02	0.95
	0.912	3.85	1.03	0.93	1.07	1.00

Table 6.3: Comparisons of critical data derived from Martin and Savitsky with experiments of Fridsma

The error from Martin's method is large in some instances which is a direct result of the under prediction of steady state-trim angle. Savitsky's equations relating trim and LCG generally predict the actual critical values from Fridsma's experiments to a much closer degree.

6.2 Validation and Results in Waves

The aim of the theoretical investigation is to provide insight into the planing craft dynamics in calm water and in waves. In this respect, the following theoretical results are presented in a manner similar to the presentation of Fridsma's results. The exceptions are that no resistance information is given, although preliminary results for added resistance calculations are given in Appendix E, and only one length to beam ratio, equal to 5, was used. In total, 13 out of his 16 configurations were theoretically analysed. Furthermore, new theoretical configurations were introduced in order to ascertain the effect of gyradius at $V_{\mathrm{knots}}/\sqrt{L_{\mathrm{feet}}} = 4$ and calm water running trim angle for $V_{\mathrm{knots}}/\sqrt{L_{\mathrm{feet}}} = 6$.

6.2.1 Validation

This section aims to validate the numerical model, NoLiPCraMP, by direct comparison with the experimental results outlined above. Effect of frequency dependence will be analysed and the effect of empirical corrections on the equations governing lift; Payne's dynamic suction, aspect ratio, and splash-up. The effect of second order terms in perturbation variables is also investigated.

6.2.1.1 Effect of Frequency Dependency

Appendix C describes the theory behind the evaluation of sectional added mass and damping required in the hydrodynamic coefficients. The two approaches are based on the assumption of frequency independence or frequency dependence. Typically, the added mass and damping coefficients are evaluated at an infinite frequency where both the added mass and damping coefficient have reached an asymptotic limit. Troesch (1992) has shown for low to moderate planing speeds that the hydrodynamic coefficients are frequency dependent, therefore it is prudent to include frequency dependence in the evaluation of added mass and damping.

Figures (A.23) to (A.35) show the predicted response of the tested craft configurations against the experimental results in the form of response amplitude operators (RAO).

The predicted response is shown for frequency dependence and independence in each case. The accelerations are given in figures (A.70) to (A.82).

The agreement between the frequency independent numerical model and experimental values for all 13 craft is fair. For at least 10 configurations, the comparisons in motion response magnitudes is very good with the slower craft, configurations C, H and L, generally showing less agreement. The qualitative aspects of all 13 tested craft in respect to their vertical motions is excellent; peak response frequencies are well defined.

$V_{\text{knots}}/\sqrt{L}_{\text{feet}} = 2$

At this speed to length ratio, the predicted results would be expected to depart substantially from the experimentally determined values. The craft at this speed are generally operating at or just below the onset of planing and as a result, their resistance is at or near a maximum. The viscous effects are not considered by the numerical model and there is no inclusion of the associated drag. Furthermore, the numerical model in this instance assumes that there is complete separation of flow off the transom corner and chines, which is not a physical representation at this speed.

Configurations C, D, H and L operate at this speed and their predicted motions are given in figures(A.25), (A.26), (A.30) and (A.34) respectively and the accelerations are given, respectively, in figures(A.72), (A.73), (A.77) and (A.81). Employing the frequency indepedent approach, the actual agreement in magnitude and peak frequency response for all these configurations is fair, especially for pitch motions and at the lower encounter frequencies. For the encounter frequencies with comparable response magnitudes, the accelerations, too, show good agreement. At higher encounter frequencies, $\lambda/L < 2$, the vertical responses are underpredicted. Also for configurations C, H and L, the heave response at the lower encounter frequencies, $\lambda/L > 3$, are over predicted.

The frequency independent predicted heave and pitch phases tend to show similar characteristics to Fridsma's experimental results, with their maximum lag occurring at about half the resonant response frequencies. Agreement is best at either end of the frequency spectrum; at the very long wavelengths and at the very short wavelengths. Pitch phases show the most agreement with experiment, reflecting the better agreement in predicted pitch response.

Making an allowance for frequency dependency would be expected to make a large difference in the predicted responses. Figures (A.150) and (A.151) show the added mass and damping curves against encounter frequency for a range of speeds and extreme drafts (just above the keel and at the chine line). At the low speed range, the added mass and damping could not be described as being asymptotic in nature. In fact the added mass values for the low encounter frequencies is well underpredicted by the asymptotic value typically used in planing analyses. Following Troesch (1992), the hydrodynamic coefficients show considerable frequency dependency at low to moderate planing speeds and better agreement in the numerical prediction of motions would be expected with this dependency in mind. Figures (A.25), (A.26), (A.30) and (A.34), show the inclusion of frequency dependent terms does little to improve the prediction of motions at the lower encounter frequencies but at the higher frequencies tends to remove the underprediction of motions. Although the agreement with experimental motion responses at longer wavelengths is worse in these configurations, the overprediction in response improves the agreement in acceleration magnitudes for the same encounter frequencies, figures (A.72), (A.73), (A.77) and (A.81). For those higher frequencies with improved motion prediction, the predicted accelerations are noticeably improved too.

With the frequency dependent approach, at wavelengths $\lambda/L \geq 3$, the predicted phase lag in heave and pitch is much more comparable to experiment, despite the poorer prediction in motion responses for these wavelengths. In fact, where the predicted motion responses show better agreement at $\lambda/L \leq 1.5$, the predicted phase lag is generally less comparable, with pitch phase lag at $\lambda/L = 1$ significantly different.

For this low craft speed, drawing conclusions for the discrepancy in predicted motions with experimental results solely from predicted responses would be unwise. Too many assumptions are made which are unwarranted at this speed and although the predicted responses are fair, compromises between hydrostatic and hydrodynamic phenomena are uncertain. It can however be tentatively proposed that at this speed, the effect of frequency dependence on predicted vertical responses is important.

$V_{\text{knots}}/\sqrt{L}_{\text{feet}} = 4$

This speed to length ratio represents the moderate post resistance hump planing speed. There is still some hydrostatic force contributing to the overall lift but, predominantly, the lift is hydrodynamic. Configurations A (figures(A.23), (A.70)), E (figures(A.27), (A.74)), F (figures(A.28), (A.75)), I (figures(A.31), (A.78)) and K (figures(A.33), (A.80)) operate at this speed. The agreement in predicted (frequency independent) and experimental vertical motion responses is very good in all cases and always at the higher encounter frequencies. At high encounter frequencies, the predicted added mass terms which govern the hydrodynamic lift are in less mathematical error. At lower frequencies though, the added mass will depart from the asymptotic value, affecting the predicted lift. However the accelerations, which do not show such favourable comparison as the predicted motions, are generally better predicted at the lower encounter frequencies. This can be explained by the relatively low accelerations experienced by the craft at longer wavelengths which are not so sensitive to inaccuracies in the numerical modelling.

Predicted heave and pitch phases at all wavelengths for all the configurations are extremely good, with two exceptions. Configuration F (figure(A.28)) has poor agreement in heave phase lag at $\lambda/L \leq 2$ and in pitch at $\lambda/L \leq 1.5$. Configuration K (figure(A.33)) shows less agreement with experiment, especially in pitch, at $\lambda/L \leq 1.5$. What is significant, given the overall agreement in pitch and heave responses and phase angles, is the error in predicting accelerations, especially at the bow and at the higher frequencies of $\lambda/L \leq 2$.

Figures (A.150) and (A.151) show that for $V/\sqrt{L} = 4$, the added mass is still very much frequency dependent. The effect of adding this dependency for this speed is to generally reduce the predicted motions at high frequencies, $\lambda/L < 2$, and increase the predicted motions at $\lambda/L > 3$. Except for configurations E and G, at lower frequencies the agreement is improved for pitch response. No configurations show an improvement in predicted heave motions on considering frequency dependency. Including frequency dependent added mass does not improve the predicted phase angles either, except for pitch phase of configuration F. In fact for $\lambda/L \leq 3$, for all configurations except F, the pitch phase agreement is worse and for $\lambda/L \leq 4$, the heave phase agreement is poorer. The generally poor agreement for phase angles just reflects the poor agreement in motion predictions.

Surprisingly, given the poor agreement in motion responses and phase angles, the predicted accelerations are generally improved by considering frequency dependent added mass, except for configuration I. Configuration E, figure (A.74), shows marked improvement in prediction of bow accelerations over the whole frequency range, although the CG accelerations are not so well predicted in the high frequency range. Configurations F, figure (A.75), and I, figure(A.78), are more comparable in the low frequency range but well underpredicted in terms of magnitude and trend at wavelengths less than 3 craft lengths. Configuration K, figure(A.80), has improved acceleration predictions on considering frequency dependency over the whole frequency range but the CG accelerations, whilst exhibiting the correct trend, are underpredicted.

$V_{\text{knots}}/\sqrt{L}_{\text{feet}} = 6$

This speed to length ratio represents the fully planing regime, where hydrodynamic lift is the predominant physical effect and buoyancy forces are negligible in comparison. Configurations B (figures (A.24), (A.71)), G (figures (A.29), (A.76)), J (figures (A.32), (A.79)) and M (figures (A.35), (A.82)) operate at this speed. More so than the lower speed to length ratios, the added mass exhibits more frequency independence. Indeed the results from the frequency independent approach at this speed are very good, with only the more heavily loaded configuration G underpredicting heave and pitch motions across the whole frequency range. Experimentally, configuration J demonstrates a second resonant peak which reflects the onset of the craft leaping from crest to crest. This second resonant peak is successfully picked up by the numerical model for the frequency independent approach.

The predicted accelerations are generally comparable with experiment. Configuration B, figure (A.71), shows good agreement in CG accelerations at the high frequency and low frequency ends but fails to predict the peak CG acceleration at $\lambda/L = 3$. The bow accelerations on the other hand seem to be fairly predicted. Configuration G, figure (A.29), has underpredicted heave and pitch responses. The predicted accelerations, figure (A.76), however show good agreement across the whole frequency range. Configuration J shows poor agreement in CG accelerations except between $1.5 \leq \lambda/L \leq 2$, figureA.79. The bow accelerations however demonstrate extremely favourable comparisons with experiment. Predicted accelerations for configuration M, figure (A.82), are only comparable for high frequency CG accelerations, although a similar trend is evident at lower frequencies despite being of lower magnitude.

The added mass and damping curves, figures (A.150) and (A.151), demonstrate only some frequency dependence at the very long wavelengths and it is expected that including frequency dependence will result in an under prediction of motions at high frequencies and an over prediction at lower frequencies. This is correct for configurations

J and M and in all the configurations the heave and pitch response is under predicted at high frequency. Consequently, the lack of predicted lift force at high frequency leads to the failure to define the second resonant peak exhibited by configuration J. The predicted accelerations are generally poor except at longer wavelengths.

Summary

At this stage, it is clear that the frequency independent approach shows very favourable comparisons with experimentally determined results for heave and pitch. Generally for the frequency dependent approach, the predicted motions are too small at higher frequencies ($V/\sqrt{L} \geq 4$, $\lambda/L \leq 3$ and too large at lower frequencies, $\lambda/L > 3$ for $V/\sqrt{L} \geq 4$. Taking the asymptotic value for added mass at high frequency leads to better predictions of motions despite the fact that mathematically the asymptote has not yet been reached. Using the correct value of added mass at high frequency significantly reduces the predicted motions. There would appear, at high frequencies, to be some loss in the theoretical prediction of lift that is compensated by the over prediction of added mass.

6.2.1.2 Effect of Second Order Perturbation Terms

Chiu and Fujino (1989) removed all the terms $O(v^n)\, n \geq 2$ where v is any motion perturbation variable in the equations of motion. Zarnick (1978) considers all the second (and higher) order terms in the equations of motion. The difference between these methods can be seen in figure (A.107) and figures (A.108), (A.109). Figure (A.107) plots the absolute error in motion response for three speed to length ratios, 2, 4 and 6, over the frequency range of $\lambda/L = 1$ to 6 for the 10° deadrise models. The maximum error does not exceed 10%. At the lower speed, $V/\sqrt{L} = 2$, the error in neglecting higher order terms is not as significant as at the higher speed, $V/\sqrt{L} = 6$. This is expected due to the increase in non-linearity in the craft response with increasing speed, hence the neglect of non-linear terms will be more obvious. At the higher speeds, the maximum errors occur at the resonant frequencies (two in the case of configuration J), figures (A.108) and (A.109). This also is not unlikely since the accurate prediction in magnitude of these resonant peaks requires the inclusion of the non-linear effects. Despite these discrepancies, the error in neglecting second order and higher terms in the hydrodynamic coefficients is usually less than 10%. A consequence of this is that the equations of motion maybe reduced to first order terms in motion perturbation variables and the individual behaviour of the hydrodynamic coefficients investigated.

6.3 Parametric Investigation

The theoretical model is justified in its use ultimately because of the overall agreement between the predicted and experimental vertical responses. One of the aims of the theoretical model was to allow a parametric investigation into the performance of a series of hard chine constant deadrise hulls by systematically changing and analysing the effect of individual parameters, Table 6.4. The results of this investigation are described in the following sections.

	$V_{\mathbf{knots}}/\sqrt{L}_{\mathbf{feet}}$		
Parameter	2	4	6
Deadrise	$\surd$	$\surd$	$\surd$
Trim	$\surd$	$\surd$	
Gyradius		$\surd$	
Load		$\surd$	
Waveheight	$\surd$	$\surd$	$\surd$

$\surd$ = Heave, Pitch, Accelerations (Bow and CG), Hydrodynamic Coefficients

Table 6.4: Test Matrix for Parametric Investigation

6.3.1 Linearity

Configurations H, A and B are used to test the linearity of the system and represent 10° deadrise craft at $V/\sqrt{L} = 2$, and 20° deadrise craft at $V/\sqrt{L} = 4$ and 6, respectively.

Heave and Pitch Motions

Figure(A.38) and figure(A.47) show the effect of waveheight on the heave and pitch motions for $H/B = 0.111, 0.222, 0.333$ for $V/\sqrt{L} = 2$. The responses are clearly linear over the whole tested frequency range.

With increasing speed $V/\sqrt{L} = 4$, the motions depart from their linear behaviour, figure(A.36). Figure(A.45) shows the motion responses to be linear only at the extreme ends of the encounter frequency spectrum and the non-linear behaviour lies in the region

$2 \leq \lambda/L \leq 3$. In this region for a unit increase in waveheight, the motions increase as a fraction of unity so that the non-linear behaviour is damped with increasing waveheight.

For $V/\sqrt{L} = 6$, the non linear motions, figure(A.37), which increase at a similar rate of increase with waveheight to that of $V/\sqrt{L} = 4$, are exhibited at $\lambda/L = 2$ and 4, figure (A.46). The pitch response grows at a much lower rate of increasing waveheight at $\lambda/L = 2$.

Fridsma also applied a spectral analysis to the motion response in irregular seas. Since spectral techniques can only be applied with meaning to linear systems, the agreement between a RAO derived from a spectral analysis and the RAO for motions in regular seas will provide a measure of the system's linearity. The results can be seen in figure (A.48) and (A.49) for configurations H and I for operations in irregular seas of $H_{1/3}/B = 0.222$ and $T_0 = 1.5$ seconds, where the modal period is chosen so that the wave spectrum is bounded by similar frequency limits used in the regular sea analysis. Configuration H operates at $V/\sqrt{L} = 2$ and as such the reponses in waves would be expected to vary linearly with waveheight. In fact there is very good agreement with the predicted response in regular waves. Configuration I on the other hand is operating at twice the speed:length ratio as configuration H and the agreement between the response in regular waves and the linear decomposition of response in irregular waves would be expected to be different due to the increased non-linearity of the system. However, even at this speed, the comparison is still very good and demonstrates that the response of configuration I is apparently linear over the whole frequency range. Spectral analysis is covered in section 7.5.1.

Accelerations

Figures(A.39), (A.42), and figures(A.40), (A.43), and figures(A.41), (A.44), show the effect of waveheight on the accelerations experienced at the bow and centre of gravity.

For $V/\sqrt{L} = 2$, figure (A.44) shows that increasing the waveheight tends to linearly increase the accelerations experienced at the CG and bow except in the very short wavelengths, $\lambda/L < 1.5$.

For the intermediate tested speed of $V/\sqrt{L} = 4$, figure (A.42) shows that the region of linear response of bow and CG accelerations with waveheight is reduced to $\lambda/L > 3$. In very short wavelengths and in the highest waves, $\lambda/L \leq 1$, the maximum bow and

CG accelerations reduce in magnitude.

At the highest speed $V/\sqrt{L} = 6$, the region of linear behaviour is further reduced to wavelengths equal to, and in excess of, six craft lengths. In the highest waves and in the shorter wavelengths there is a tendency for the accelerations to reduce in magnitude.

Hydrodynamic Coefficients

Figure A.110 and figure A.111 show the behaviour of the hydrodynamic coefficients with increasing waveheight for $V_{\text{knots}}/\sqrt{L_{\text{feet}}} = 4$. The pure heave and pitch added mass and inertia coefficients increase with increasing waveheight over the whole frequency range. Also, increasing the encounter frequency increases the magnitude of m_{33} and m_{55} until a maximum value is reached at $\lambda/L = 2$. From this point on these two coefficients reduce again in value with increasing encounter frequency, with attenuation in higher encountered waves. The cross-coupling coefficients reflect the same trends but in a reciprocal fashion; increasing waveheight reduces the coefficient magnitudes whilst increasing the frequency also reduces the magnitudes until $\lambda/L = 2$ whereupon the coefficients start to increase again in value. For all frequencies there is strong linear behaviour with increasing waveheight, with the exception of the very high frequencies and waveheights for the pure heave coefficient, m_{33}.

The damping terms are affected by waveheight significantly at higher encounter frequencies and for $H/B > 0.222$. In fact where the change in added mass and inertia terms were if anything attenuated in magnitude with increasing waveheight, the change in magnitude of the damping terms of n_{33}, n_{35} and n_{55} are increased. The absolute magnitude of all the damping coefficients increase with increasing waveheight, except for the cross-coupling term of pitch induced heave, n_{35} where in very high waves and at high frequency, $\lambda/L \leq 2$, the absolute value decreases. In terms of linearity with waveheight, all coefficients show this behaviour for low frequencies, $\lambda/L \geq 3$.

Generally, the absolute magnitudes of the stiffness coefficients increase with waveheight for all encounter frequencies. However there is an exception in c_{35} for the very high encounter frequency of $\lambda/L = 1$ and a waveheight of $H/B = 0.222$ where the absolute stiffness reduces. The waveforcing terms reflect the same trends with increasing waveheight.

Figure A.112 and figure A.113 shows the variation of the hydrodynamic coefficients with increasing waveheight at the highest speed of $V_{\text{knots}}/\sqrt{L}_{\text{feet}} = 6$. The trend in hydrodynamic coefficient values with waveheight are similar to the lower speed trends. However, there is a pronounced non-linear behaviour at $\lambda/L = 4$ for all the coefficients, except for the wave-forcing coefficients, e_3 and e_5, which are linear for all frequencies.

The added mass and inertia coefficients reflect an increase in the frequency range of non-linear behaviour, from the very high encounter frequencies of $\lambda/L = 1$ to $\lambda/L = 4$. Furthermore, there is increasing non-linear behaviour with decreasing encounter frequency until the maximum non-linear behaviour at $\lambda/L = 4$. After this point, at very long wavelengths, the trend becomes more linear.

The damping coefficients of n_{33} and n_{53} show strong linear behaviour at all frequencies except for $\lambda/L = 4$. The trend of pitch induced heave damping, n_{35}, and pure pitch damping, n_{55}, is non-linear and becomes increasingly more non-linear towards $\lambda/L = 4$.

The stiffness and wave-forcing terms shown in figure A.113 demonstrate strong linearity with increasing waveheight for all wavelengths except for $\lambda/L = 4$.

Summary

Motions show marked non-linear behaviour with increasing waveheight except at the very high and very low encounter frequencies. CG and bow accelerations demonstrate linear behaviour with increasing waveheight for a frequency range that diminshes towards the longer waves with increasing speed. For $V/\sqrt{L} = 2$, despite non linear accelerations at $\lambda/L < 1.5$, the motions linearly increase with waveheight over all wavelengths. For low waveheights $H/B \leq 0.111$, the motions could be described as generally linear with wave height.

The hydrodynamic coefficients reflect the linear trends associated with increasing waveheight, and the movement of this linear trend towards longer wavelengths as speed is increased.

6.3.2 Effect of Speed and Deadrise

Three speed to length ratios, $V/\sqrt{L} = 2$, 4 and 6 were tested for configurations with 10°, 20° and 30° deadrise cross-sections at $H/B = 0.111$.

Heave and Pitch Motions

For all deadrise configurations, the increase in speed not only increases the resonant motions but shifts the resonant response to longer wavelengths, $\lambda/L \geq 3$, and reduces the frequency bandwidth for maximum motions, figures (A.50), (A.51), (A.52), and figures (A.54), (A.55), (A.56). The effect of increasing speed though is to reduce the motions at short wavelengths, except for the case of configuration J (which represents the highest speed and smallest deadrise angle).

Phase angles show expected contouring behaviour at very long wavelengths, i.e. the motions at the CG show no phase lag[1]. Phase lag increases with increase in wave frequency until wavelengths reach from 1.5 to 2 craft lengths. Phase lag then appears to remain constant or decrease with higher wave frequency. The size of the maximum lag increases with increasing craft speed.

Accelerations

Accelerations increase with increasing speed for all deadrise variants over the whole frequency range, figures (A.60), (A.61), (A.62) and figures (A.63), (A.64), (A.65). The effect of deadrise is to reduce the peak accelerations throughout the speed range. At longer wavelengths, $\lambda/L > 3.5$ the accelerations tend to increase more linearly with speed for increasing deadrise angles.

Hydrodynamic Coefficients

Figures (A.95), (A.96) and (A.97), (A.98) and (A.99), (A.100) show the effect of increasing deadrise on the hydrodynamic coefficients whilst (A.101), (A.102) and (A.103), (A.104) and (A.105), (A.106) show the effect of increasing speed. Generally, the values of pure heave, m_{33}, and pitch, m_{55} decrease with increasing speed. The absolute magnitudes of the cross-coupling terms, m_{35} and m_{53}, are equal and remain very similar in magnitude with increasing speed, although for the 10° deadrise configurations, the cross-coupling terms reduce to zero for $\lambda/L = 3$. The effect of deadrise on these terms is negligible for $V_{\text{knots}}/\sqrt{L}_{\text{feet}} = 2$. For $V_{\text{knots}}/\sqrt{L}_{\text{feet}} = 4$, increasing deadrise reduces the added mass and inertia terms, whilst at $V_{\text{knots}}/\sqrt{L}_{\text{feet}} = 6$, although the magnitudes are smaller to start with, the added mass and inertia terms increase with increasing deadrise.

---

[1] Pitch phase is plotted relative to waveheight and so is 90° out of phase with waveslope. Contouring condition therefore corresponds to 90° pitch phase lead

Increasing speed generally reduces the amount of damping in the system. This change becomes more obvious on increasing the deadrise angle. The n_{53} term which was most important in calm water stability remains the only positive term and on increasing speed this value tends to zero. At $\lambda/L = 3$ for $V_{\text{knots}}/\sqrt{L_{\text{feet}}} = 6$, this term significantly increases above the value at all other encounter frequencies, which is true for all increasing deadrise angles, although attenuated in magnitude. At this wavelength, the other damping terms become more negative.

As the speed increases, the craft's absolute hydrodynamic stiffness reduces and so too the magnitude of the wave forcing terms. Increasing deadrise has a smaller opposite effect in that the absolute magnitudes of the stiffness and waveforcing terms increases.

Summary

The effect of speed on motions and accelerations is dramatic. With increasing speed the vertical dynamics increase and the motions and accelerations exhibit highly tuned responses over the input frequency range, which are reflected in the behaviour of the hydrodynamic coefficients, especially in the added mass and inertia cross-coupling terms (m_{35} and m_{53}) and the heave induced pitch damping term (n_{53}). These effects of increased speed are attenuated by increasing deadrise angle.

6.3.3 Effect of Radius of Gyration

Two new configurations were theoretically constructed in order to investigate the effect of increasing gyradius at $V_{\text{knots}}/\sqrt{L_{\text{feet}}} = 4$. Configuration Q was tested with a gyradius of 30% of the craft length whilst configuration R with a 20% gyradius. Both configurations have 30° deadrise and were compared to configuration K which has a gyradius of 25% of the craft length.

Heave and Pitch Motions

Figure (A.53) shows that the heave and pitch responses and phase angles are barely affected by increasing the gyradius. However, for this deadrise angle and at this speed, the effect of increasing the gyradius is to increase the motions at longer wavelengths, $\lambda/L \geq 2.5$ and reduce the motions in shorter waves, $\lambda/L < 2.5$. Increasing the gyradius results in increased lag of the respective motions at the CG with respect to wave elevation across the whole frequency range.

Accelerations

Following from the negligible impact on the heave and pitch responses and phase angles, the accelerations at the CG are only marginally affected, figure (A.69). The manner in which they are affected is the same with increasing gyradius in the sense that at $\lambda/L \geq 2.5$ the accelerations are slightly increased and in shorter waves, $\lambda/L < 2.5$, the accelerations are reduced. The bow accelerations are significantly more influenced by the increased gyradius and show identical trends as with the other vertical responses. The reduced bow accelerations at $\lambda/L = 1$ are about 0.5g's less with a 10% increase in gyradius.

Hydrodynamic Coefficients

Figures (A.87) and (A.88) show that the variation of the gyradius has a negligible effect on all the hydrodynamic coefficients except for pure pitch added mass coefficient, m_{55}. However the slight variation in magnitude can be characterised. Increasing the gyradius increases the absolute magnitude of all the hydrodynamic coefficients at wavelengths $6 > \lambda/L \geq 1.5$. For the very high frequencies where $\lambda/L < 1.5$ the absolute magnitude decreases. Apart from the pure pitch added mass coefficient, m_{55}, the only exception to this behaviour is with the pure pitch wave forcing term, e_5, which always remains less than the absolute magnitude of coefficient values for smaller gyradii.

Summary

Increasing the gyradius for a 30° deadrise configuration increases the motions in longer waves, $\lambda/L \geq 2.5$, and reduces the motions in shorter waves, $\lambda/L < 2.5$. Increasing the gyradius also reduces the bow accelerations in the very short waves, $\lambda/L \leq 1$.

The hydrodynamic coefficients also show limited variation on increased gyradius, except for the pure pitch added mass/inertia coefficient, m_{55}. This is not suprising since a 10% increase in gyradius will produce 100% increase in inertia.

6.3.4 Performance at $V_{\mathrm{knots}}/\sqrt{L_{\mathrm{feet}}} = 2$

The effect of trim was analysed indirectly by investigating the effect of the movement of the LCG whilst keeping the gyradius the same. The tests were carried out in waves of $H/B = 0.111$.

Effect of Deadrise

Configurations H, C and L represent the 10°, 20° and 30° deadrise models respectively. The calculated calm water running trim for these configurations is 4.3°, 4.27° and 4.93° compared to 4.00° for the same position of LCG used in the experiments, approximately 62% of the craft length aft of the stem. Gyradius is fixed at 25% of the craft length. To reduce the disagreement in calm water running trim between configuration L and the others, the LCG is moved forward to provide a revised running trim of 4.27°.

For this speed and waveheight, the heave and pitch motions are unaffected by the increase in deadrise angle for this speed, figure (A.50), although Fridsma does report a slight increase in heave response at higher deadrise angles. Figure (A.60) shows that accelerations also remain independent of deadrise.

The 10° deadrise hydrodynamic coefficients show strong frequency dependency for $1 < \lambda/L < 3$. Increasing the deadrise angle from 10° to 30° reduces the dependency of the magnitude of the hydrodynamic coefficients upon the frequency of oscillation. The pure heave and pitch added mass and inertia terms reduce in absolute magnitude. However, whilst the symmetric cross-coupling terms do increase in absolute magnitude from 10° to 20°, there is little if no change in value by increasing the deadrise angle further from 20° to 30°. The absolute magnitude of all the other hydrodynamic coefficients reduces fairly linearly (with the exception of the high frequency dependent region for the 10° deadrise configuration) with increasing deadrise angle.

Effect of Trim

Configurations C and D represent 20° deadrise craft operating with two distinct LCG positions of 62% and 67.5%, respectively, of the craft length aft of the stem. The numerical model predicts a calm water running trim of 4.27° for configuration C and 8.10° for configuration D. This compares with Fridsma's calm water running trim of 4.00° for configuration C and 6.00° for configuration D. Gyradius is 25% of the craft length for each configuration.

Figure (A.57) and figures (A.25), (A.26) show that whilst Fridsma's experiments demonstrate negligible difference in heave motions at resonance when increasing the calm water running trim angle, there is a predicted decrease in heave motions from the non-linear frequency independent numerical model. The effect of increasing trim angle on resonant pitch response is better predicted, but has less effect than demonstrated by

Fridsma's experiments where there was an increase in the order of 20% at resonance. The pitch phase lag for the 8.10° craft is less than that for the 4.27° craft.

Fridsma's experiments show that the maximum bow and CG accelerations, occuring between $1 \leq \lambda/L \leq 2$, increase by around 40% (figures (A.72) and (A.73)). The frequency independent results for CG accelerations show little change with increase in trim but bow accelerations show a marked increase in magnitude, approximately 70%, with the 8.10° configuration. The accelerations are so poorly predicted however, that there is little benefit in extracting information relating to parametric variation.

All the hydrodynamic coefficients show little frequency dependence at this speed and for this deadrise angle. Doubling the trim angle at this speed:length ratio reduces the absolute added mass and inertia terms by a value between 15% and 50%, which usually indicates an increase in motion response, as will become clearer in the later tests. The absolute value of the damping coefficients is reduced with the exception of pure heave damping, n_{33}. The pitch induced heave damping, n_{53}, was shown in operations in calm water to be the most influential coefficient in terms of vertical craft stability. A reduction in magnitude of this term, coupled with an increasingly negative pure heave damping term, n_{33}, might explain any increase in vertical motions. Whilst this is true for pitch, the decrease in resonant motions for heave is still not clear.

The stiffness term, c_{35} increases in absolute value by approximately 20% whilst the heave induced pitch stiffness is decreased by a similar amount. The wave forcing term, e_3, is reduced approximately 20% and the wave moment increased by approximately 40%, which also helps explain the increase in pitch motions.

6.3.5 Performance at $V_{\text{knots}}/\sqrt{L}_{\text{feet}} = 4$

Fridsma conducted most of his parametric studies at this speed to length ratio and found a function C_λ that could collapse the motion data for varying load and length to beam ratios. Although the motion responses exhibit non-linearity around $2 \leq \lambda/L \leq 3$, the very long and short wavelengths still have a linear relation to waveheight.

Effect of Deadrise

Configurations I, A and K refer to deadrise angles of 10°, 20° and 30° respectively.

They have calculated calm water running trims of 5.68°, 5.77° and 6.43° respectively compared to 4.00° used by Fridsma for the same LCG positions. In order to isolate the effect of changing the deadrise on the vertical dynamics, the position of the LCG for configuration K is moved approximately 4% of the craft length further forward. This produces a calm water running trim of 5.67° which is much closer to the other configuration's calm water trim values.

The disagreement in theoretical calm water running trim given the same location for LCG used by Fridsma is a likely cause of discrepancy between the experimental and theoretical vertical responses; the theoretical values are around 30% higher. However, it is clear to see that by increasing deadrise the effect on the motions is just as insignificant at this higher speed as at $V/\sqrt{L} = 2$, figure (A.51). For $\lambda/L \leq 2$, the increasing deadrise sees the motions lag less. For $\lambda/L > 2$ there is no change in motion phases.

Increasing deadrise angle though does reduce the size of the accelerations, figure (A.61). Although accelerations are not as well predicted as the motions, the same trends seen experimentally are clear. For $\lambda/L > 2$, the increase in deadrise has no effect on the magnitude of the CG accelerations. However, for $\lambda/L < 2$, the CG accelerations are reduced dramatically by increasing the deadrise from 10° to 30° and by a similar amount experienced experimentally, approximately 50% for $\lambda/L = 1.5$ and 1.

Bow accelerations show similar patterns to the CG accelerations although the influence of change in deadrise becomes more important from $\lambda/L < 3$. Bow accelerations are reduced by approximately 50% at $\lambda/L = 1$ by increasing the deadrise angle from 10° to 30°.

Figure (A.97) and (A.98) show the effect of changing the deadrise on the hydrodynamic coefficients. Varying the deadrise angle from 10° to 30° results in only a marginal change in the magnitude of the hydrodynamic coefficients, an absolute variation in magnitude of no more than 10%. However it is possible to observe that the largest variations in absolute magnitude occur when increasing the deadrise angle from 20° to 30°, with the exception of the pure heave added mass/inertia term, m_{33} and the symmetric cross-coupling terms, m_{35} and m_{53}.

Effect of Trim

To test the effect of altering the position of the LCG and therefore the influence of trim angle on vertical responses, the 20° deadrise configurations A and E were used. Configuration A has a LCG position of 59% and a calm water running trim of 5.77°. Configuration E has a LCG position of 65.5% and a calm water running trim of 7.05°. Otherwise they are identical.

The effect of this 6.5% increase in LCG position is to increase the heave motions at resonance, $3 < \lambda/L < 4$, by approximately 20%, figure (A.58), and the pitch motions at resonance by approximately 40%. However, the phase angles for $3 < \lambda/L < 4$ remain unchanged. For $\lambda/L < 3$, the increased trim (i.e. increased distance of LCG from stem, configuration E) results in increased lag in motion responses compared to wave elevation.

The accelerations are also affected by the increased movement of the LCG aft. As with Fridsma's findings, the increase in accelerations at the CG and at the bow, from $\lambda/L < 3$, range from 50% to 100% by increasing the calm water running trim angle, figure (A.67).

The added mass and inertia hydrodynamic coefficients show approximately a 15% decrease in magnitude on increasing the trim angle across the whole frequency range. However, this loss of lift is complimented by a decrease in hydrodynamic damping. The most significant reduction in damping comes from the n_{53} term where there is a 50% loss. There is also a 20% loss in damping from the other cross-coupling term and a 30% loss in pure pitch damping. The damping in pure heave is reduced by only 4%. Furthermore, the hydrodynamic stiffness is also reduced and significantly so in respect to the heave induced pitch term, c_{53}; approximately 50% for all wavelengths. Waveforcing terms are also reduced; 33% reduction for e_3 and 40% for e_5. However the waveforcing terms are typically small in magnitude constituting only about 5% of the total lift.

Effect of Load

Configurations E and F represent the two different loadings of $C_\Delta = 0.608$ and $C_\Delta = 0.912$ respectively. Otherwise they are identical.

The effect of increasing the load, is to reduce the heave motions at resonance by approximately 20% and pitch motions by 25%, figure (A.59), which is 5% less in each case than Fridsma's findings. Maximum phase lag is increased for the heavier load, configuration F.

Accelerations are slightly reduced with increased load. The frequency independent results predict that whilst the bow accelerations remain very much unchanged over the whole frequency range, the CG accelerations are reduced by 30% at $\lambda/L = 1$ for the higher load, figure (A.68).

Figure (A.89) and (A.90) shows the effect of load on the hydrodynamic coefficients for $V_{\text{knots}}/\sqrt{L}_{\text{feet}} = 4$. The effect of increasing the load is seen in the fairly constant increase in added mass and inertia coefficients across the whole frequency range. The cross-coupling terms are only increased by around 8% in magnitude, whilst the pure heave and pitch terms are increased by about 30% at all wavelengths.

The hydrodynamic damping terms all become more negative on increased load except for n_{53} which becomes more positive. Increasing the load also increases the absolute size of the restoring force and wave-forcing terms.

6.3.6 Performance at $V_{\textbf{knots}}/\sqrt{L}_{\textbf{feet}} = 6$

At this speed the craft motions are extremely non-linear with increasing waveheight. Because the momentum of the craft at very high speed allows a platforming condition at higher encounter frequencies, the motion response is actually less than for lower speeds. At resonant frequency, the motion and acceleration responses show highly tuned behaviour and little damping exists. For low deadrise craft, the magnitude of the accelerations prohibit practical use.

Effect of Deadrise

Configurations J, B and M represent craft of 10°, 20° and 30° deadrise respectively operating at this speed to length ratio in waveheights equal to 0.111 beams. Their calculated calm water running trim angles are 4.35°, 4.19° and 4.27° respectively compared to 4.00° used by Fridsma for the same LCG positions.

Figures (A.52) show the effect of deadrise on the motions. Increasing the deadrise makes a dramatic reduction in the craft's resonant response at around $\lambda/L = 4$. An increase in deadrise from 10° to 30° sees a predicted 35% decrease in heave motions and 48% decrease in pitch motions at resonance, compared with respective 25% and

50% decreases seen experimentally.

As with all the other tested configurations, the peak accelerations at the bow and CG, occurring at $\lambda/L = 3$, do not coincide with the peak motion responses, occurring at $\lambda/L = 4$. CG accelerations are reduced by approximately 75% over the whole frequency range by increasing the deadrise from 10° to 30°, figure (A.62). The peak acceleration exhibited by the 10° deadrise craft is removed almost entirely by increasing the deadrise to 30°. The same is true for the bow accelerations; the peak acceleration is significantly reduced to a level comparable with the rest of the frequency range, which in general is about 75% less than the bow accelerations experienced by the 10° deadrise craft.

Figures (A.99) and (A.100) show the effect of increasing deadrise upon the hydrodynamic coeffcients. The frequency dependence of the coefficients is evident at this high speed:length ratio and highly tuned for $\lambda/L = 3$. The magnitude of the peak variation is attenuated by increasing the deadrise angle.

The cross-coupling terms of the added mass and inertia coefficients approach zero for small deadrise angles and at $\lambda/L = 3$, whilst the pure heave and pitch terms rapidly increase in value at this wavelength. The change in the value of these terms is most obvious by increasing the deadrise angle from 10° to 20°. Further increase in deadrise only attenuates the peak magnitudes.

Increasing the deadrise angle from 10° to 20° also has a dramatic effect upon the damping coefficients of pitch induced heave, n_{35} and pure pitch, n_{55}, with approximately a 15% increase absolute magnitude. With increasing deadrise thereafter, there is little variation. Pure heave damping varies little in magnitude despite the variation of deadrise, approximately only 5%. There is little variation of the heave induced pitch damping, n_{53}, except for a large increase (approximately 50%) for $\lambda/L = 3$.

The stiffness terms reduce in absolute magnitude with increasing deadrise, with obvious changes in c_{53} at $\lambda/L = 3$ for the 10° deadrise configuration. Vertical wave force and wave induced moment increase in absolute magnitude with increasing deadrise angle.

6.4 Conclusions

The non-linear theoretical model, NoLiPCraMP , has been employed in order to analyse the effects of parametric changes upon the vertical dynamics of various hard-chine constant deadrise planing craft. The confidence in this model's ability to accurately quantify the vertical dynamic effects has been achieved by comparison with the previous experimental work of Fridsma (1969) and theoretical results of Chiu and Fujino (1989), Zarnick (1978) and Troesch (1992).

The effect of frequency dependent added mass and damping coefficients upon the predicted vertical responses of the various craft configurations was investigated. It is concluded that in the areas of high curvature of the added mass and damping versus frequency curves, better predictions of vertical responses is achieved by considering the frequency dependency of the added mass and damping.

At very high wave encounter frequencies, at speeds higher than $V/\sqrt{L} = 6$ and/or in very short wavelengths ($\lambda/L \ll 1$), the frequency independent and dependent approaches would be expected to predict the same vertical responses. The rounding of the extracted polynomial coefficients (employed in the NoLiPCraMP algorithm for evaluating added mass and damping coefficents at a prescribed draft and oscillation frequency) cause an underprediction of the added mass and damping at the very small drafts, typically found near the bow regions. A consequence of this is an inaccuracy in the trimming moment due to loss of predicted lift at the forward end of the craft and therefore a discrepancy between the two approaches despite the theoretical equivalence in hydrodynamic coefficients for high encounter frequency. This could be remedied by having separate polynomial fits to model added mass and damping at very low drafts.

Linearising the equations of motion by neglecting second and higher order effects, as in the case of Chiu and Fujjino (1989) and Chou et al (1991), has a small effect on the predicted vertical responses, with larger errors occuring at high speeds and larger encounter frequencies ($V/\sqrt{L} \geq 6$, $\lambda/L \leq 1.5$). This allows the investigation into dynamic effects by consideration of the hydrodynamic coefficients.

A parametric investigation was carried out that fulfilled the test matrix of table 6.4. The investigation was centred around the speed:length ratio of $V/\sqrt{L} = 4$ (which corresponds to a Froude number of 1.2) and is a typical operational planing speed for which a large proportion of data exists (eg. Fridsma (1969)).

For all speed:length ratios, the effect of increasing deadrise angle is to reduce the accelerations significantly at the bow and CG, especially in high frequency waves ($\lambda/L < 3$). The amount of difference increasing deadrise angle makes is more profound the higher the speed:length ratio becomes. Although there are significant benefits upon reduced accelerations with increasing deadrise angle, the effect on motions only becomes more obvious for $V/\sqrt{L} > 4$, whereupon the resonant motions decrease by around 30% for heave and 50% for pitch. For $V/\sqrt{L} \leq 4$, pitch and heave motions increase slightly with increasing deadrise.

The effect of increasing calm water running trim by about 20% is to increase the resonant motions by approximately 35%. The CG accelerations increase from 10% at $\lambda/L = 4$ to 20% at $\lambda/L = 1$. Bow accelerations follow a similar trend. The increase of all these quantities is exacerbated by increasing speed.

Increasing speed from $V/\sqrt{L} = 2$ to 6 increases motion and acceleration responses and shifts the maximum motion response to waves of two to four times the craft length.

Increasing load by about one half again reduces the heave and pitch motions at resonance by about 20% and reduces the accelerations experienced at the CG and bow, most significantly (between 20% to 40%) in higher frequency waves ($\lambda/L < 4$).

Increasing gyradius was found to slightly increase the motions and accelerations from $\lambda/L \geq 2.5$ and reduce the motions and accelerations in waves of length $\lambda/L < 2.5$.

The accelerations seem to correlate strongly with the behaviour of the hydrodynamic coefficients. Peak accelerations or increase in rate of change of acceleration with frequency occur where the hydrodynamic coeffcients experience well defined minima or maxima. Furthermore, the variation in magnitude of the maxima or minima of pure heave added mass/inertia, m_{33}, and pure pitch added mass/inertia, m_{55}, compare with the percentage change in magnitude of the resonant heave and pitch motions respectively. Usually these quantities are the largest of the hydrodynamic coefficients, given that they contain the craft mass and inertia.

The behaviour of the pure added mass and inertia terms for $V/\sqrt{L} \geq 4$ is opposite to the symmetric cross-coupling terms, whilst the absolute values of all the damping terms follow the same trend as the pure added mass and inertia terms. On changing a parameter's value, the subsequent increase in pure added mass/inertia coefficients, m_{33} and m_{55}, corresponds to a decrease in resonant heave and pitch response, and conversely there is an increase in resonant motion response on a decrease in pure heave and pitch added mass/inertia coefficients. The relation between the respective increase in added mass/inertia terms with a decrease in resonant response does not preclude the importance of the damping and stiffness behaviour, but is mentioned in favour of those other terms behaviour because of the usually comparable percentage change of added mass/inertia with the change in resonant response.

Chapter 7

Irregular Seas

The sea-keeping performance of a planing craft in regular waves has been examined. However, to expect a vessel to operate in a wave environment that is purely regular is unreasonable. Unfortunately, the prediction of craft motions in an irregular sea is complicated by the randomness of the input forcing function. Therefore, to predict vessel motions, an irregular or confused sea needs to be rationalised. The method by which this rationalisation can be achieved is through the use of statistical analysis. Typical parameters used in the statistical analysis of any irregular time history are quantities such as mean wave amplitude, mean wave height, mean period between peak values, mean zero crossing period, variance of wave elevation about the mean, standard deviation about the mean and so forth.

For the purpose of investigating solely vertical motions, only long crested irregular head seas will be considered, i.e. those that are one-dimensional (frequency dependent) and have direction opposite to that of the craft forward motion. There are problems associated with the Doppler Shift, or encounter frequency, for example a vessel travelling in following seas may be travelling faster than the wave group velocity so that, to an observer on the vessel, the sea appears to be a head sea. Restricting to head seas, these problems are avoided.

7.1 Fourier Series

The construction or decomposition of an irregular sea surface can be brought about by the principle of superposition. If a sea surface can be treated as an addition of waves of varying frequency, amplitude and phase then an irregular sea can be represented by a Fourier series,

$$\zeta(t) = \sum_{n=1}^{\infty} A_n \cos(\omega_n t) + B_n \sin(\omega_n t) \tag{7.1}$$

where,

$$\omega_n = \frac{2\pi n}{T_H} \tag{7.2}$$

$$A_n = \frac{2}{T_H} \int_0^{T_H} \zeta(t) \cos(\omega_n t)\, dt \tag{7.3}$$

$$B_n = \frac{2}{T_H} \int_0^{T_H} \zeta(t) \sin(\omega_n t)\, dt \tag{7.4}$$

Equation (7.1) may be written as,

$$\zeta(t) = \sum_{n=1}^{\infty} \zeta_{n0} \cos(\omega_n t + \epsilon_n) \tag{7.5}$$

where the coefficients are,

$$\zeta_{n0} = \sqrt{A_n^2 + B_n^2} \tag{7.6}$$

and the phase angles are given by,

$$\tan \epsilon_n = -\frac{B_n}{A_n} \tag{7.7}$$

7.2 Wave Energy Spectrum

Another fundamental concept behind irregular sea analysis is in relation to the amount of energy stored in the wave system. If one was to take a unit area of the sea surface, one could define in that area the proportion of energy contributed by a frequency band from a total frequency range. The wave energy spectrum is then defined so that the area bounded by the frequency range ω and $\omega + \delta\omega$, the hatched area of figure (A.114), is proportional to the total energy of all the wave components within that range of frequencies.

Summing all the areas from $\omega = 0$ to $\omega = \infty$ provides a total proportional to the energy contained in that unit area of sea,

$$\text{area under spectrum} = \int_0^\infty S(\omega)d\omega \tag{7.8}$$

In this manner the relative importance of the component sine waves that make up an irregular sea can be quantified. The wave energy spectrum therefore provides frequencies required for the Fourier series and the corresponding amplitudes from the wave energy spectral ordinates.

The wave energy spectrum can also provide details such as the variance and standard deviation of the surface elevation from the mean and a spectral width parameter, ε, which describes the general spread of component frequencies. If $\varepsilon = 0$ then the spread of frequencies is narrow and the distribution of maxima and minima about the mean is Rayleighian, with few positive minima and few negative maxima. On the other hand, if $\varepsilon = 1$, then the wave energy spectrum is termed as being broad banded with more negative maxima and positive minima due to the increased number of frequency components. If a spectrum is broad banded then the distribution of maxima and minima about the mean is Gaussian.

The variance is described as being equal to the area enclosed by the wave energy spectrum, and as such is the zeroth moment of area of the wave energy spectrum, termed m_0, i.e.,

$$m_0 = \int_0^\infty S(\omega)\, d\omega \tag{7.9}$$

Cartwright and Longuet-Higgins show that the significant waveheight, $H_{1/3}$, is equal to 4 times the standard deviation for a Rayleighian distribution of wave amplitudes, i.e.,

$$H_{1/3} = 4\sqrt{m_0} \tag{7.10}$$

or for $\varepsilon > 0$,

$$H_{1/3} = 4\sqrt{m_0}\sqrt{1 - \frac{\varepsilon^2}{2}} \tag{7.11}$$

In more general terms the nth moment of the wave energy spectrum about $\omega = 0$ can be written as,

$$m_n = \int_0^\infty \omega^n S(\omega)\, d\omega \tag{7.12}$$

7.2.1 Choice of Wave Spectra

By a suitable choice of spectrum, $S(\omega)$, a specific sea state can be created from which the distribution of maxima (or minima), $\zeta_{\max(\min)}$, should follow a random probability density distribution if it is truly representative of the sea surface. Depending upon the spectral width parameter, ε, and the non-dimensional maxima (or minima) of $\zeta_{\max(\min)}$, the statistics associated with the probability distribution are known to be represented by the limits of a Gaussian (broad-banded, $\varepsilon = 1$) or Rayleighian (narrow-banded, $\varepsilon = 0$) distribution. Various spectra have been developed, each with their own characteristics and a brief outline of some are given in the subsections below, for example, Pierson-Moskowitz (1964), ITTC (1978), Bretschneider (1952, 1957) and JONSWAP (Hasselman, 1973 and Ewing, 1975).

7.2.1.1 Pierson- Moskowitz Spectrum

Pierson and Moskowitz (1964) selected certain measured spectra based upon a large amount of oceanographic records and then grouped those spectra into a family of five wind speeds. From this spectral family, an idealised sea spectra representing fully developed seas was formed with no frequency elements associated with swell generated from far off sources.

This method loses its applicability in ship design since it is based on a single parameter of wind strength and fully developed seas created by very high winds are known to be rare (Lewis 1988) as duration and fetch are insufficient for spectral stability.

7.2.1.2 Bretschneider Spectrum

The Bretschneider (1952), (1957) spectrum is based on two parameters which allow significant wave period and waveheight to be assigned separately. These two parameters can be directly related to the extensive data available on observed waveheights and periods.

The Bretschneider spectral form is assumed to adequately represent any seaway but in reality multi-modal spectra are commonly found. Also, swell from distant storms is found in measured data, the components of which are limited in high frequency since those components take longer to arrive at the observation point. The Bretschneider spectra however have very well defined high frequency limits so that there is a significant contribution to the total energy within the system supplied by high frequency components. This could lead to ship high frequency responses greater than that which would physically occur (St Denis 1980). If the deviations in form between the Bretschneider and measured spectra are collectively small, then the Bretschneider spectra can lead to a good measure of ship performance.

7.2.1.3 Ochi 6-Parameter Spectrum

In an attempt to improve the Bretschneider spectra in its basic form, Ochi and Hubble (1976) introduced a shape parameter, λ (which when equal to 1.0 produced the Bretschneider form). The uni-modal spectrum thus formed had three parameters based upon frequency, waveheight and λ. Adding this spectrum to another which covered higher frequency components led to a 6-parameter multi-modal spectrum which could have much better agreement with real sea spectra depending on the assignment of values to the parameters.

7.2.1.4 JONSWAP

The limited fetch conditions found in areas such as the North Sea led to the need for a better representation of sea states currently offered by other spectra. The Joint North Sea Wave Project was set up to provide extensive oceanographic measurements in the attempt to meet this need. The subsequent spectral fit found that the sort of spectrum created is simply of a Bretschneider form.

7.2.1.5 ITTC Spectrum

The 15th International Towing Tank Conference recommended the use of a form of the Bretschneider spectrum for average rather than fully-developed seas since this allowed for a more realistic representation of the sea surface when more specifically appropriate spectral forms are unknown.

7.3 Theoretical Treatment

The choice of wave spectrum used is at this stage based upon one which whilst simple to employ in a computer algorithm is also a justifiable representation of a sea surface. The Pierson-Moskowitz spectrum is not considered because of its over simplicity, being based on one parameter and its applicability to only fully-developed seas with very high wind strengths. The JONSWAP spectrum is probably the most realistic environment for high speed planing since it is unlikely that that sort of craft will find use in trans-oceanic journeys; planing craft operations are usually restricted to areas with limited fetch. Since the JONSWAP spectrum is based upon the Bretschneider form, it is the Bretschneider form that will be used or more specifically, the ITTC form; it allows a more generalised, yet still a realistic approach, to sea surface representation.

The ITTC spectrum can be represented by the spectral energy density function $S(\omega)$,

$$S(\omega) = \frac{A}{\omega^5} \exp\left(-B/\omega^4\right) \tag{7.13}$$

This is the basic Bretschneider spectrum but with,

$$A = \frac{487 H_{1/3}^2}{T_0^4}, \; B = \frac{1949}{T_0^4}, \; T_0 = 2\pi\frac{m_0}{m_1}, \; H_{1/3} = 4\sqrt{m_0} \tag{7.14}$$

Usual practice is to construct the spectrum $S(\omega)$ and then divide into strips of equal frequency intervals, $\delta\omega$. Taking the centre ordinate of each strip defines the average frequency component for that interval and a corresponding average energy value $S_n(\omega)$. The average component wave amplitude for that interval, ζ_n, is then,

$$\zeta_n = \sqrt{2 S_n(\omega)\, \delta\omega} \tag{7.15}$$

Taking the centre ordinate was subsequently found to be erroneous (Faltinsen 1990) in producing realistic sea states. Faltinsen described an alternative method by picking random centre frequencies but Payne (1995) suggests this method does not fulfil the randomness criteria described by Cartwright and Longuet-Higgins (1956) either.

Payne (1995) describes Pierson's (1961) approach for defining the random frequencies as those which form the boundaries to n equal energy strips, figure (A.115). Since m_{o_n} is equal for all n, then the component amplitudes must necessarily be equal. Payne proposed that this method means that a constructed sea meets the necessary randomness criteria proposed by Cartwright and Longuet-Higgins (1956).

A separate module has been incorporated into the program that allows for an irregular sea surface to be constructed from an ITTC wave energy density spectrum. The spectrum is defined by significant waveheight, $H_{1/3}$, and modal period, T_0. Table 7.1 characterises typical most probable modal periods found in the eastern Atlantic (Sea Area 9) for various significant waveheights. By appropriate scaling, corresponding model values for $H_{1/3}$ and T_0 can be derived.

$H_{1/3}$ (m)	T_0 (secs)
2	11.00
4	13.00
6	13.90
8	14.20
10	14.30
12	14.45

Table 7.1: Significant Waveheight vs Modal Period
Sea Area 9; All Seasons; All Directions (Hogben, Dacunha and Olliver(1986))

The NoLiPCraMP program models the craft response to an irregular sea in two distinct ways. Firstly, the frequency dependent approach is complex to apply because of the multiple frequency components present in the encountered irregular sea. The sectional added mass and damping are therefore evaluated for only one frequency component, the modal encounter frequency from the modal wave period, T_0. The second approach assumes that regardless at which frequency a sectional strip may be oscillating, the added mass and damping are assumed to be equivalent to their asymptotic values, i.e. the sectional added mass and damping are evaluated at infinite encounter frequency. The difference between these two approaches is obvious, but the consequence of each approach on the motions is not. For the frequency independent approach, the damping coefficient approaches zero and the only motion damping terms which exist are from the added mass terms, the added mass coefficients themselves being finite and constant. The 'frequency dependent' approach assumes that for a finite significant wave amplitude, the modal frequency will always be finite and the damping coefficient will invariably be greater than zero. More damping terms exist as a result but their effect on the motion predictions are countered by the change in the added mass terms.

7.4 Results Analysis

For linear systems, spectral analysis can be used. The product of the square of the craft response in regular waves with the irregular wave energy spectrum provides a irregular sea response spectrum. This technique is the primary method for describing craft motion behaviour and is the basis for comparing one configuration with another. For non-linear systems though, this method cannot be readily applied since the motions are no longer linearly related to waveheight. Instead, what is required are the statistical properties of the craft response which can then allow direct comparison between different configurations. For example, an irregular sea surface time history, assumed to be derived from a narrow banded wave energy spectrum, can have its wave elevations described by a zero mean Gaussian distribution and its wave amplitudes by a Rayleighian distribution. By knowing the standard deviation, both distributions are uniquely defined by mathematical expressions. Differences between sea states can therefore be made on the basis of their average or significant waveheights.

7.4.1 Wave and Motion Amplitude Distributions

It is commonly assumed that wave amplitudes measured from an irregular time history follow a Rayleighian distribution whilst the wave elevation is distributed normally (Gaussian). However, the broadness of the frequency spectra, $\varepsilon_{\max}$, is rarely equal to the limiting values of one or zero and so the distributions can more generally be cast as *generalised* Rayleigh distributions which account for broadness in the frequency spectra. The generalised Rayleigh distribution used by Fridsma (1971) follows from

Rice (1945) from whence it was derived in connection with determining the distribution of maxima, $\zeta_{\max}$, arising from a broad frequency spectrum and is given as,

$$\begin{aligned} Q(Z, \varepsilon_{\max}) &= \frac{1}{\sqrt{2\pi}} \int_{Z/\varepsilon_{\max}}^{\infty} \exp\,(-\frac{x^2}{2})\,dx \\ &\quad + \sqrt{1-\varepsilon_{\max}^2}\; exp(-\frac{Z^2}{2}) \int_{-\infty}^{\frac{Z\sqrt{1-\varepsilon_{\max}^2}}{\varepsilon_{\max}}} exp(-\frac{x^2}{2})\,dx \end{aligned} \tag{7.16}$$

where,

$$Z = \frac{\zeta_{\max} - \overline{\zeta}_{\max}}{\sqrt{m_{0_s}}} \tag{7.17}$$

and the mean, $\overline{\zeta}_{\max}$ of the maxima $\zeta_{\max}$, and $\sqrt{m_{0_s}}$, or standard deviation, is known.

Note that when $\varepsilon_{\max} \to 0$ then,

$$Q(Z, 0) = \begin{cases} 1 & Z < 0 \\ Z\,exp(-\frac{Z^2}{2}) & Z \geq 0 \end{cases} \tag{7.18}$$

which is equal to the Rayleigh distribution. If $\varepsilon_{\max}$ is small but larger than zero, then the distribution can be described as a *distorted* Rayleigh distribution.

When $\varepsilon_{\max} \to 1$ then,

$$Q(Z, 1) = \frac{1}{\sqrt{2\pi}} \int_{Z}^{\infty} \exp\,(-\frac{x^2}{2})\,dx \tag{7.19}$$

which is equal to the Gaussian distribution. The value $\varepsilon_{\max}$ can be evaluated from the proportion, r, of negative maxima to total maxima in the time history,

$$\varepsilon_{\max}^2 = 1 - (1 - 2r)^2 \tag{7.20}$$

The smaller the value of r, the less broad is the probability distibution which is indicative of fewer frequency components within the measured signal. The above equations are identical for the distribution of minima with the subscript *min* replacing *max*.

All motion time histories will be described theoretically as having their maxima and minima distributed in a generalised Rayleigh fashion, whether the time histories are experimental or theoretical in origin. Actual experimental or theoretical maxima and minima occurring within the time histories are sorted in ascending order of magnitude and grouped in 15 equal intervals or classes. Within each class, the frequency of a maxima or minima occurrence is noted and the probability distribution and the cumulative probability distribution, $Q(Z, \varepsilon_{\max/\min})$, formed. From these measured distributions, the theoretical fit to generalised Rayleigh distributions can be compared.

7.4.2 Accelerations

Following from Fridsma (1971) and Zarnick (1979), the distribution of impact accelerations (negative minima) can be assumed to follow an exponential distribution. The probability distribution function, $f(\eta)$, is,

$$f(\eta) = \frac{1}{\overline{\eta}}\, exp(\frac{-\eta}{\overline{\eta}}) \tag{7.21}$$

where $\overline{\eta}$ = average peak acceleration

Therefore the corresponding cumulative distribution function, $Q(\eta) = \int_0^\infty f(\eta)\, d\eta$, is,

$$Q(\eta) = exp(\frac{-\eta}{\overline{\eta}}) \tag{7.22}$$

As with the wave and motion amplitude data, the negative(impact) peak acceleration data is sorted and classed in ascending order, from which the experimentally or theoretically measured distributions are formed. The correlation with an exponential distribution can then be found by applying equation (7.22).

7.5 Theoretical Results

7.5.1 Spectral Analysis

The theoretical generated wave elevations at the craft CG were fast Fourier transformed in order to check that the input waveform contained the correct frequency components and that no aliasing was occurring through too low a sampling rate. A typical wave energy spectra is given in figure (A.116) with 10 component frequency values, calculated through equal energy divisions. The FFT results are plotted on the same graph and demonstrate that the frequency components are being correctly identified within the program. The individual peaks from the FFT are well defined and the overall magnitudes are relatively equal. With more samples, i.e. a smaller integration interval or larger run time, the definition improves and the peak magnitudes reach very similar values, close to the individual input component amplitudes. This is as expected since the basis of equal energy division of the wave energy spectrum should produce component waves of equal amplitude.

The motion response spectra in the frequency domain were formed from FFTs of the individual motion time histories, which were then normalised by the RMS or standard deviation of the respective time series. Since the encountered wave spectrum is known, the derivation of the motion transfer functions can be obtained by the square root of the ordinates of the motion response spectra divided by the equivalent ordinate of the wave encounter spectra. In this manner, transfer functions for craft behaviour which is considered generally linear ($V_{kt}/\sqrt{L_{ft}} \leq 4$) can be constructed from irregular sea motion histories. Two examples of spectral analysis applied to speed:length ratios less than 4 are given in figure (A.48) and figure (A.49) and discussed in section 6.3.1.

7.5.2 Statistical Analysis

As described in section 7.4.1, the maxima and minima of all motions and accelerations were stored, sorted and classed and the probability and cumulative probability distributions calculated along with the mean maxima or minima values and RMS of maxima or minima values. The cumulative probability distribution was then plotted against motion class values, normalised by removing the offset (mean) and dividing by the standard deviation, equation (7.17).

7.5.2.1 Frequency Independent Hydrodynamic Coefficients

NoLiPCraMP was run with frequency independent hydrodynamic coefficients for configuration J in a sea state of $H_{1/3}/B = 0.222$. The cumulative probability distribution of heave maxima from the heave motion response is plotted in figure (A.118). The line graph plotted on the same axes is a generalised Rayleigh distribution based on the frequency broadness, $\varepsilon_{\max}$, and the mean value of all the heave maxima (CG down). The length of the simulation is 50 seconds with an integration interval of 0.01 seconds which corresponds to 5000 samples. The comparison between the measured and theoretical distributions is very fair, but with the exception that the probability of higher heave magnitudes are over predicted by the theoretical distribution.

Figure (A.120) shows the comparison of the measured cumulative distribution of pitch maxima (bow up) against the theoretically assumed distribution. Once again, the agreement is good but as with the heave maxima, the probability of higher pitch values is overpredicted by the theoretical distribution.

Figure (A.122) to figure (A.123) show the agreement between the cumulative probability distribution of the measured accelerations and the exponential distribution. Once again, agreement is fair but the higher peak accelerations are overpredicted by the exponential distribution, figure (A.124) and figure (A.125).

It is likely that the higher peak values, whose probability of occurrence is obviously low, may be picked up by a longer run time, increasing the chance of higher peak values occurring, thereby providing better correlation between measured and theoretically determined probabilities.

7.5.2.2 Frequency Dependent Hydrodynamic Coefficients

The modal encounter frequency was used to approximate the effect of the observed frequency content on the hydrodynamic coefficients. The consequence of this approach on the applicability of various theoretical probability distributions to describe motion responses is demonstrated by figure (A.119) for the distribution of heave maxima, figure (A.121) for pitch maxima distribution. This is in direct comparison with the frequency independent approach with identical craft configuration J operating in the same environment

The correlation between measured and theoretical distributions remain fair for all the distributions of motion maxima and minima, albeit with more scatter of the measured probabilities about the theoretically predicted probabilities. However the agreement between the predicted and measured probability distributions for the accelerations is greatly improved compared with the frequency independent approach, figures (A.126) and (A.127) compared with figures (A.124) and (A.125), for frequency dependency.

7.5.2.3 Effect of Significant Waveheight

The effect of waveheight has already been shown in the results of the regular wave tests to be considerable at higher planing speeds, $V_{kt}/\sqrt{L_{ft}} > 4$. Looking at the significant 1/10th highest heave and pitch motions for a $V_{kt}/\sqrt{L_{ft}} = 6$ with significant waveheight, $H_{1/3}/B = 0.222$, 0.444, 0.666, figures (A.128) and (A.129), the expected trend is born out. Likewise, the accelerations at the bow and CG increase with increasing waveheight, figure (A.130).

Although it has already been shown that the extraction of information from regular sea results can be erroneous, the natural frequency of the craft, or λ/L, varies little with waveheight. From the results for regular seas, it is apparent that the peak motions for high speed planing occur from wavelengths around 3 to 4 boat lengths. A cause of the increased motions with waveheight can therefore be attributed to the shape of the wave energy spectra. As waveheight increases, the modal frequency reduces providing more energy to excite the craft nearer the craft's own natural frequency, figure (A.134).

7.5.2.4 Effect of Deadrise

Also shown in figures (A.128), (A.129) and (A.130), is the effect of deadrise on the vertical motions and accelerations for the same speed to length ratio, where deadrise, β, takes the values of 10°, 20° and 30° . It is immediately obvious that the heave and pitch motions are reduced significantly when the deadrise angle is greater than 10°. However, increasing the deadrise from 20° to 30° does not improve the motion response much more until $H_{1/3}/B$ is greater than 0.444. In higher sea states, the 30° deadrise configuration exhibits less motion.

The effect of increasing deadrise on craft accelerations is very pronounced. The bow accelerations almost seem to follow a linear trend with increasing deadrise angle, so that tripling the deadrise angle reduces the bow accelerations by two-thirds at $V_{kt}/\sqrt{L_{ft}} = 6$. The accelerations at the CG are less effected, only reducing by 50% for the same increase in deadrise.

7.5.2.5 Effect of Speed

Speed is a prime factor dictating planing craft performance in rough water. Three speed to length ratios are tested, $V_{kt}/\sqrt{L_{ft}} = 2$, 4 and 6. These relate to three distinct dynamic environments. For $V_{kt}/\sqrt{L_{ft}} = 2$, the planing hull behaves much like a displacement craft where the buoyancy forces dominate over the hydrodynamic lift. The mean heave and pitch motions are equivalent to their steady state running values in calm water, which tends to suggest that the effect of the encountered waves on the vertical motions is purely to deflect the craft from its calm water attitude with no secondary (non-linear) dynamic effects; the craft almost contouring the waves, except at very high wave frequency ($\lambda/L < 2$). If the craft is fully contouring the waves, the distribution of motion maxima and minima would be expected to follow a Rayleighian distribution equivalent in broadness to the Rayleigh distribution representing wave amplitude, with r values close for each distribution. In fact, the r values for heave and pitch maxima and minima are zero, implying that whilst the wave amplitude distributions are 'broad' in nature, the craft response is not and that the inertia present in the response does not allow the craft to fully contour the waves.

The peak accelerations at the bow and CG are lowest at this speed as would be expected from the low pitch and heave excursions as the craft is almost contouring the waves.

At $V_{kt}/\sqrt{L_{ft}} = 4$, the craft is considered to be past the hump associated with maximum resistance and is now considered to be almost fully planing, with its rise in the height of CG in calm water approaching a maximum. There is still some significant hydrostatic force, but the predominant lift is hydrodynamic in origin. From figure (A.132) the 1/10th significant heave motions (i.e the difference between maxima and minima) have increased as would be expected since the craft is likely to impact into the infrequent large waves without necessarily riding over them. As a result the sudden increase in hydrostatic force produces a large increase in the total lift acting on the craft. For this particular 10° configuration, though, the significant 1/10th highest pitch motion actually reduces which does seem to be rather unusual given the increase in expected heave motion.

With the greater likelihood of impact, the average peak bow and CG accelerations have increased dramatically.

At $V_{kt}/\sqrt{L_{ft}} = 6$, the craft's CG in calm water would have reached its maximum position and the running trim will have dropped back to an optimum level. Efficient planing is now the key, with the aspect ratio of beam to wetted length increasing to a maximum. The craft's significant 1/10th highest heave motion is not greatly increased beyond the condition at $V_{kt}/\sqrt{L_{ft}} = 4$, figure (A.132). However the 1/10th highest pitch motion is nearer what would be expected as the craft leaps from wave crest to wave crest, suffering the effects of impact into the less frequent larger waves.

Accordingly, the average peak accelerations increase again as a direct consequence of the violent motions experienced.

Ultimately, the effect of speed is to increase the 1/10th highest motions above those motions experienced at low speeds with a corresponding increase in average peak accelerations. What is interesting though is the change in average motion with increasing speed. The average heave and pitch motions actually reduce with increasing speed. This is not so unusual when one considers the craft transcending through a *contouring* to a *platforming* condition. Whilst the craft is contouring, the average excursions of motions about the mean will be of the same order as the wave amplitude. However, at higher speeds, the craft's inertia will restrict response to waves of relatively small waveheight and the craft will effectively leap from crest to crest with little excursion from its average position. When a larger wave is encountered, however, the craft's high speed and inertia will act against it producing 1/10th significant motions higher than at lower speeds.

Chapter 8

Experimental Investigation

Much of the previous theoretical and experimental work on planing has been centred around calm water performance (see Chapter 2 for a discussion of these works). The complex surface flows generated by the hull lead to complications in the theoretical prediction of lift. Experimental work has been undertaken to identify the various components of lift and the effect of hull geometry parameters and speed. The dynamic lift of a planing hull has been shown to be strongly dependent on wetted surface and theory shows that the lift force is governed by the craft speed and distribution of added mass along the length (itself a function of wetted surface). Payne (1995) describes the difficulty that experimenters have in relating the lift force to individual parameters, especially wetted lengths which are difficult to measure consistently. Indeed the amount of scatter between individual experimenters results is high. Consequently any efforts to curve-fit the data results in a misinterpretation of the physical effect the very curve fits are trying to identify. Theorists relying on empirical curve-fits to relate specific lift components to their derived expressions discover that their theories have general exceptions as to their applicability, figure (A.135). The problem of identification of specific qualities is even more complicated by the craft's operation in a seaway.

An experimental investigation was carried out herein in order to achieve two aims. Firstly, to verify the vertical responses measured by Fridsma for a particular craft configuration to further justify using his data and validate the theory. Secondly, to apply a new technique to measure specific quantities, such as wetted surface, in a consistent manner which is repeatable from test to test, in this way enabling the degree of scatter discussed above to be reduced.

8.1 Computer Vision Data Acquisition

For craft travelling at high speed, the amount of generated spray reduces the ability of resistance and capacitance probes to accurately quantify wetted length and surface values. Techniques to avoid this problem and to investigate underwater surface flows have involved the use of still photographs, e.g. Savitsky (1964), Brown (1971), and limited video analysis, e.g. Fridsma (1969).

More than just those physical effects mentioned above can be analysed by video though. All displacements, velocities and accelerations can also be measured. The benefits of accurately acquiring information by video are enormous. Video data which is acquired, converted to digital form and digitally analysed is effectively a *computer vision system.*

Conventionally, large amounts of instrumentation and equipment are required to acquire all the necessary data from tank testing. This results in added weight to the model, more calibration and the increased possibility of noisy cross-talk in multiplexed signals. Computer vision avoids these problems by capturing all the data at once without any interference with the model and the effects it is trying to measure. Video capture has no influence on the objects in question. There is no added damping due to moving mechanisms that would ordinarily be monitoring displacement, velocities and accelerations; these can all be measured remotely. The system is self-calibrating since all the calibration information is contained within each *frame*[1] of information. The equipment required with this technique is reduced to a power source, high definition video cameras and a powerful computer.

Once the data has been recorded, it can be reviewed at any time with focus on any particular phenomenon desired. Provided the video analysis hardware and software are capable enough, any video footage of any object moving in any environment (from a stationary viewpoint) could be analysed. This information can be archived, then analysed and critically re-evaluated at any point.

The restriction on this type of data acquisition is at present large since the hardware

---

[1] Standard video records 25 snapshots, or frames, of an event it is capturing every second.

and software required for accurate automatic identification of *points of interest*[2] from frame to frame is expensive. The final extraction of the points of interest are carried out herein by the human eye. So although one of the main advantages is the amount of information that can be captured simultaneously, the actual amount of information that can be processed at present is limited to a few frames, equivalent to a couple of seconds of data.

8.2 Experimental Set-up

Only one craft configuration based upon the same lines as Fridsma's constant deadrise monohulls was constructed and tested. The testing facility was the towing tank at Southampton Institute. The maximum tow speed of the carriage is 4.2ms^{-1} which because of scaling problem restricts the size of the model to 1.25m and if towed at maximum speed is equivalent to Fridsma's speed to length coefficient, $V_k/\sqrt{L_{ft}}$, equal to 4. A 30° deadrise angle was chosen making the model equivalent to Fridsma's configuration K.

L/B	5
B/D	1.6
k_y/B	1.235
LCG/B	1.95
C_Δ	0.608
VCG (above keel)	0.35m
Model Length	1.25m
Beam, B	0.25m
Depth, D	0.15625m
Deadrise, β	30°
Displacement, Δ	93.2N

Table 8.1: Experimental Model Particulars equivalent to Fridsma's Configuration K

The craft is towed at the centre of gravity and is free to roll, pitch and heave. Following Fridsma (1969), the tests are carried out at constant speed and the effect of surge is neglected. Craft heave and pitch are measured in the standard way with translational and rotational transducers. Acceleration is extrapolated at the centre of gravity and

---

[2] Points of interest are specific loactions within the frame for which coordinate information is required

measured at the bow using an accelerometer. Resistance is measured from the dynamometer. Wave elevation is measured approximately one metre abeam of the CG using a sting-type wave probe. All data is acquired and output using the Wolfson Unit Data Acquisition software suite.

For the benefit of computer vision data acquisition, a grid is defined on one side of the model in 8cm by 1cm blocks and below the chine in 1cm by 1cm blocks. A black and white self-illuminating underwater camera is mounted just above the waterline normal to the direction of tow and opposite the centre of gravity. The camera is connected to a standard VHS video recorder and a monitor. The lighting is on-axis to remove shadows.

At this stage, it is unimportant for the recorded images to be horizontal. As previously mentioned, the computer vision system is self-calibrating and as long as there exists a known horizontal datum in the image then that can be used as the reference. Also depth of field and known reference points provide a constant calibration for any point at any distance away from the camera.

The trigger point for electronic data acquisition was automatic and data was acquired over 15m which equates to around 3 seconds for a tow speed of 4.2ms^{-1}. The computer vision data acquisition was triggered manually after the electronic acquisition had started and stopped before the electronic acquisition stopped. This enabled the video capture of purely steady-state planing and not the capture of information as the craft decelerated at the end of its run.

The VHS information was then digitised using standard Silicon Graphics Media Recorder and Converter software and decomposed into individual JPEG-compressed frames so that 25 frames corresponded to 1 second of real-time data. Each frame was analysed by eye using the image editor XV-3.10a for about a third of the total data acquisition time, around 25 frames. Coordinate information from each digitised frame was taken regarding the deck profile, carriage rail profile, keel/water intersection point and spray sheet/chine intersection. The calibration was taken from the known grid size on the model hull, and the camera orientation from the carriage rail profile. Problems wih parallax is readily checked for and negligible. The coordinate data was then converted into real quantities and output in the form of heave and pitch displacements and wetted length data. Obviously any other required information can be readily extracted.

An example sequence is shown in figure (A.142). This sequence is for an experimental run into waves twice the boat length. Two points of interest have been highlighted on the deck edge and the outline of the spray area overlaid onto each image.

Calm water tests were carried out initially before towing the craft into regular head waves ranging in wavelength from 1 to 6 boat lengths.

8.3 Experimental Results - Calm Water

8.3.1 Sinkage and Trim

Figure (A.136) shows the sinkage and trim of the craft from zero to full speed. The broken lines are Fridsma's results. The results are comparable although it appears that the new model requires a higher speed for the centre of gravity to rise. The new model sits lower in the water at full planing speed than Fridsma's with a slightly increased trim angle.

8.3.2 Resistance

The resistance results are also shown in figure (A.136) and show that the new craft has a slightly larger resistance hump and the final resistance is also higher. This is accounted for by the model sitting lower in the water at full planing speed and with a higher trim angle, adversely affecting the lift vector angle.

8.3.3 Wetted Data

Wetted keel data is measured from the computer vision data acquisition for the range of speeds from zero to full planing speed of $V_k/\sqrt{L_{ft}} = 4$. Comparison with Fridsma's result is good but does show a slight increase in magnitude over the whole speed range, which further helps explain the increased resistance.

8.4 Experimental Results - Regular Waves

For a discussion of this particular craft configuration's performance in waves, see section 6.2.1.

8.4.1 Heave and Pitch Motions

Figure (A.137) and figure (A.138) shows the heave and pitch responses of the craft in regular waves ranging from wavelengths of 1 to 6 craft lengths. The solid lines relate to the measured response through the standard electronic data acquisition whilst the squares correspond to the computer vision data acquisition approach. The error bands represent a 5% error in visual measurement and will be discussed subsequently. The test results varied little on repetition and discrepancies are not presented. The results shown herein are for one particular experimental set which is used as a benchmark. The reason for this is so that the CVDA can be compared directly to the standard electronic data acquisition results, which would be impossible if an average result measured from all the experimental test runs was used.

The magnitude of the peak responses and the frequencies at which they occur agree very well with Fridsma's results for both the standard and computer vision data acquisition approaches. However, at longer wavelengths, the boat responses are larger especially for pitch. This is an interesting result since it tends to make the agreement with theory for both pitch and heave much closer at the longer wavelengths, shown by the circles in the aforementioned figures, where previous comparison with Fridsma's results for the same configuration are less favourable. However, the calm water discrepancies in running trim and sinkage will affect the overall motions enough to explain these differences and the theory's improved agreement is purely incidental. The phase behaviour of the motions relative to the wave elevation at the centre of gravity agree well with Fridsma's results.

The computer vision data acquisition is limited at present by the time required to analyse each digital frame by hand and identify all the points of interest. The time histories for heave and pitch response for durations no longer than 1.5 seconds are shown in figure (A.143) to figure (A.147). These time-histories show the correct frequency and for the part of the run recorded very similar magnitude in response to the corresponding time history from the electronic data acquisition. However, using these limited time histories to extract heave and pitch RAO's would be unwise since there is too little information to make a direct comparison with the results from the analysis of data through the standard electronic data acquisition. To circumvent this, a simple test was carried out which involved the original video footage of the test runs. The analogue footage was quickly run frame by frame over the whole recorded run length and the maximum heave and pitch position marked onto a television monitor. In this manner, all the peak motions were recorded and the results are those shown by the squares on figures (A.137) and (A.138). The error bands mentioned previously are due to the inaccuracy in pinpointing to one pixel[3] the specific points of interest because of the ability of the video playback device to freeze each individual frame. This problem does not exist with digital images.

8.4.2 Accelerations

The accelerations at the bow and centre of gravity were found to have very good agreement over the whole frequency range with Fridsma's results. This is expected due to the good agreement with heave and pitch responses and phase information. The larger motions at longer wavelengths, $\lambda/L > 4$, does little to affect the peak impact accelerations which are small in magnitude anyway.

8.4.3 Added Resistance

Figure (A.140) shows the rough water resistance of the craft over decreasing encounter frequencies. At longer wavelengths, the craft resistance approaches the calm water value shown in figure (A.139). However, as with the calm water resistance, the resistance in waves is larger than Fridsma's results.

The resistance increment or added resistance is shown in figure (A.141). This describes the reduction in added resistance with decreasing encounter frequency and in fact at the longer wavelengths, the resistance drops below the calm water value.

---

[3] A recorded image is made of individual pixels. In the images described herein, an image is constructed from 1024x760 pixels

8.4.4 Wetted Data

Wetted keel length data is shown in figure (A.143) to figure (A.147). The maximum wetted values occur when heave is a minimum; the pitch angle attenuates the size of the wetted length change. The mean wetted keel length does not change significantly with change in encounter frequency and is approximately 3.75 craft beams in magnitude[4]. The mean wetted keel lengths are comparable to the calm water wetted keel length at the same speed, figure (A.136).

The mean wetted keel length does seem to increase slightly with decreasing encounter frequency. The implication of this alone would seem to be that the resistance in waves increases slightly with decreasing encounter frequency which is the opposite of what is shown in figure (A.140) and figure (A.141). However, resistance for planing craft is not a function of wetted keel length but a function of mean wetted length. At longer wavelengths, the mean wetted length (an average of the chine and keel wetted lengths) will approach the calm water running value, this requires a slight reduction in the mean wetted chine length to compliment the slight increase in mean wetted keel length.

As the magnitude of the wetted surface approaches the calm water running value, the resistance would be expected to as well. However it has already been seen that the resistance at longer encountered wavelengths reduces the resistance below the calm water value. Consequently, for a slightly increasing wetted keel length, the wetted chine length must reduce fairly significantly for the resistance to be less in long waves than in calm water.

This rather involved discussion of wetted lengths demonstrates the importance they play in the resistance and lift of the planing craft. A method for predicting these two quantities based upon the wetted lengths would be advantageous which requires the prediction of the wetted lengths in the first instance. In calm water, Savitsky (Savitsky 1964) describes an expression for wetted lengths based upon trim angle, beam and deadrise and from these expressions relates the subsequently generated lift and resistance. If these expressions for wetted lengths could be applied dynamically for use in waves then lift and resistance in waves could be predicted.

---

[4] Wetted length in figure (A.146) has a value of 2 added to all the amplitudes. This is purely to improve visual comparisons on the graph.

Savitsky's expression for wetted keel length in calm water planing is given as

$$L_k = L_m + \frac{b \tan\beta}{2\pi \tan\tau} \tag{8.1}$$

where τ is the steady-state trim angle and L_m is the mean wetted length and b is the chine beam

L_k is not a function of time, but if it were then a dynamic equation could be hypothesised as

$$L_k(t) = L_m(t) + \frac{b \tan\beta}{2\pi \tan(\theta(t))} \tag{8.2}$$

where $\theta(t)$ is the instantaneous pitch angle and is a function of time. Since chine wetted lengths have not been measured, $L_m(t)$ is replaced by an arbitrary constant, in this instance equal to the calm water mean wetted keel length of 3.75 craft beams. For small pitch angles then the variation in wetted length is in phase with pitch which as noted earlier is not so. Introducing heave into the above equation and fitting coefficients so that the expression matches measured results leads to,

$$L_k(t) = A\left\{B + \left(L_e + \frac{b \tan\beta}{2\pi \tan(\theta(t))}\right) - D.z(t)\right\} + C$$

where $z(t)$ is the instantaneous heave. Fitting the coefficients A, B and C and D to data indicated that $D = B$ hence,

$$L_k(t) = A\left\{B + \left(L_e + \frac{b \tan\beta}{2\pi \tan(\theta(t))}\right) - B.z(t)\right\} + C \tag{8.3}$$

This equation is not explicit, has no rigorous mathematical basis and merely represents curiosity on the part of the author to relate calm water predictions of wetted data to the dynamic wetted data in waves. The solid lines in figure (A.143) to figure (A.147) show the predicted wetted keel lengths from equation (8.3) with actual measured wetted keel length. The results show very good agreement as expected since the coefficients are varied until the predicted results match. However, figure(A.149) shows the variation of the coefficients with wavelength and demonstrates a positive linear relationship for the coefficients with increasing wavelength. This implies that despite the simple approach outlined above, the calm-water time-independent wetted keel length predictions can be manipulated into evaluating the dynamic wetted keel length in waves. It therefore seems possible to predict the dynamic wetted lengths given only limited data of beam and deadrise and the time data of heave and pitch and from there a tentative hypothesis for the evaluation of dynamic lift and resistance.

Troesch (1992) employed a similar technique in investigating the dynamic variation of wetted lengths of craft undergoing forced perturbations in either heave or pitch. Equation (4) of that paper was plotted against the measured values from analogue video tape analysis and showed excellent agreement in terms of predicted wetted keel lengths. Chine lengths were not as well predicted, but again correct identification of water/chine intersection was difficult due to the obtrusive prescence of the spray jet.

8.5 Conclusions

One of the aims of the experimental program was, in a limited way, to verify the results of Fridsma's experiments thereby providing some justification in the use of his data for comparison with the numerical models described herein. To this end, the new experimental results compared very well with those of almost thirty years ago, although slight discrepancies in calm water steady-state running conditions were found and, in waves, discrepancies in the heave and pitch responses at the longer wavelengths. These discrepancies actually increase the theoretical models agreement with experiment for this configuration.

The use of a computer vision data acquisition technique demonstrated its importance in being able to identify specific points of interest and remotely capture large amounts of data. Unfortunately, this approach is limited at present by available hardware and software.

The computer vision data acquisition allowed the capture of wetted keel length data. Analysing this data and applying a tentative dynamic variation to Savitsky's calm water equations suggests an ability to predict forces of lift and drag in waves. Indeed, Troesch (1992) reached a similar conclusion, surmising that whilst the wetted chine lengths are heavily influenced by the free surface behaviour, the wetted keel lengths are well predicted by assuming a dynamic variation of calm water equations. Although this technique is not rigorously founded, or proven in terms of force prediction, it is an interesting hypothesis that requires further investigation.

Chapter 9

Discussion

The aim of the work carried out herein was to provide a theoretical means with which to evaluate planing craft performance in calm water and in waves. The complexity of planing craft dynamics and its associated effects meant that within the scope of this work, the problem was reduced to the vertical plane motions and the neglect of resistance components.

Chapter 1 described the important characteristics of pitch and heave instability, or porpoising, in calm water and the vertical response in waves, namely heave, pitch, accelerations and added resistance. The understanding of these phenomena would provide an efficient and consistent approach to planing hull design. This can be achieved by investigating the effect of perturbations in the design variables upon specific responses of interest.

A parametric investigation of the effect of planing hull design variables requires an accurate and efficient numerical technique. Previous approaches were reviewed in Chapter 2 and the final approach chosen was based upon a slender body strip-theory. This strip theory is based upon the sea-plane float impact research initiated by Munk(1924). The hull is decomposed into transverse sections which enable the three dimensional problem to be reduced to a summation of two dimensional problems for which solutions can be readily derived. This strip theory approach provides results which are comparable with experiment and often exceed the accuracy of the results of full three dimensional solutions and panel methods.

Chapter 3 described the manner in which the two dimensional problem is solved and is based upon impact theory. To an observer in a fixed slice of fluid normal to the direction of planing craft forward motion, the passage of the hull through that fixed transverse slice produces the same effect as an impacting body of the same section would upon the surrounding fluid. This impact is directly analogous to the impulsive motion of the rigid double body moving in an infinite fluid without circulation.

Attempts to remove some of the effects of various approximations required to achieve the above analogies have been presented. The effect of aspect ratio, a three dimensional correction, has a significant effect upon the predicted hydrodynamic lift of planing bodies. The assumption of no circulation around the double body in an infinite fluid is analogous to the condition that there is no separation of the fluid flow when the body is impacting upon the interface. A crossflow drag term is added which allows for the incremental lift for when the flow separates off the chines. This crossflow drag term is equal to the added mass increase due to chine immersion.

At lower planing speeds, there is a more obvious compromise between hydrostatic and hydrodynamic contributions to the overall lift experienced by the planing hull. Applying a manometer model for the drop in localised wetted draft at the transom increases the applicability of the calculated total lift experienced by the planing hull at lower speeds.

The frequency domain linear model was presented in Chapter 4 and is based upon the theory proposed by Martin(1978a, 1978b) which is in an abstracted form in Appendix B. This model is used to evaluate the stability boundaries of the planing craft in calm water and to demonstrate the neccesity, even in calm water performance, of the inclusion of time-dependent wetted lengths in improving the prediction of craft response.

The neglect of the time-dependency of the wetted area in the linear model certainly precludes the use of this approach in accurately identifying the vertical responses in waves. A time-domain model was presented in Chapter 5 that considers the variable wetted length for the planing craft undergoing heave and pitch motion.

The specific results of parametric variation upon the porpoising boundaries and the effect upon planing craft motions in waves will not be repeated here. The results from the linear model developed herein is very comparable to Martin(1978a, 1978b) own published results. Any differences are attributed to the extraction of data from Martin's graphically presented results and rounding errors within the program. The conclusions of Martin's investigation into the parametric variation of design parameters will be the same. However, the main point is in the application of the non-linear model to establish much more accurate boundary conditions for porpoising, which shows the benefits of including the effect of time-varying wetted lengths and providing further validation to the approximations of crossflow and aspect ratio.

The application of the non-linear time-domain numerical model, with frequency independent added mass and damping terms, provided generally good agreement with the experiments of Fridsma(1969, 1971). Furthermore, the removal of second and higher order terms from the equations of motion had a limited effect upon the accuracy of the predicted motions in waves and also in calm-water. Removing the higher order terms provides an ability to investigate the response of the craft in terms of the behaviour of the hydrodynamic coefficients, isolating specific terms that dictate craft perfomance. For example, the heave induced pitch damping term, n_{53}, was discovered as being indicative of the craft's porpoising boundary in calm water, being the only damping term remaining positive for stability. The frequency domain approach shows a similar characteristic for the equivalent damping term, $M_{\dot{z}}$, which tends to zero as the stability boundary is approached. All the other damping terms become increasingly negative for both the time-domain theory and the frequency domain theory. The implication of this is that the influence of specific parametric changes could be understood by the effect of changes upon the magnitude and behaviour of the hydrodynamic coefficients.

The added mass and damping terms employed in the hydrodynamic coefficients of the equations of motion are typically considered to be independent of frequency. Within the framework of wedge impact theory, this is dependent upon the free surface boundary condition being described by equation (3.8). If the frequency of oscillation is considered low, then the value of added mass for the same immersed section is different, equation (3.87). An investigation into the effect of frequency dependence upon the vertical responses was described in Chapter 3, section 3.5, and initiated in Chapter 5.

Frequency dependence of the added mass and damping terms has been shown to be most significant for craft operations at low speeds and in waves of low encounter frequencies which reflects the findings of Troesch(1992). This does not suggest that the inclusion of this dependency increases, in all cases, the accuracy of the predicted vertical responses for these conditions. In fact, whilst the pitch response and accelerations are usually better predicted, the heave response tends to be in considerable error. The theory is developed around the accurate prediction of hydrodynamic lift force, so an attempt to improve the model in the low speed/low encounter frequency region of planing by solely examining of the effect of frequency dependent added mass and damping terms may be somewhat unjustified.

The general tendency to overpredict motion responses at low frequency and lead to underpredictions at high frequency may point to the failure of NoLiPCraMP in applying the damping coefficient correctly at a given encounter frequency. Figure A.151 shows that at low frequency the damping force is significant and if not modelled correctly will result in the overprediction of lift force.

The inclusion of frequency dependence has produced no significant improvement in the vertical motions expected from the work of Troesch(1992), Chiu and Fujino(1989) and Chou et al(1991) which points to the breakdown of the computer program in the correct application of the theory. The general improvement in the prediction of accelerations is considered incidental.

The behaviour of planing craft in irregular seas was investigated in Chapter 7. An ITTC spectrum was constructed from significant waveheights and modal periods associated with conditions in the eastern Atlantic, table 7.1. Linearity of system response was found, by the use of spectral analysis and in seas with enountered frequency content comparable to regular wave tests, to be applicable upto speed:length ratio of 4 and for $3 < \lambda/L < 2$ at $V_{kt}/\sqrt{L_{ft}} = 4$.

The application of the frequency independent approach led to good agreement in the expected comparisons of heave and pitch motion probability distributions with generalised Rayleigh probability distributions. Accelerations agreed well with the expected probability distributions at high probability of exceedence, however the higher numerically predicted accelerations were less likely to occur than those theoretically predicted by the exponential distribution. The inclusion of frequency dependence by consideration of the modal encounter period resulted in negligible improvement in probability distribution fits for heave motions, and generally worse agreement in pitch maxima and minima distributions, but increased accuracy in the prediction of the occurance of bow accelerations.

An experimental investigation into the vertical motions of one particular craft configuration, configuration K, was carried out in order to compare the direct time-histories of experiment with theory. The experiments also allowed the application of a new technique in data acquisition using a computer vision system to acquire large amounts of visual data simultaneously. The use of a Computer Vision Data Acquisition (CVDA) system has a number of advantages in that the system is easy to use, self-calibrating, unintrusive, able to capture large amounts of visual data simultaneously and allows the analysis of particular phenomena at will. Unfortunately, automation of the capture of *points of interest* was outside the scope of this thesis, but human eye measurements from the digitised images provided extremely good agreement with standard electronic data acquisition results.

The wetted data, fundamental in planing craft performance, could be captured easily and discrepancies in the percieved boundaries of wetted area are reduced. It was also found there was a strong argument for the application of a dynamic variation to calm water wetted length predictions in accurately predicting the time-varying wetted lengths. As a result it is hypothesised that a dynamic application of calm water planing equations can provide valuable insight into the lift and drag components of planing craft operation in waves.

Chapter 10

Conclusions

Theoretical and experimental investigations have been carried out which improve the understanding and performance prediction of the complex behaviour of planing craft in calm water and in waves.

A modified strip theory analysis is successfully applied for evaluating vertical motions of planing craft in calm water, regular and irregular seas. The shortcomings of solving the equations of motion in the frequency domain for calm water performance are identified and agreement with experimental results improved with solution in the time domain. For example, the hull wetted surface, which has significant implications on generated lift, is very sensitive to perturbations in heave or pitch, requiring this particular problem to be solved in the time domain.

The time domain analysis allows investigation into the vertical dynamic effects of heave and pitch motions and accelerations in waves which are important to structural survivability and crew operability. Furthermore, the analysis allows examination of the behaviour of the hydrodynamic coeffcients used in the equations of motion and identification of the important terms, such as n_{53} for craft stability.

The developed theories allow the effect of parametric changes upon planing craft performance to be examined with confidence, allowing optimisation and further understanding of planing craft design. Preliminary investigation, for example, demonstrates the importance of deadrise upon planing craft stability and seakeeping in calm water and in waves.

Experiments were carried out in calm water and in waves over a range of speeds to provide data for validation purposes. These data were found to correlate well with earlier published data for a similar hullform, providing confidence in the experimental base.

As part of the experimental programme, a new computer vision data acquisition system, CVDA, is investigated. This system's benefits over standard electronic data acquisition techniques include being a remote system, easy to set-up and reduced set-up time, self-calibrating and able to capture and process large amounts of information, thereby allowing investigation of specific phenomena at leisure. This system's importance is demonstrated by the ability to measure wetted surface area which has allowed a relationship between calm water predictions and the dynamic wetted area in waves to be formed.

The overall research programme has provided important insight into the vertical dynamic effects associated with high speed planing craft in calm water and in waves. Furthermore, the developed theoretical tools, supported by the experimental work, provide a sound basis for predicting these effects.

Chapter 11

Future Work

The work described herein demonstrates that there is much scope for future investigation of planing craft dynamics using simple wedge impact theory. Although the full physical effects are not modelled rigorously, this two-dimensional approach lends itself to efficient evaluation of planing craft performance. Consequently, as an extension to the parametric investigation, a statistical reliability analysis may be applied that can aid optimisation of planing craft design. For example the effect of changing a particular parameter upon the subsequent physical response may lead to a statistical distribution from which optimal criteria can be extracted. The use of a full three-dimensional model is at present time-consuming and in order to achieve the best use of reliability methods, large numbers of different parameters need changing, which tends to preclude full dimensionality.

Although the motions in head seas have been investigated, following seas can be readily applied by altering the influence of the vertical orbital velocities. Furthermore, an extension to account for surge would be trivial but informative for operations in following seas. The use of impact theory upon the transverse stability of planing craft has also shown promising results (Lewandowski 1996), (Xu & Troesch 1999), (Zhao et al 1997) allowing the coupling into roll to be investigated and possible extension to the other degrees of freedom.

Experimental tests are required to further test the validity of the numerical models. Towing tank testing in irregular seas is required. Also with the application of a vertical planar motion mechanism to conduct forced oscillation tests in heave and pitch, the associated hydrodynamic coefficients can be determined and directly compared with the numerical simulations, highlighting the shortcomings of the numerical model. Further validation of the numerical model can be accomplished by consideration of the predicted responses of hull forms that are more likely to be physically representative of modern planing hull design. Data for these hulls is currently being collated by the Department of Naval Architecture and Marine Engineering at the National Technical University of Athens.

The use of a computer vision data acquisition system (CVDA) has been shown to offer many advantages. However in terms of efficiency, the technique at present is limited. What is required is the automation of the system and eventually real-time processing. With the advancement in computer technology and software, the realisation of this may not be too far distant.

Appendix A

Figures

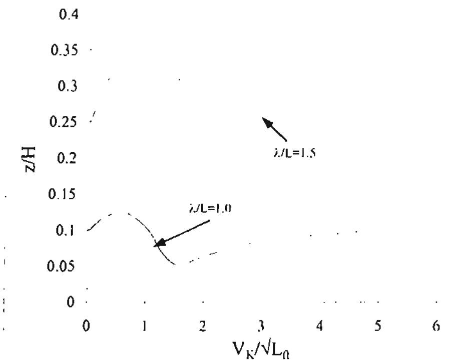

Figure A.1: Heave Response for Planing in Head Seas

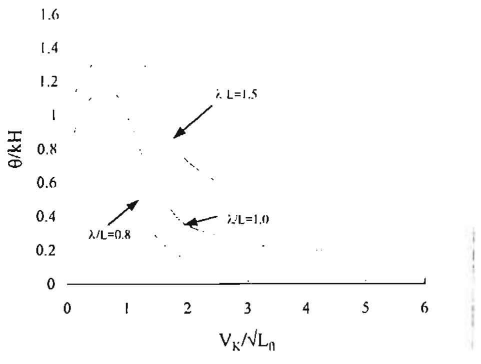

Figure A.2: Pitch Response for Planing in Head Seas

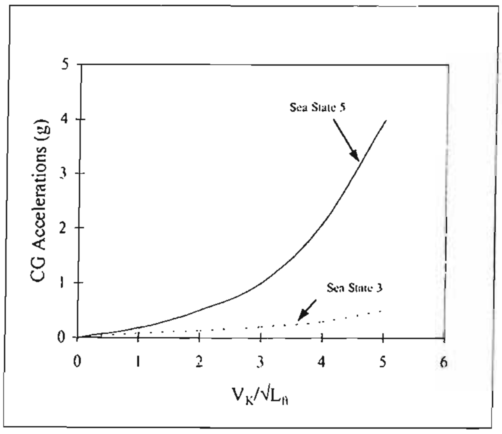

Figure A.3: Accelerations for Planing in Head Seas

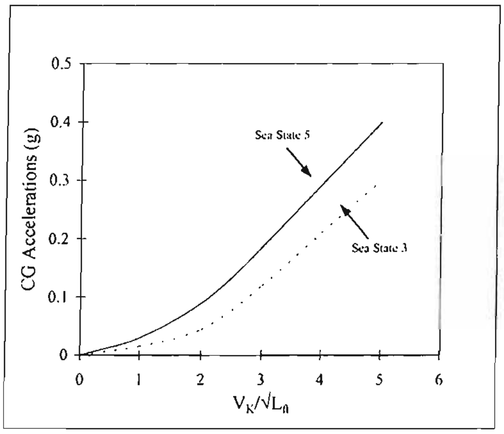

Figure A.4: Accelerations for Planing in Following Seas

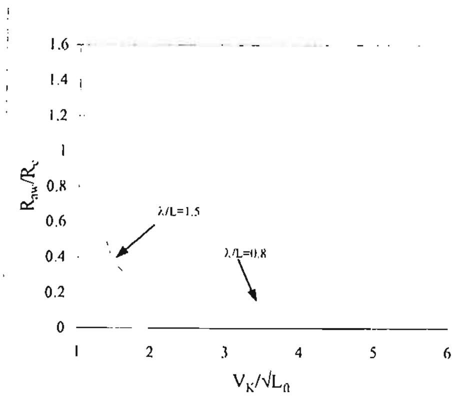

Figure A.5: Added Resistance for Planing in Head Seas

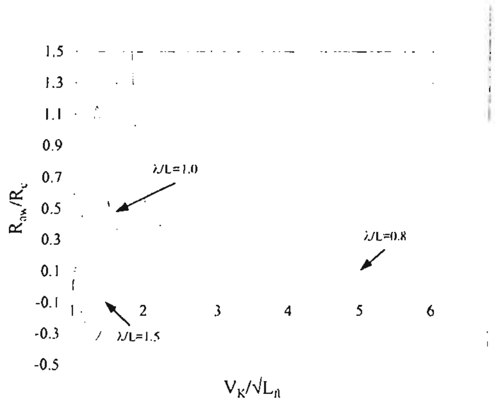

Figure A.6: Added Resistance for Planing in Following Seas

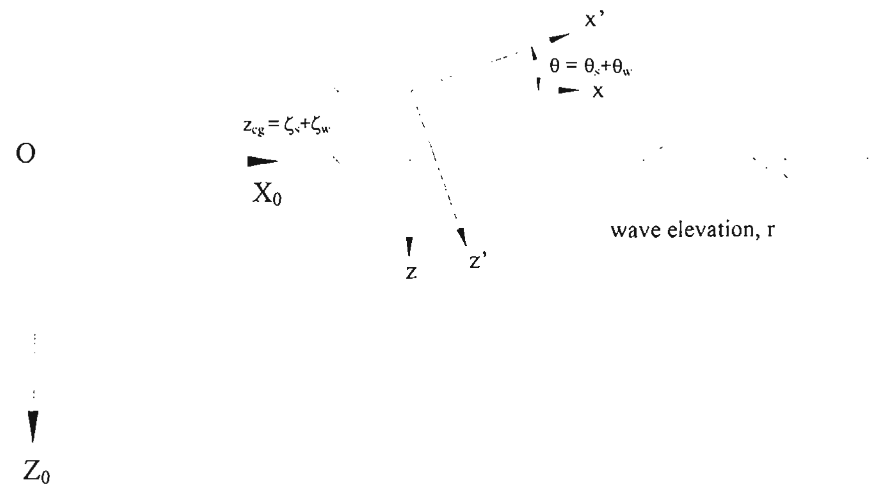

Figure A.7: Coordinate System

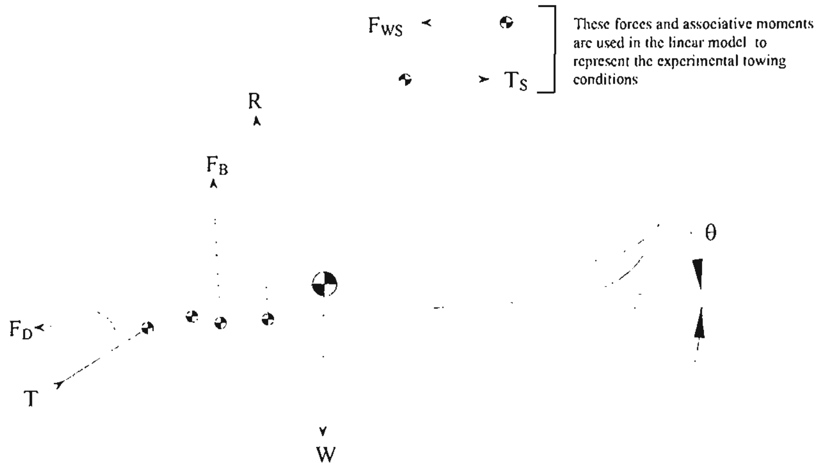

These forces and associative moments are used in the linear model to represent the experimental towing conditions

Figure A.8: Action of Various Forces Associated With Planing

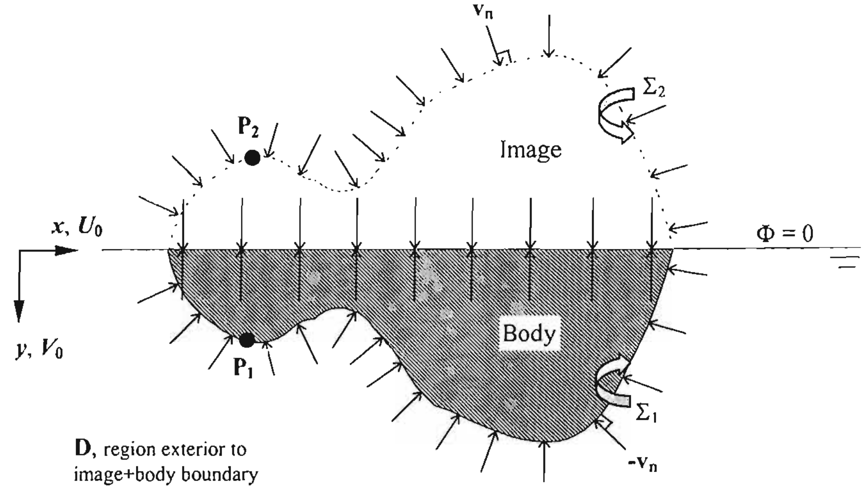

Figure A.9: Representation of Impulsive Motion by a Rigid Double Body Approach

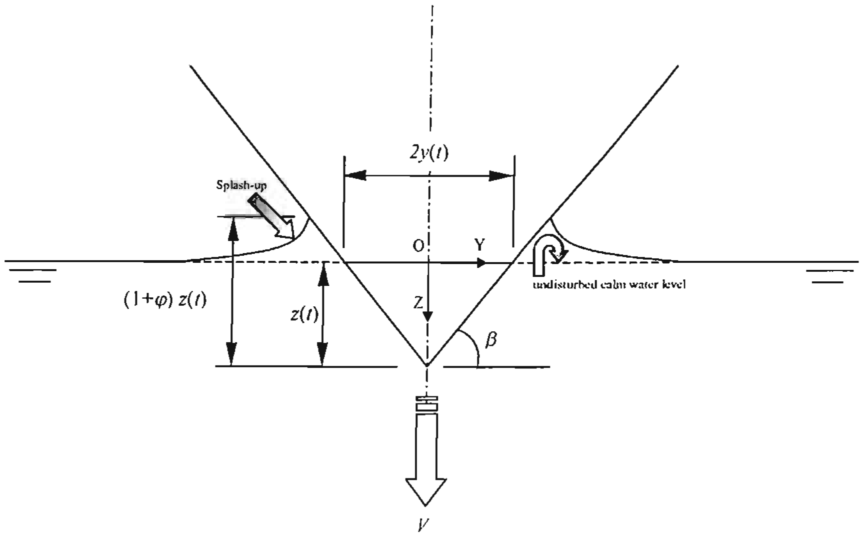

Figure A.10: Impacting Wedge Problem - Expanding Flat Plate Splash-up or Wave-rise also shown

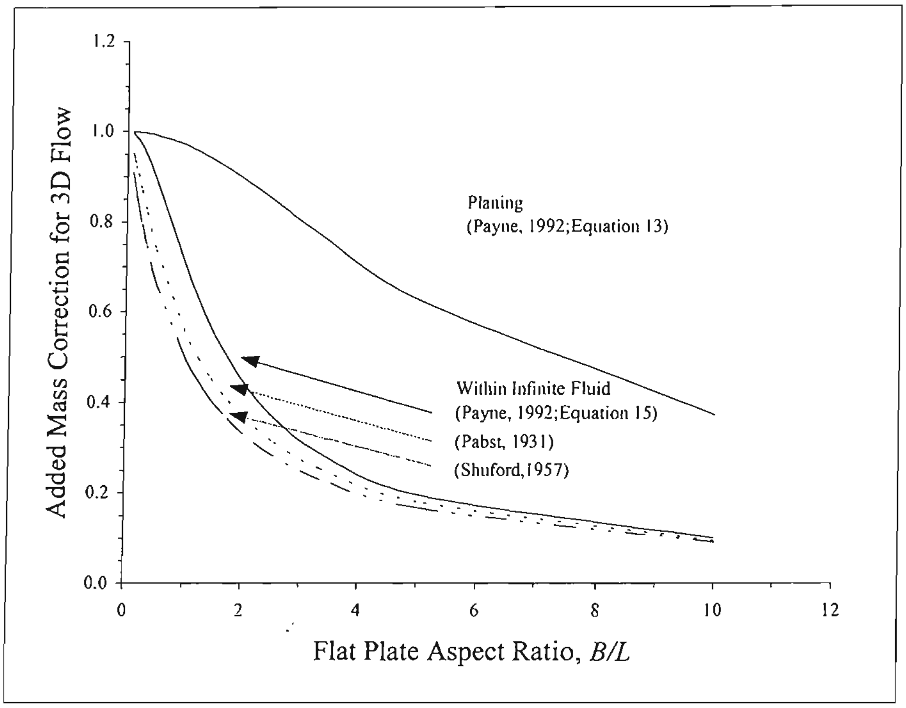

Figure A.11: Aspect Ratio Correction

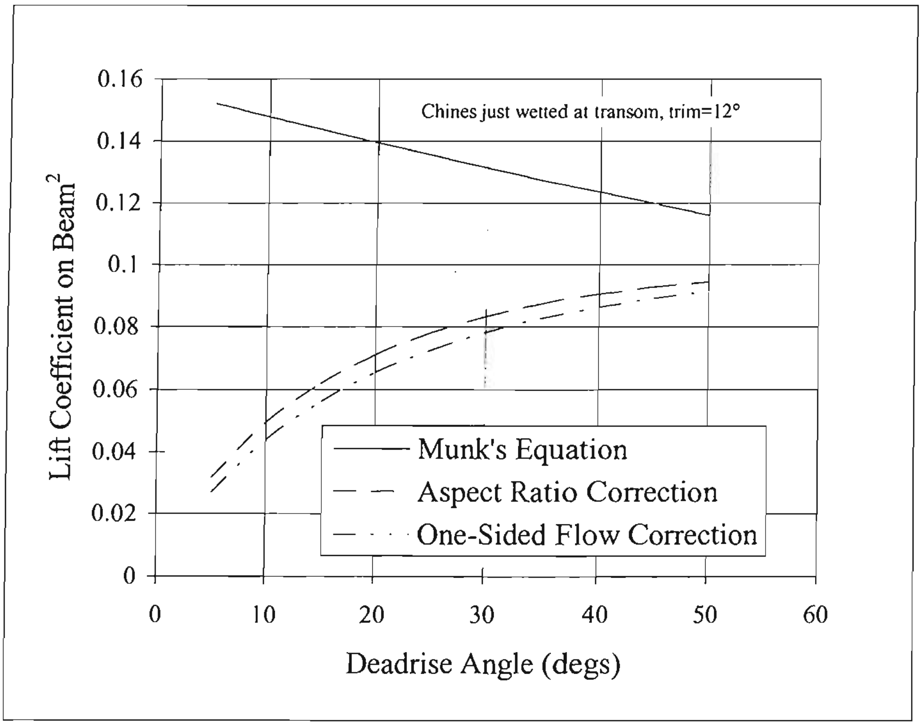

Figure A.12: Effect of Payne's Corrections for Predicted Lift against Deadrise

Chines just wetted at transom, trim=12°

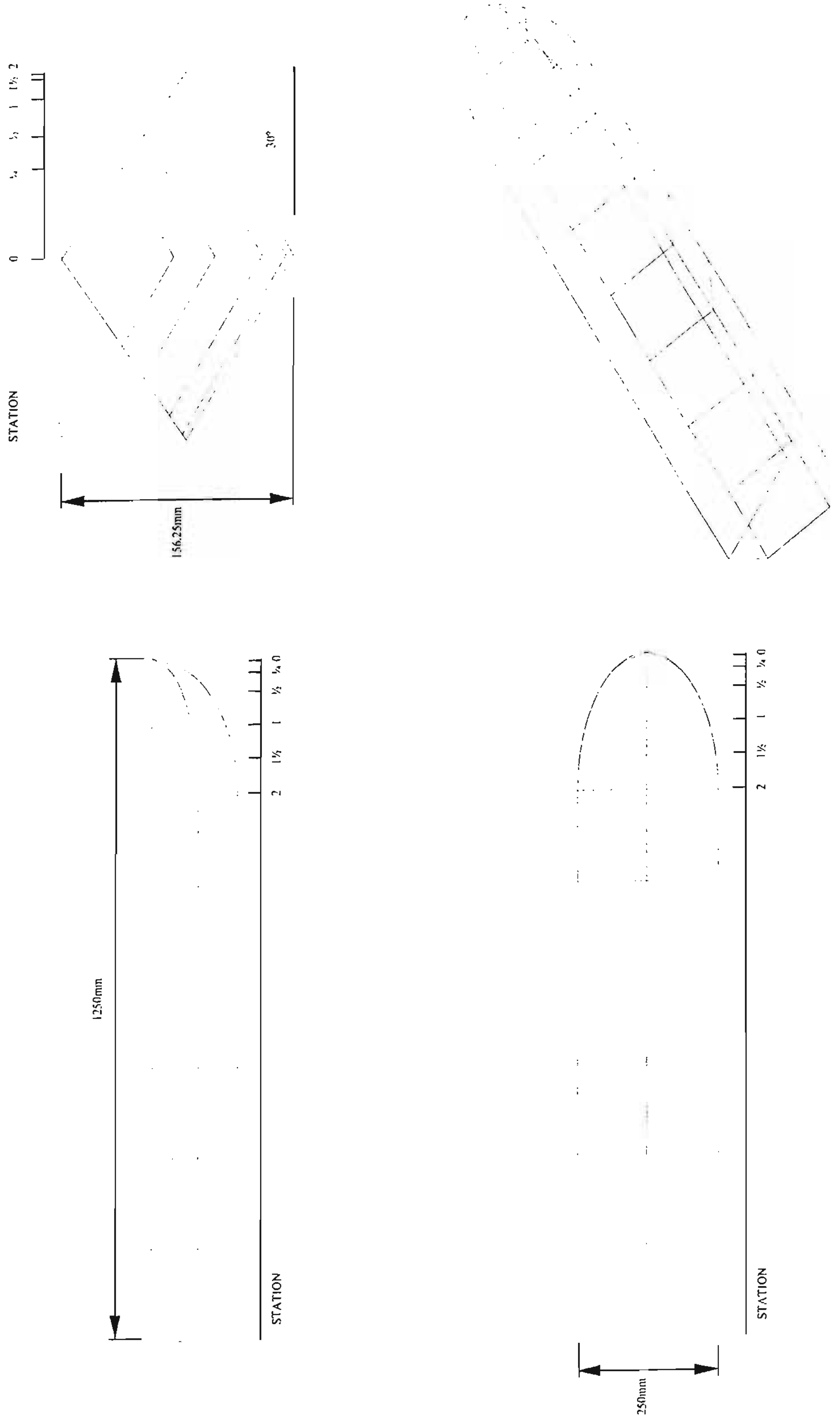

Figure A.13: Model Lines Plan

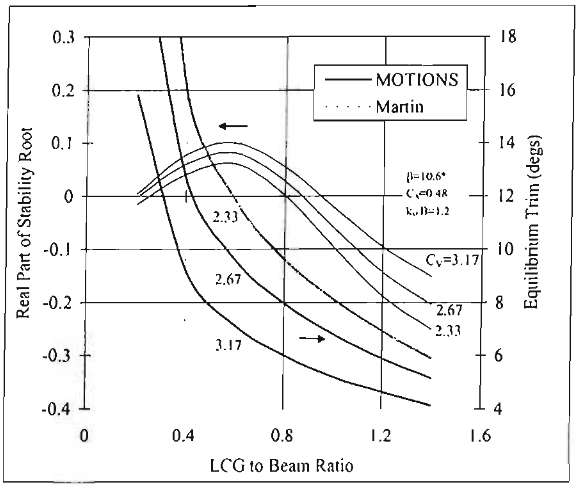

Figure A.14: Variation of Least Stable Root with LCG

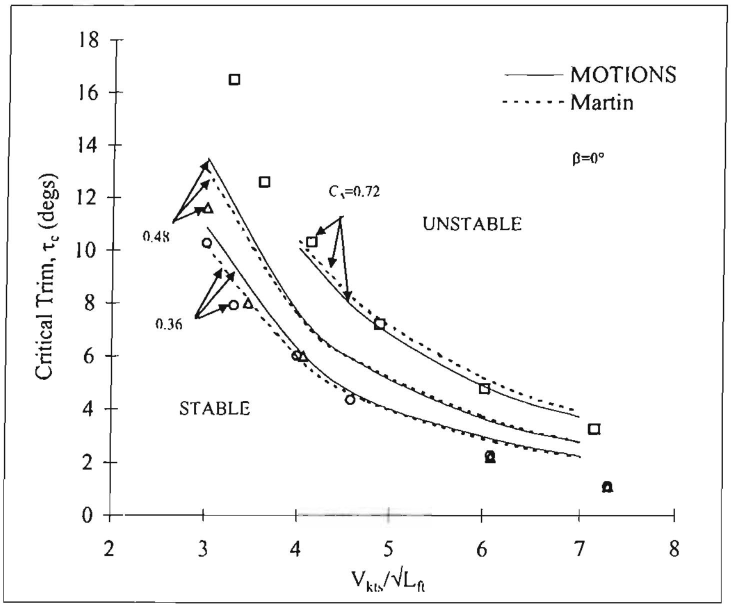

Figure A.15: Variation of Critical Trim with Speed and Load, 0° Deadrise

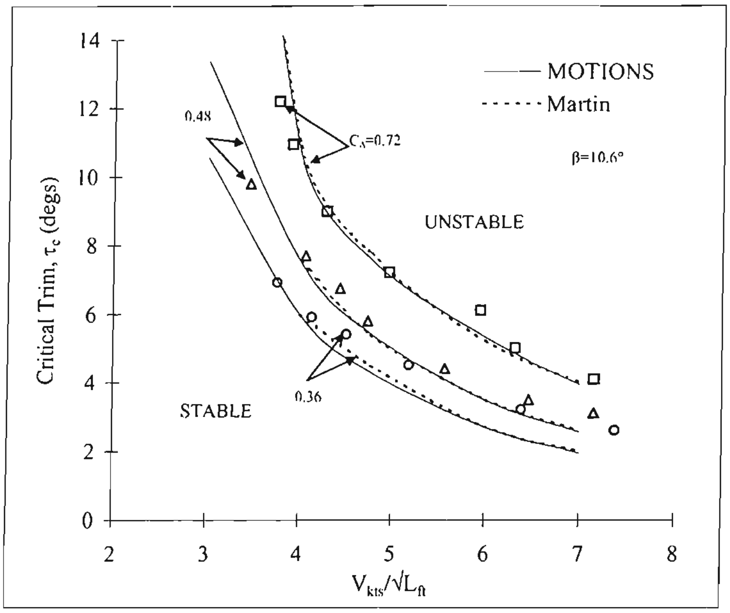

Figure A.16: Variation of Critical Trim with Speed and Load, 10.6° Deadrise (Linear)

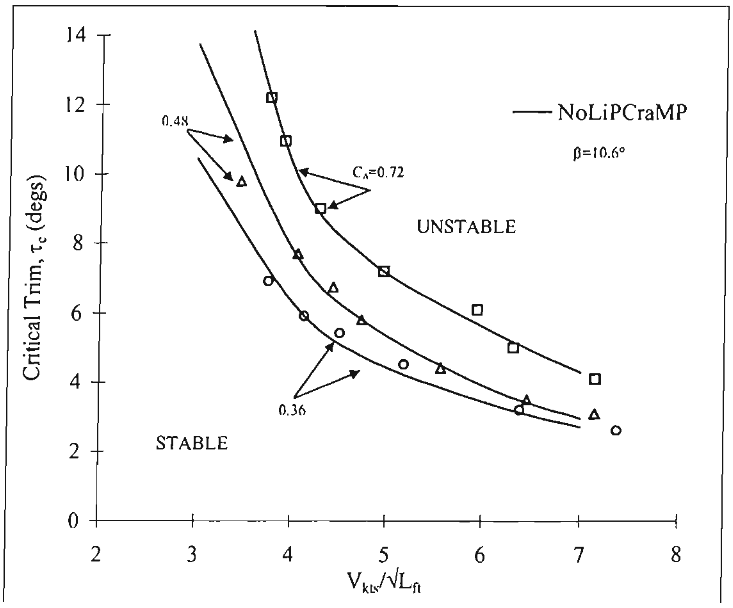

Figure A.17: Variation of Critical Trim with Speed and Load, 10.6° Deadrise (Non-linear)

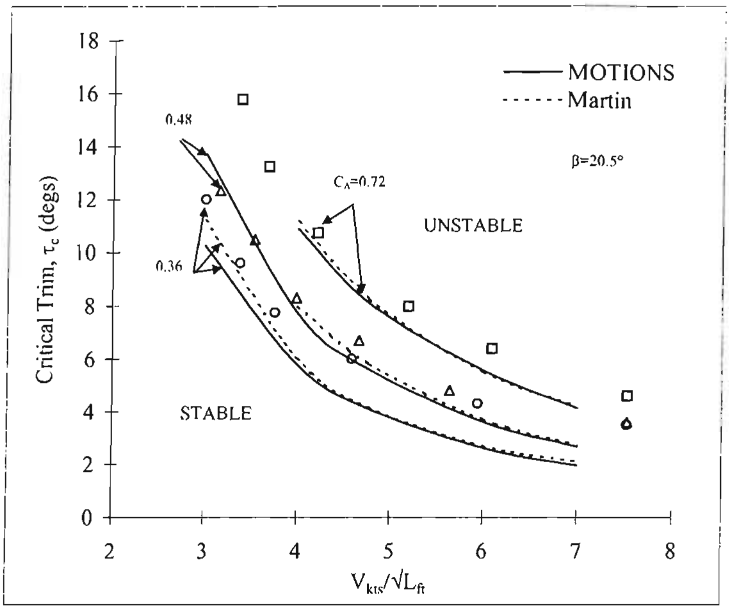

Figure A.18: Variation of Critical Trim with Speed and Load, 20.5° Deadrise

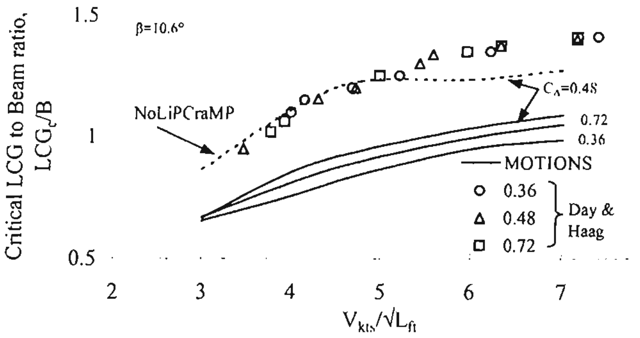

Figure A.19: Variation of Critical LCG with Load and Velocity for 10.6° Deadrise

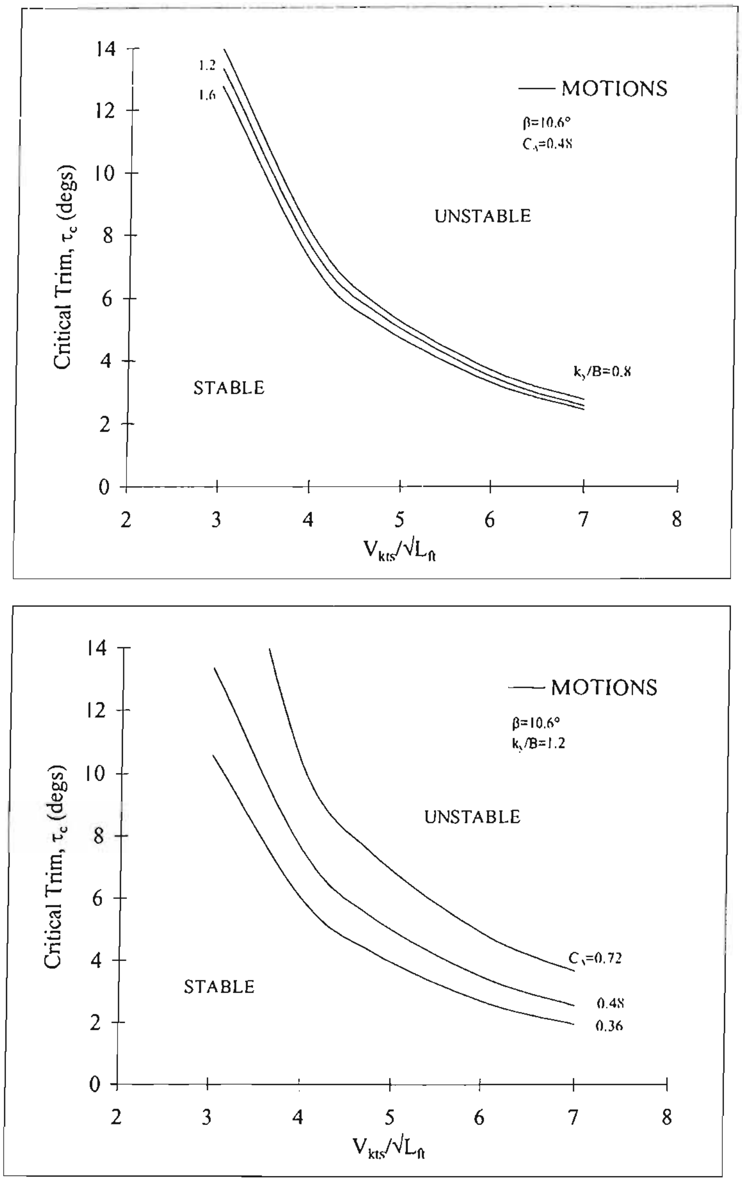

Figure A.20: Variation of Critical Trim with Gyradius and Load, 10.6° Deadrise

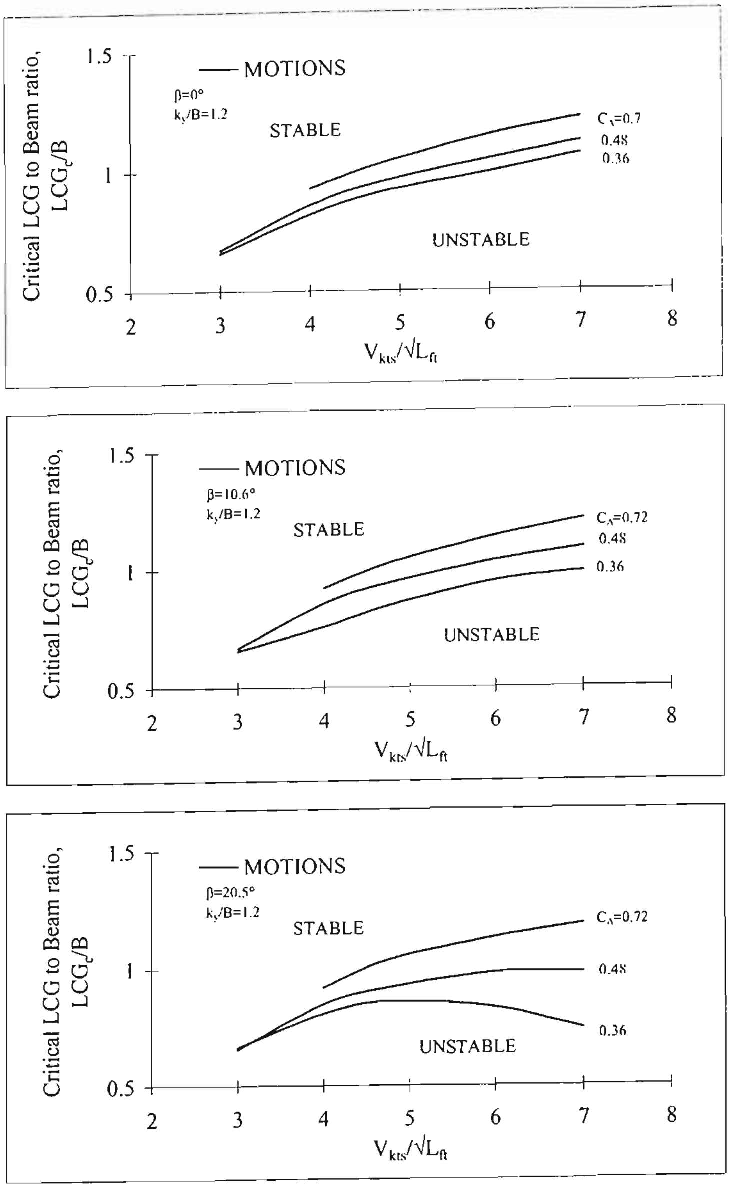

Figure A.21: Variation of Critical LCG with Deadrise and Load

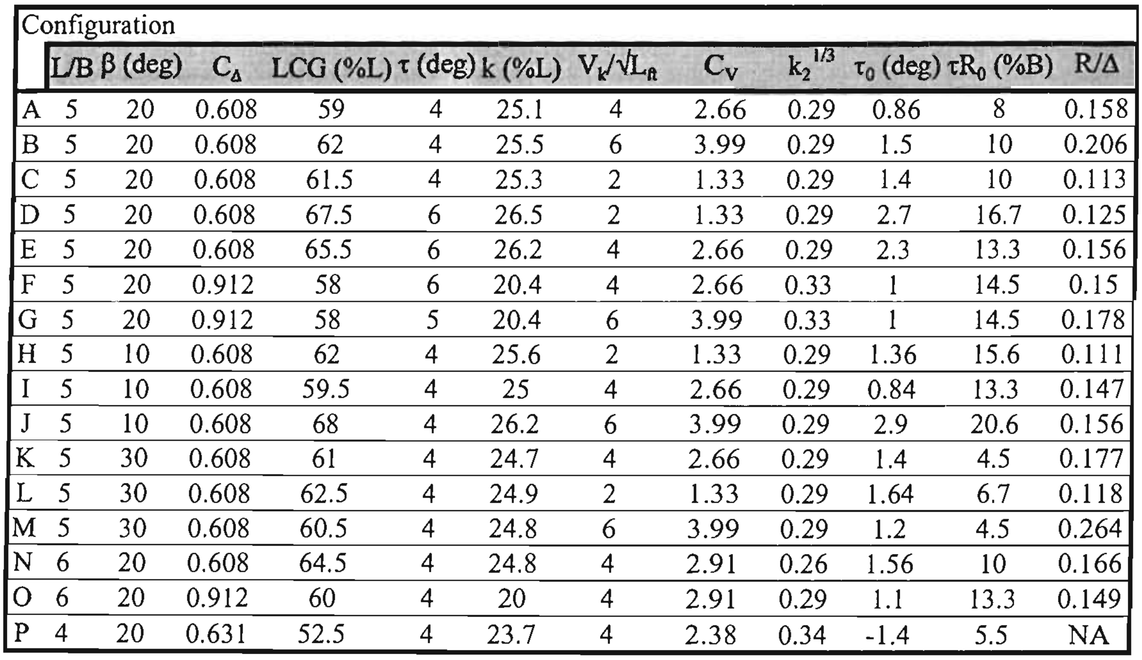

Configuration	L/B	β (deg)	C_Δ	LCG (%L)	τ (deg)	k (%L)	$V_k/\sqrt{L_{ft}}$	C_V	$k_2^{1/3}$	τ_0 (deg)	τR_0 (%B)	R/Δ
A	5	20	0.608	59	4	25.1	4	2.66	0.29	0.86	8	0.158
B	5	20	0.608	62	4	25.5	6	3.99	0.29	1.5	10	0.206
C	5	20	0.608	61.5	4	25.3	2	1.33	0.29	1.4	10	0.113
D	5	20	0.608	67.5	6	26.5	2	1.33	0.29	2.7	16.7	0.125
E	5	20	0.608	65.5	6	26.2	4	2.66	0.29	2.3	13.3	0.156
F	5	20	0.912	58	6	20.4	4	2.66	0.33	1	14.5	0.15
G	5	20	0.912	58	5	20.4	6	3.99	0.33	1	14.5	0.178
H	5	10	0.608	62	4	25.6	2	1.33	0.29	1.36	15.6	0.111
I	5	10	0.608	59.5	4	25	4	2.66	0.29	0.84	13.3	0.147
J	5	10	0.608	68	4	26.2	6	3.99	0.29	2.9	20.6	0.156
K	5	30	0.608	61	4	24.7	4	2.66	0.29	1.4	4.5	0.177
L	5	30	0.608	62.5	4	24.9	2	1.33	0.29	1.64	6.7	0.118
M	5	30	0.608	60.5	4	24.8	6	3.99	0.29	1.2	4.5	0.264
N	6	20	0.608	64.5	4	24.8	4	2.91	0.26	1.56	10	0.166
O	6	20	0.912	60	4	20	4	2.91	0.29	1.1	13.3	0.149
P	4	20	0.631	52.5	4	23.7	4	2.38	0.34	-1.4	5.5	NA

Figure A.22: Hard Chine, Constant Deadrise, Craft Configuration Parameters (Fridsma 1969)

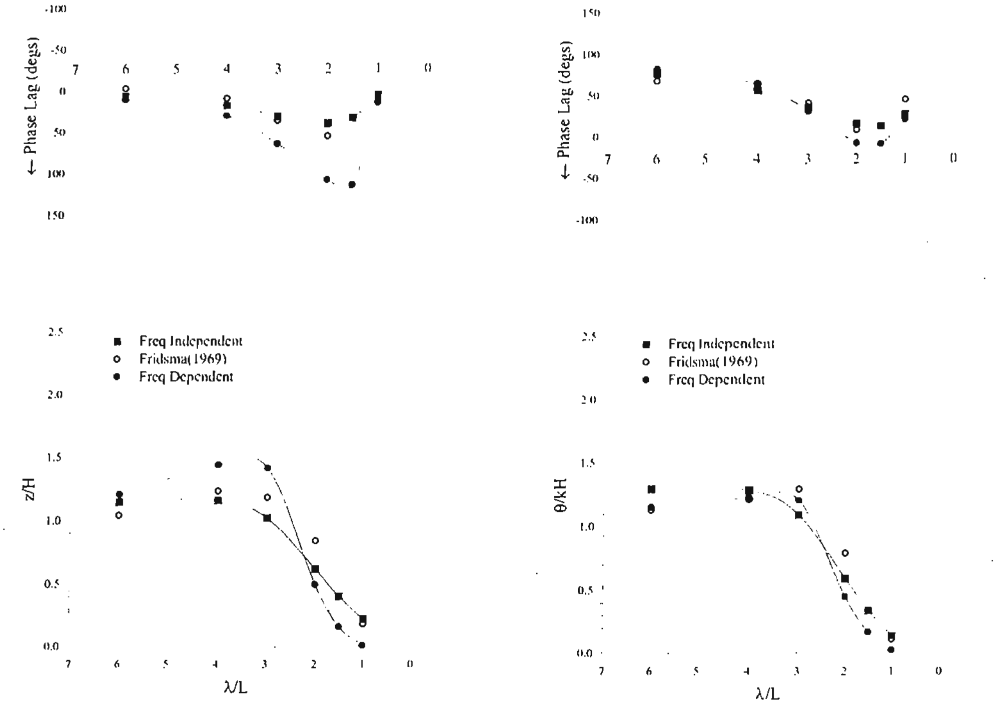

Figure A.23: Heave and Pitch Transfer Functions for Configuration A
$V/\sqrt{L} = 4$, $\beta = 20°$, $C_\Delta = 0.608$, $L/B = 5$, $H/B = 0.111$

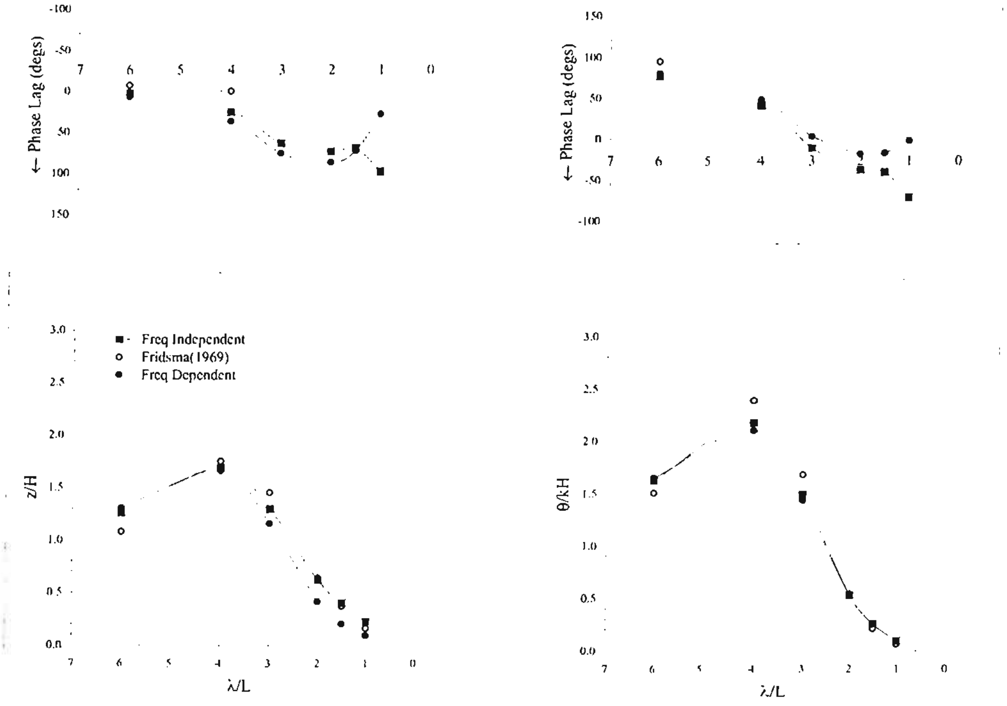

Figure A.24: Heave and Pitch Transfer Functions for Configuration B
$V/\sqrt{L} = 6$, $\beta = 20°$, $C_\Delta = 0.608$, $L/B = 5$, $H/B = 0.111$

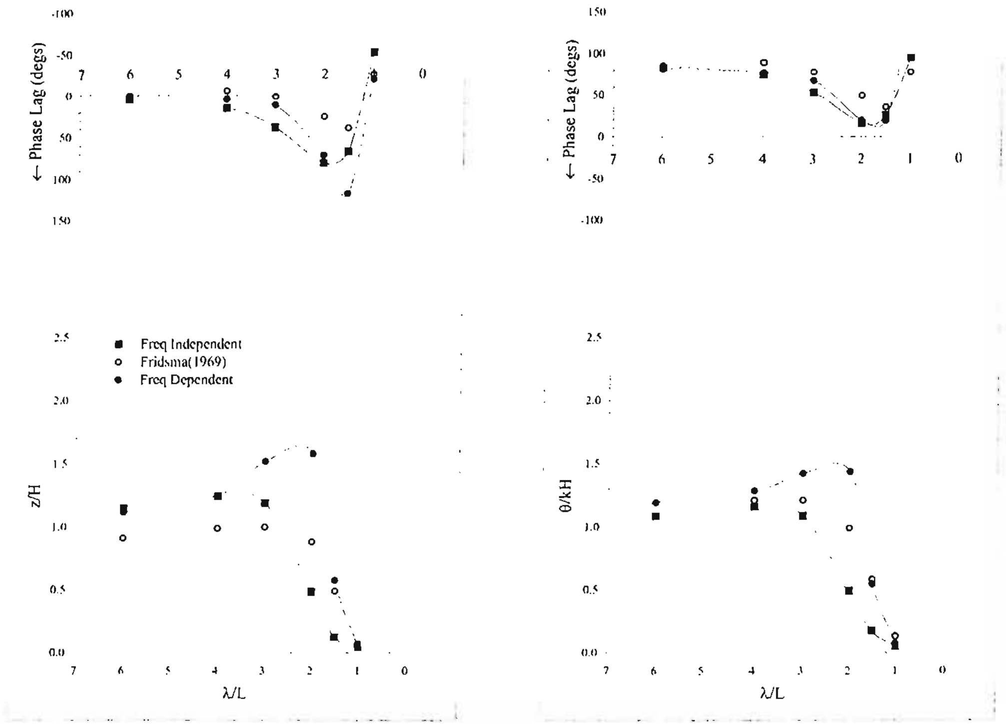

Figure A.25: Heave and Pitch Transfer Functions for Configuration C
$V/\sqrt{L} = 2$, $\beta = 20°$, $C_\Delta = 0.608$, $L/B = 5$, $H/B = 0.111$

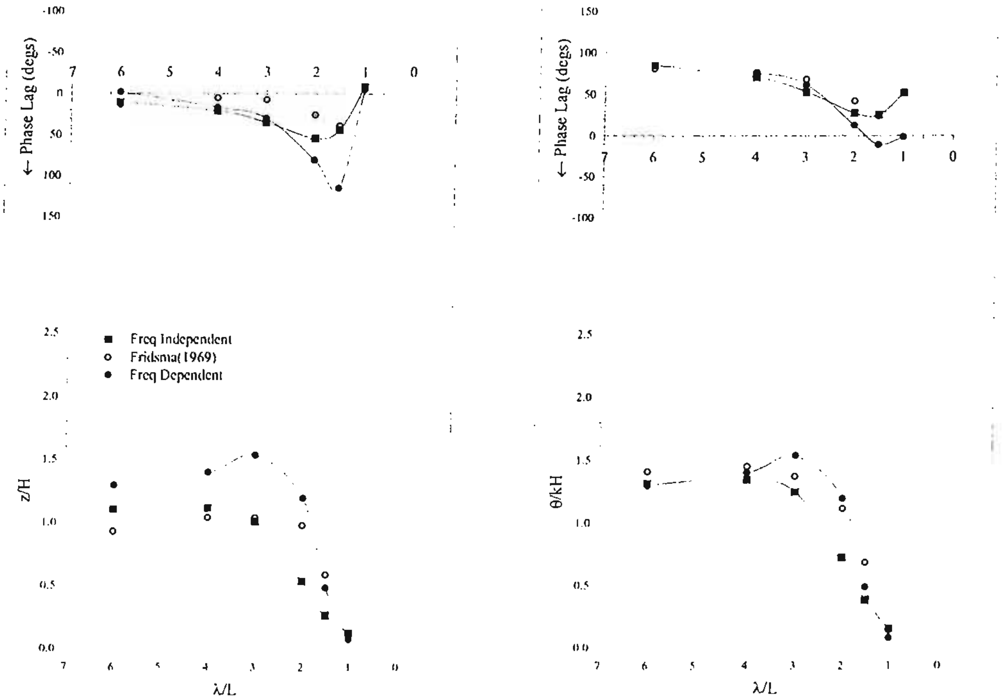

Figure A.26: Heave and Pitch Transfer Functions for Configuration D
$V/\sqrt{L} = 2$, $\beta = 20°$, $C_\Delta = 0.608$, $L/B = 5$, $H/B = 0.111$

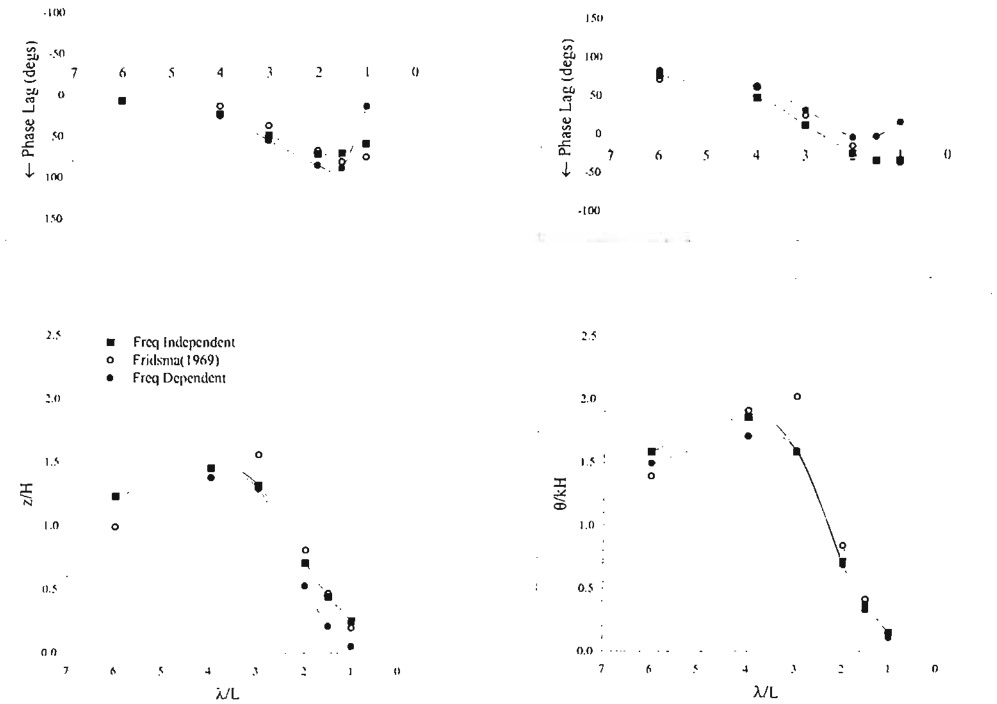

Figure A.27: Heave and Pitch Transfer Functions for Configuration E
$V/\sqrt{L} = 4$, $\beta = 20°$, $C_\Delta = 0.608$, $L/B = 5$, $H/B = 0.111$

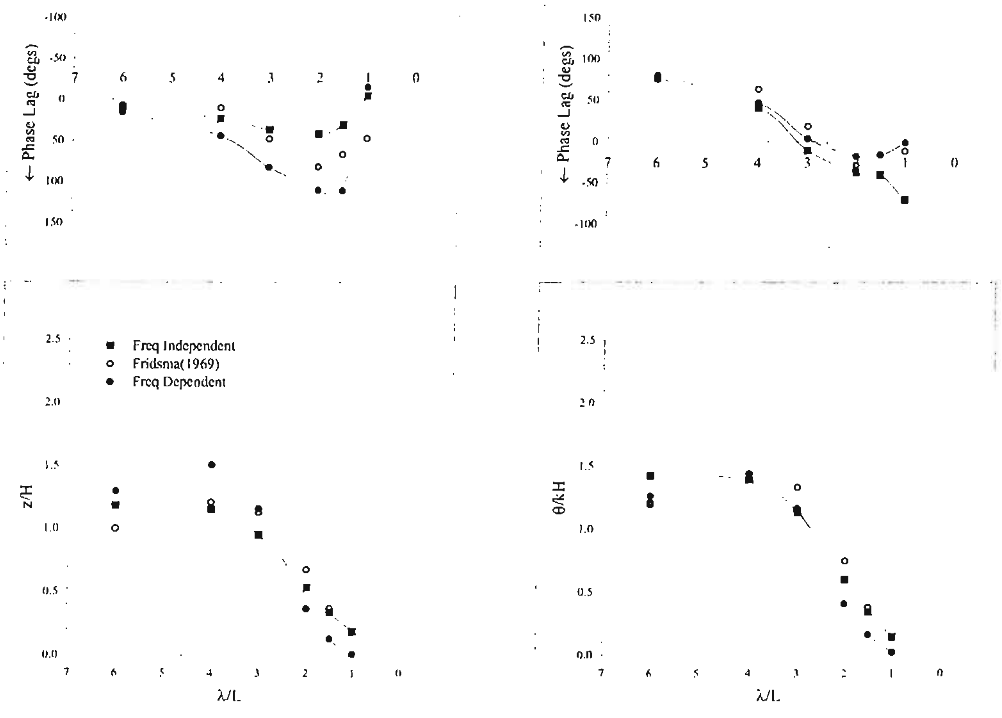

Figure A.28: Heave and Pitch Transfer Functions for Configuration F
$V/\sqrt{L} = 4$, $\beta = 20°$, $C_\Delta = 0.912$, $L/B = 5$, $H/B = 0.111$

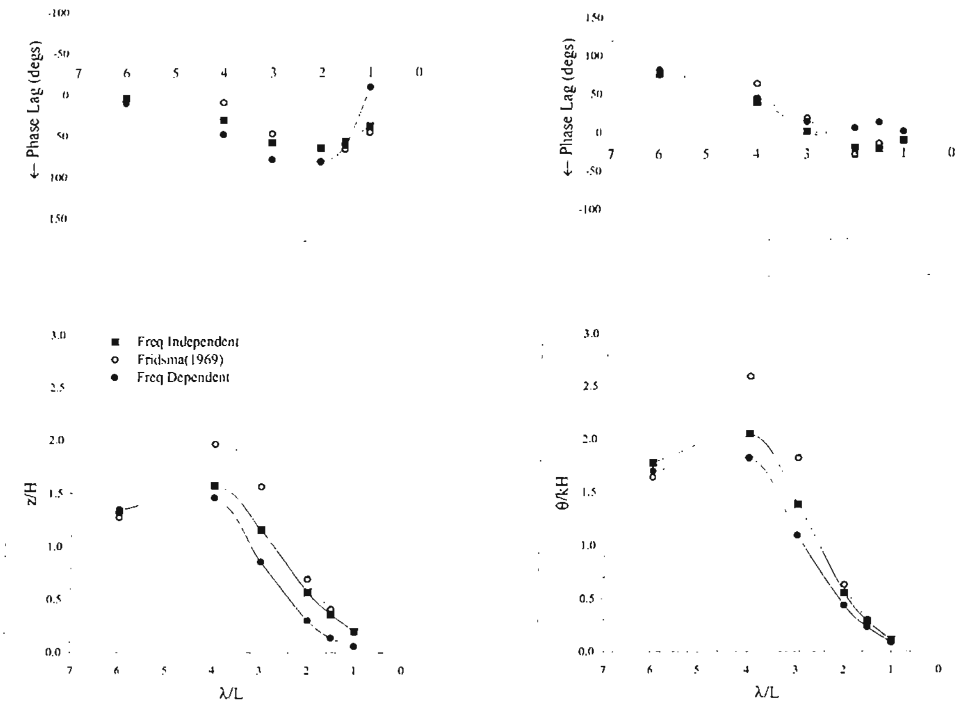

Figure A.29: Heave and Pitch Transfer Functions for Configuration G
$V/\sqrt{L} = 6$, $\beta = 20°$, $C_\Delta = 0.608$, $L/B = 5$, $H/B = 0.111$

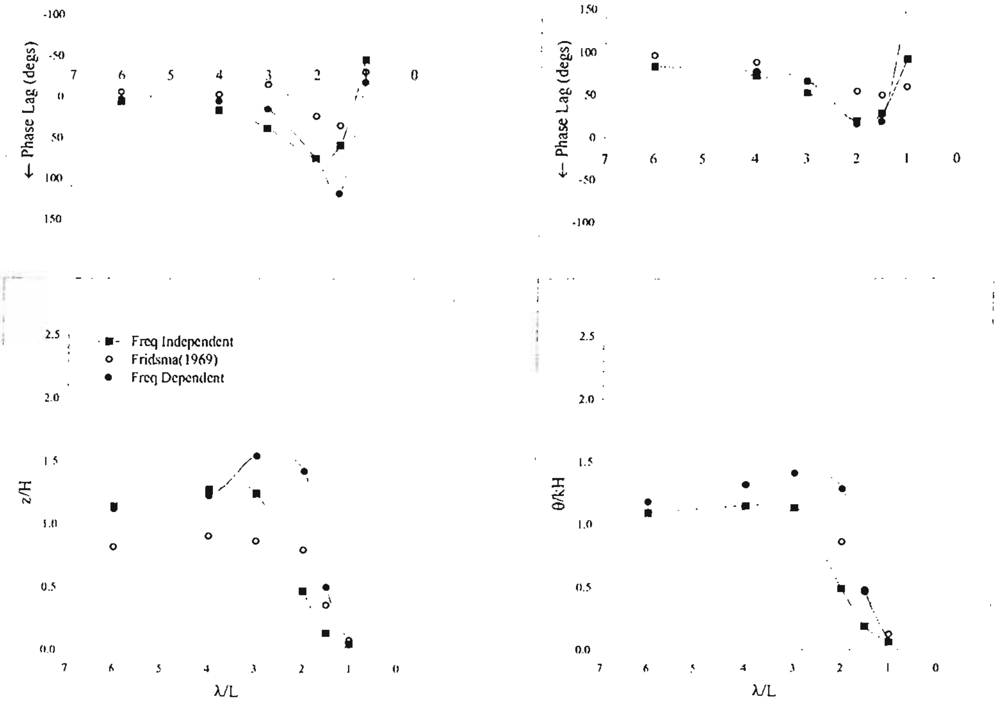

Figure A.30: Heave and Pitch Transfer Functions for Configuration H
$V/\sqrt{L} = 2$, $\beta = 10°$, $C_\Delta = 0.608$, $L/B = 5$, $H/B = 0.111$

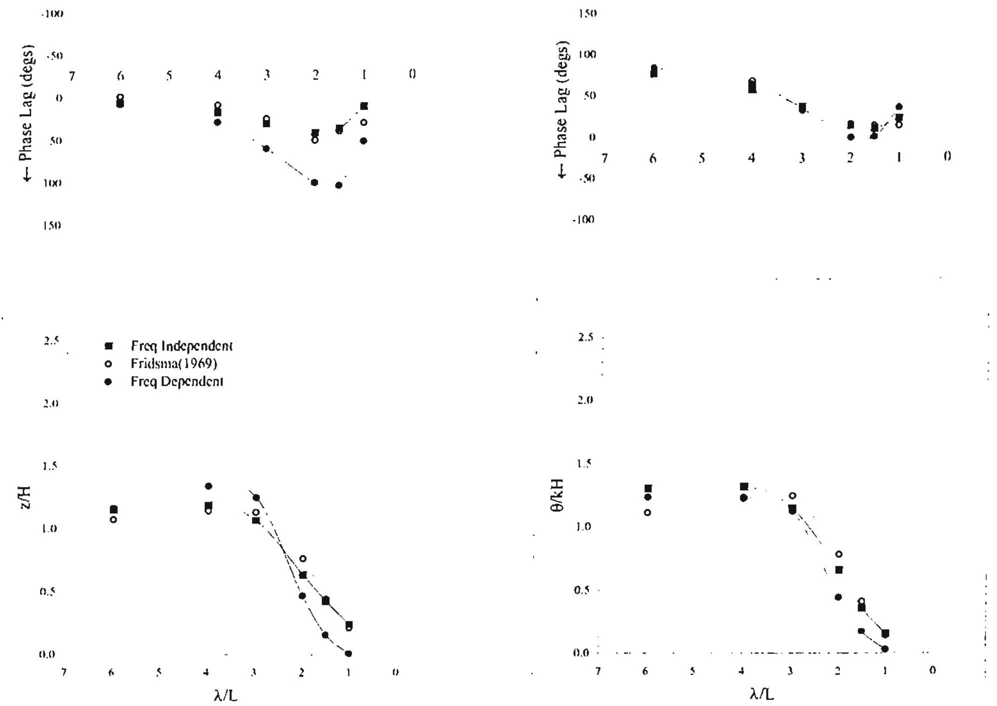

Figure A.31: Heave and Pitch Transfer Functions for Configuration I
$V/\sqrt{L} = 4$, $\beta = 10°$, $C_\Delta = 0.608$, $L/B = 5$, $H/B = 0.111$

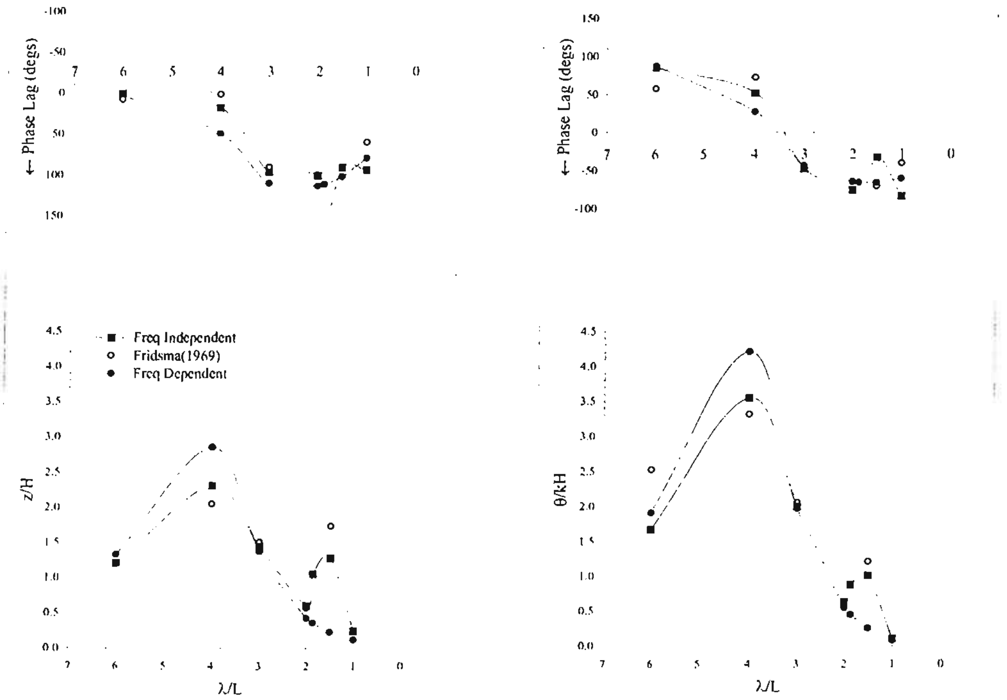

Figure A.32: Heave and Pitch Transfer Functions for Configuration J
$V/\sqrt{L} = 6$, $\beta = 10°$, $C_\Delta = 0.608$, $L/B = 5$, $H/B = 0.111$

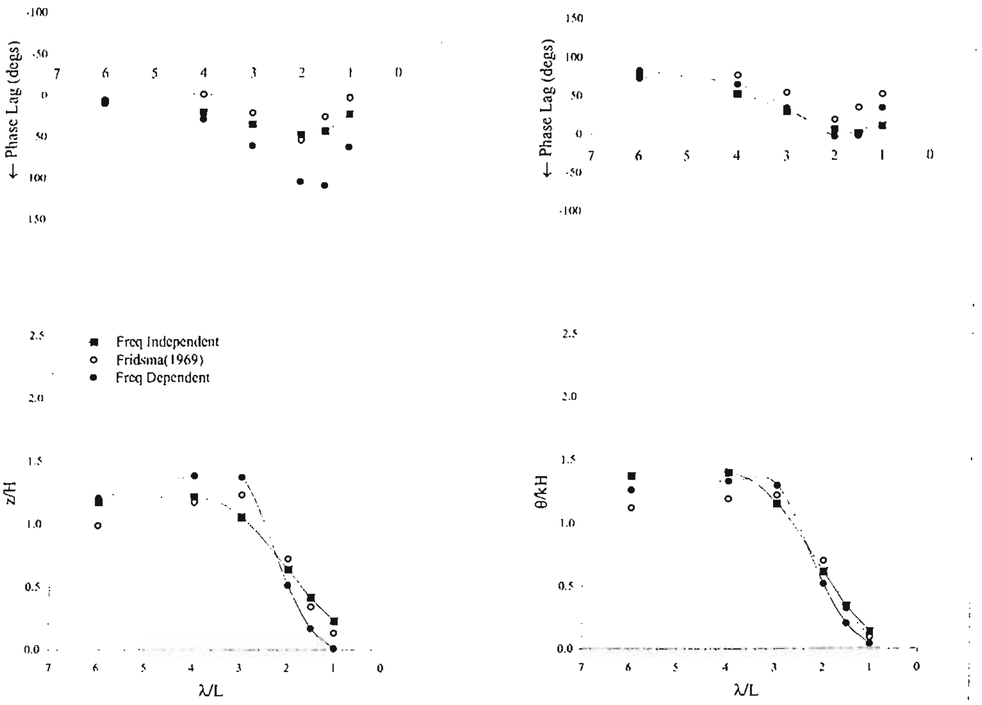

Figure A.33: Heave and Pitch Transfer Functions for Configuration K
$V/\sqrt{L} = 4$, $\beta = 30°$, $C_\Delta = 0.608$, $L/B = 5$, $H/B = 0.111$

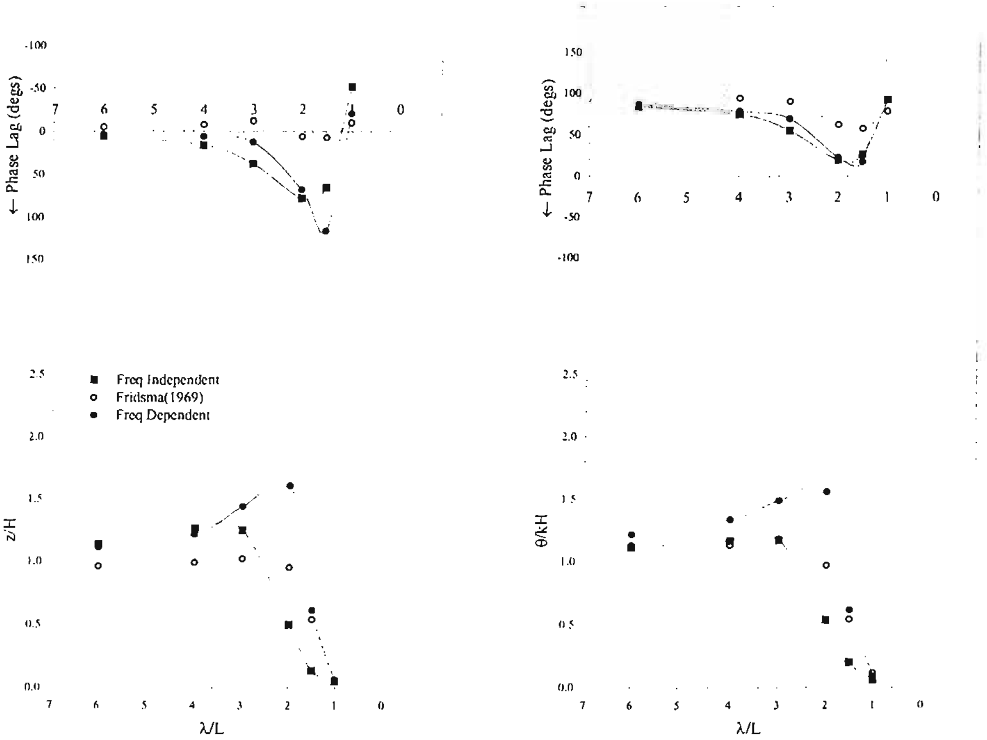

Figure A.34: Heave and Pitch Transfer Functions for Configuration L
$V/\sqrt{L} = 2$, $\beta = 30°$, $C_\Delta = 0.608$, $L/B = 5$, $H/B = 0.111$

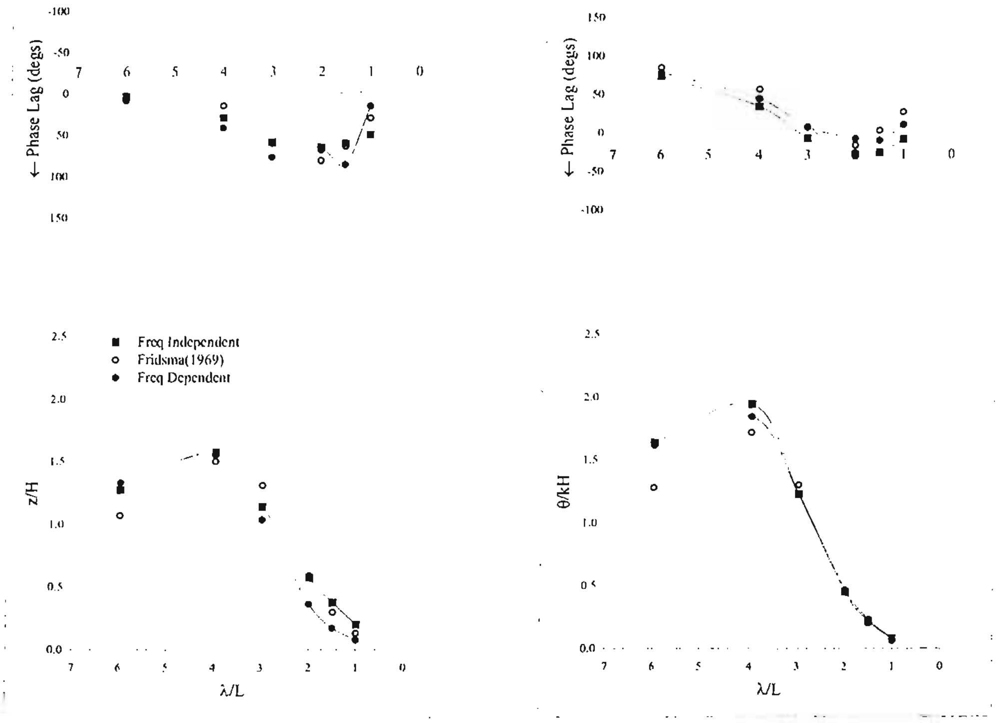

Figure A.35: Heave and Pitch Transfer Functions for Configuration M
$V/\sqrt{L} = 6$, $\beta = 30°$, $C_\Delta = 0.608$, $L/B = 5$, $H/B = 0.111$

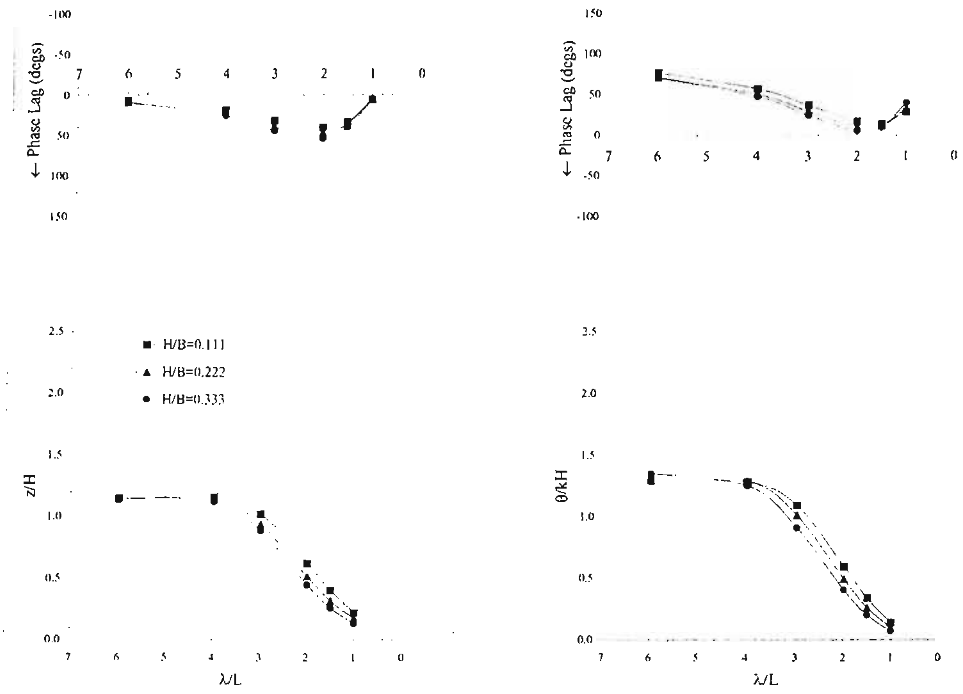

Figure A.36: Linearity of Heave and Pitch Responses for Configuration A
$V/\sqrt{L} = 4$, $\beta = 20°$, $C_\Delta = 0.608$, $L/B = 5$, $H/B = 0.111, 0.222, 0.333$

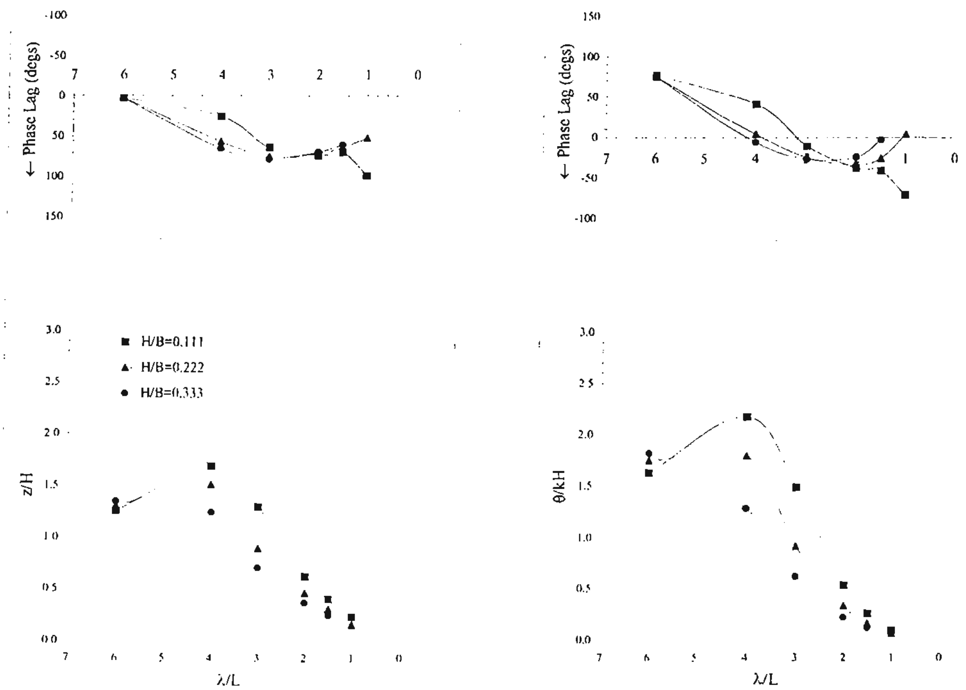

Figure A.37: Linearity of Heave and Pitch Responses for Configuration B
$V/\sqrt{L} = 6$, $\beta = 20°$, $C_\Delta = 0.608$, $L/B = 5$, $H/B = 0.111, 0.222, 0.333$

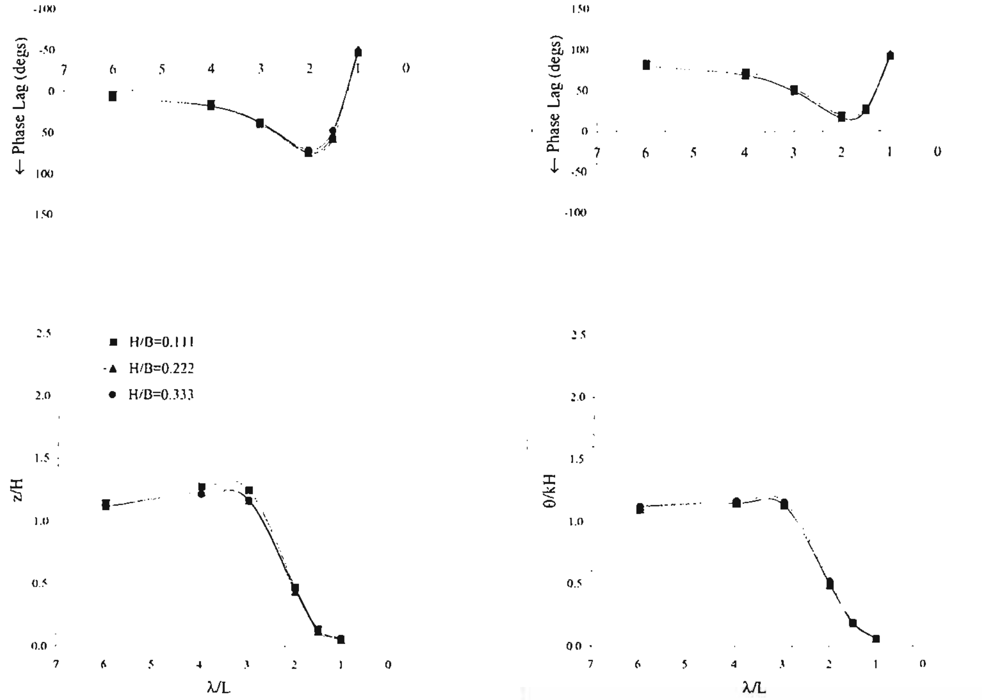

Figure A.38: Linearity of Heave and Pitch Responses for Configuration H
$V/\sqrt{L} = 2$, $\beta = 10°$, $C_\Delta = 0.608$, $L/B = 5$, $H/B = 0.111$, 0.222, 0.333

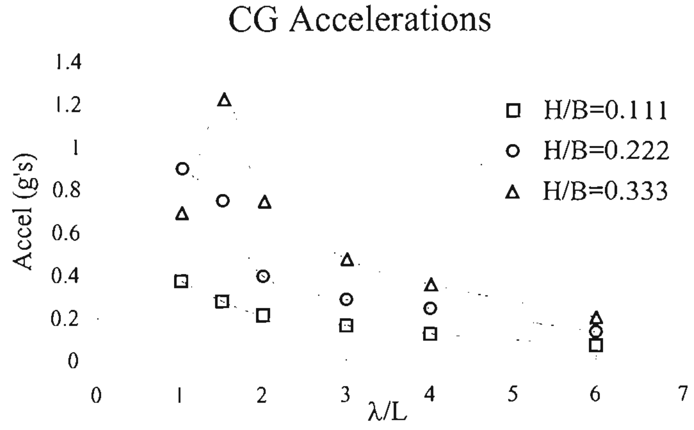

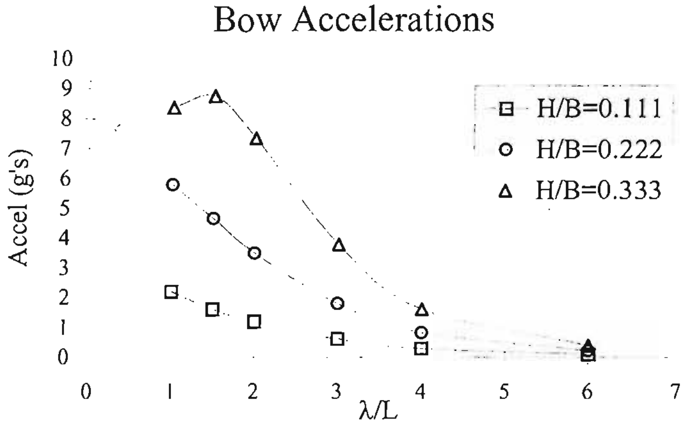

Figure A.39: Effect of Waveheight on Accelerations for Configuration A
$V/\sqrt{L} = 4$, $\beta = 20°$, $C_\Delta = 0.608$, $L/B = 5$, $H/B = 0.111, 0.222, 0.333$

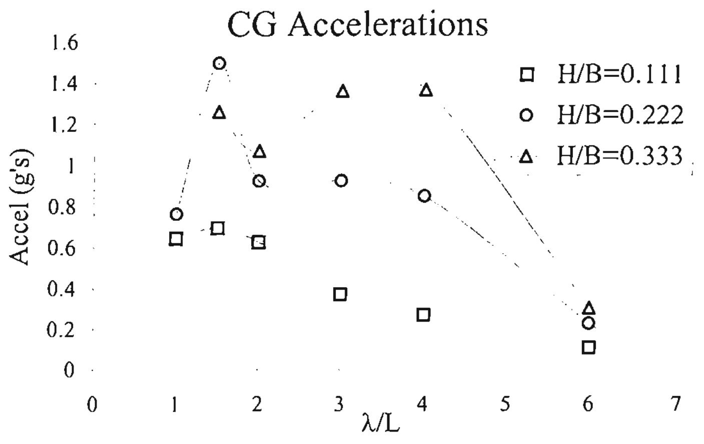

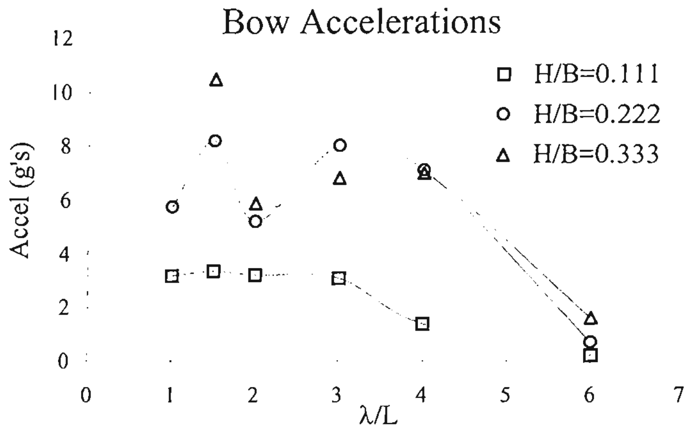

Figure A.40: Effect of Waveheight on Accelerations for Configuration B
$V/\sqrt{L} = 6$, $\beta = 20°$, $C_\Delta = 0.608$, $L/B = 5$, $H/B = 0.111, 0.222, 0.333$

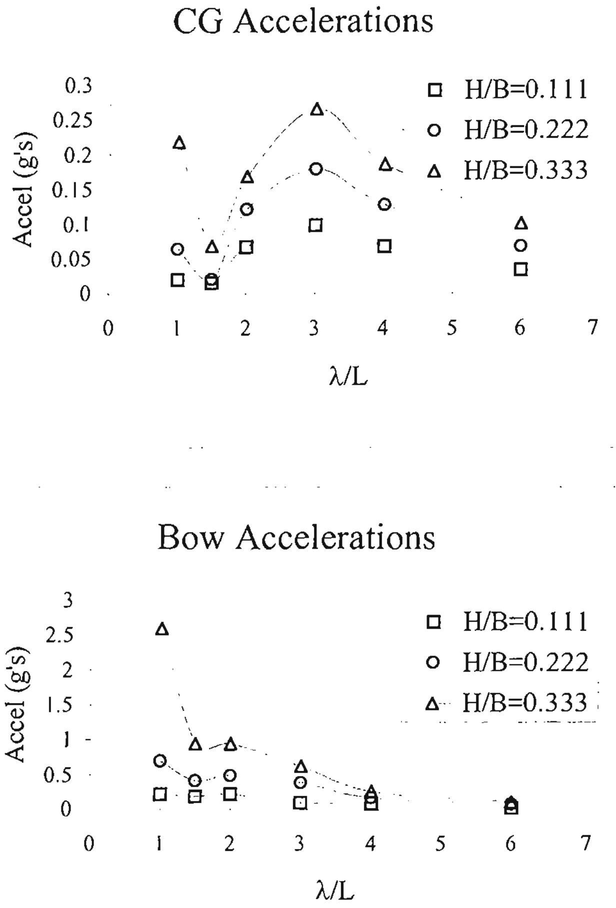

Figure A.41: Effect of Waveheight on Accelerations for Configuration H
$V/\sqrt{L} = 2$, $\beta = 10°$, $C_\Delta = 0.608$, $L/B = 5$, $H/B = 0.111, 0.222, 0.333$

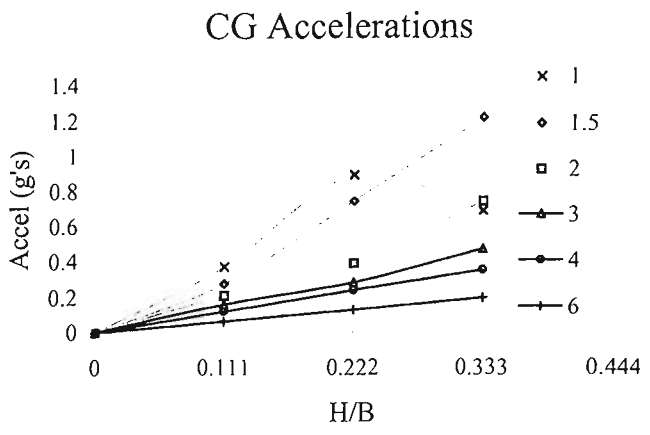

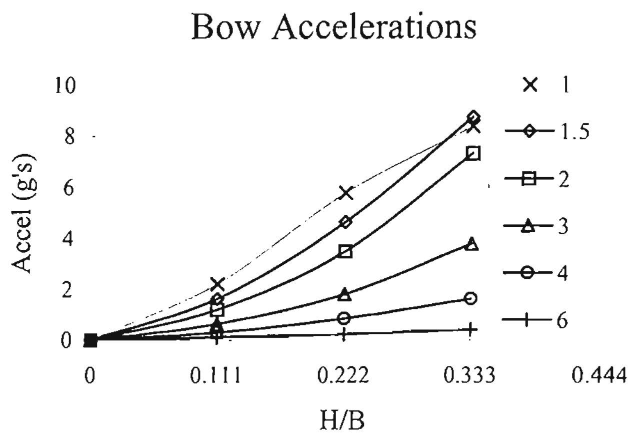

Figure A.42: Linearity of Accelerations with Waveheight for Configuration A
$V/\sqrt{L} = 4$, $\beta = 20°$, $C_{\Delta} = 0.608$, $L/B = 5$, $H/B = 0.111, 0.222, 0.333$

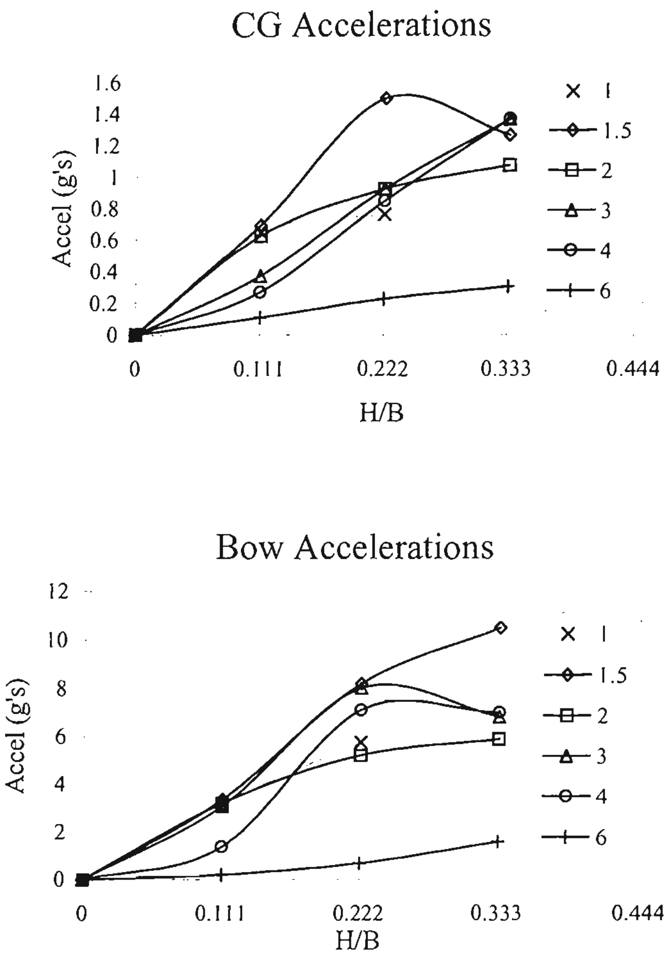

Figure A.43: Linearity of Accelerations with Waveheight for Configuration B
$V/\sqrt{L} = 6$, $\beta = 20°$, $C_\Delta = 0.608$, $L/B = 5$, $H/B = 0.111$, 0.222, 0.333

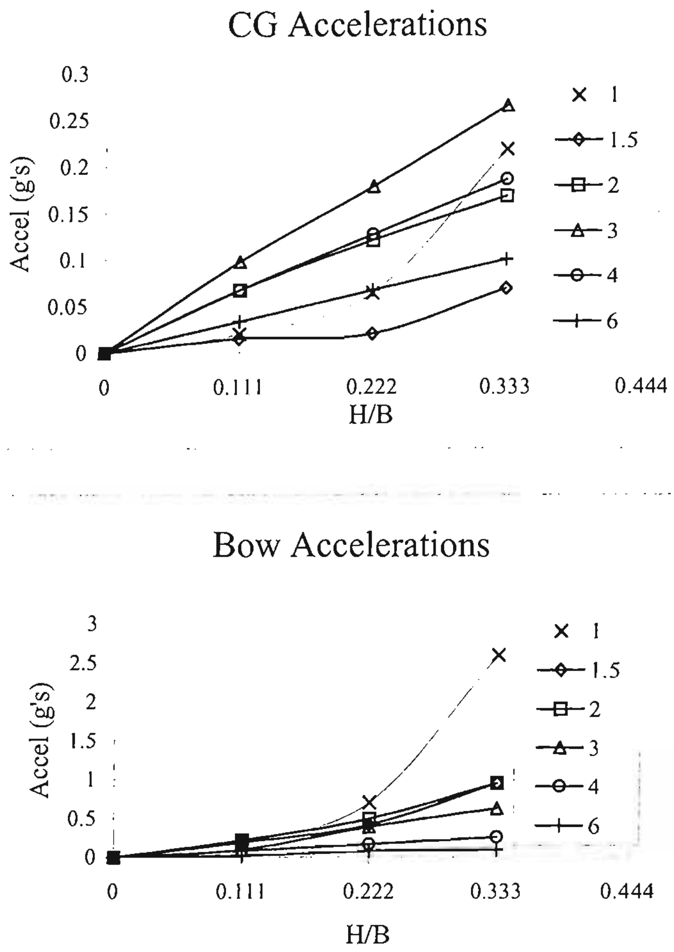

CG Accelerations

Bow Accelerations

Figure A.44: Linearity of Accelerations with Waveheight for Configuration H
$V/\sqrt{L} = 2$, $\beta = 20°$, $C_\Delta = 0.608$, $L/B = 5$, $H/B = 0.111, 0.222, 0.333$

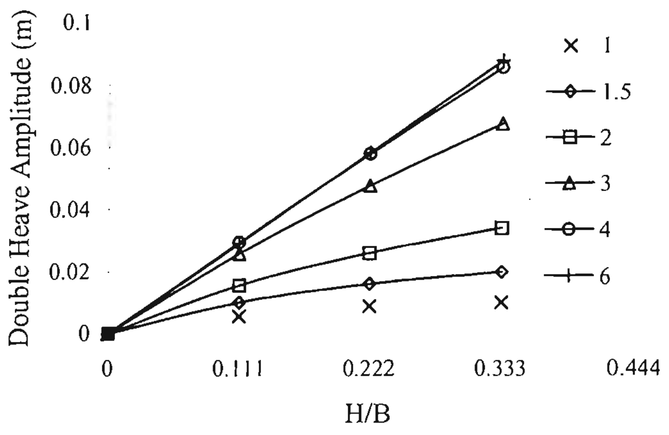

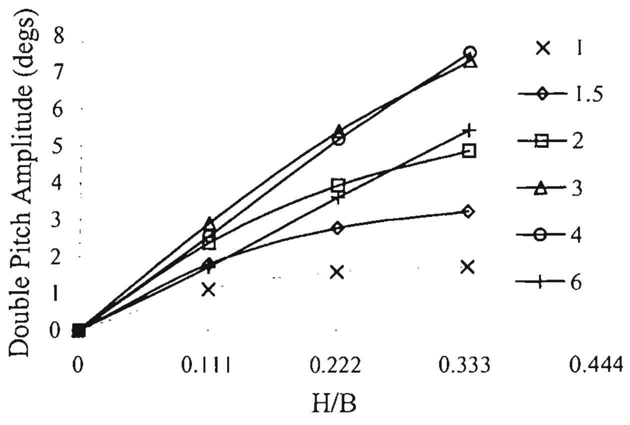

Figure A.45: Linearity of Heave and Pitch Responses for Configuration A
$V/\sqrt{L} = 4$, $\beta = 20°$, $C_\Delta = 0.608$, $L/B = 5$, $H/B = 0.111, 0.222, 0.333$

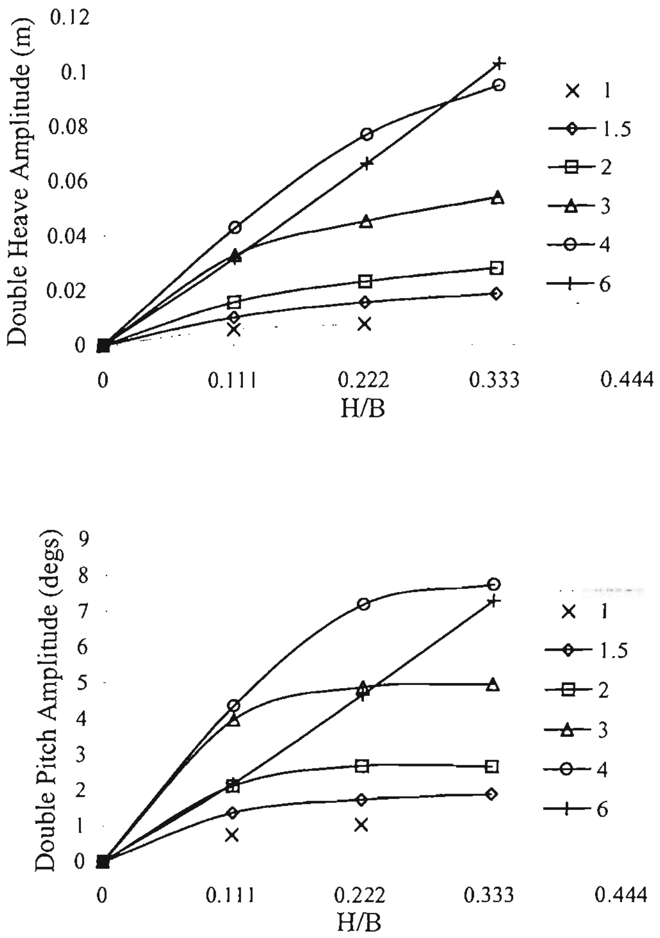

Figure A.46: Linearity of Heave and Pitch Responses for Configuration B
$V/\sqrt{L} = 6$, $\beta = 20°$, $C_\Delta = 0.608$, $L/B = 5$, $H/B = 0.111, 0.222, 0.333$

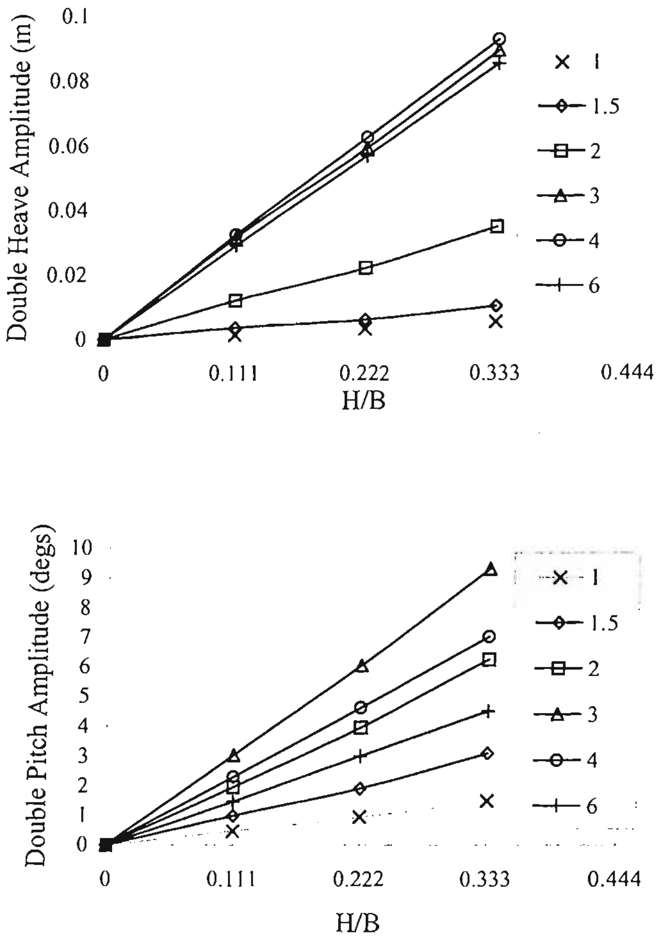

Figure A.47: Linearity of Heave and Pitch Responses for Configuration H
$V/\sqrt{L} = 2$, $\beta = 10°$, $C_\Delta = 0.608$, $L/B = 5$, $H/B = 0.111, 0.222, 0.333$

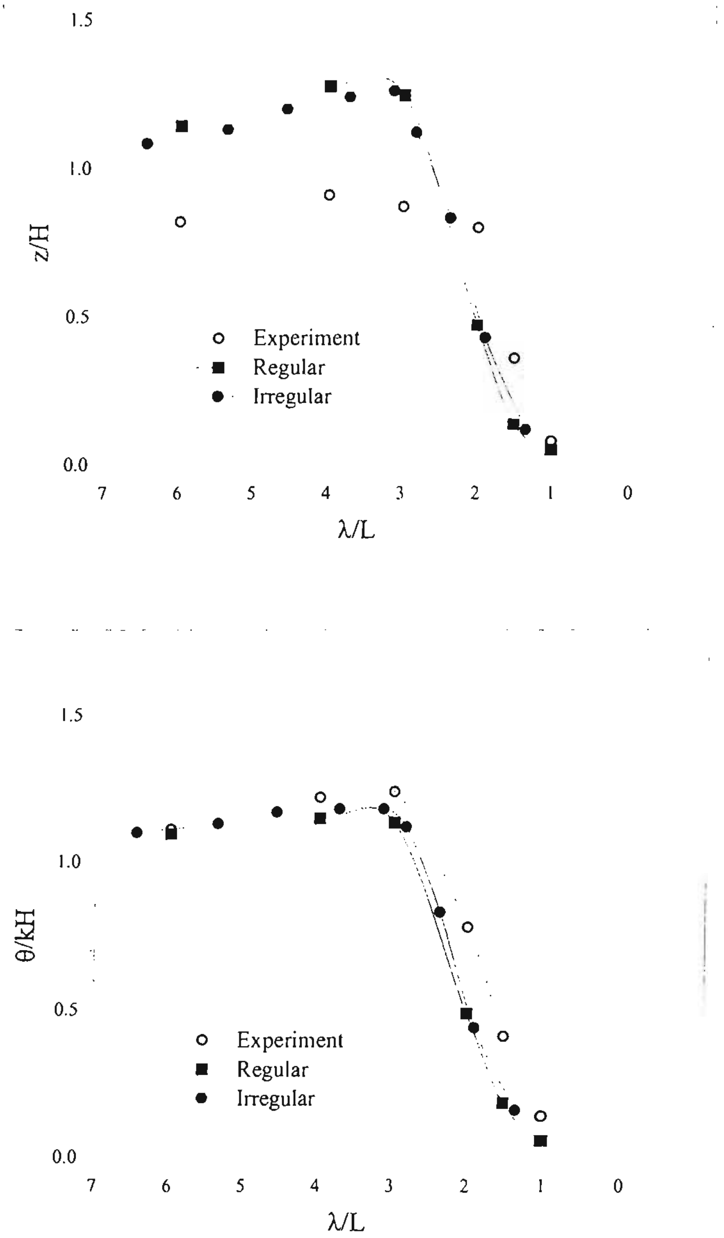

Figure A.48: Spectral Analysis of Heave and Pitch Responses for Configuration H in Irregular Seas
$V/\sqrt{L} = 2$, $\beta = 10^{\circ}$, $C_{\Delta} = 0.608$, $L/B = 5$, $H_{1/3}/B = 0.222$

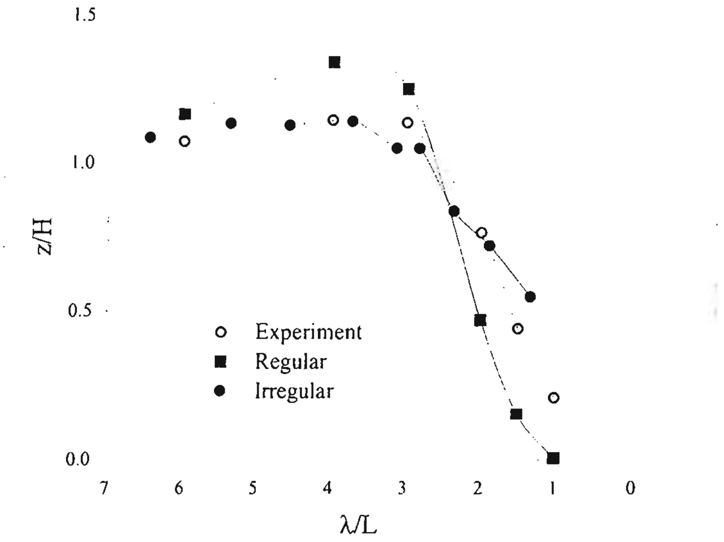

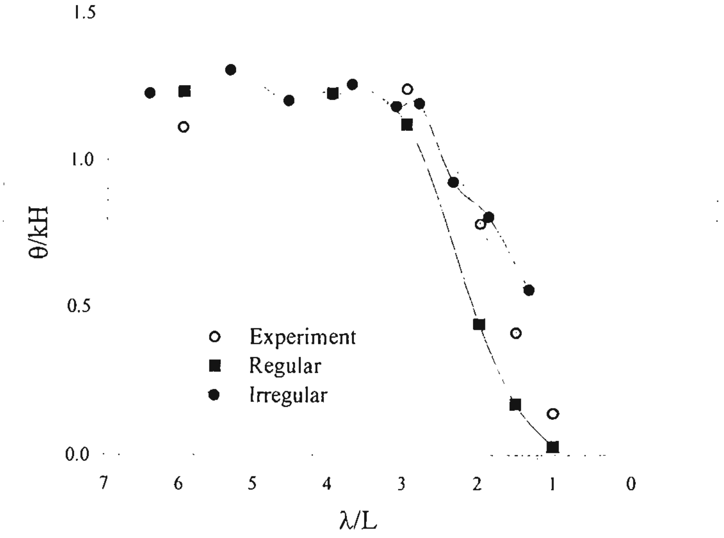

Figure A.49: Spectral Analysis of Heave and Pitch Responses for Configuration I in Irregular Seas

$V/\sqrt{L} = 4$, $\beta = 10°$, $C_\Delta = 0.608$, $L/B = 5$, $H_{1/3}/B = 0.222$

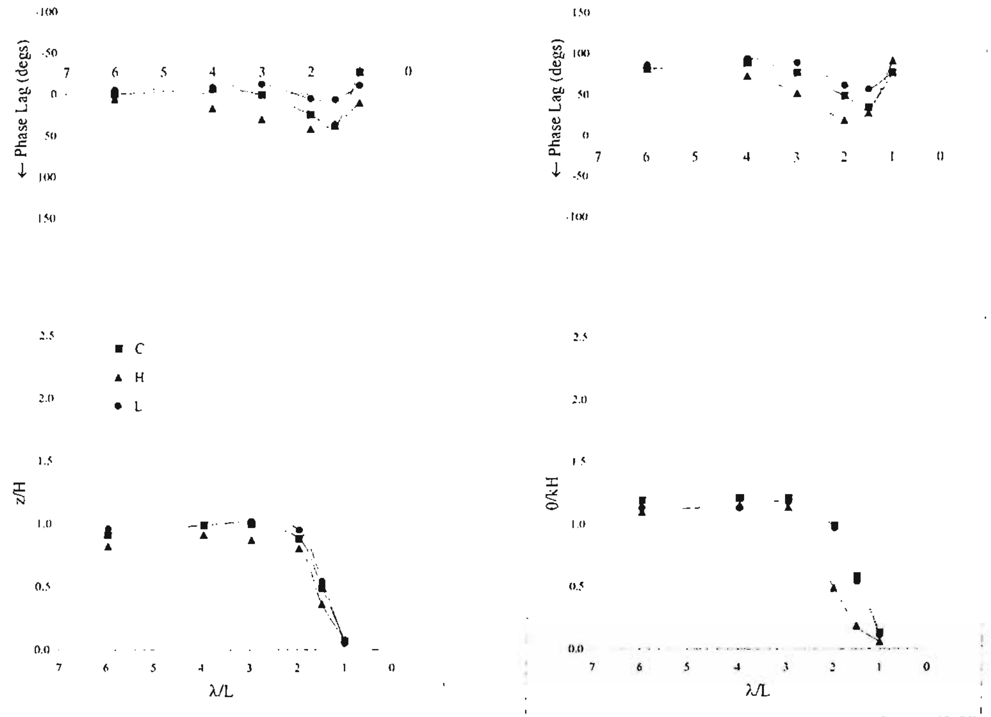

Figure A.50: Effect of Deadrise on Heave and Pitch Responses for $V/\sqrt{L} = 2$
$\beta = 10°, 20°, 30°, C_\Delta = 0.608, L/B = 5, H/B = 0.111$

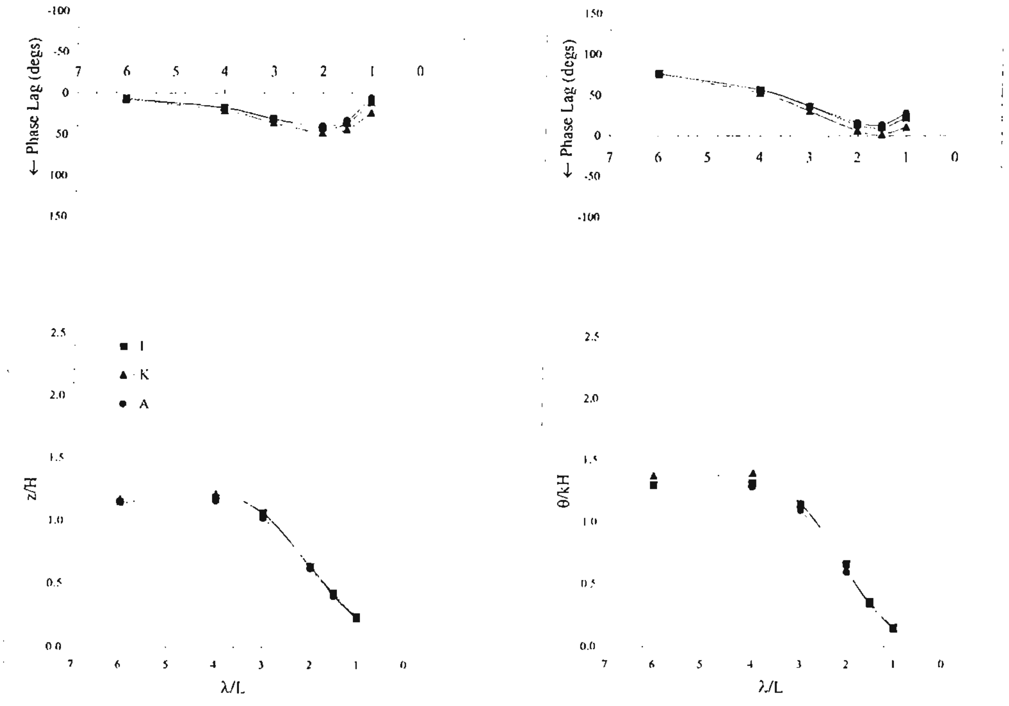

Figure A.51: Effect of Deadrise on Heave and Pitch Responses for $V/\sqrt{L} = 4$
$\beta = 10°, 20°, 30°, C_\Delta = 0.608, L/B = 5, H/B = 0.111$

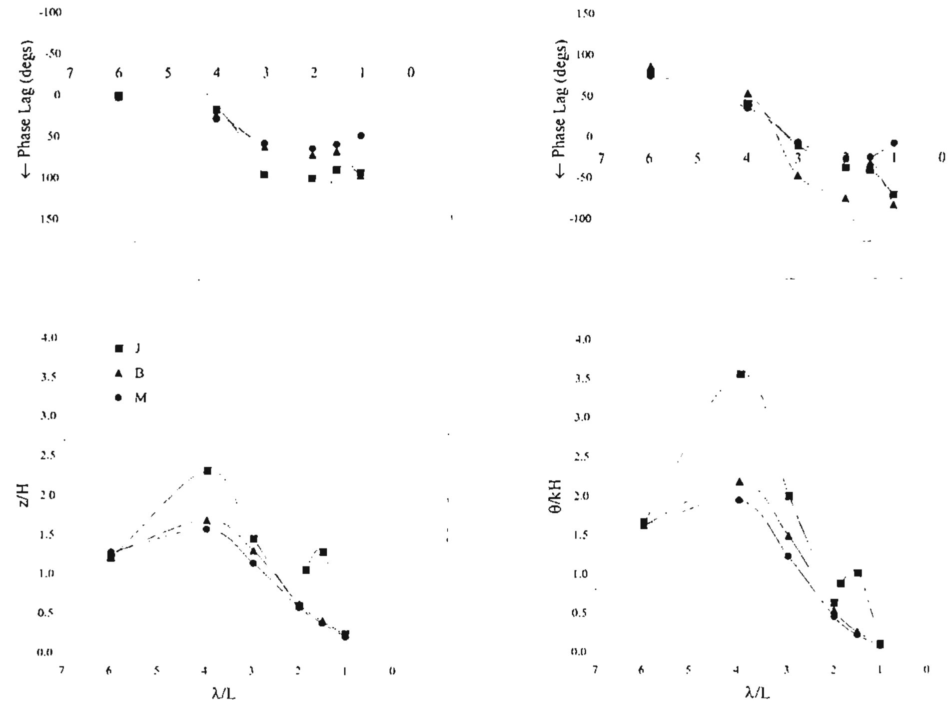

Figure A.52: Effect of Deadrise on Heave and Pitch Responses for $V/\sqrt{L} = 6$
$\beta = 10°, 20°, 30°, C_\Delta = 0.608, L/B = 5, H/B = 0.111$

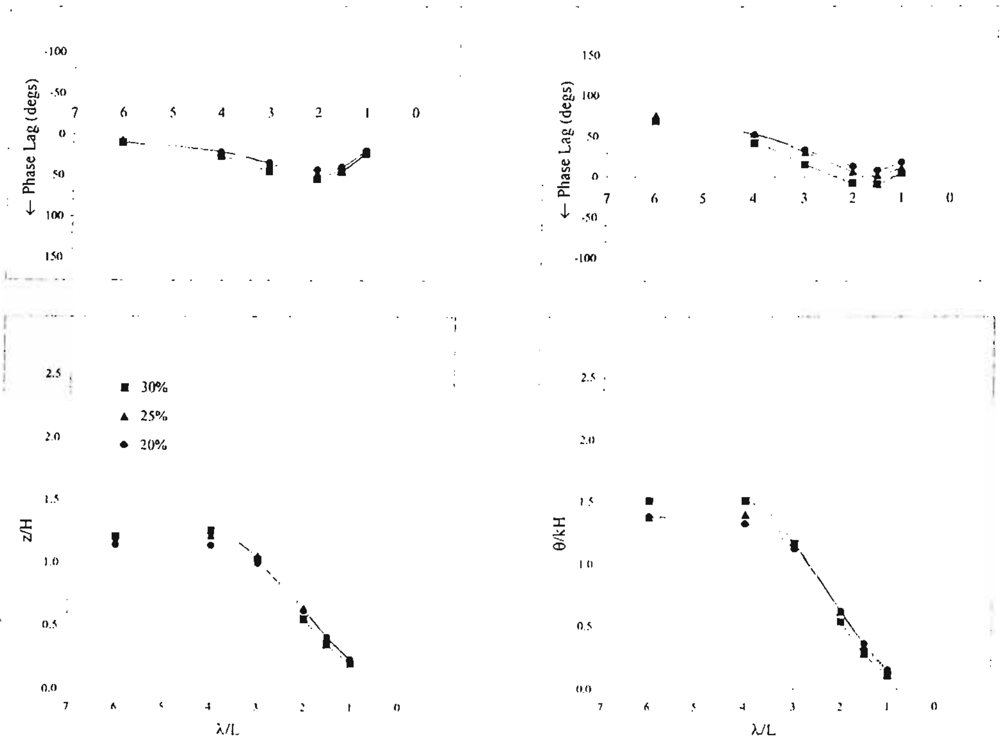

Figure A.53: Effect of Gyradius on Heave and Pitch Responses for $V/\sqrt{L} = 4$
$k_y/B = 20\%L, 25\%L, 30\%L, \beta = 20°, C_\Delta = 0.608, L/B = 5, H/B = 0.111$

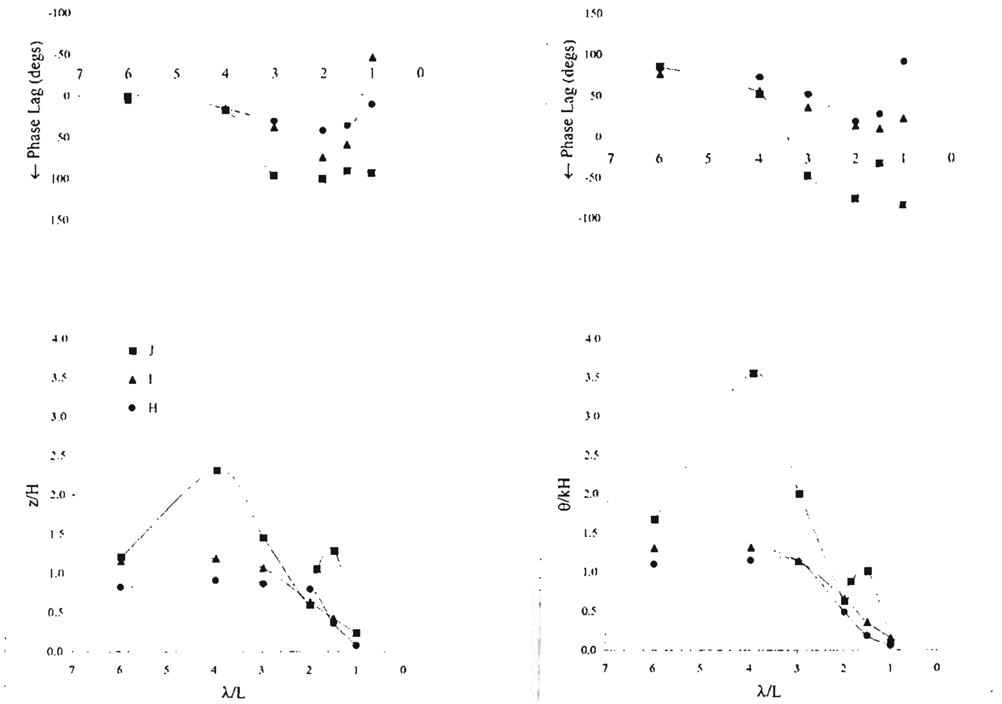

Figure A.54: Effect of Speed on Heave and Pitch Responses for 10° Deadrise
$V/\sqrt{L} = 2, 4, 6$, $C_\Delta = 0.608$, $L/B = 5$, $H/B = 0.111$

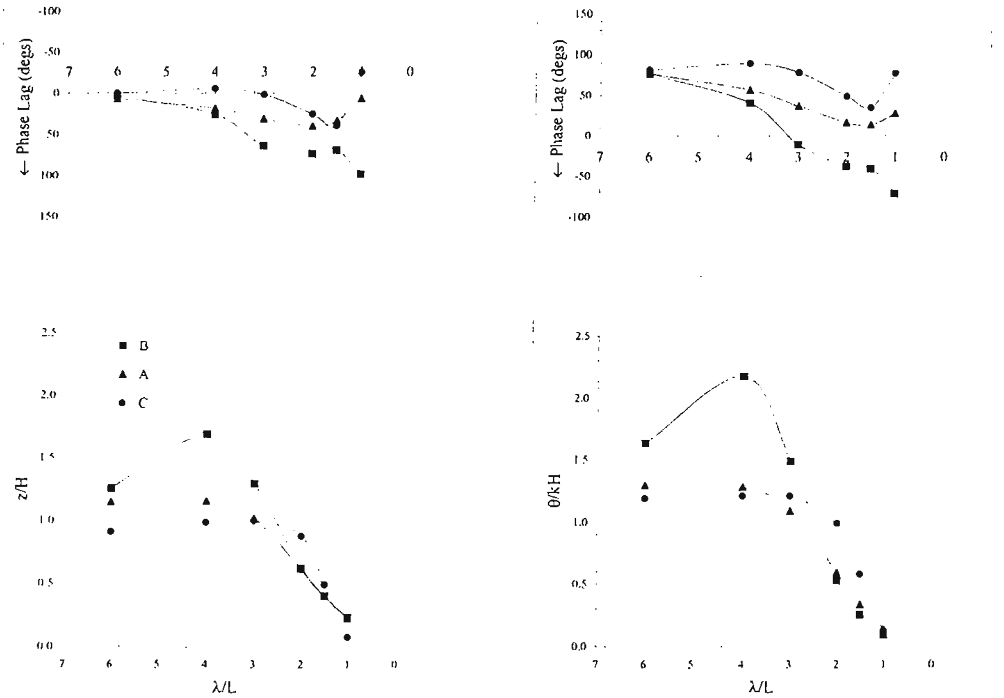

Figure A.55: Effect of Speed on Heave and Pitch Responses for 20° Deadrise
$V/\sqrt{L} = 2, 4, 6$, $C_\Delta = 0.608$, $L/B = 5$, $H/B = 0.111$

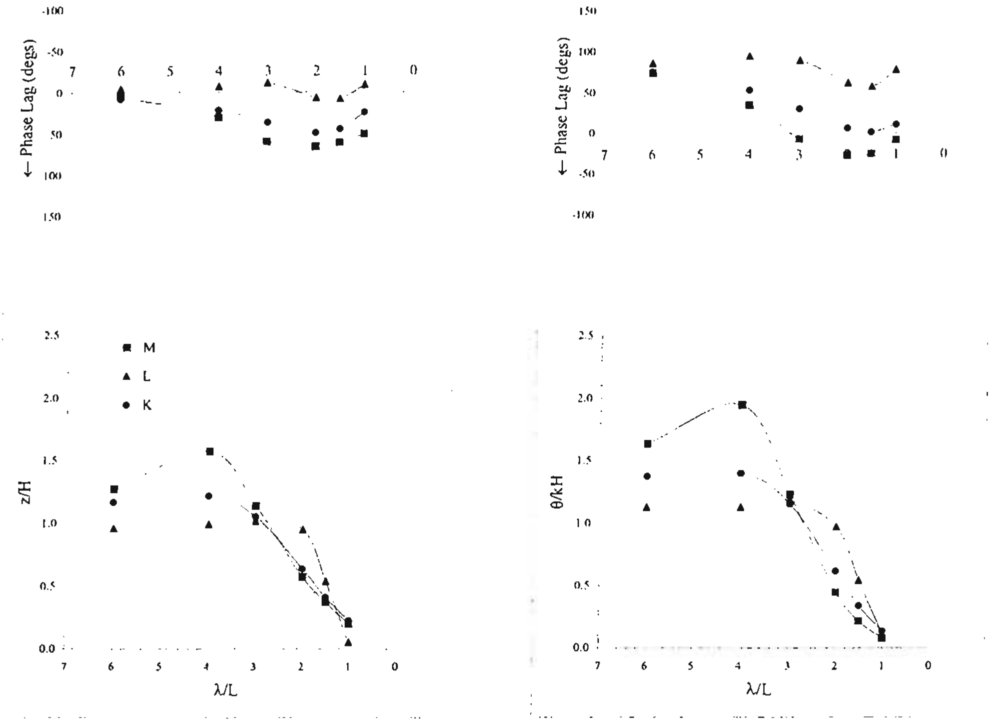

Figure A.56: Effect of Speed on Heave and Pitch Responses for 30° Deadrise
$V/\sqrt{L}$ = 2, 4, 6, C_Δ = 0.608, L/B = 5, H/B = 0.111

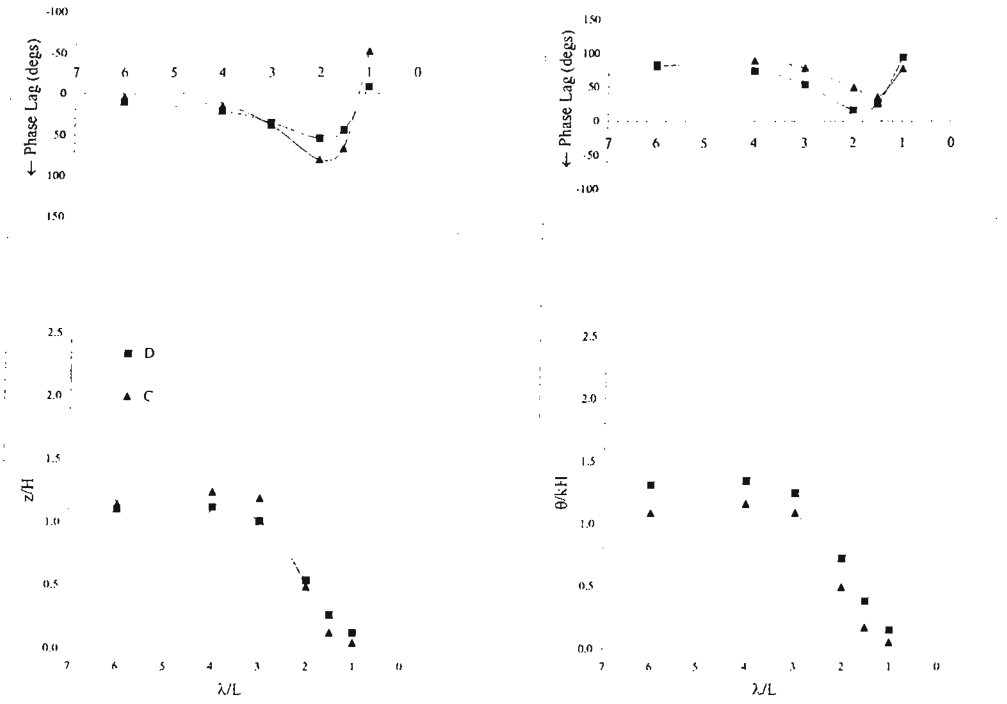

Figure A.57: Effect of Trim on Heave and Pitch Responses
τ = 4.27°, 8.10°, $V/\sqrt{L}$ = 2, β = 20°, C_Δ = 0.608, L/B = 5, H/B = 0.111

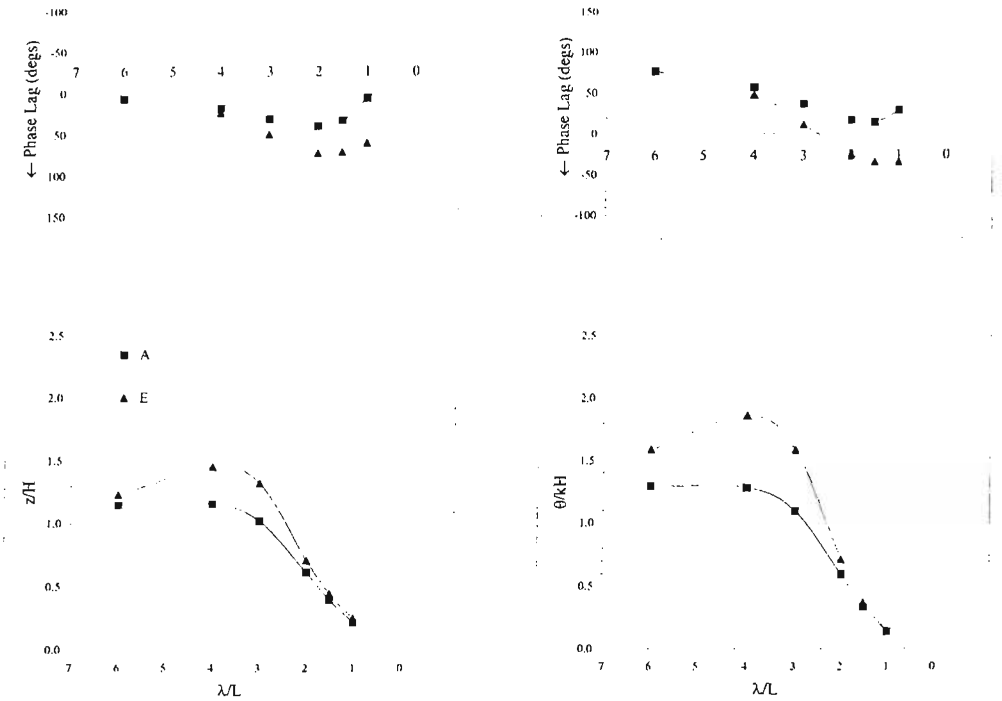

Figure A.58: Effect of Trim on Heave and Pitch Responses
$\tau = 5.77°,\ 7.05°,\ V/\sqrt{L} = 4,\ \beta = 20°,\ C_\Delta = 0.608,\ L/B = 5,\ H/B = 0.111$

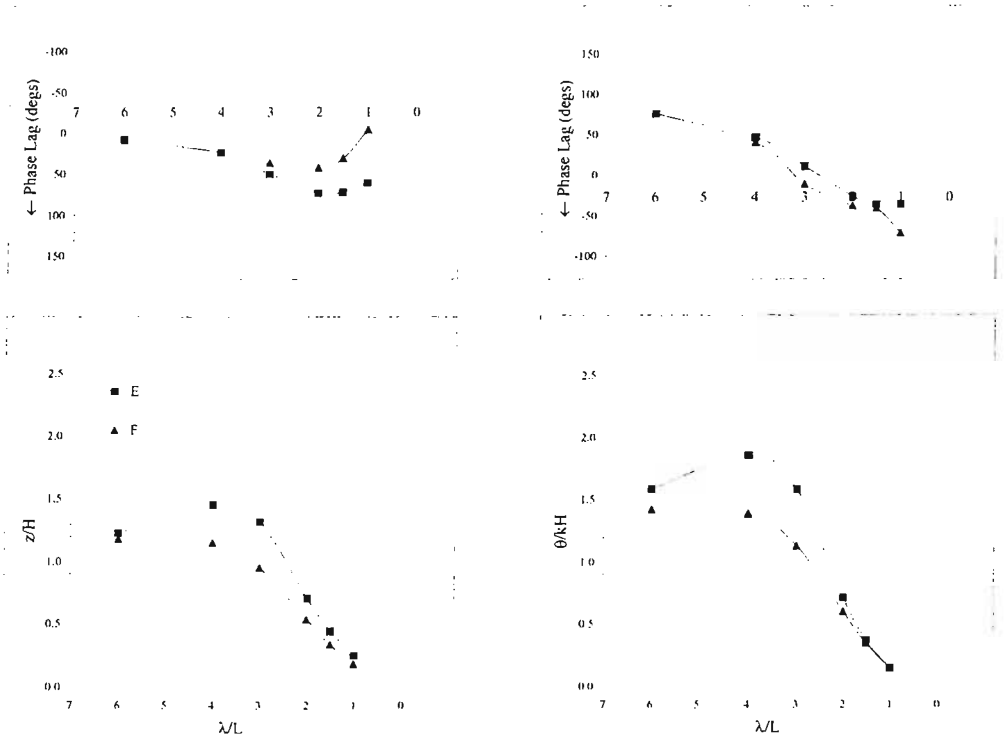

Figure A.59: Effect of Load on Heave and Pitch Responses
$V/\sqrt{L} = 4,\ C_\Delta = 0.608,\ 0.912,\ L/B = 5,\ H/B = 0.111$

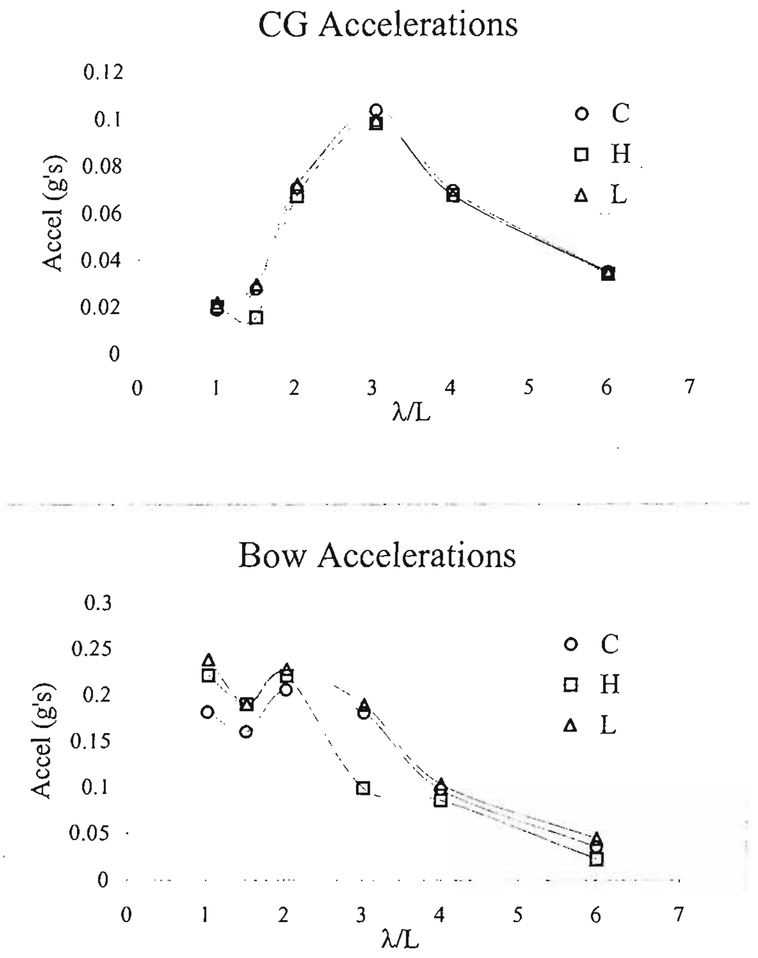

Figure A.60: Effect of Deadrise on Accelerations for $V/\sqrt{L} = 2$

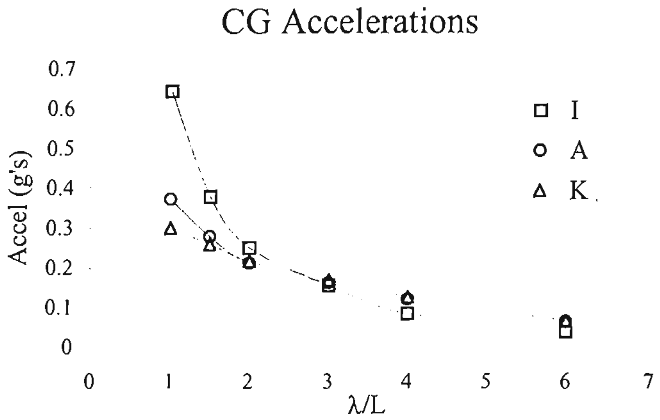

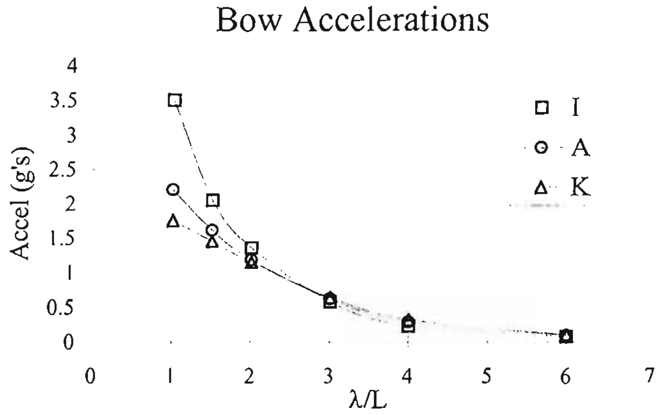

Figure A.61: Effect of Deadrise on Accelerations for $V/\sqrt{L} = 4$

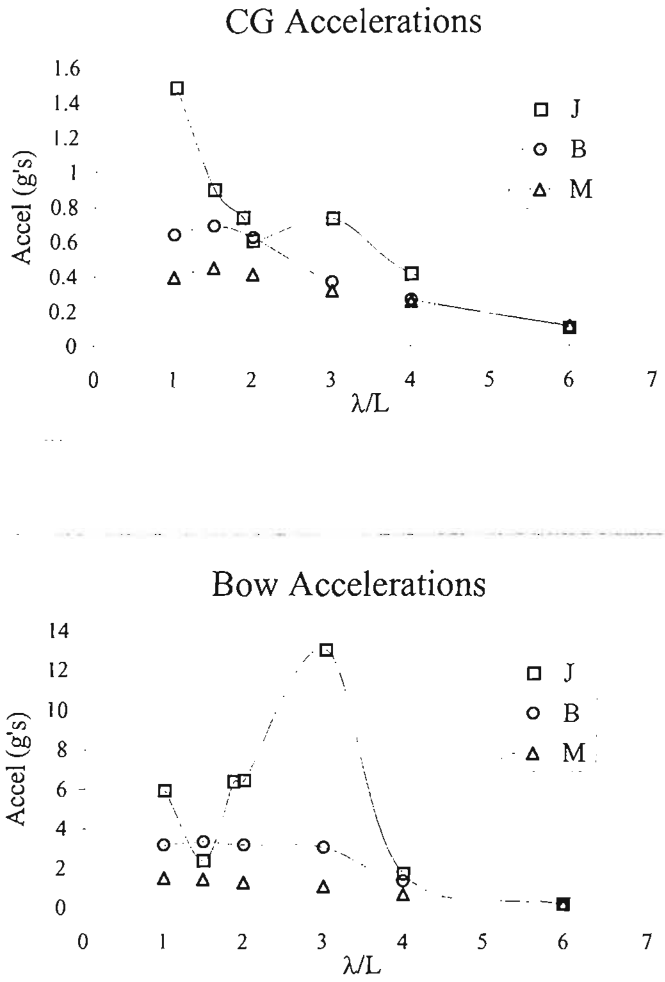

Figure A.62: Effect of Deadrise on Accelerations for $V/\sqrt{L} = 6$

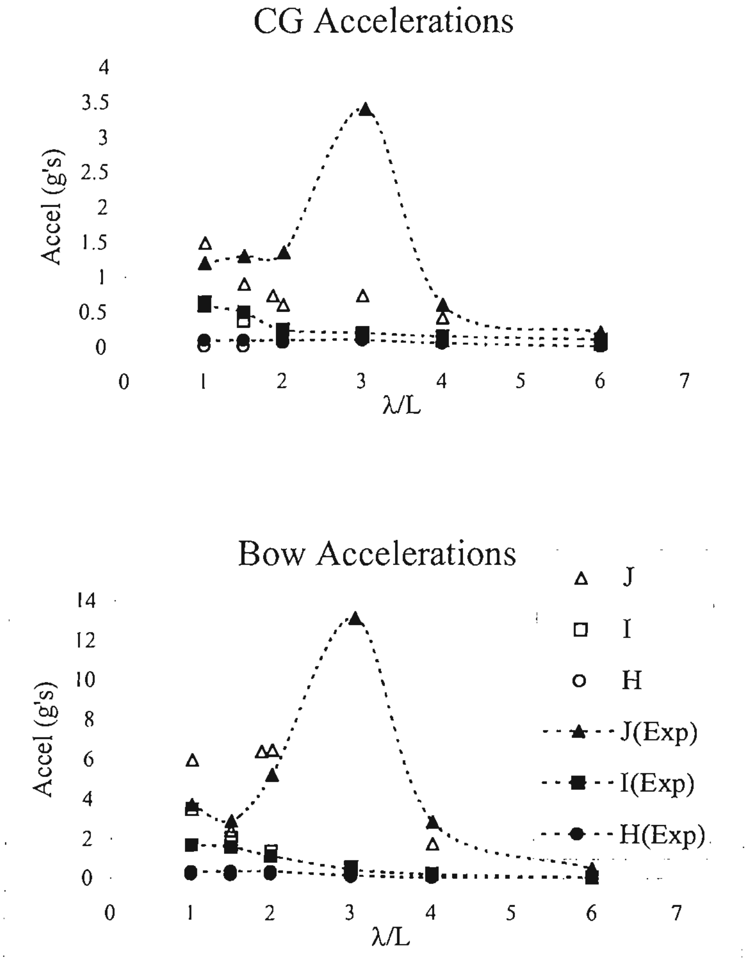

Figure A.63: Effect of Speed on Accelerations for 10° Deadrise

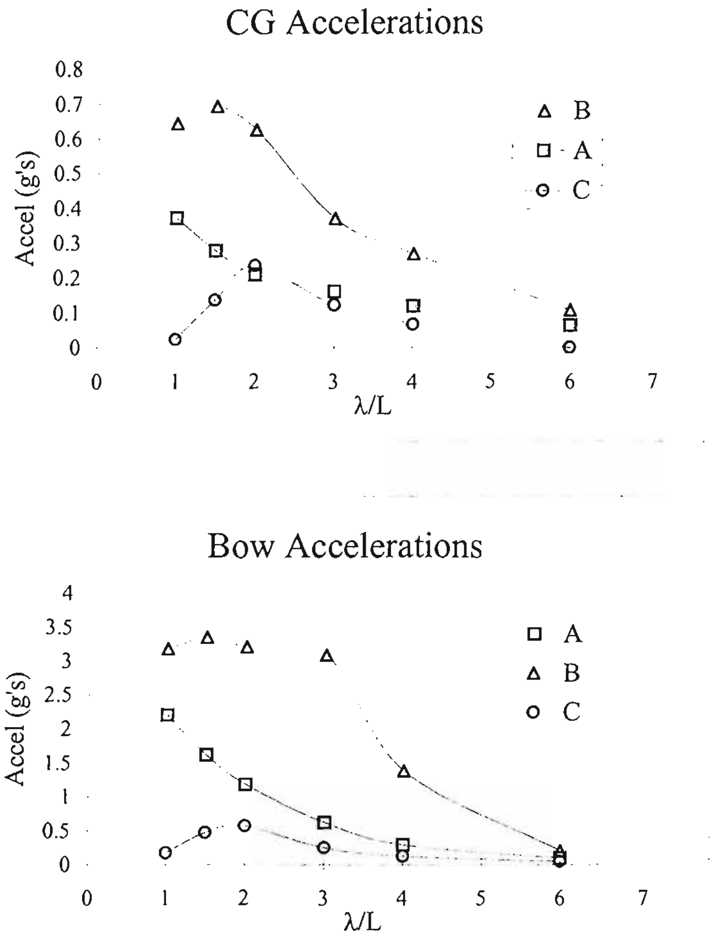

Figure A.64: Effect of Speed on Accelerations for 20° Deadrise

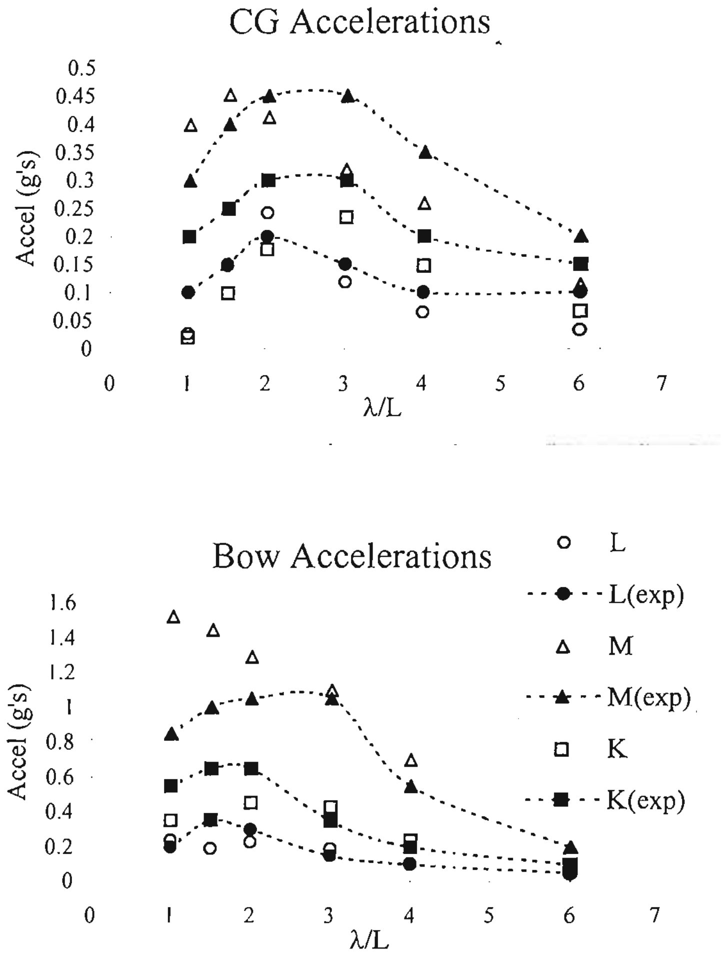

Figure A.65: Effect of Speed on Accelerations for 30° Deadrise

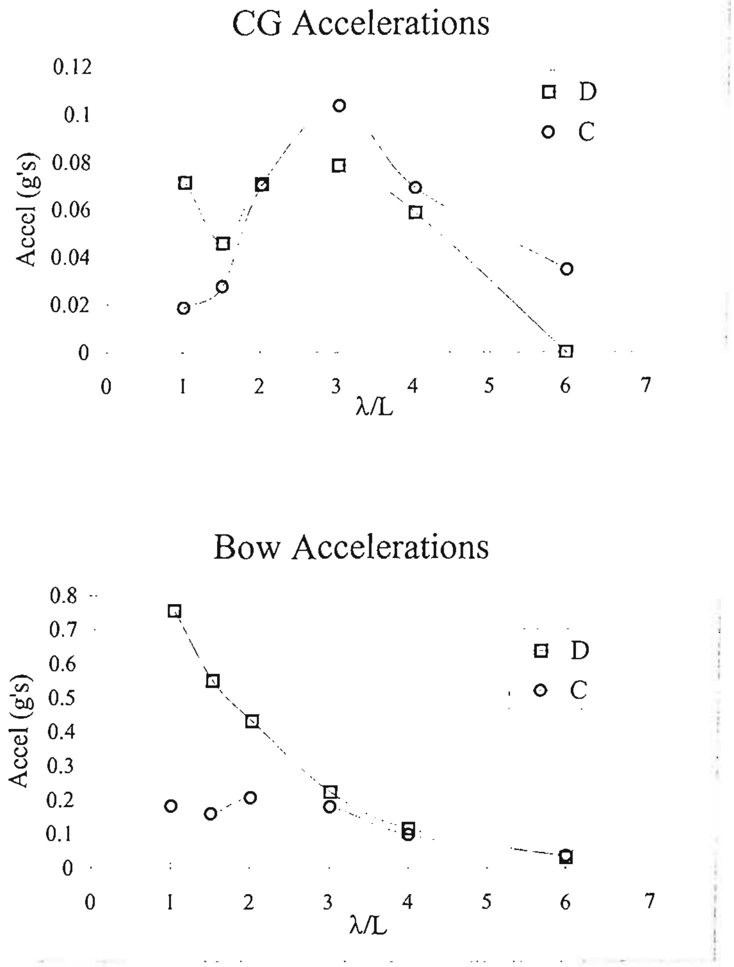

Figure A.66: Effect of Trim on Accelerations for $V_{\mathrm{knots}}/\sqrt{L}_{\mathrm{feet}} = 2$

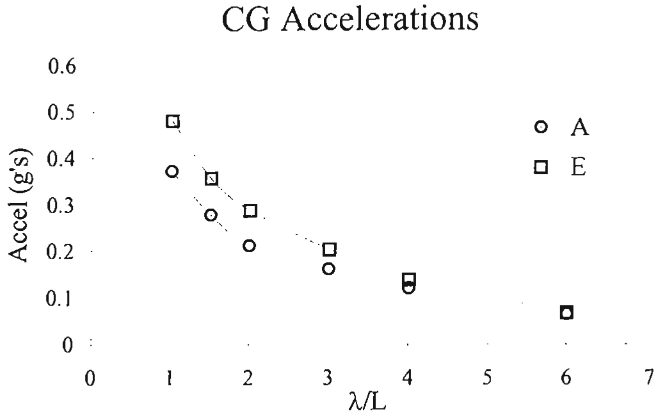

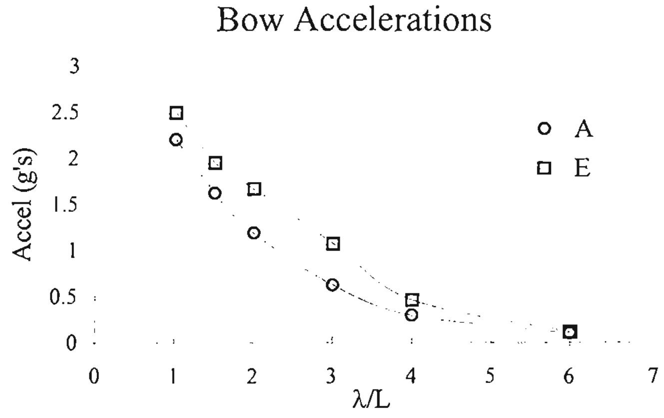

Figure A.67: Effect of Trim on Accelerations for $V_{\text{knots}}/\sqrt{L_{\text{feet}}} = 4$

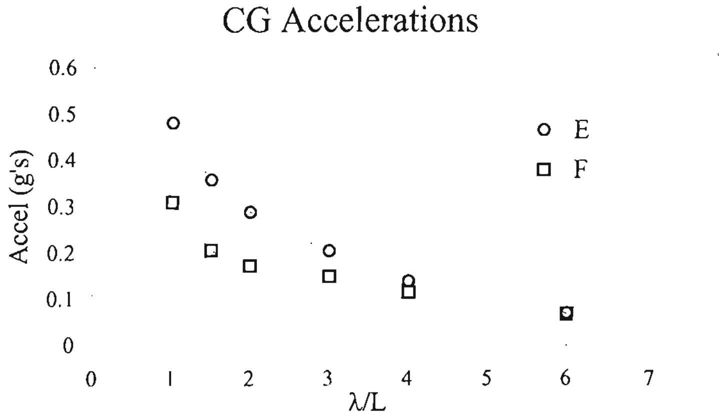

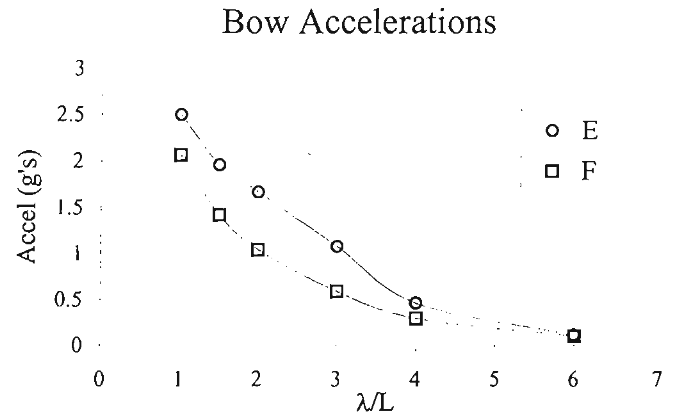

Figure A.68: Effect of Load on Accelerations for $V_{\text{knots}}/\sqrt{L_{\text{feet}}} = 4$

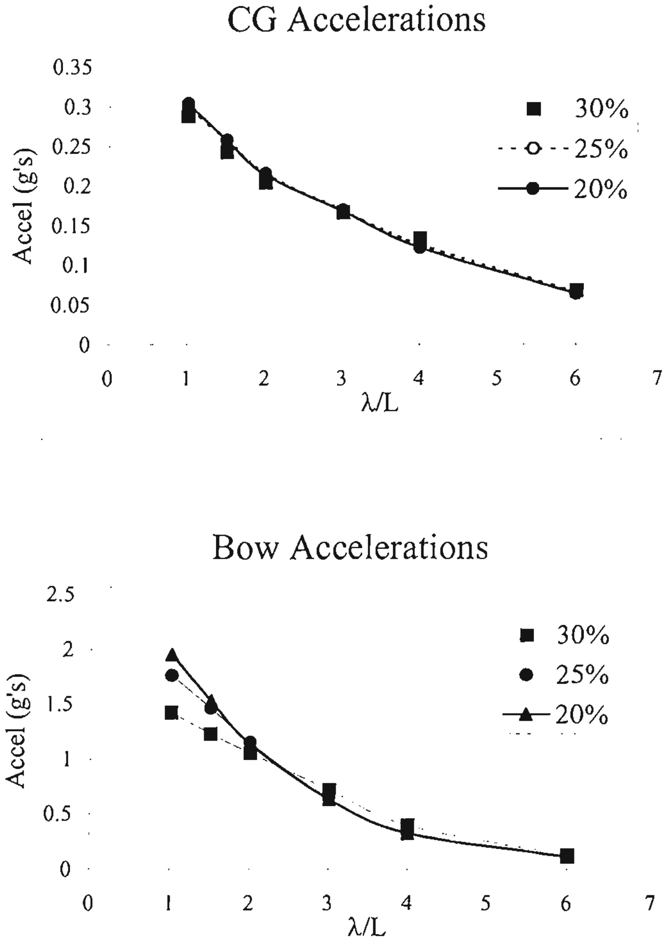

Figure A.69: Effect of Gyradius on Accelerations for $V_{\text{knots}}/\sqrt{L}_{\text{feet}} = 4$

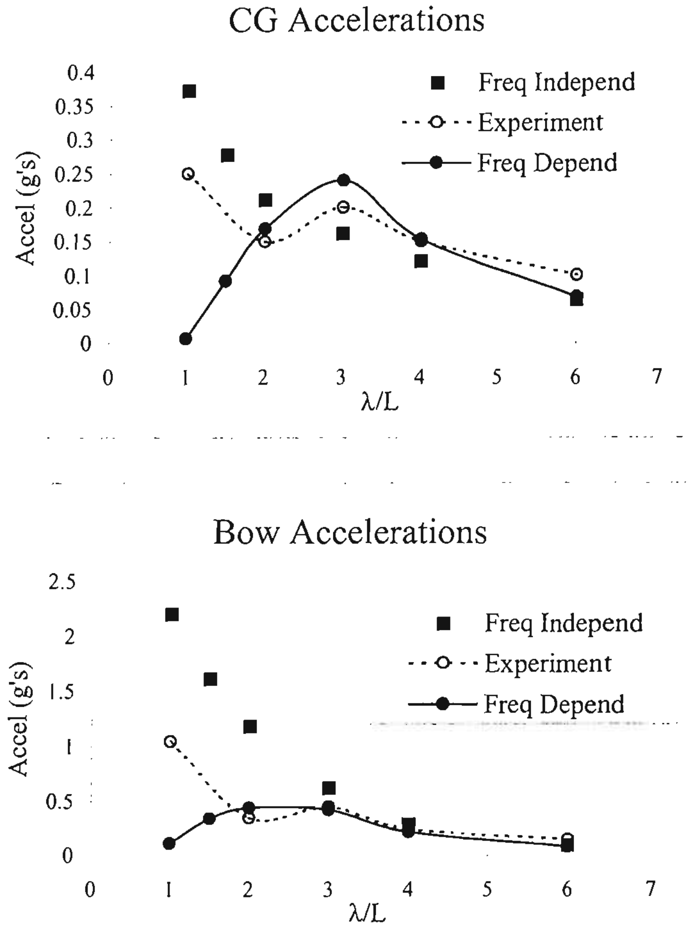

Figure A.70: CG and Bow Accelerations for Configuration A
$V/\sqrt{L} = 4$, $\beta = 20°$, $C_\Delta = 0.608$, $L/B = 5$, $H/B = 0.111$

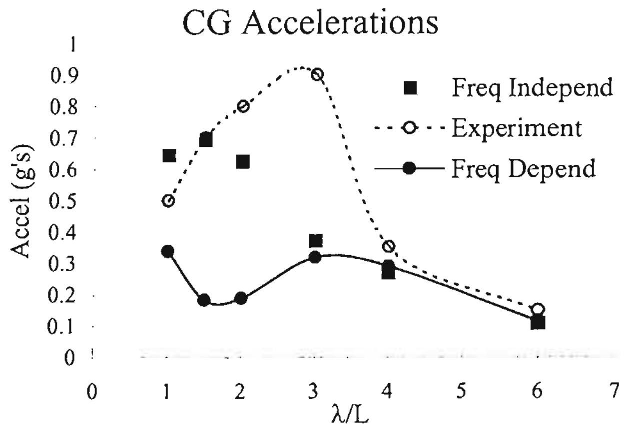

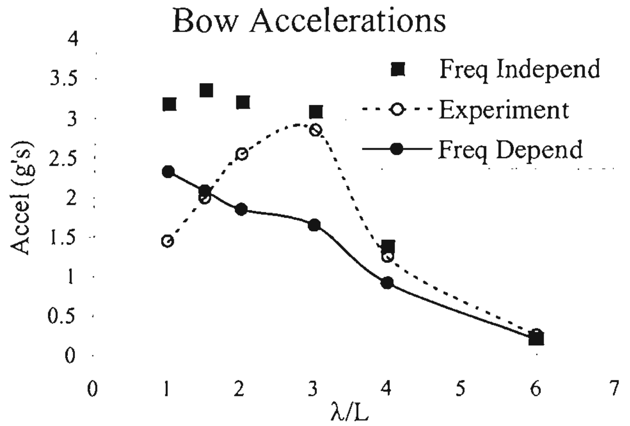

Figure A.71: CG and Bow Accelerations for Configuration B
$V/\sqrt{L} = 6$, $\beta = 20°$, $C_\Delta = 0.608$, $L/B = 5$, $H/B = 0.111$

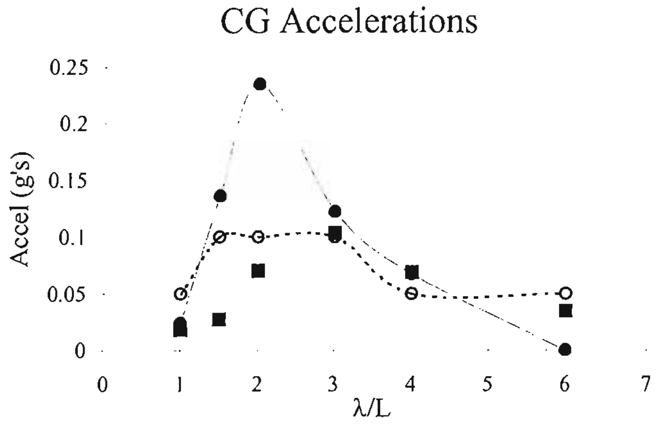

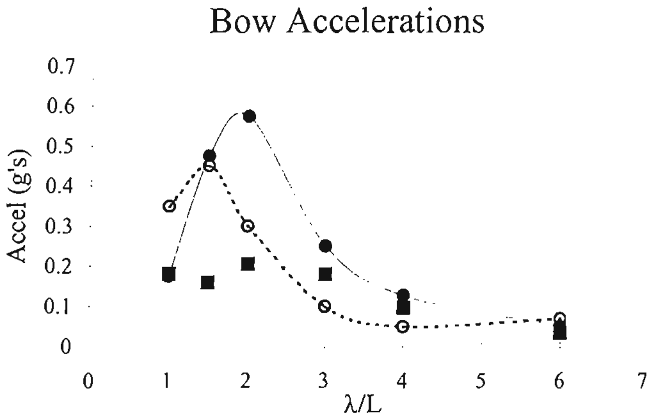

Figure A.72: CG and Bow Accelerations for Configuration C
$V/\sqrt{L} = 4$, $\beta = 20°$, $C_\Delta = 0.608$, $L/B = 5$, $H/B = 0.111$

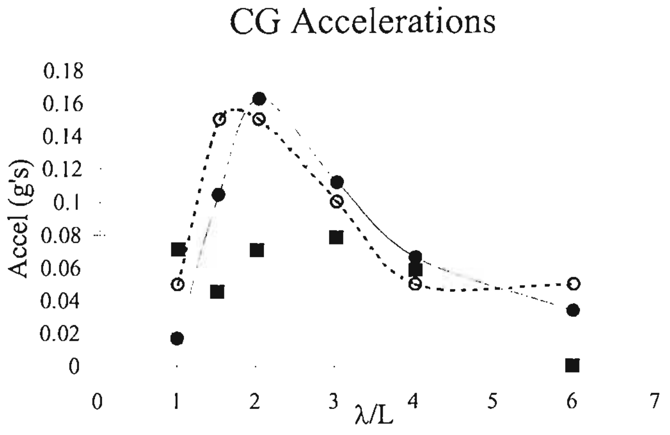

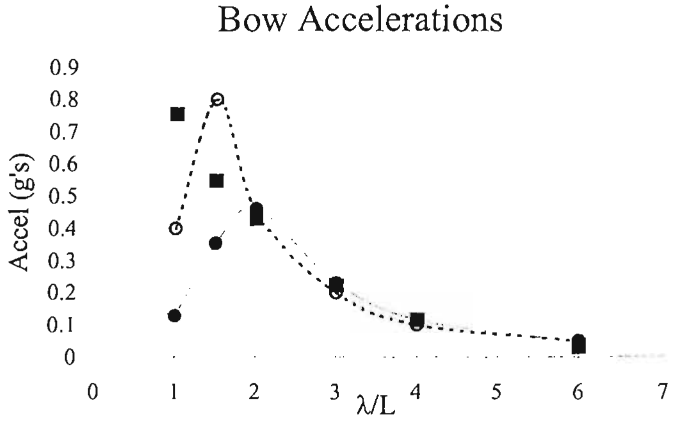

Figure A.73: CG and Bow Accelerations for Configuration D
$V/\sqrt{L} = 4$, $\beta = 20°$, $C_\Delta = 0.608$, $L/B = 5$, $H/B = 0.111$

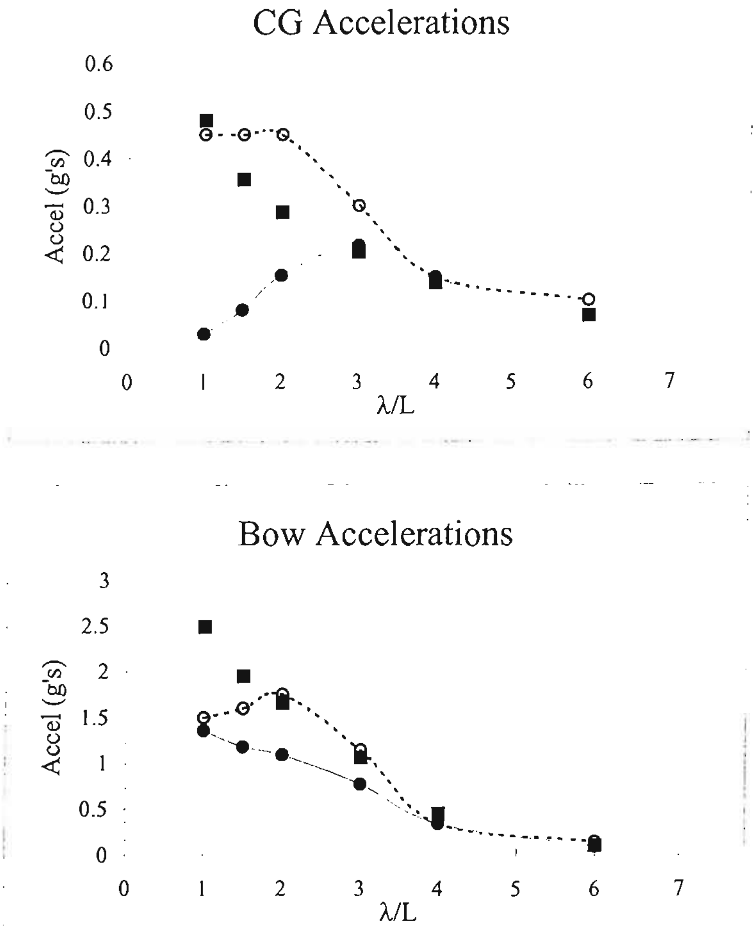

Figure A.74: CG and Bow Accelerations for Configuration E
$V/\sqrt{L} = 4$, $\beta = 20°$, $C_\Delta = 0.608$, $L/B = 5$, $H/B = 0.111$

CG Accelerations

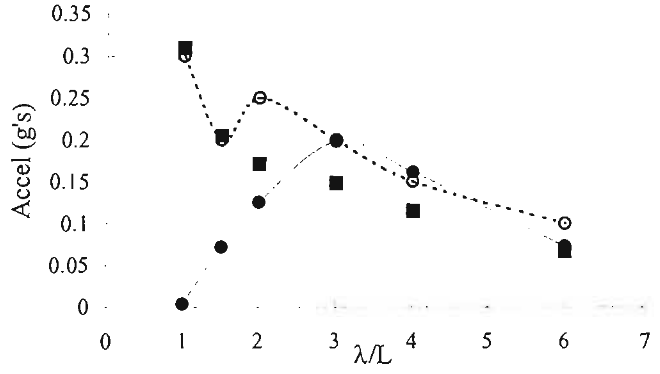

Bow Accelerations

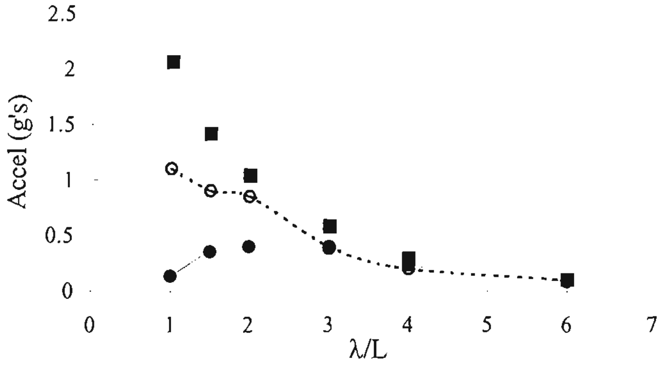

Figure A.75: CG and Bow Accelerations for Configuration F
$V/\sqrt{L} = 4$, $\beta = 20°$, $C_\Delta = 0.608$, $L/B = 5$, $H/B = 0.111$

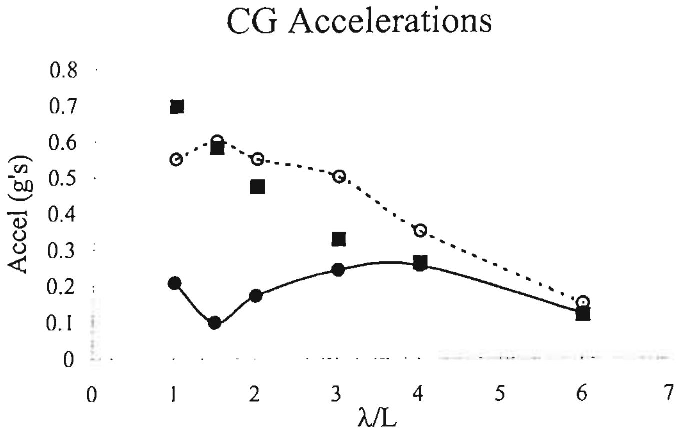

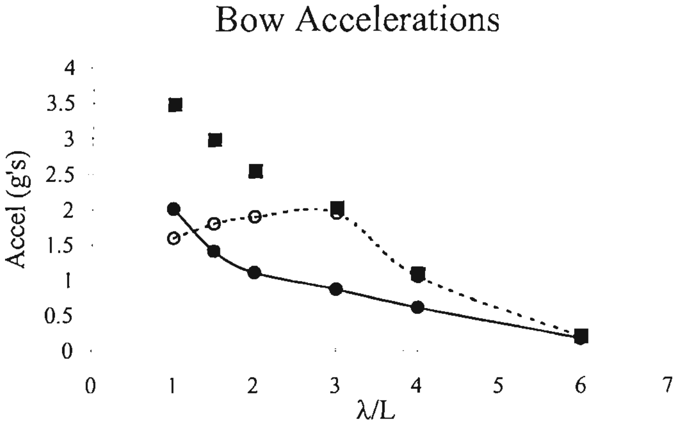

Figure A.76: CG and Bow Accelerations for Configuration G
$V/\sqrt{L} = 4$, $\beta = 20°$, $C_\Delta = 0.608$, $L/B = 5$, $H/B = 0.111$

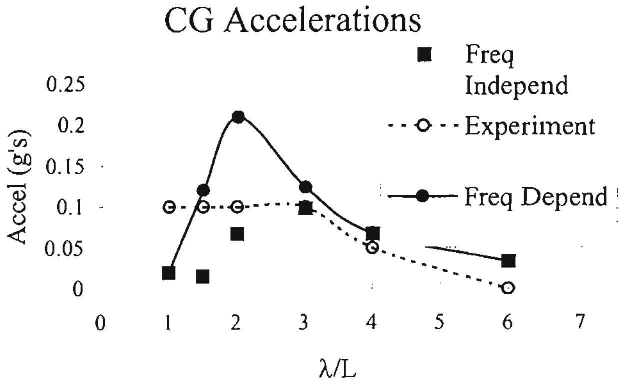

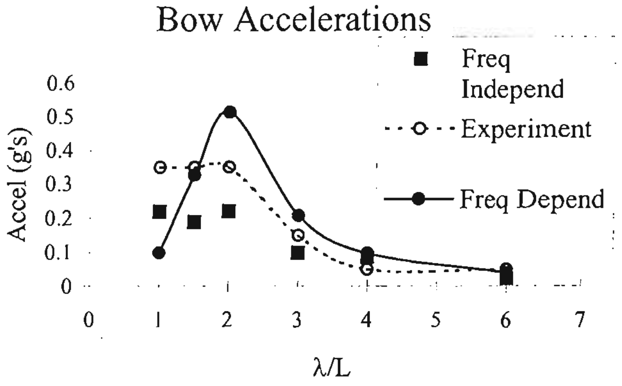

Figure A.77: CG and Bow Accelerations for Configuration H
$V/\sqrt{L} = 4$, $\beta = 20°$, $C_\Delta = 0.608$, $L/B = 5$, $H/B = 0.111$

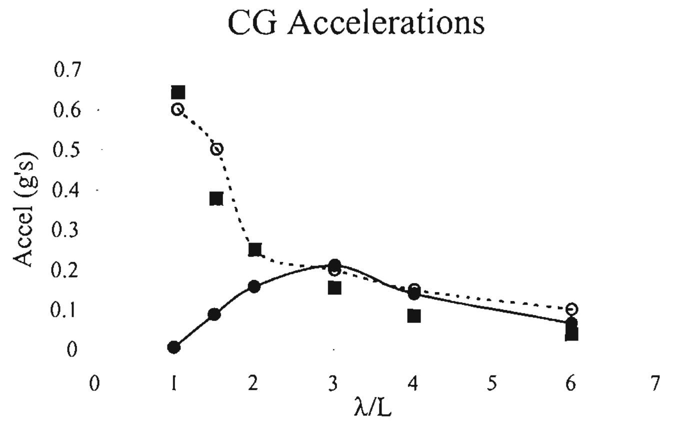

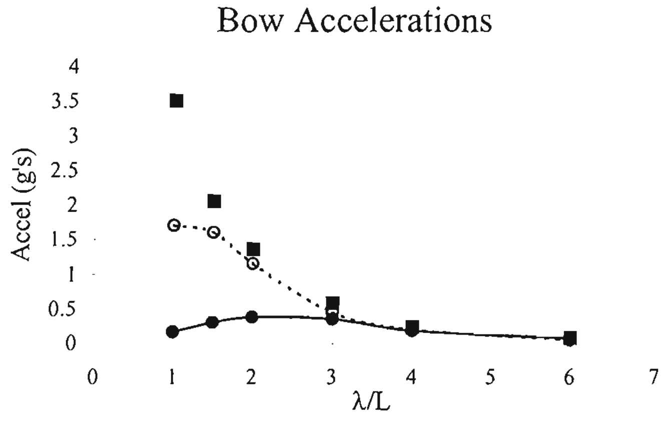

Figure A.78: CG and Bow Accelerations for Configuration I
$V/\sqrt{L} = 4$, $\beta = 20°$, $C_\Delta = 0.608$, $L/B = 5$, $H/B = 0.111$

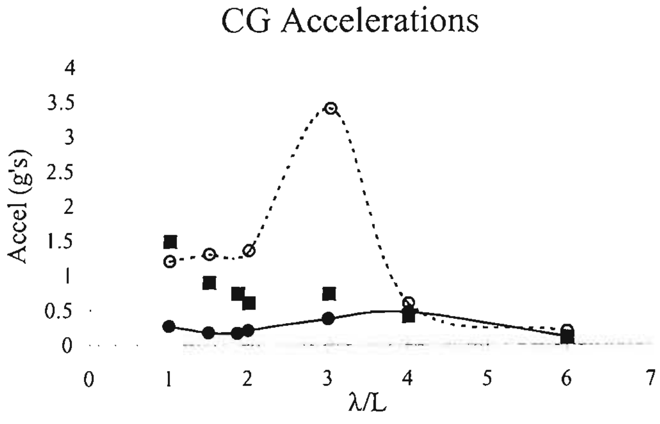

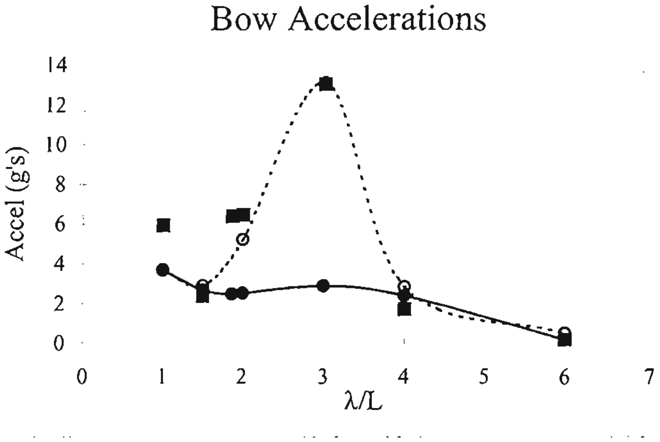

Figure A.79: CG and Bow Accelerations for Configuration J
$V/\sqrt{L} = 4$, $\beta = 20°$, $C_\Delta = 0.608$, $L/B = 5$, $H/B = 0.111$

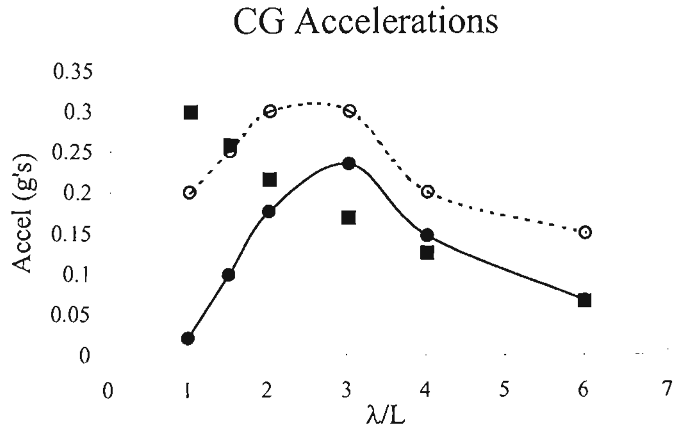

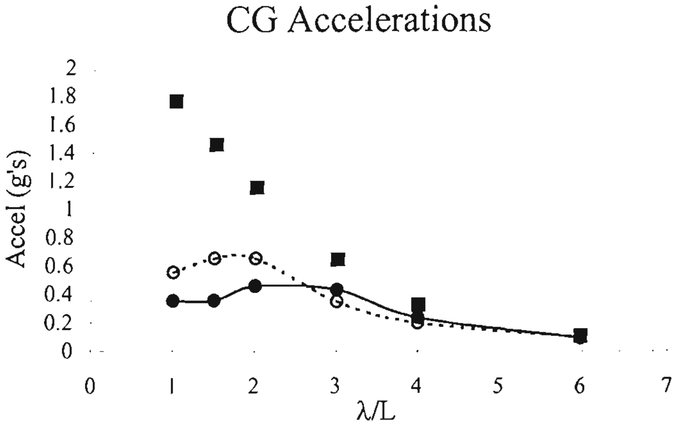

Figure A.80: CG and Bow Accelerations for Configuration K
$V/\sqrt{L} = 4$, $\beta = 20°$, $C_\Delta = 0.608$, $L/B = 5$, $H/B = 0.111$

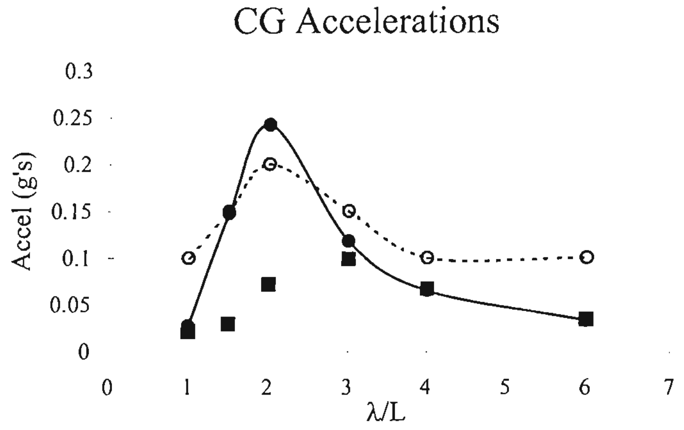

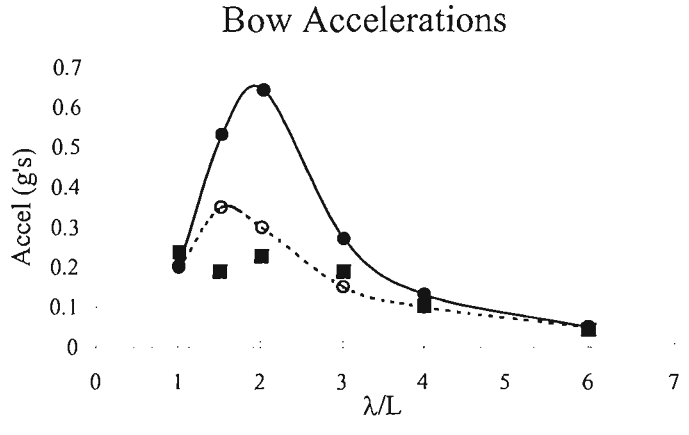

Figure A.81: CG and Bow Accelerations for Configuration L
$V/\sqrt{L} = 4$, $\beta = 20°$, $C_\Delta = 0.608$, $L/B = 5$, $H/B = 0.111$

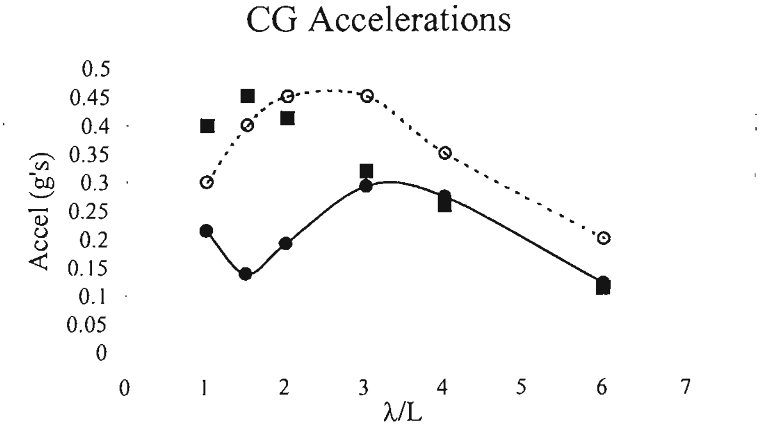

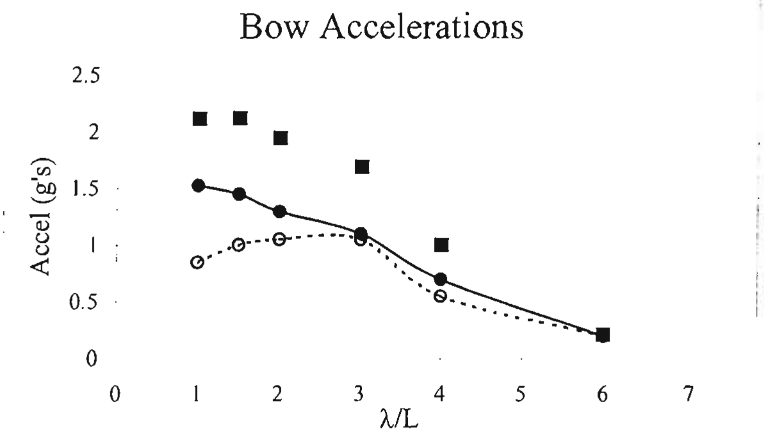

Figure A.82: CG and Bow Accelerations for Configuration M
$V/\sqrt{L} = 4$, $\beta = 20°$, $C_\Delta = 0.608$, $L/B = 5$, $H/B = 0.111$

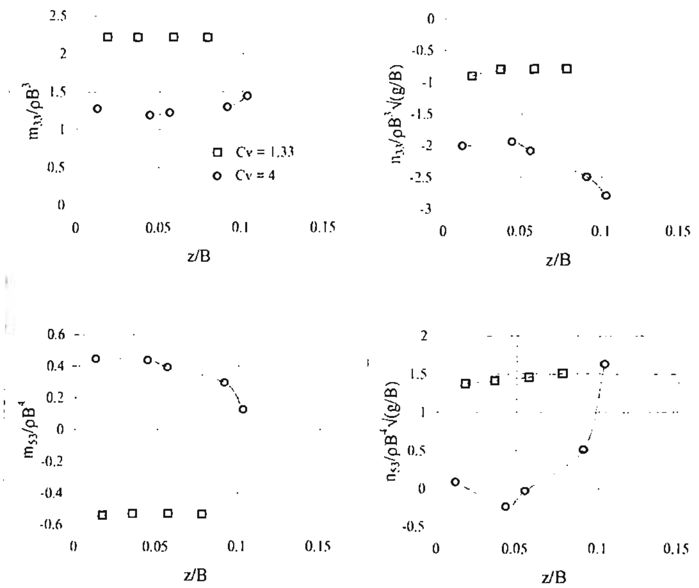

Figure A.83: Effect of Heave Amplitude and Velocity on Added Mass and Damping Coefficients

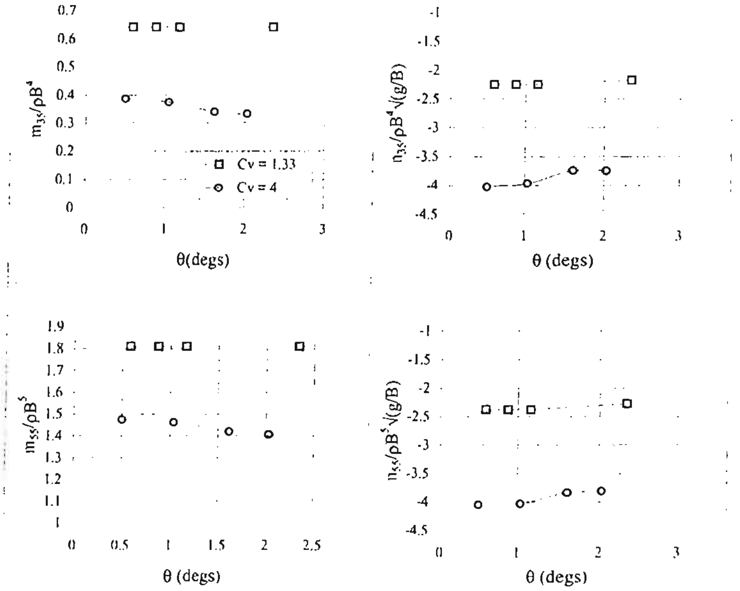

Figure A.84: Effect of Pitch Amplitude and Velocity on Added Mass and Damping Coefficients

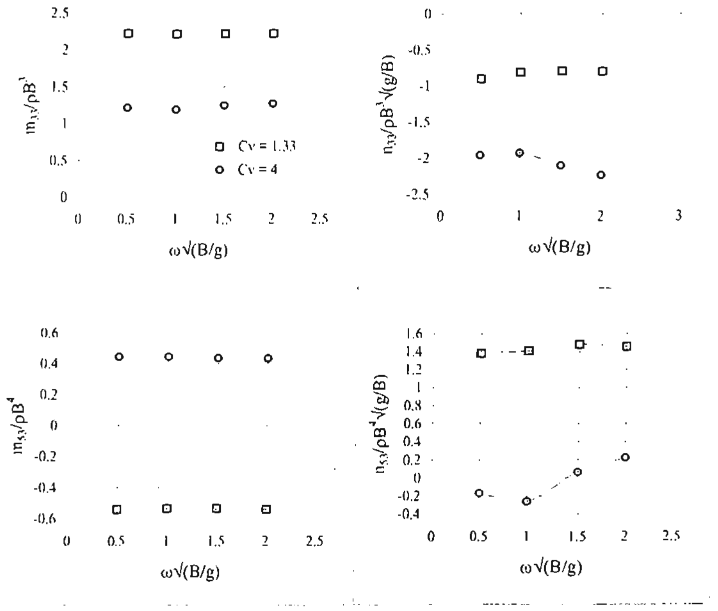

Figure A.85: Effect of Heave Motion Frequency and Velocity on Added Mass and Damping Coefficients

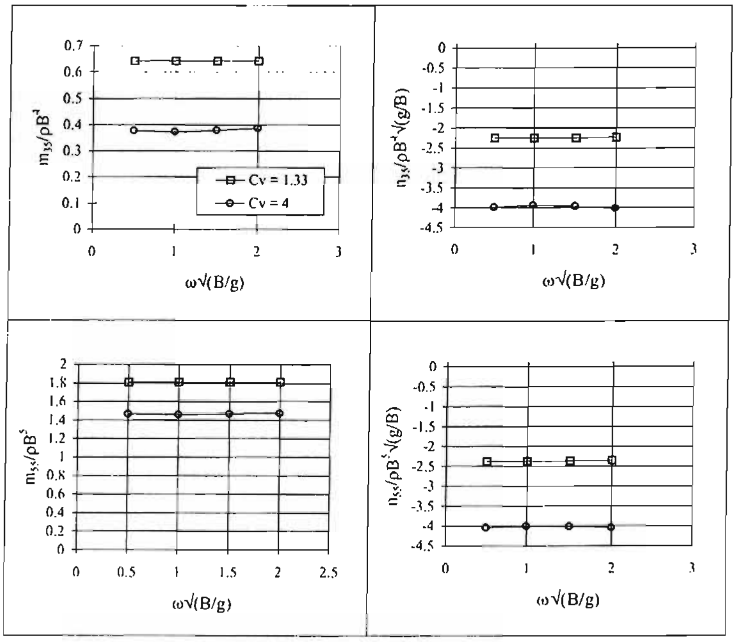

Figure A.86: Effect of Pitch Motion Frequency and Velocity on Added Mass and Damping Coefficients

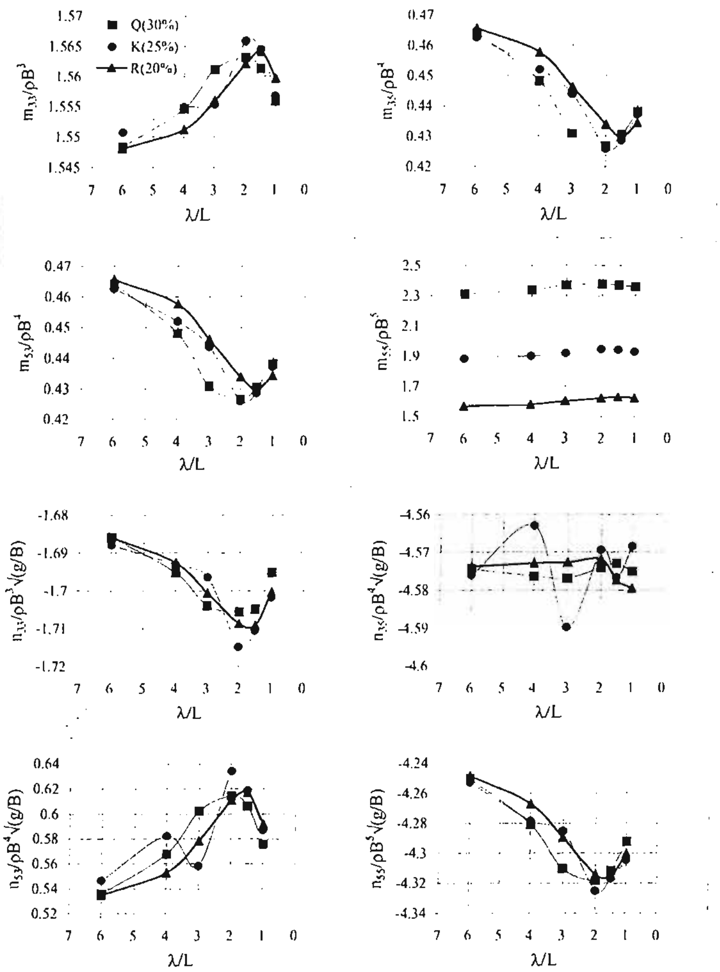

Figure A.87: Effect of Gyradius on Added Mass and Damping Coefficients for $V_{\text{knots}}/\sqrt{L_{\text{feet}}} = 4$

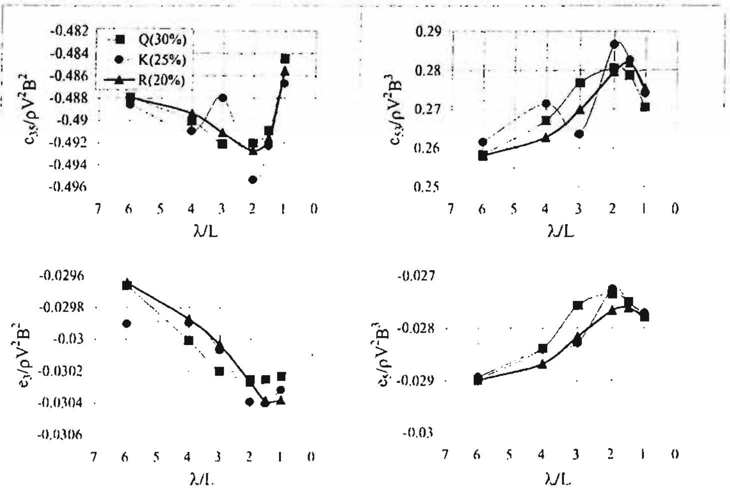

Figure A.88: Effect of Gyradius on Stiffness and Wave-forcing Coefficients for $V_{\text{knots}}/\sqrt{L_{\text{feet}}} = 4$

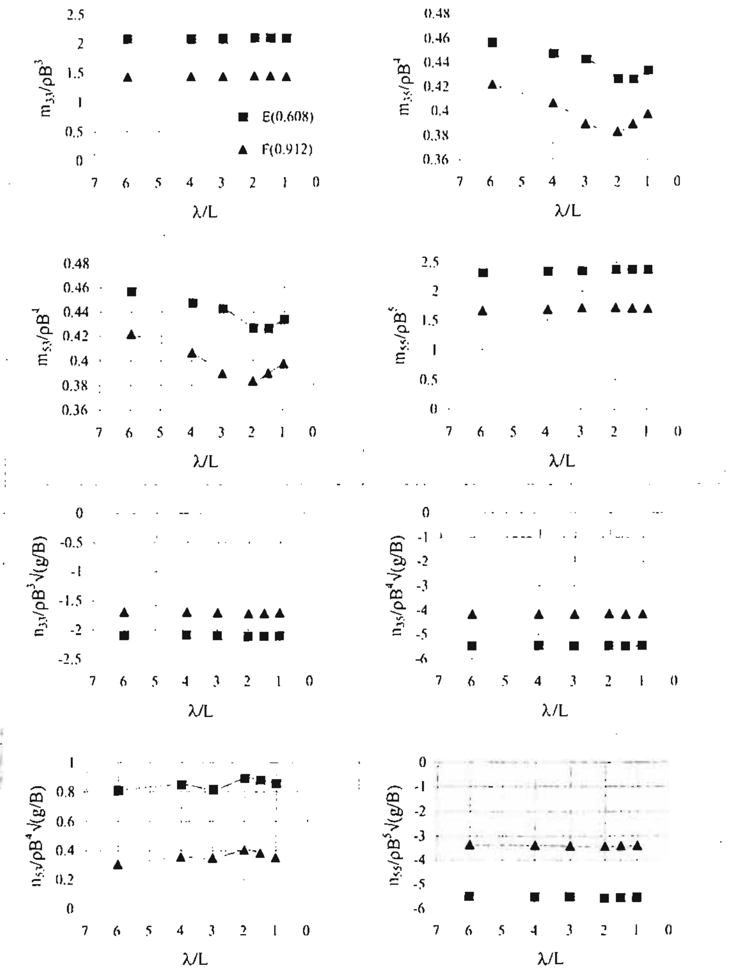

Figure A.89: Effect of Load on Added Mass and Damping Coefficients for $V_{\text{knots}}/\sqrt{L}_{\text{feet}} = 4$

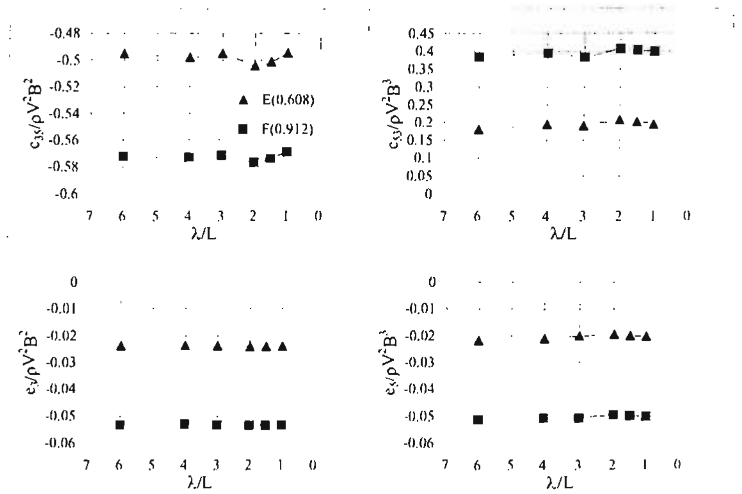

Figure A.90: Effect of Load on Stiffness and Wave-forcing Coefficients for $V_{\text{knots}}/\sqrt{L}_{\text{feet}} = 4$

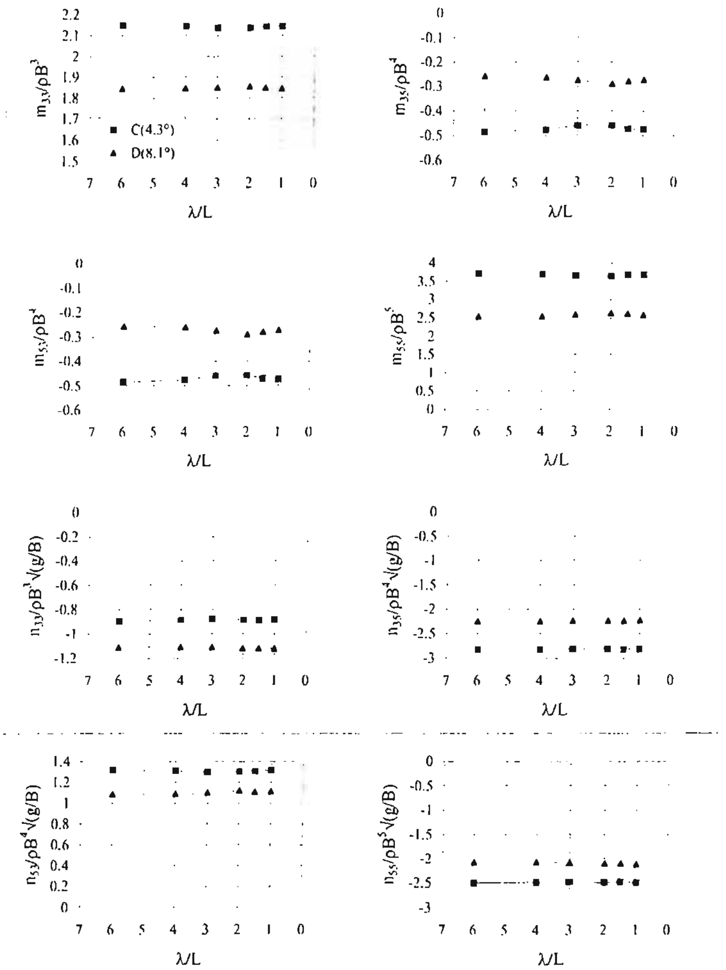

Figure A.91: Effect of Trim on Added Mass and Damping Coefficients for $V_{\text{knots}}/\sqrt{L_{\text{feet}}} = 2$

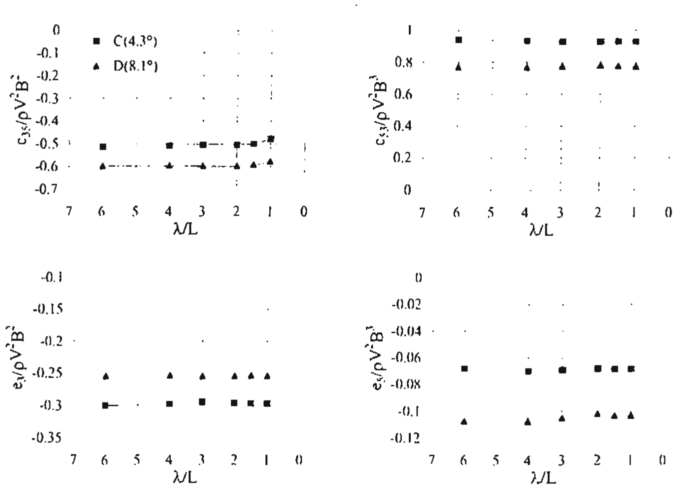

Figure A.92: Effect of Trim on Stiffness and Wave-forcing Coefficients for $V_{\text{knots}}/\sqrt{L_{\text{feet}}} = 2$

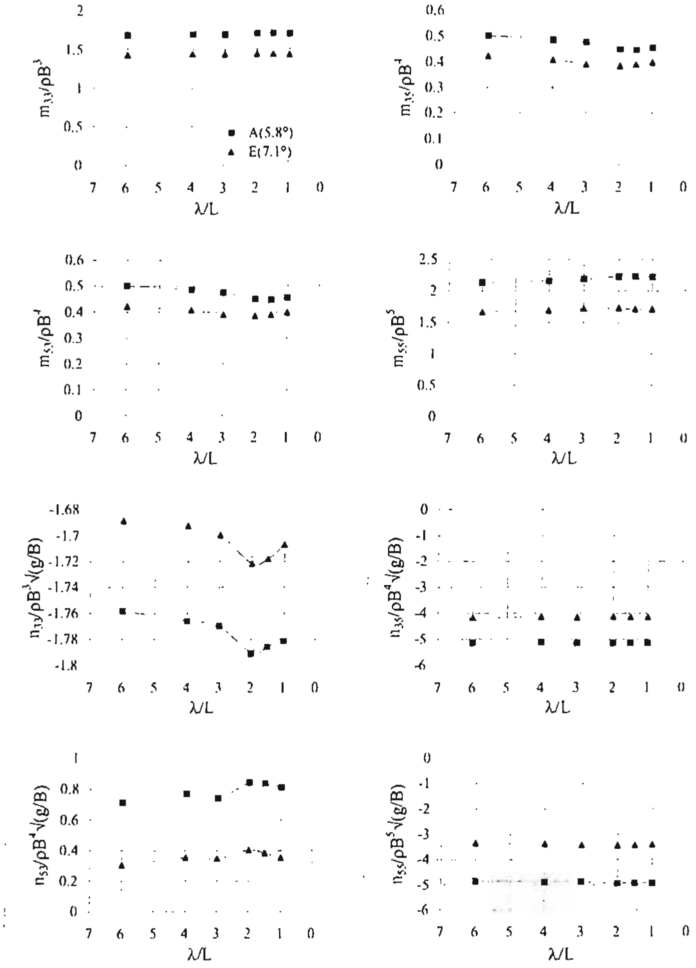

Figure A.93: Effect of Trim on Added Mass and Damping Coefficients for $V_{\text{knots}}/\sqrt{L}_{\text{feet}} = 4$

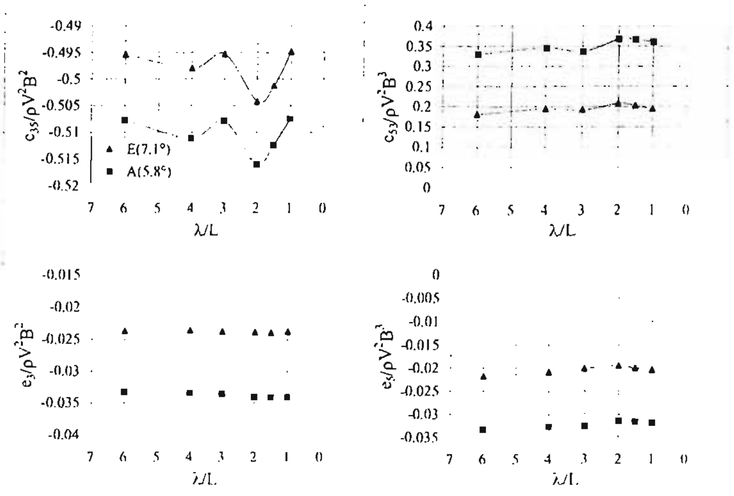

Figure A.94: Effect of Trim on Stiffness and Wave-forcing Coefficients for $V_{\text{knots}}/\sqrt{L}_{\text{feet}} = 4$

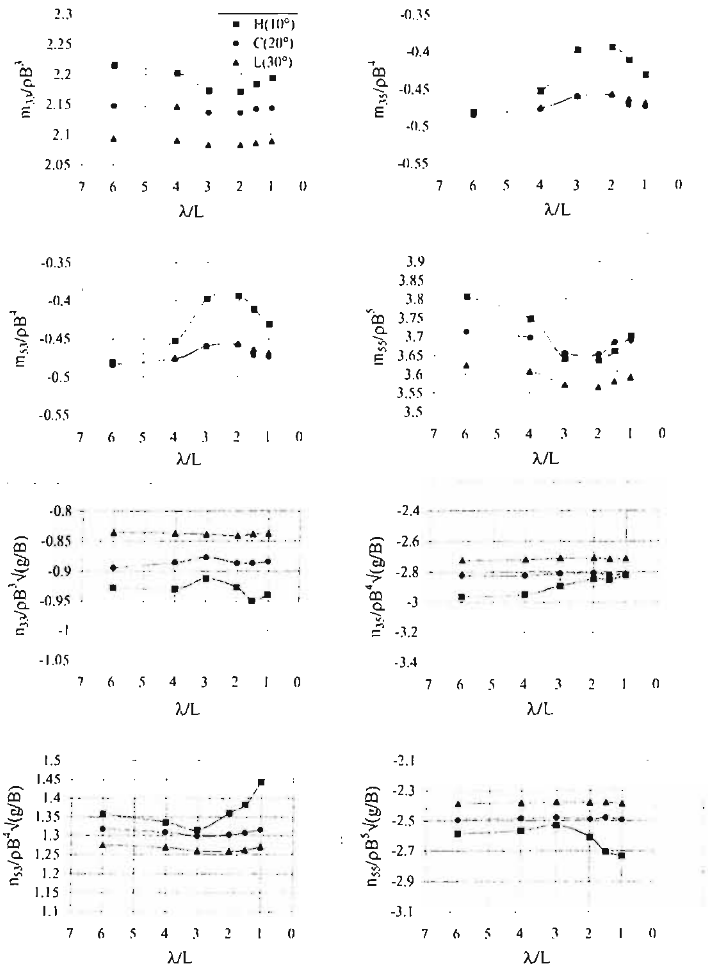

Figure A.95: Effect of Deadrise on Added Mass and Damping Coefficients for $V_{\text{knots}}/\sqrt{L_{\text{feet}}} = 2$

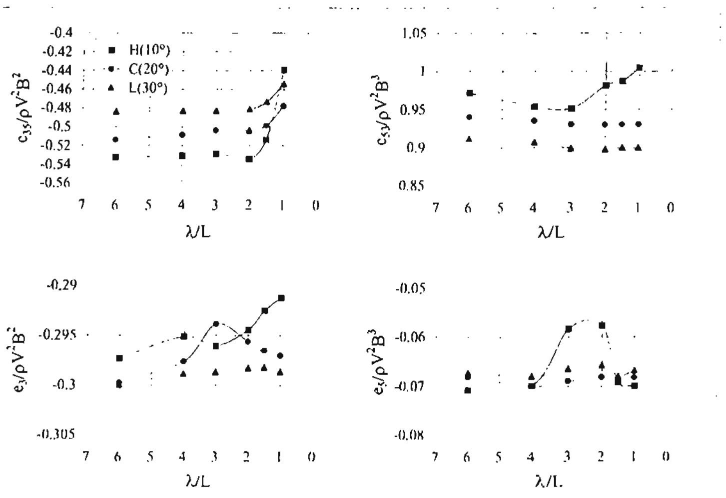

Figure A.96: Effect of Deadrise on Stiffness and Wave-forcing Coefficients for $V_{\text{knots}}/\sqrt{L_{\text{feet}}} = 2$

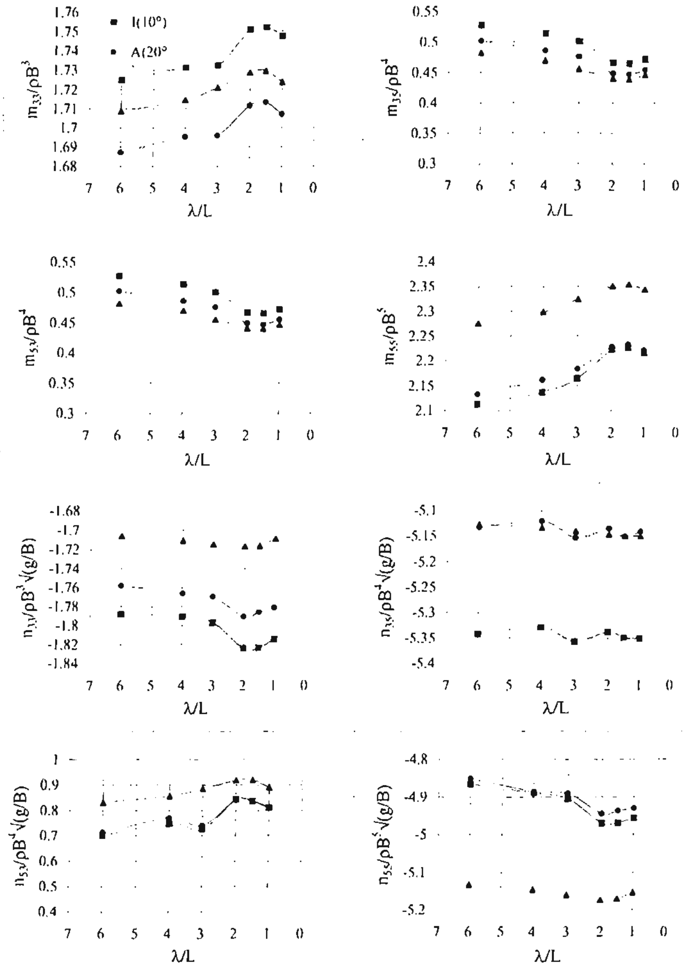

Figure A.97: Effect of Deadrise on Added Mass and Damping Coefficients for $V_{\text{knots}}/\sqrt{L}_{\text{feet}} = 4$

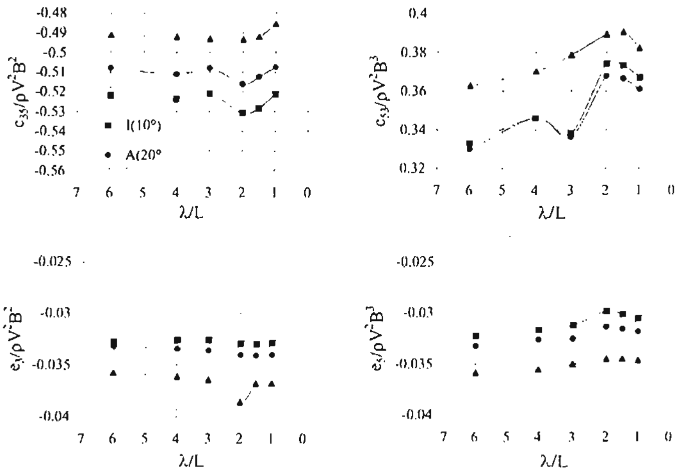

Figure A.98: Effect of Deadrise on Stiffness and Wave-forcing Coefficients for $V_{\text{knots}}/\sqrt{L}_{\text{feet}} = 4$

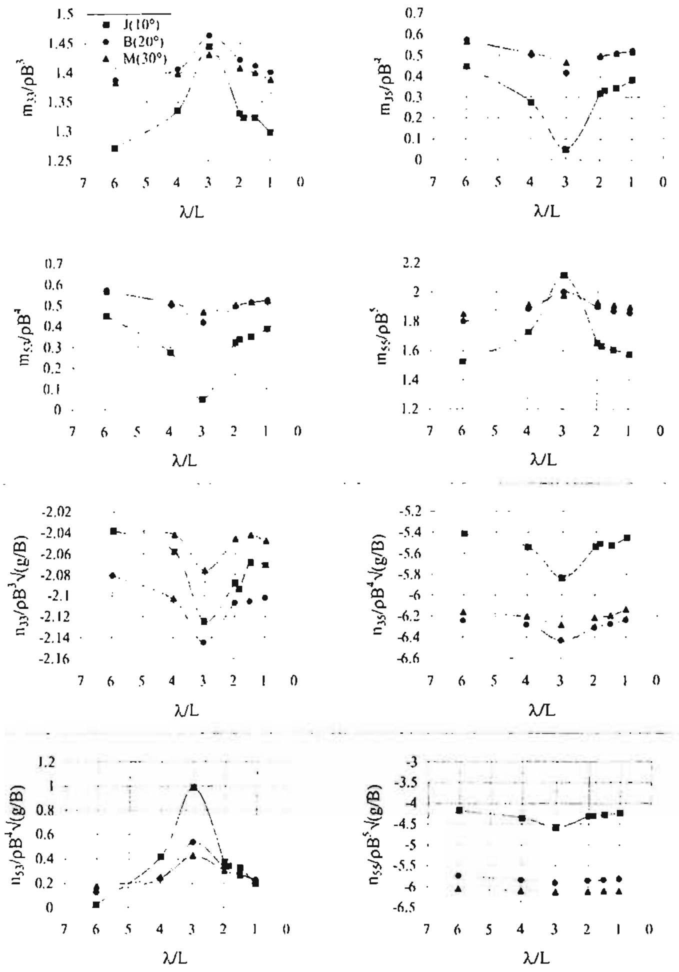

Figure A.99: Effect of Deadrise on Added Mass and Damping Coefficients for $V_{\text{knots}}/\sqrt{L}_{\text{feet}} = 6$

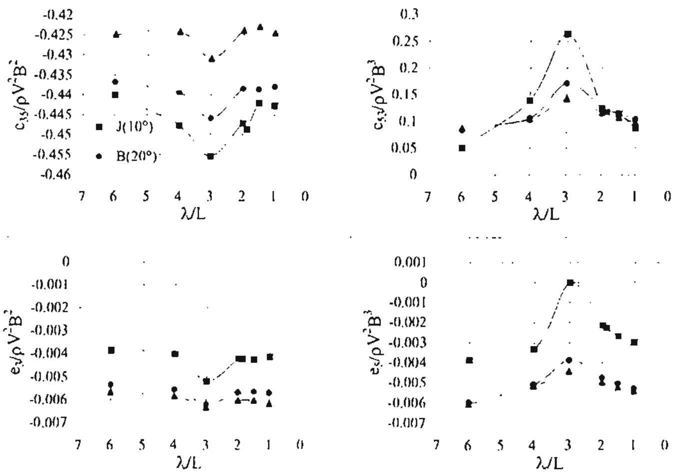

Figure A.100: Effect of Deadrise on Stiffness and Wave-forcing Coefficients for $V_{\text{knots}}/\sqrt{L}_{\text{feet}} = 6$

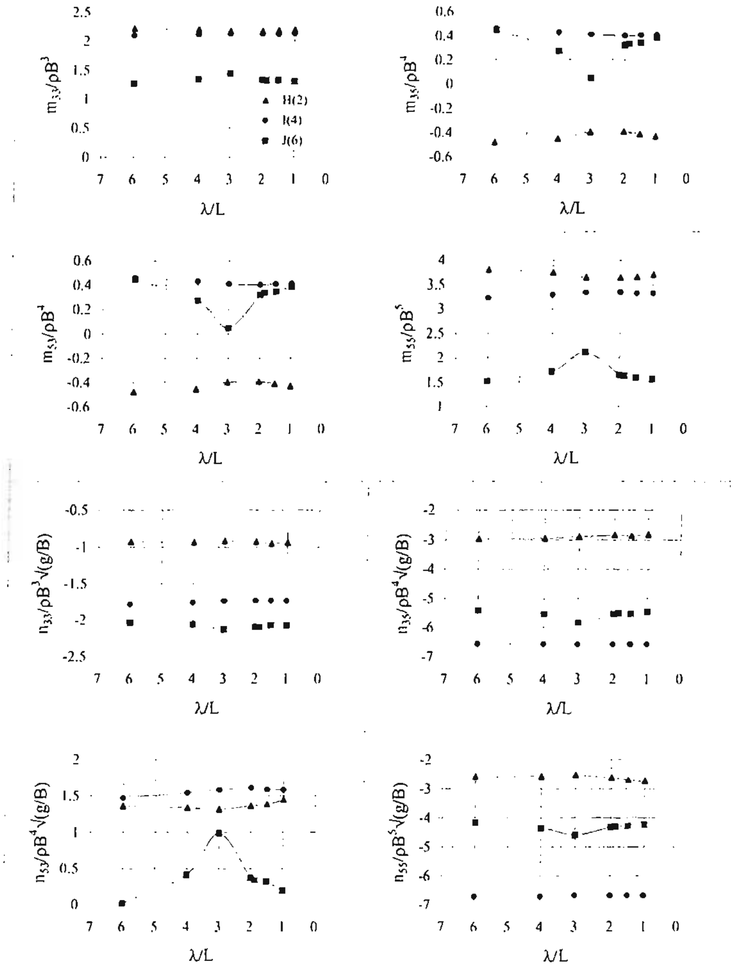

Figure A.101: Effect of Speed on Added Mass and Damping Coefficients for 10° Deadrise

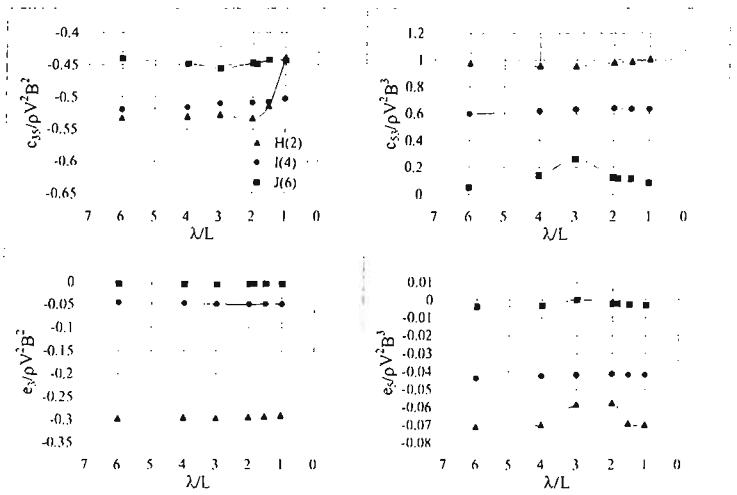

Figure A.102: Effect of Speed on Stiffness and Wave-forcing Coefficients for 10° Deadrise

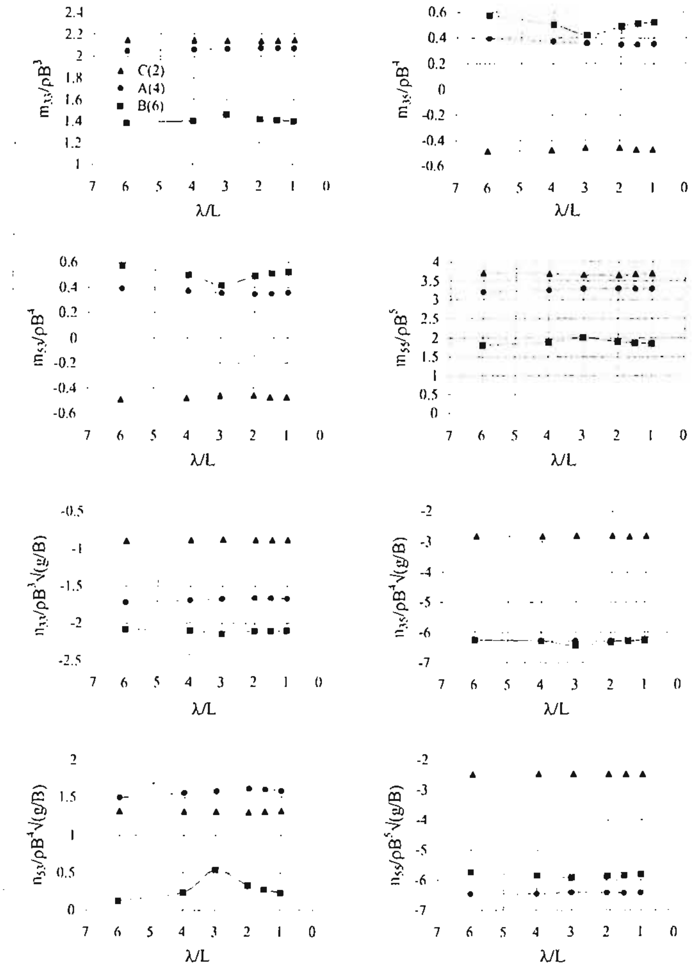

Figure A.103: Effect of Speed on Added Mass and Damping Coefficients for 20° Deadrise

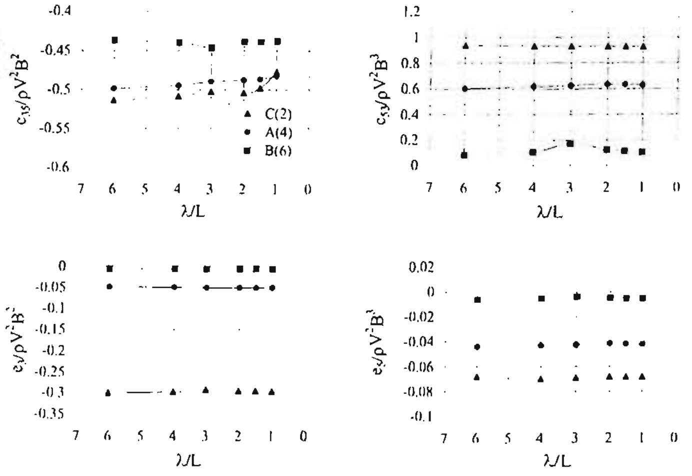

Figure A.104: Effect of Speed on Stiffness and Wave-forcing Coefficients for 20° Deadrise

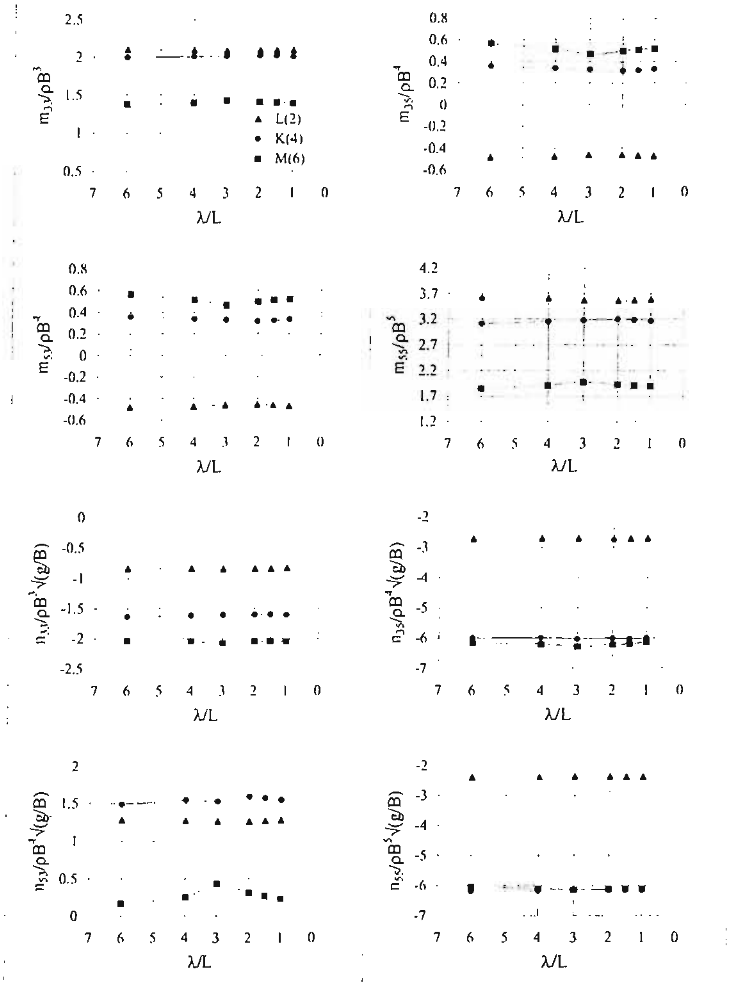

Figure A.105: Effect of Speed on Added Mass and Damping Coefficients for 30° Deadrise

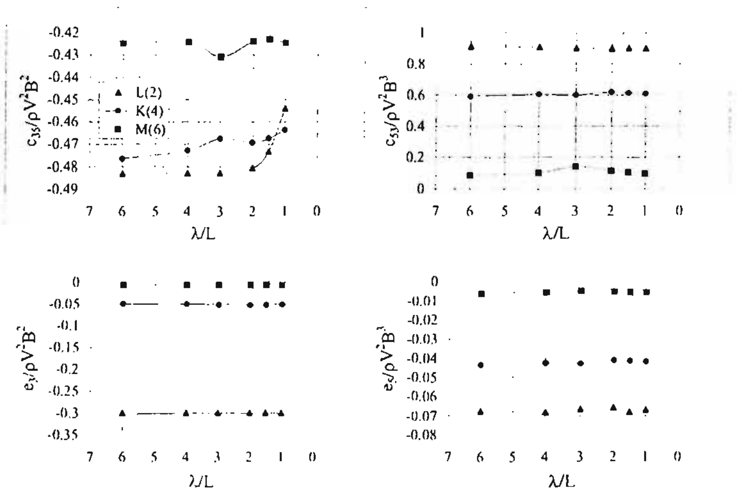

Figure A.106: Effect of Speed on Stiffness and Wave-forcing Coefficients for 30° Deadrise

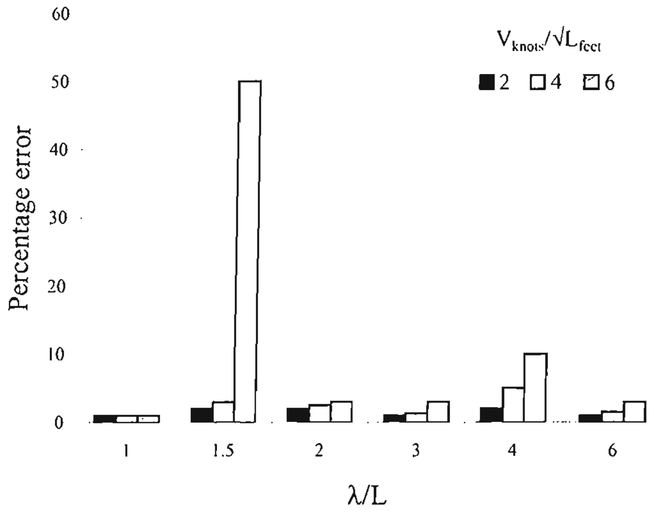

Figure A.107: Calculated Error in Predicted Motion Reponses by Removing Higher Order ($O(\epsilon^n)$, $n \geq 2$) Perturbation Terms

$\beta = 10°$, $V/\sqrt{L} = 2$, 4 and 6

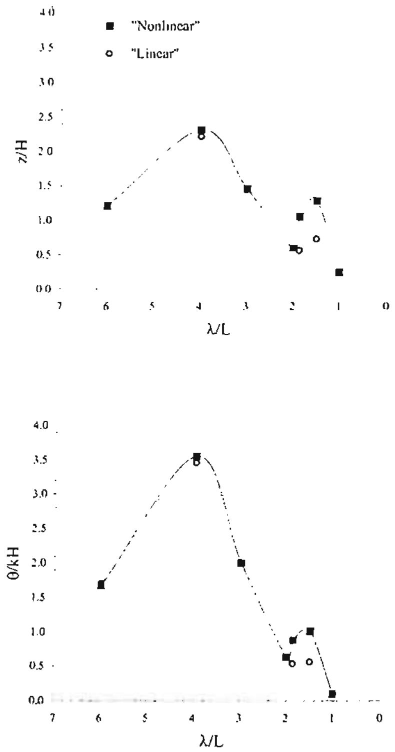

Figure A.108: Effect of Removing Higher Order ($O(\epsilon^n)$, $n \geq 2$) Perturbation Terms on Predicted Motion Reponses for Craft Configuration J

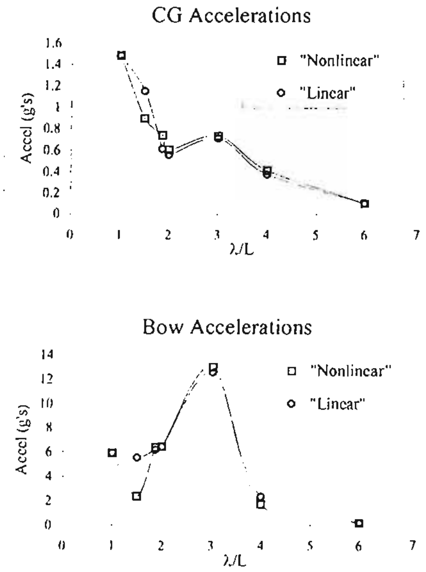

Figure A.109: Effect of Removing Higher Order ($O(\epsilon^n)$, $n \geq 2$) Perturbation Terms on Predicted Accelerations for Craft Configuration J

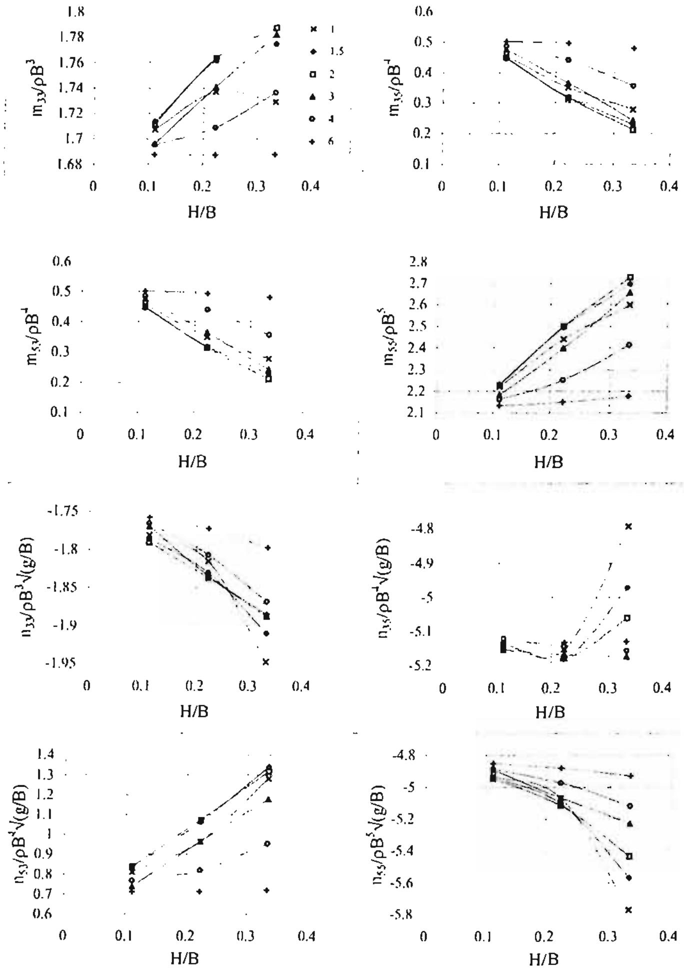

Figure A.110: Effect of Waveheight on Added Mass and Damping Coefficients for Configuration A ($\beta = 20°$, $V/\sqrt{L} = 4$)

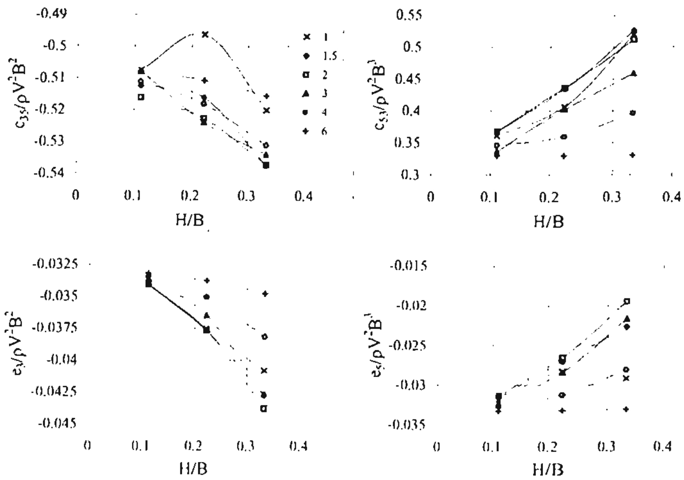

Figure A.111: Effect of Waveheight on Stiffness and Wave-forcing Coefficients for Configuration A ($\beta = 20°$, $V/\sqrt{L} = 4$)

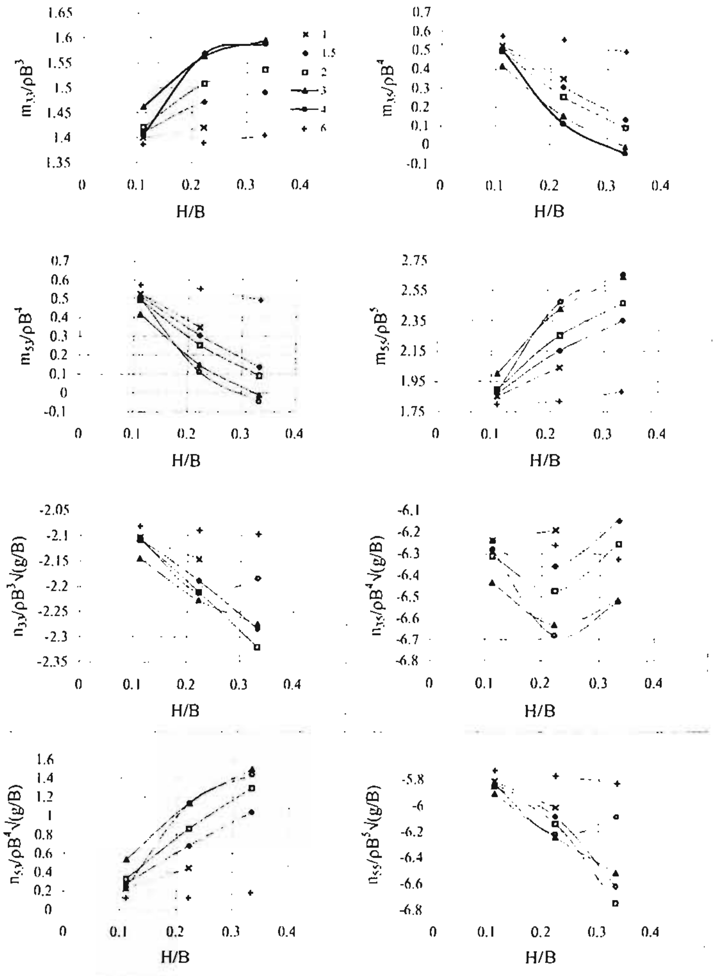

Figure A.112: Effect of Waveheight on Added Mass and Damping Coefficients for Configuration B ($\beta = 20°$, $V/\sqrt{L} = 6$)

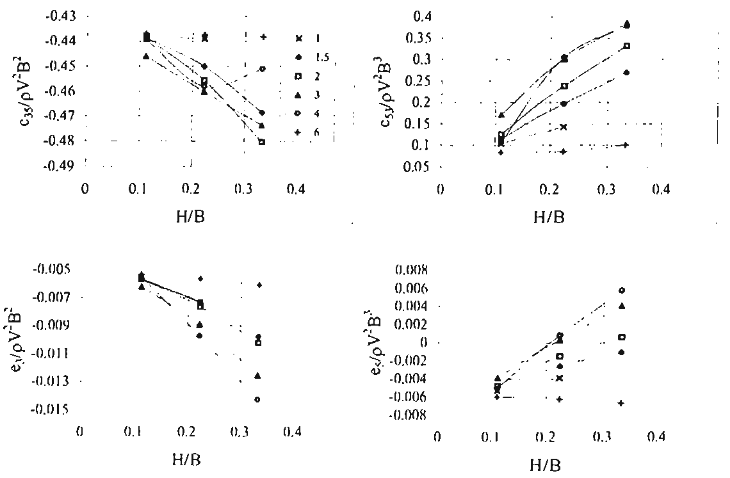

Figure A.113: Effect of Waveheight on Stiffness and Wave-forcing Coefficients for Configuration B ($\beta = 20°$, $V/\sqrt{L} = 6$)

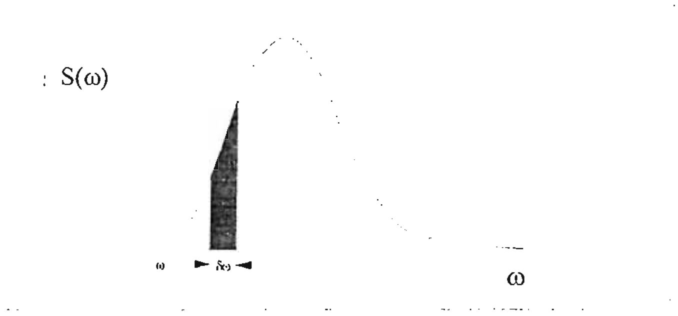

Figure A.114: Wave Energy Spectrum

Hatched area corresponds to the proportion of total wave energy within a sea contributed by the frequencies bounded by ω and $\omega + \delta\omega$

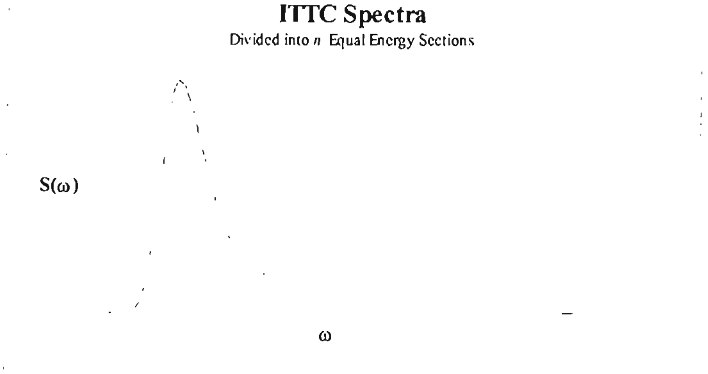

Figure A.115: Division of ITTC Spectra into Equal Energy Divisions (Payne 1995)

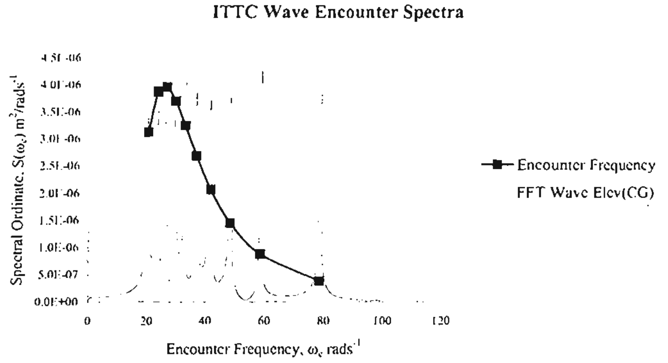

Figure A.116: ITTC Wave Encounter Spectra, 10 Component Frequencies

FFT results from NoLiPCraMP Generated Sea Surface ($H_{1/3}/B = 0.222$)

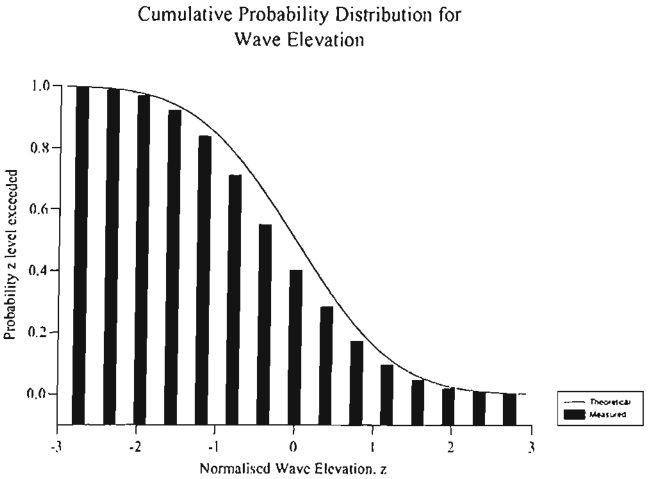

Figure A.117: Theoretical (Normal) and Measured (NoLiPCraMP) Probability Distribution for Wave Elevation

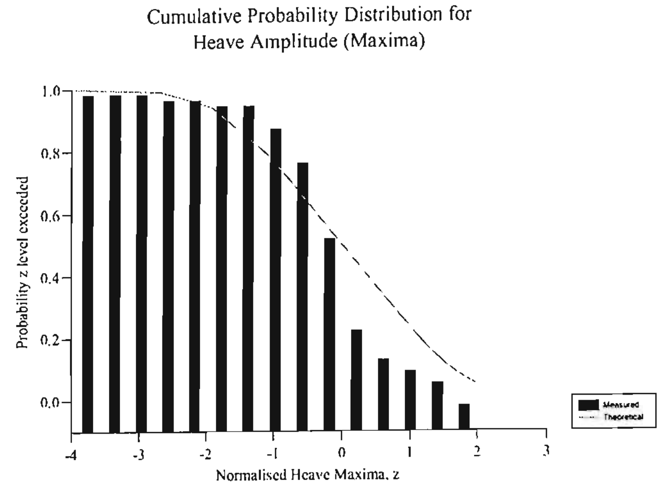

Figure A.118: Theoretical (Generalised Rayleigh) and Measured (NoLiPCraMP) Probability Distribution for Heave Maxima - Frequency Independent

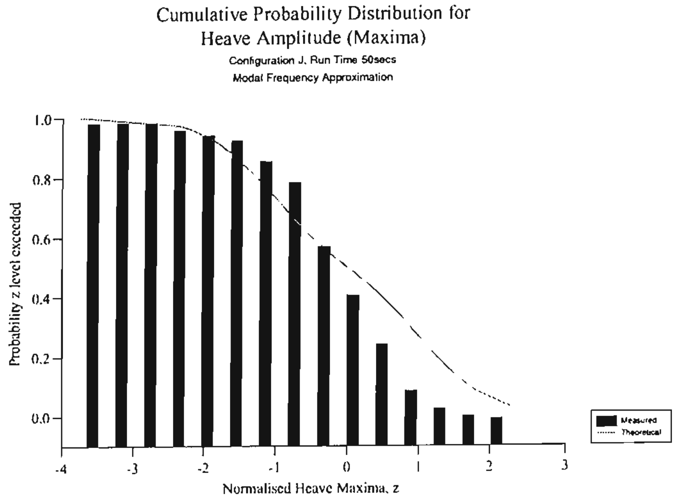

Figure A.119: Theoretical (Generalised Rayleigh) and Measured (NoLiPCraMP) Probability Distribution for Heave Maxima - Frequency Dependent

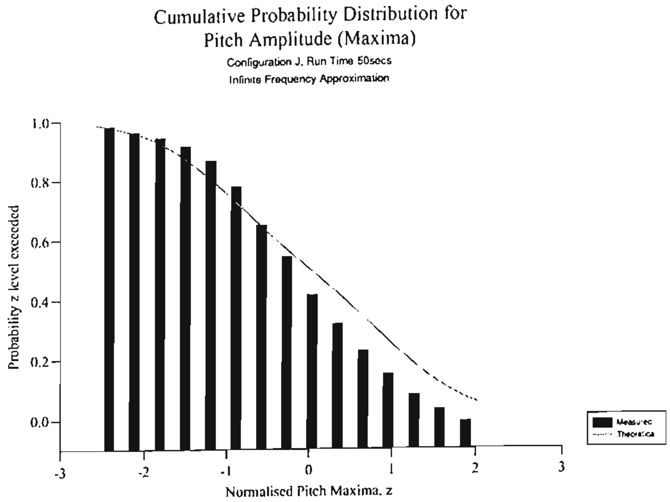

Figure A.120: Theoretical (Generalised Rayleigh) and Measured (NoLiPCraMP) Probability Distribution for Pitch Maxima - Frequency Independent

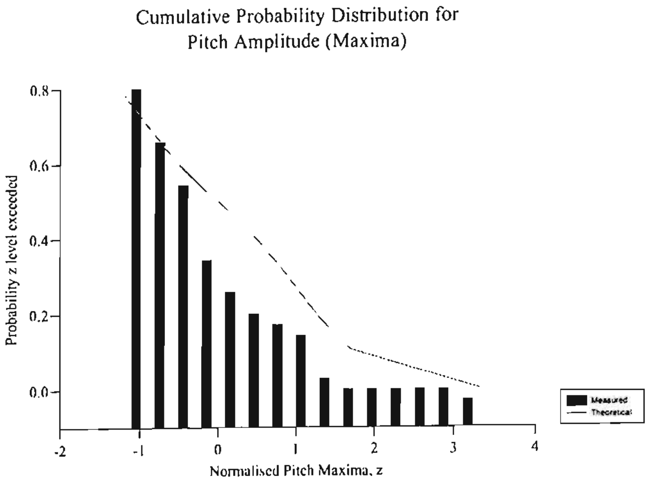

Figure A.121: Theoretical (Generalised Rayleigh) and Measured (NoLiPCraMP) Probability Distribution for Pitch Maxima - Frequency Dependent

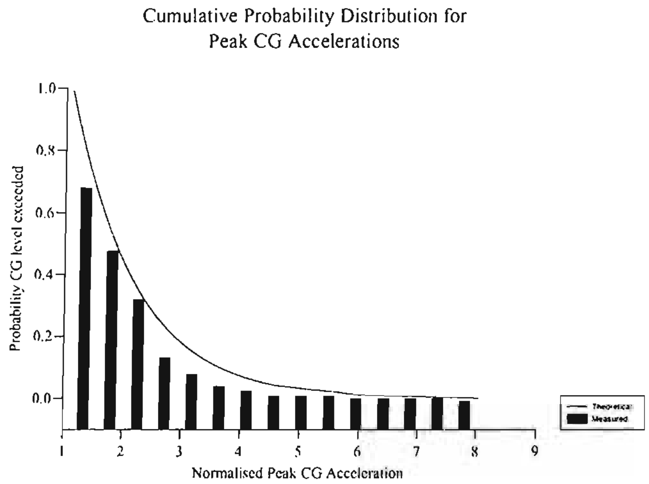

Figure A.122: Theoretical (Exponential) and Measured (No-LiPCraMP) Probability Distribution for CG Acceleration - Frequency Independent

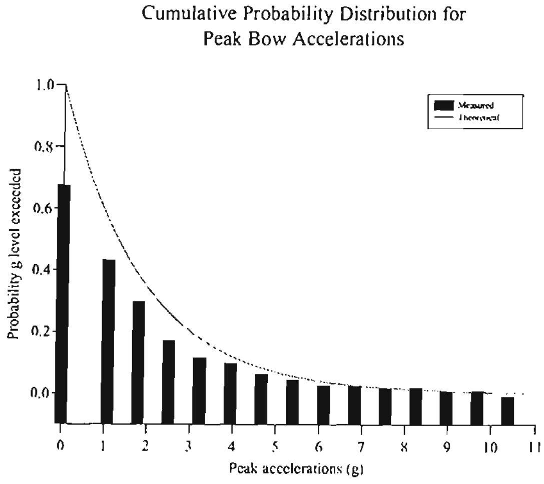

Figure A.123: Theoretical (Exponential) and Measured (No-LiPCraMP) Probability Distribution for Bow Acceleration - Frequency Independent

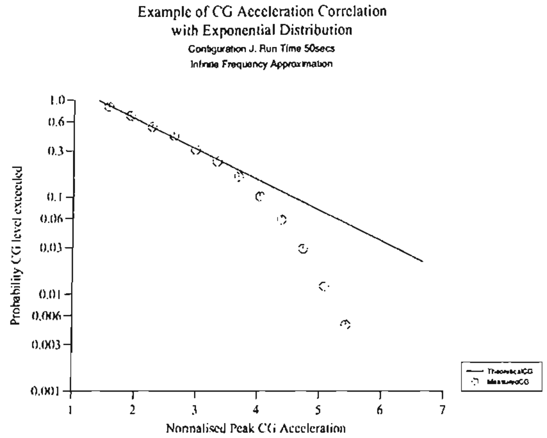

Figure A.124: Correlation between Theoretical (Exponential) and Measured (NoLiPCraMP) Probability Distribution for CG Acceleration - Frequency Independent

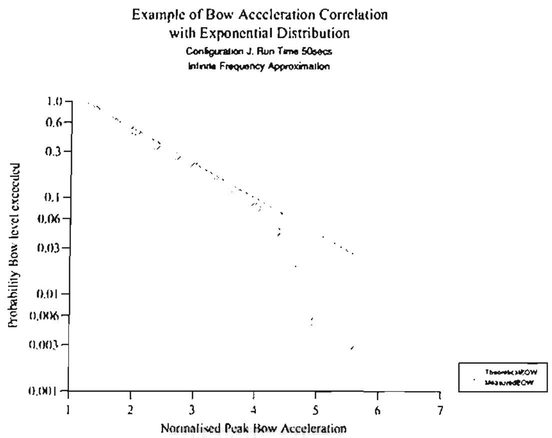

Figure A.125: Correlation between Theoretical (Exponential) and Measured (NoLiPCraMP) Probability Distribution for Bow Acceleration - Frequency Independent

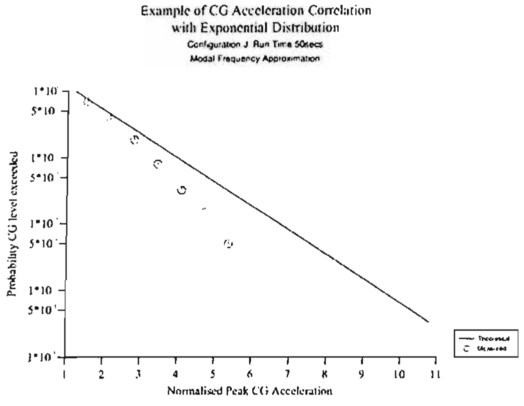

Figure A.126: Correlation between Theoretical (Exponential) and Measured (NoLiPCraMP) Probability Distribution for CG Acceleration - Frequency Dependent

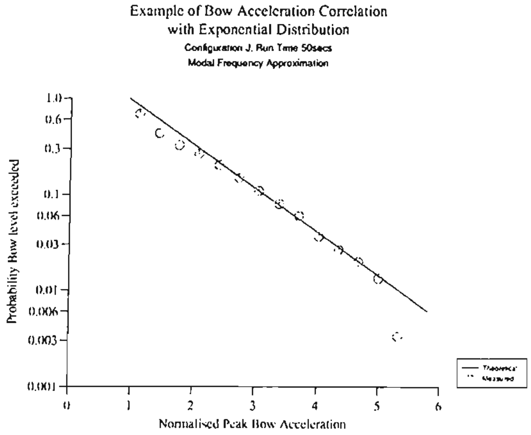

Figure A.127: Correlation between Theoretical (Exponential) and Measured (NoLiPCraMP) Probability Distribution for Bow Acceleration - Frequency Dependent

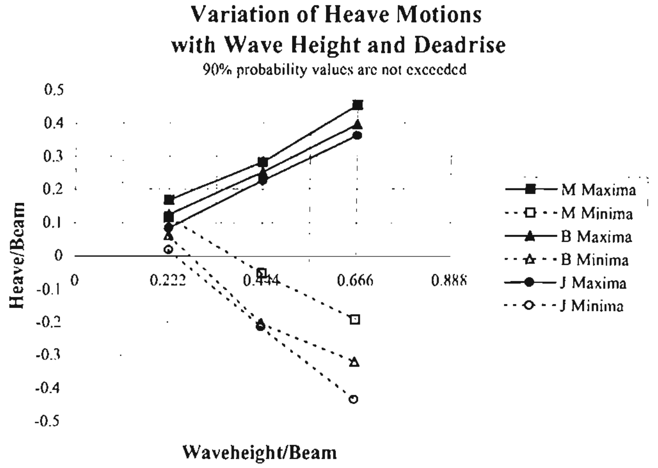

Figure A.128: Variation of Heave Motions with Waveheight and Deadrise
10% Probability of Excedance

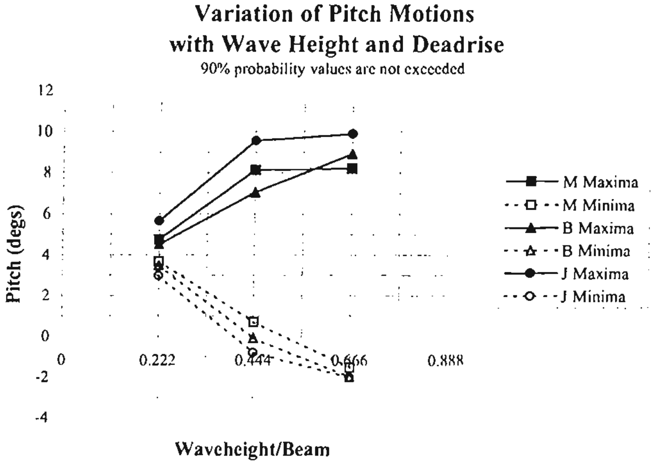

Figure A.129: Variation of Pitch Motions with Waveheight and Deadrise
10% Probability of Excedance

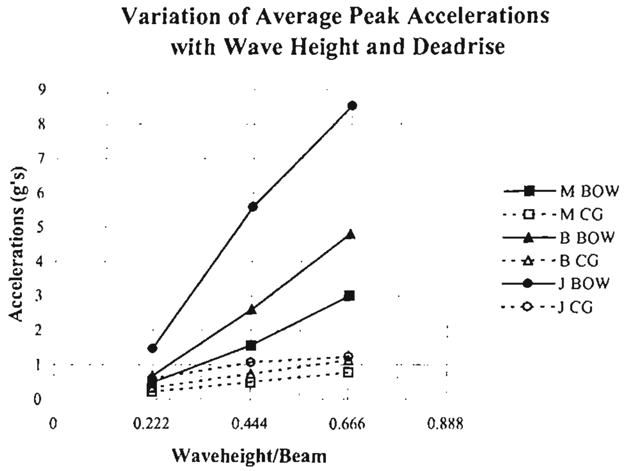

Figure A.130: Variation of Average Peak Accelerations with Waveheight and Deadrise

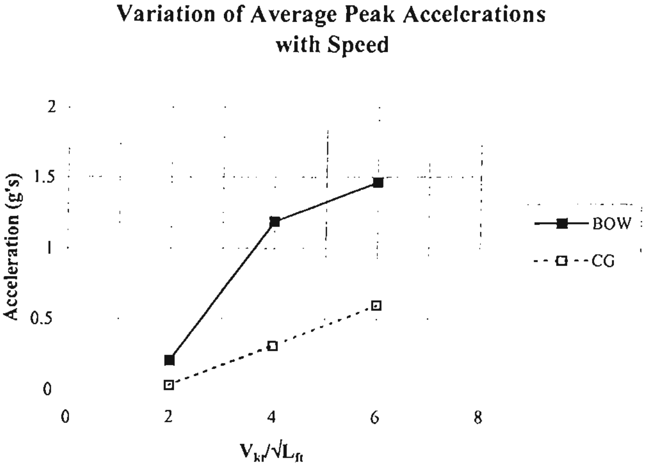

Figure A.131: Variation of Average Peak Accelerations with Speed

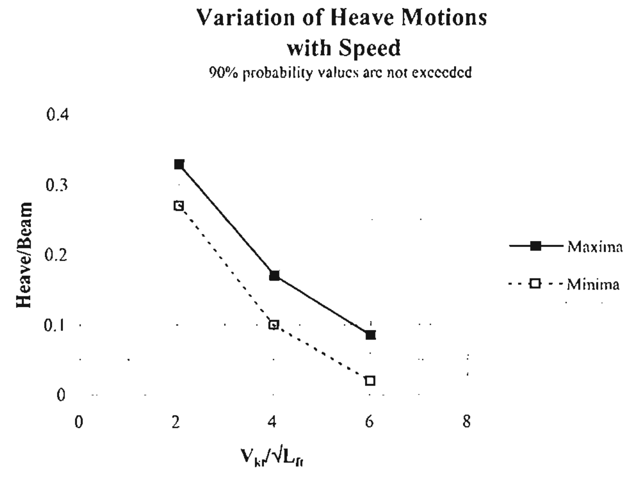

Figure A.132: Variation of Heave Response with Speed
10% Probability of Excedance

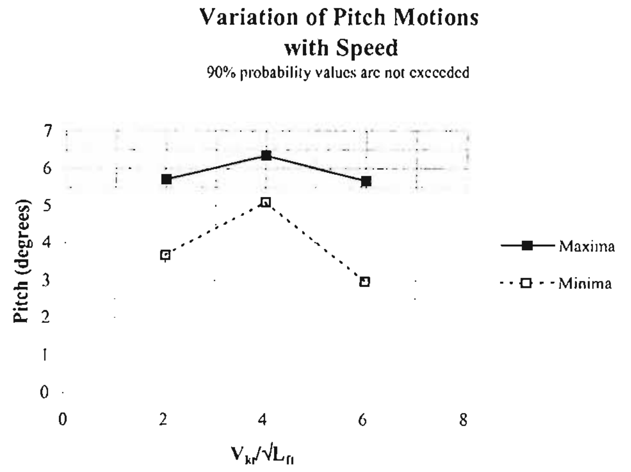

Figure A.133: Variation of Pitch Response with Speed
10% Probability of Excedance

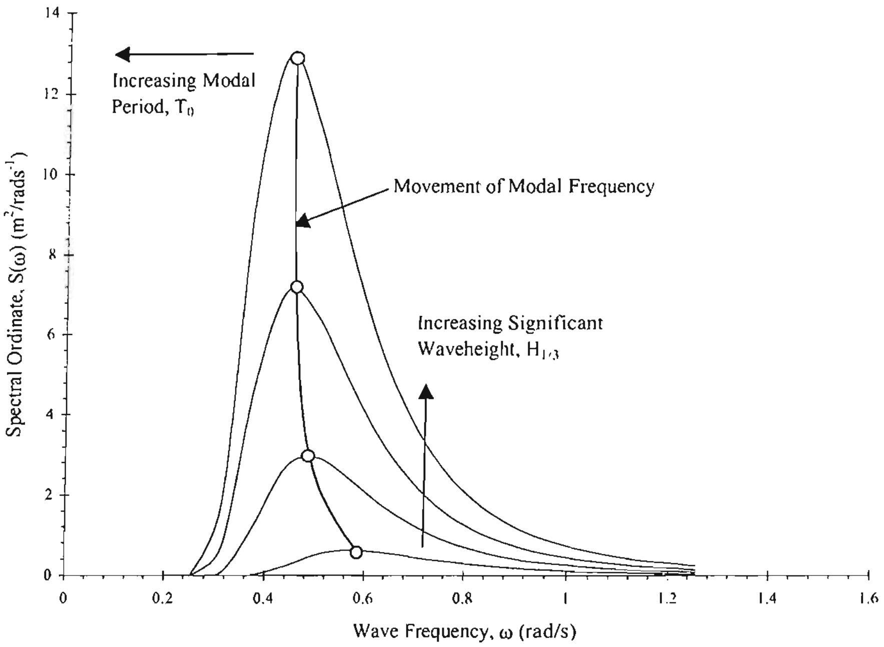

Figure A.134: Movement of Modal Frequency with Increasing Waveheight

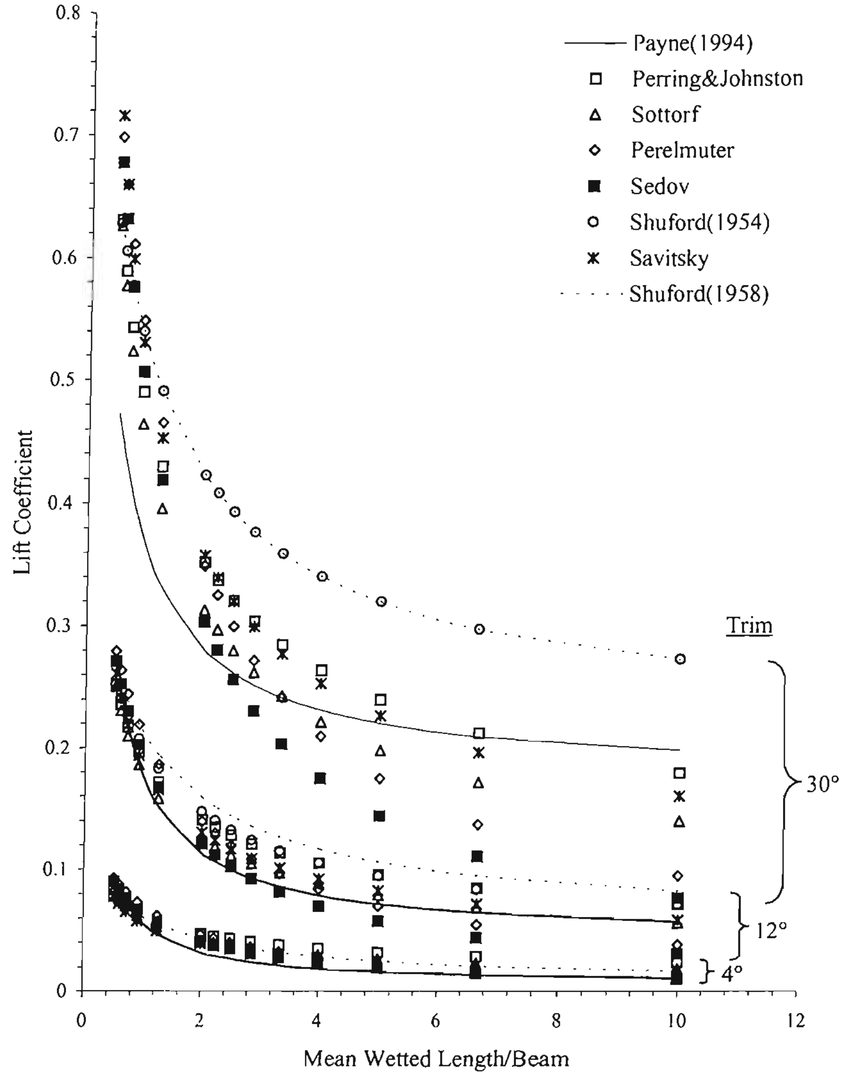

Figure A.135: Comparison of Various Theories for the Evaluation of Lift for a Flat Plate

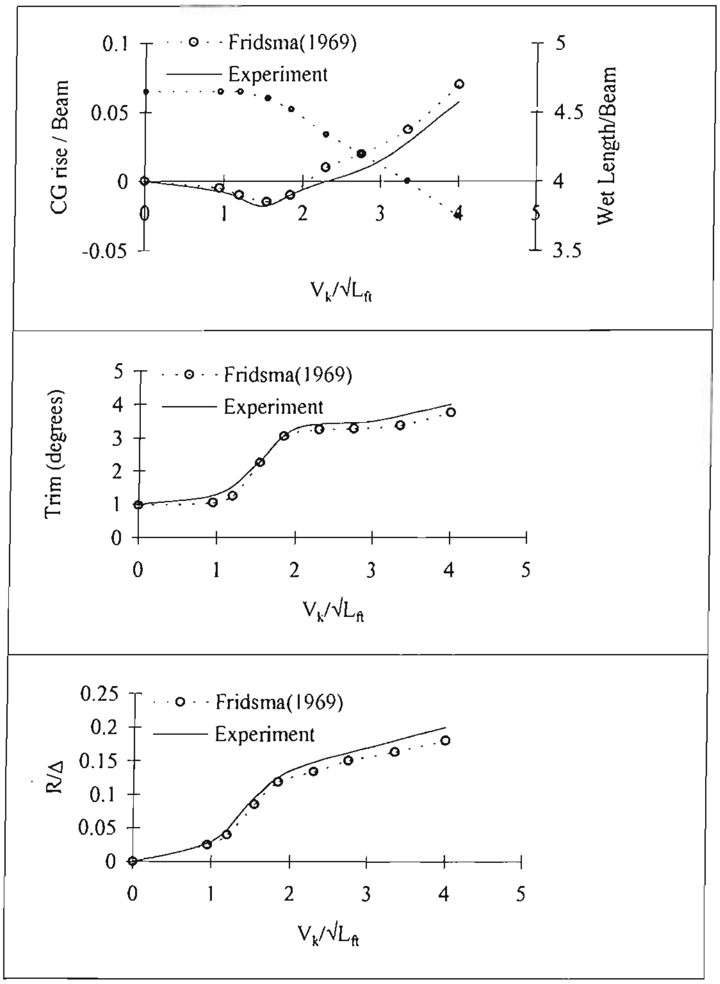

Figure A.136: Rise of CG and Change in Running Trim with Speed for Configuration K

CG rise relative to Zero Speed Condition

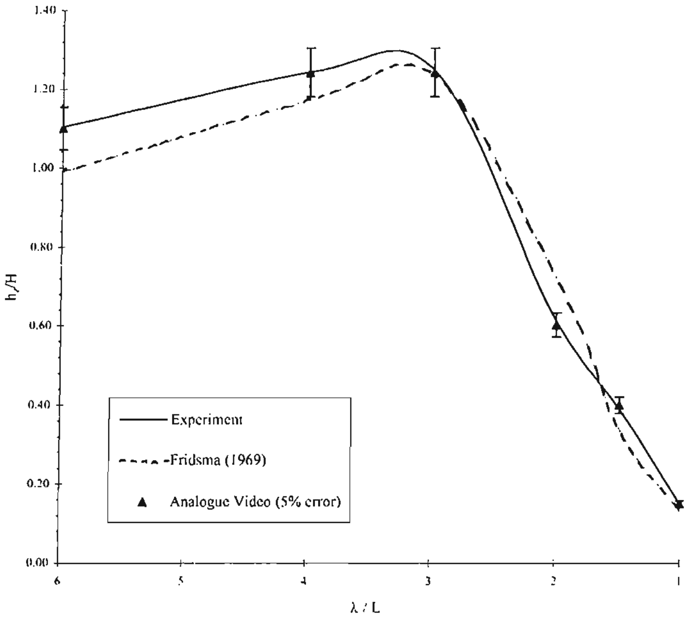

Figure A.137: Comparison of New Experimental Results for Heave with Fridsma (1969)

Also shown is results from analogue video analysis

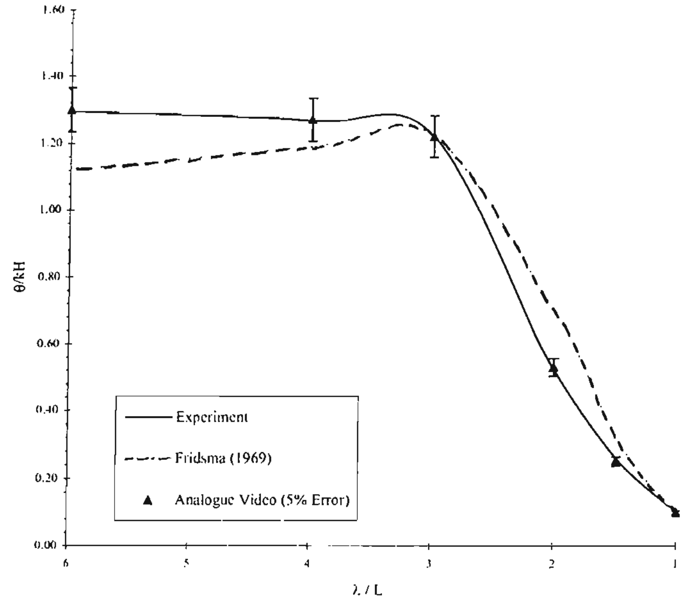

Figure A.138: Comparison of New Experimental Results for Pitch with Fridsma (1969)

Also shown is results from analogue video analysis

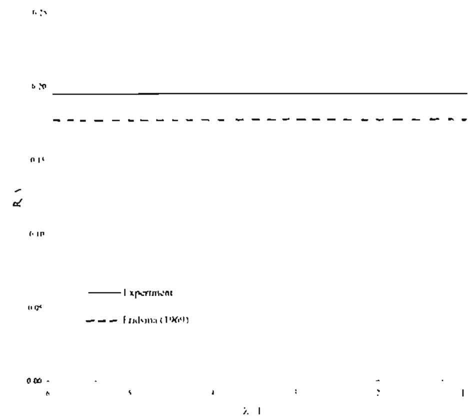

Figure A.139: Comparison of New Experimental Results for Calm Water Resistance with Fridsma (1969)

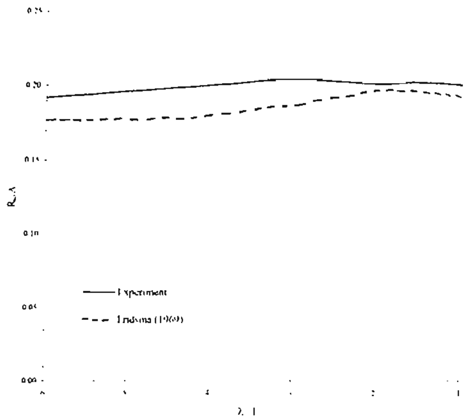

Figure A.140: Comparison of New Experimental Results for Rough Water Resistance with Fridsma (1969)

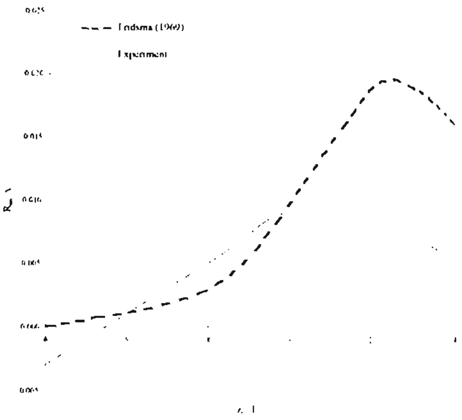

Figure A.141: Comparison of New Experimental Results for Added Resistance with Fridsma (1969)

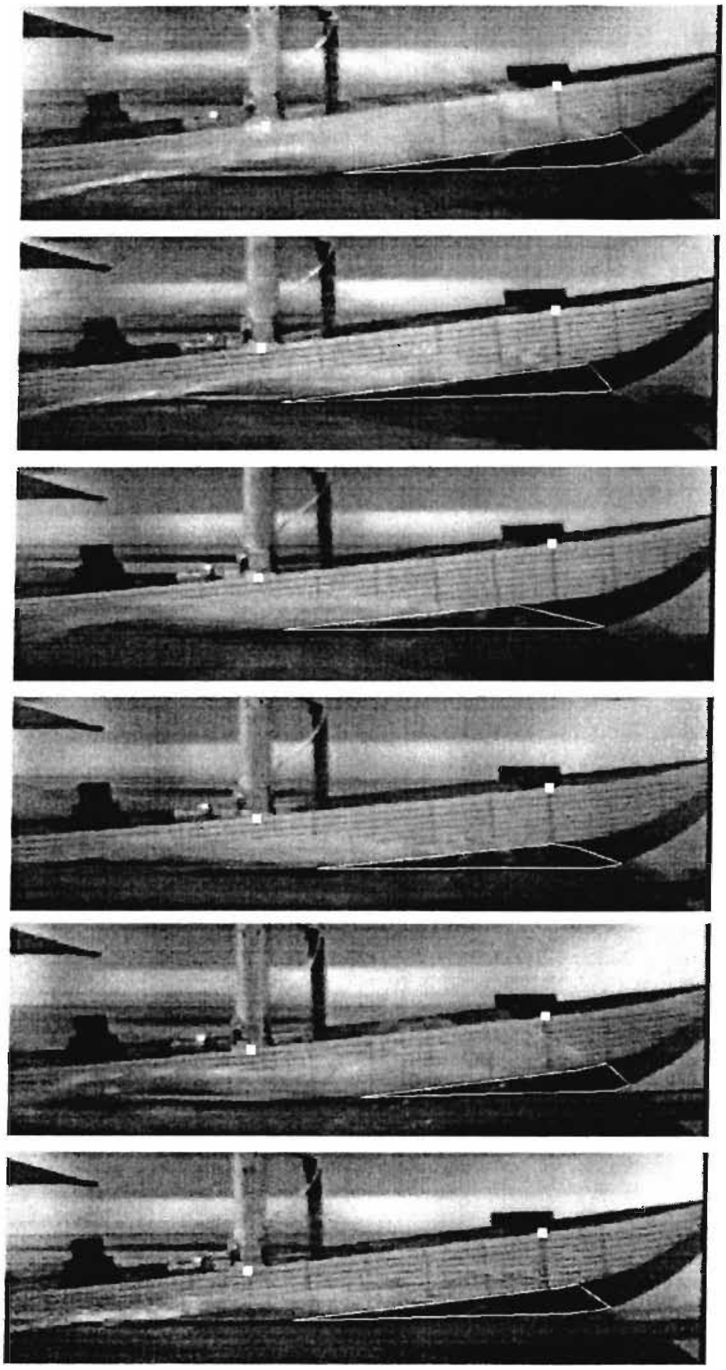

Figure A.142: Frame Sequence of Configuration K

$V/\sqrt{L} = 4$, $\beta = 30°$, $C_\Delta = 0.608$, $L/B = 5$, $H/B = 0.111$, $\lambda/L = 2$

Each frame shown relates to every 5th frame captured or 0.1 seconds. White squares show *points of interest*. White boundary at bow/water intersection shows the *spray area*.

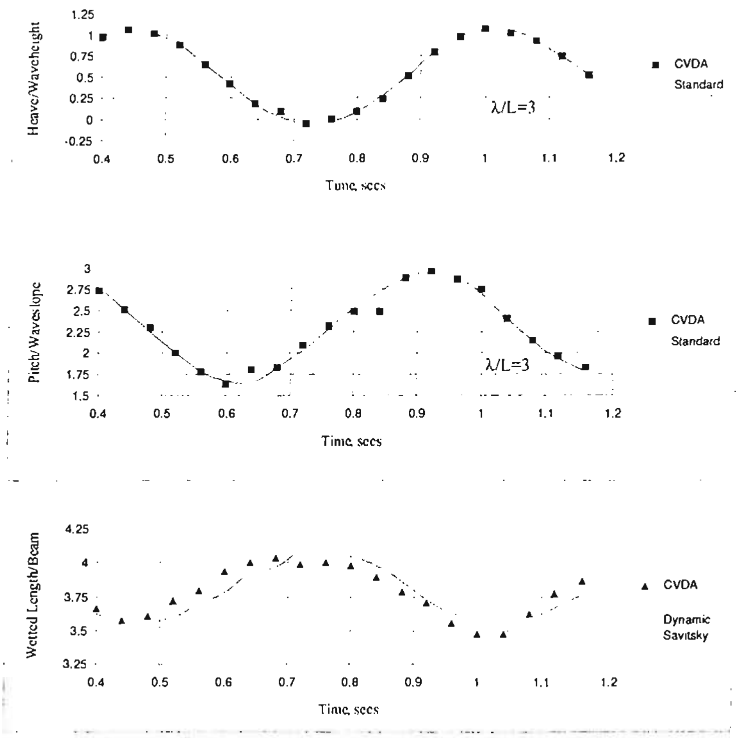

Figure A.143: Comparison between Computer Vision Data Acquisition and Standard Instrumentation
$V/\sqrt{L} = 4$, $\beta = 30^\circ$, $C_\Delta = 0.608$, $L/B = 5$, $H/B = 0.111$, $\lambda/L = 3$

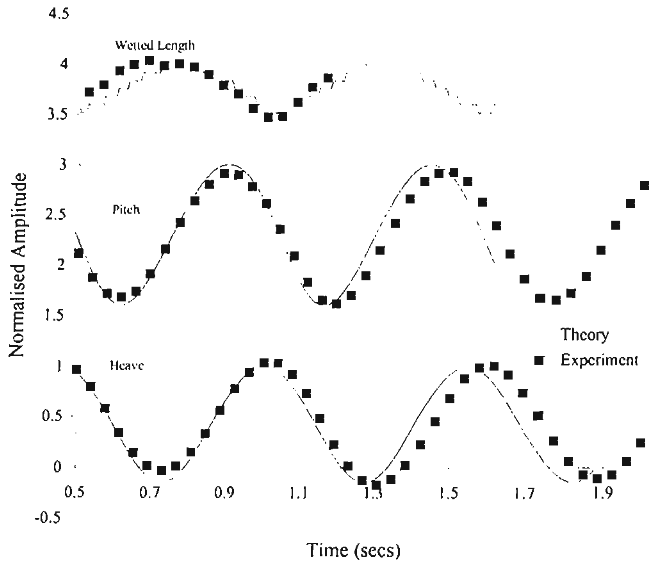

Figure A.144: Comparison between Experiment and Theory
$V/\sqrt{L} = 4$, $\beta = 30^\circ$, $C_\Delta = 0.608$, $L/B = 5$, $H/B = 0.111$, $\lambda/L = 3$

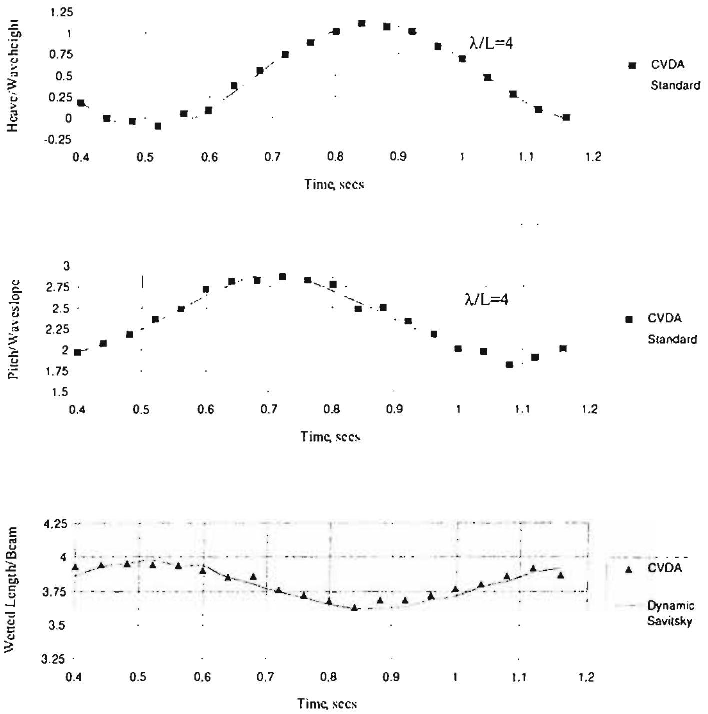

Figure A.145: Comparison between Computer Vision Data Acquisition and Standard Instrumentation
$V/\sqrt{L} = 4$, $\beta = 30°$, $C_\Delta = 0.608$, $L/B = 5$, $H/B = 0.111$, $\lambda/L = 4$

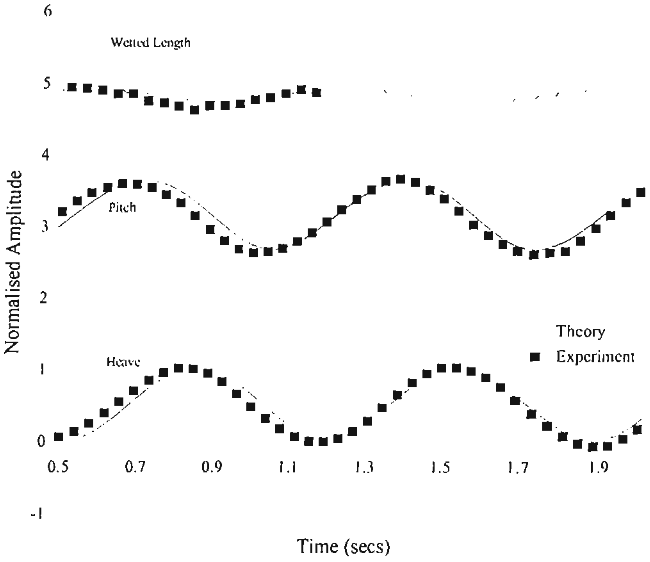

Figure A.146: Comparison between Experiment and Theory
$V/\sqrt{L} = 4$, $\beta = 30°$, $C_\Delta = 0.608$, $L/B = 5$, $H/B = 0.111$, $\lambda/L = 4$
A value of 2 has been added to all wetted length amplitudes

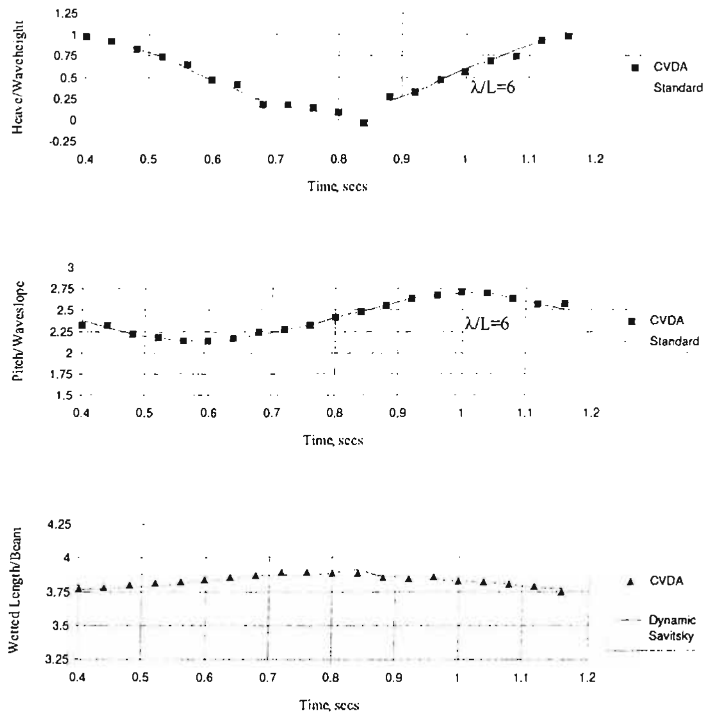

Figure A.147: Comparison between Computer Vision Data Acquisition and Standard Instrumentation
$V/\sqrt{L} = 4$, $\beta = 30°$, $C_\Delta = 0.608$, $L/B = 5$, $H/B = 0.111$, $\lambda/L = 6$

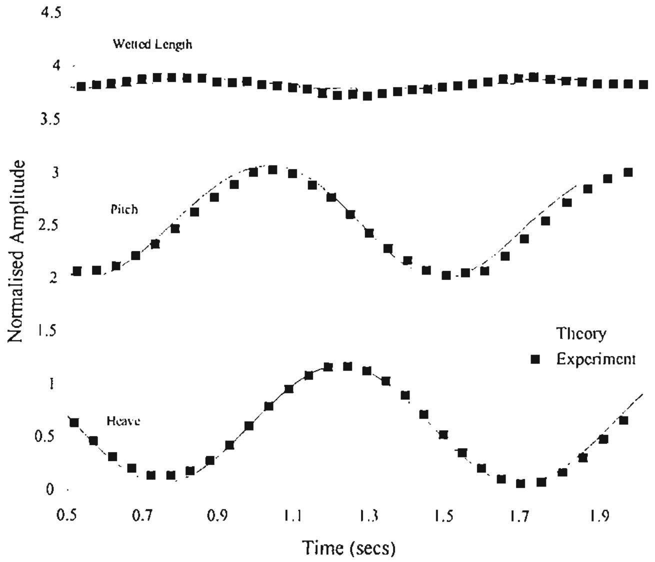

Figure A.148: Comparison between Experiment and Theory
$V/\sqrt{L} = 4$, $\beta = 30°$, $C_\Delta = 0.608$, $L/B = 5$, $H/B = 0.111$, $\lambda/L = 6$

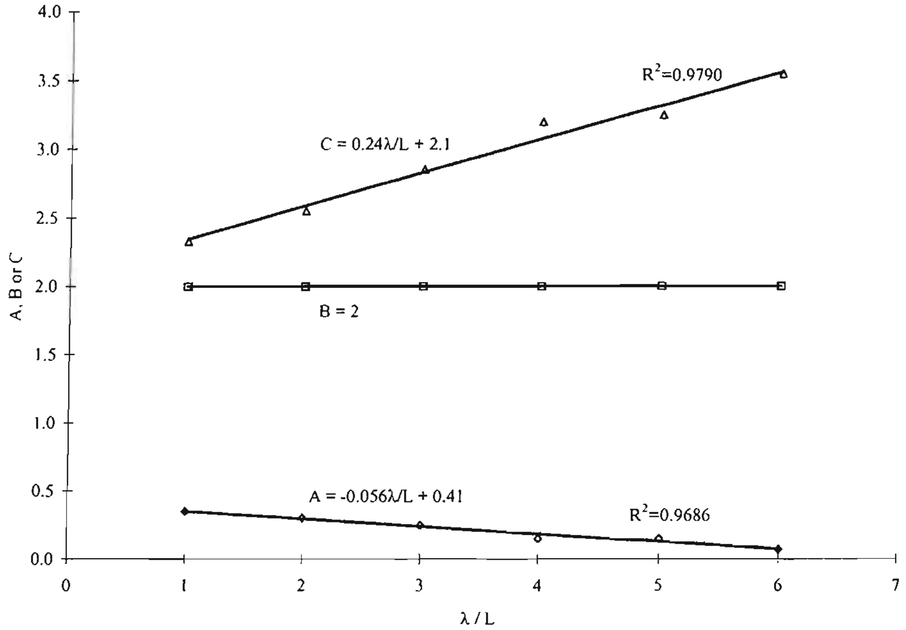

Figure A.149: Behaviour of Fitted Coefficients with Wavelength (Coefficients employed in the dynamic variation of Savitsky's wetted length equation)

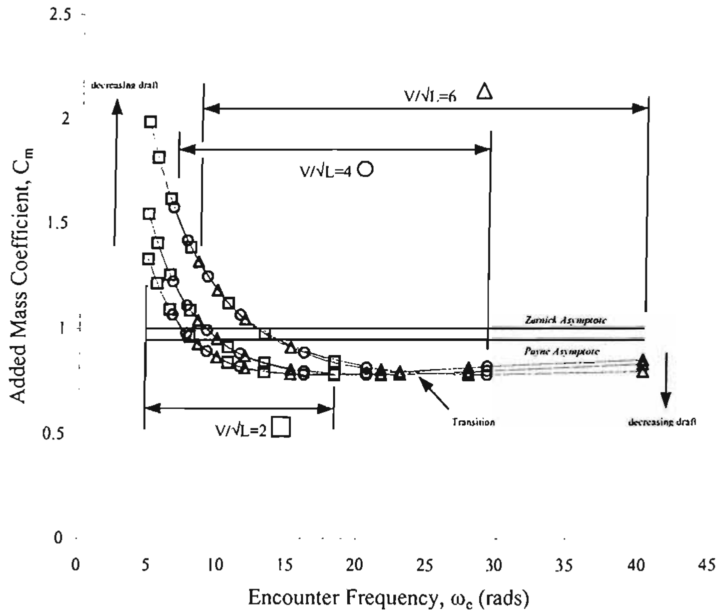

Figure A.150: Added Mass Coefficient versus Frequency and Draft for 10° Deadrise

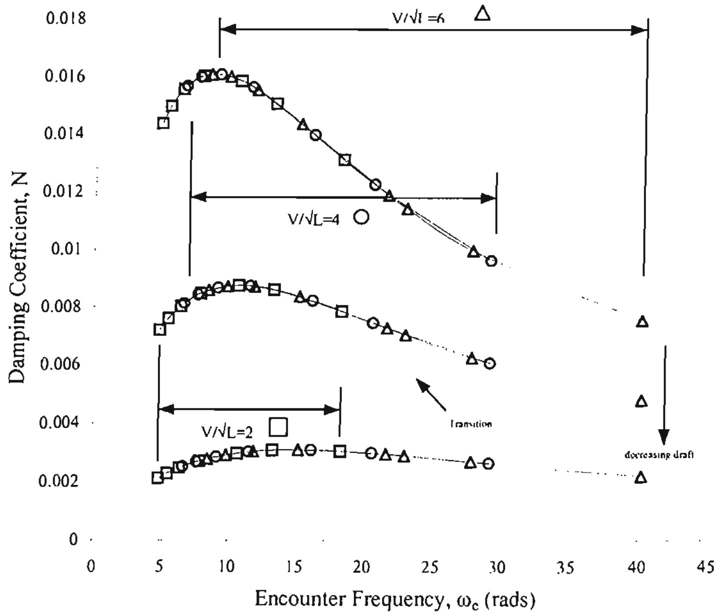

Figure A.151: Damping Coefficient versus Frequency and Draft for 10° Deadrise

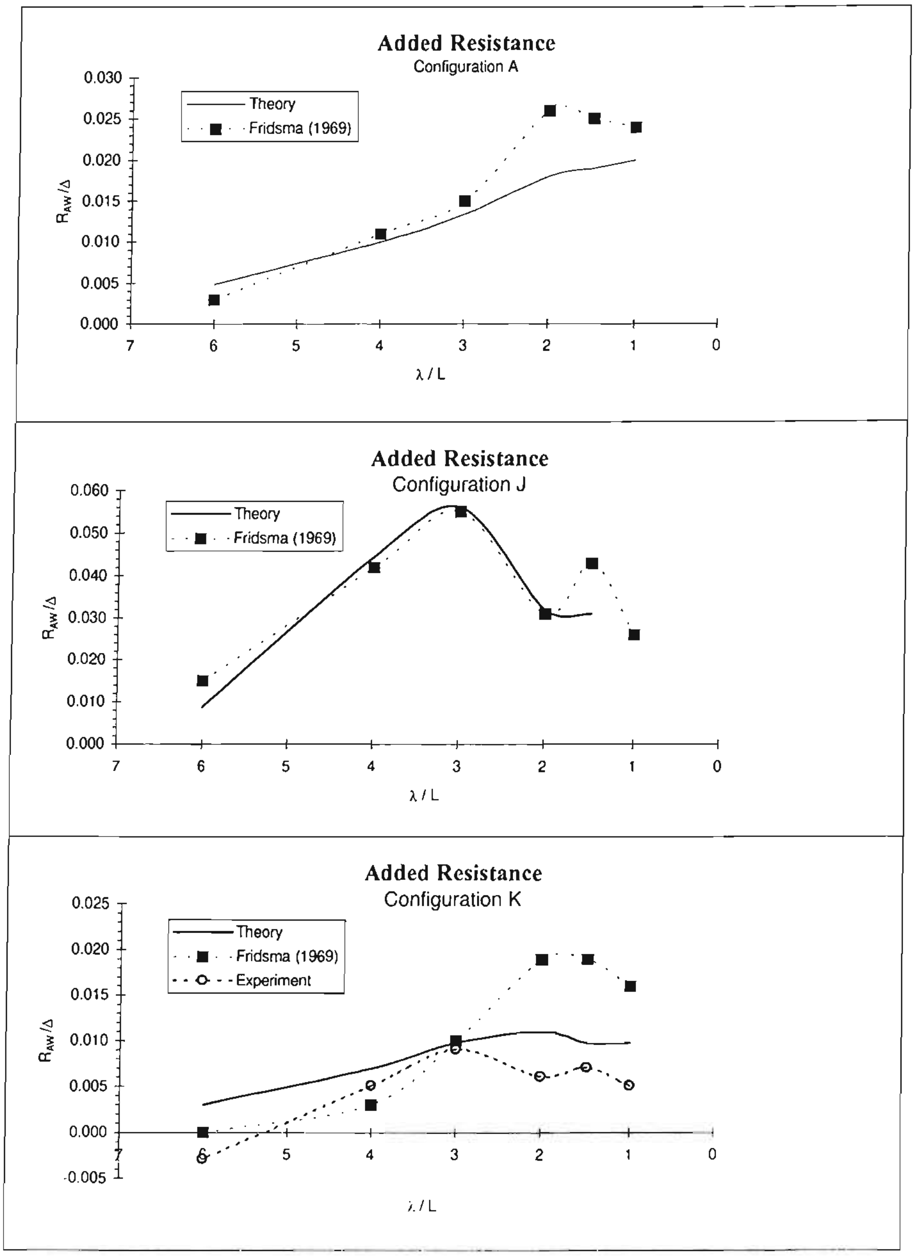

Figure A.152: Experimental (Fridsma (1969)) and Theoretical Added Resistance of Various Craft Configurations

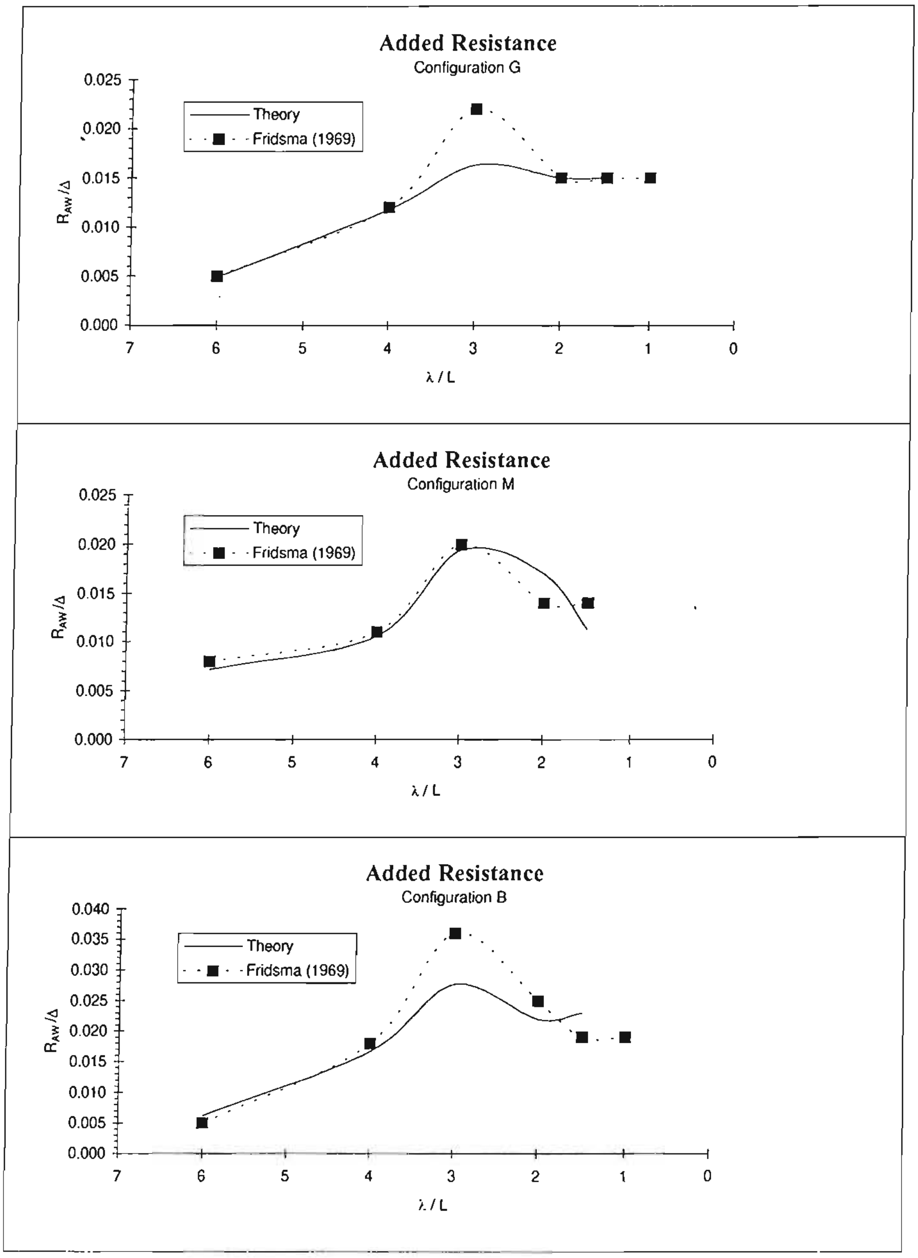

Figure A.153: Experimental (Fridsma (1969)) and Theoretical Added Resistance of Various Craft Configurations

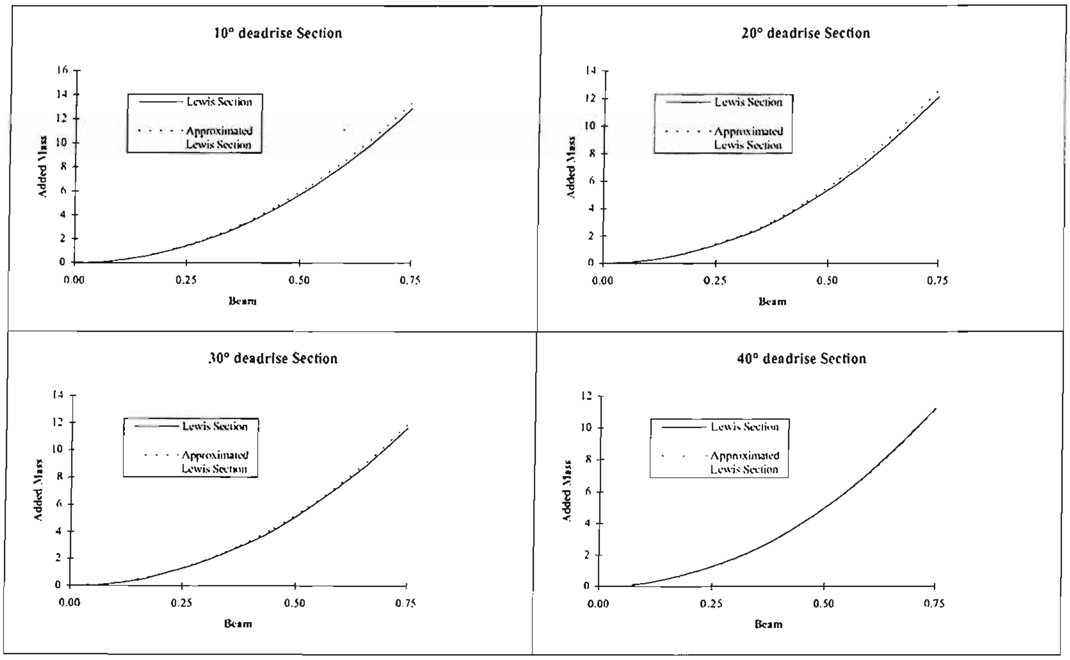

Figure A.154: Added Mass of Lewis Vee-forms (Lewis 1929) and Payne's(1995) $C_m = (1 - \frac{\beta}{2\pi})^2$

Appendix B

Linear Theory for Planing Craft in Waves

B.1 Equations of Motion

The non-dimensional equations of motion for a planing craft in waves are given by,

$$\begin{aligned} (m - Z_{\ddot{z}})\ddot{z} - Z_{\dot{z}}\dot{z} - Z_z z - Z_{\ddot{\theta}}\ddot{\theta} - Z_{\dot{\theta}}\dot{\theta} - Z_\theta\theta &= (Z)_w \, e^{-i\omega_e t} && \text{(B.1)} \\ -M_{\ddot{z}}\ddot{z} - M_{\dot{z}}\dot{z} - M_z z + (I_y - M_{\ddot{\theta}})\ddot{\theta} - M_{\dot{\theta}}\dot{\theta} - M_\theta\theta &= (M)_w \, e^{-i\omega_e t} && \text{(B.2)} \end{aligned}$$

where $(Z)_w$ is the complex amplitude of the wave excitation force and $(M)_w$ is the complex amplitude of the wave excitation moment. The coefficients of the motion variables are the stability derivatives of the craft.

The calm water forces of figure (A.8) are resolved by Martin (1978a) such that the steady-state force and moment equations are as follows. The forces are related to a right-handed body fixed axis system with the origin at the craft centre of gravity and OX positive forwards (parrallel to calm water surface), OY positive to starboard and OZ positive vertically down.

Resolving the forces vertically,

$$W = (F_{DS} + F_{BS})\cos\tau - F_{FS}\sin\tau = -Z_S \qquad \text{(B.3)}$$

where Z_s is the non-dimensional lift component.

Resolving the forces horizontally,

$$T_S = (F_{DS} + F_{BS}) \sin\tau + F_{FS} \cos\tau + F_{WS} = -D_S \tag{B.4}$$

where D_s is the non-dimensional drag component

Summing moments about centre of gravity,

$$M_{WS} + M_{TS} + M_{DS} + M_{BS} + M_{FS} = 0 = M_S \tag{B.5}$$

B.1.1 Determination of Steady State Force and Moment Contributions

B.1.1.1 Hydrodynamic Normal Force, F_D, and Hydrodynamic Moment, M_D

Martin's theory is based upon a strip theory where the flow over the hull is considered to occur in transverse planes which are fixed in space and orientated normal to the keel. The momentum of each layer of water transverse to the keel is $\mu\zeta ds$, where μ is the two-dimensional added mass of the section of the hull at a point s, interacting with the section of the flow plane of length ds, and ζ is the component of the velocity of the body normal to the keel at that point. The coordinate s is measured from the foremost immersed station along the keel. The normal force on the section ds of the hull is the time rate of change of the momentum of the layer of water ds at s,

$$dF_D = \frac{d}{dt}\left(\mu\dot{\zeta}\right) ds \tag{B.6}$$

Both μ and $\dot{\zeta}$ will in general be functions of the longitudinal position coordinate x and time t. The time derivative is therefore,

$$\frac{d}{dt} = -U\frac{\partial}{\partial x} + \frac{\partial}{\partial t} \tag{B.7}$$

where U is the steady state speed.

The normal hydrodynamic force over the entire hull is obtained by integrating equation (B.6) along the wetted length of the hull l_k and multiplying by a correction factor $\phi(\lambda)$

to account for the three-dimensionality of the flow,

$$F_D = \phi\left(\lambda\right) \int_0^{l_k} \frac{d}{dt}\left(\mu\dot{\zeta}\right) ds \tag{B.8}$$

where λ is the mean wetted length to beam ratio. The integral may be expressed as the sum of a velocity term and an acceleration term,

$$F_D = \phi\left(\lambda\right) \left[\int_0^{l_k} \dot{\zeta}\frac{d\mu}{dt} ds + \int_0^{l_k} \mu\frac{d\dot{\zeta}}{dt} ds\right] \tag{B.9}$$

The longitudinal and heave perturbation velocities and accelerations are, respectively, denoted by u, $\dot{u}$, z, $\dot{z}$. The pitch angle perturbations are $\dot{\theta}, \ddot{\theta}$. Martin (1978a) obtained the following relationships,

$$\frac{ds}{dx} = -\cos\tau \tag{B.10}$$

$$\frac{\partial\zeta}{\partial x} = -\sin\tau \tag{B.11}$$

$$\frac{\partial\zeta}{\partial t} = u\sin\tau + \dot{z}\cos\tau - \dot{\theta}\left(a - s\right) \tag{B.12}$$

where τ is the equilibrium trim angle of the boat and a is the value of s at the transverse flow-plane through the boat centre of gravity. From these equations and equation (A.6) we have to the first order in the perturbations,

$$\dot{\zeta} = U\sin\tau + u\sin\tau + \dot{z}\cos\tau - \dot{\theta}\left(a - s\right) \tag{B.13}$$

$$\dot{\zeta} = U\sin\tau + u\sin\tau + \dot{z}\cos\tau - \dot{\theta}\left(a - s\right) \tag{B.14}$$

$$\frac{d\mu}{dt} = \dot{\zeta}\frac{\partial\mu}{\partial\zeta} = \dot{\zeta}\frac{\partial\mu}{\partial s}\cot\tau \tag{B.15}$$

On substituting these equations into equation (B.9), dropping the second order perturbation terms, and integrating, Martin obtained,

$$F_D = F_{DS} + \Delta F_D \tag{B.16}$$

where

$$F_{DS} = \phi\left(\lambda\right)\mu_s U^2 \sin\tau\cos\tau \tag{B.17}$$

$$\begin{aligned}\Delta F_D &= \left(\frac{2F_{DS}}{U}\right)\left(u+\dot{z}\cot\tau+\frac{\dot{\theta}l_g}{\sin\tau}\right)\\ &+\phi\left(\lambda\right)\left[\left(\dot{u}\sin\tau+\ddot{z}\cos\tau\right)\int_0^{l_k}\mu ds-\ddot{\theta}\int_0^{l_k}\mu\left(a-s\right)ds\right]\end{aligned} \tag{B.18}$$

F_{DS} represents the steady state hydrodynamic normal force ΔF_D represents the linearised force contributions from surge, heave and pitch perturbations in velocity and acceleration. Horizontal and vertical components of ΔF_D yield the force stability derivatives.

Similarly, the hydrodynamic moment is obtained by the product of the normal force and moment arm from the centre of gravity, $(a-s)$, such that,

$$M_D=\phi\left(\lambda\right)\int_0^{l_k}(a-s)\frac{d}{dt}\left(\mu\dot{\zeta}\right)ds \tag{B.19}$$

and from similar substitutions to produce F_D, we find,

$$M_D=M_{DS}+\Delta M_D \tag{B.20}$$

where,

$$M_{DS}=\phi\left(\lambda\right)U^2\sin\tau\cos\tau\left[\int_0^{l_k}\mu ds-l_g\mu_s\right] \tag{B.21}$$

$$\begin{aligned}\Delta M_D &= \left(\frac{2M_{DS}}{U}\right)\left(u+\dot{z}\cot\tau\right)\\ &\quad\left(\lambda\right)2U\cos\tau\left[\mu_s l_g^2+\int_0^{l_k}\mu\left(a-s\right)ds\right]\dot{\theta}\\ &\quad+\phi\left(\lambda\right)\left(\dot{u}\sin\tau+\ddot{z}\cos\tau\right)\int_0^{l_k}\mu\left(a-s\right)ds\\ &\quad-\phi\left(\lambda\right)\ddot{\theta}\int_0^{l_k}\mu\left(a-s\right)^2ds\end{aligned} \tag{B.22}$$

Again, the coeffiecients of the perturbation terms are the moment stability derivatives with respect to velocity and acceleration perturbations.

B.1.1.2 Sectional Added Mass Distribution

In order to solve equations (B.16) and (B.20), expressions for sectional added mass need to be derived.

Martin considered the variation of μ with s along the keel length. In order to do this, Martin employed Wagner's (1932) expression for added mass upto chine immersion,

$$\mu = \frac{\rho\pi\zeta^2}{2} f(\beta)^2 \qquad (Wagner 1932) \tag{B.23}$$

where if β is the deadrise angle in radians,

$$f(\beta) = \frac{\pi}{2\beta} - 1 \tag{B.24}$$

and an expression for added mass over the chine,

$$\mu = \frac{\rho\pi b^2}{8}(f(\beta)\tan\beta)^2 + B\frac{\rho}{2}b(\zeta - \zeta_c) \tag{B.25}$$

where B is a function of deadrise and b is the boat beam.

The first term in equation (B.25) comes from the value of added mass at the point of chine immersion where $z = z_c = b/2.\tan\beta$. The second term comes from an estimate of the effect of chine depth based on Schnitzer (1953) and Bobyleff (Lamb 1932) for infinite chine immersion. Martin tried to show that the point of chine immersion is not as obvious as the above equations suggest because of the complexity of the flow. To circumvent this problem, Martin fitted the steady state normal force equation to available steady state data.

Shuford (1958) assumed that the planing hull normal force, F_{DS}, at high speeds was made up of the sum of low aspect ratio wing lift and a crossflow drag term. The resulting expression fitted well with data obtained by many experimenters, enveloping a range of trim angles between 2° and 30°, wetted lengths from 1 to 7 beams and deadrise angles between 0° and 50°,

$$F_{DS} = \frac{1}{2}\rho U^2 S\left[\frac{\pi A}{2(1+A)}\sin\tau\cos\tau\,(1-\sin\beta) + C_{D,c}\sin^2\tau\cos^2\tau\cos\beta\right] \tag{B.26}$$

where $C_{D,c}$ is the crossflow drag coefficient, S is the planform area of the wetted portion of the hull (λb^2) and A is the aspect ratio ($b^2/S = 1/\lambda$)

If s_{c1} decribes the distance s from the point of keel-calm water intersection to the point of effective chine immersion and s_{c2} describes the distance s from the point of keel-calm water intersection to the point at which the effect of chine immersion begins to grow, then from these limits for variation in added mass along the hull length, Martin improved the simple equations (B.23) and (B.25) so that,

$$\mu_a = \begin{cases} \frac{\rho\pi}{2}(f(\beta)s\tan\tau)^2 & 0 < s \le s_{c1} \\ \frac{\rho\pi}{2}(f(\beta)s_{c1}\tan\tau)^2 & s_{c1} < s \le l_k \\ \frac{\rho}{2}Bb\tan\tau(s - s_{c2}) & s_{c2} < s \le l_k \end{cases} \tag{B.27}$$

where $\zeta = s\tan\tau$. The sectional added mass at any section, μ, is therefore the sum of the contributions at that section.

Finally, from equation (B.27), one can write,

$$\mu_s = \frac{\rho\pi}{2}\left(f(\beta)s_{c1}\tan\tau\right)^2 + \frac{\rho}{2}Bb\tan\tau(l_k - s_{c2}) \tag{B.28}$$

so that the steady state hydrodynamic normal force is, from equation (B.17),

$$F_{DS} = \frac{\rho U^2}{2}\left[\phi(\lambda)\pi\left(f(\beta)s_{c1}\tan\tau\right)^2\sin\tau\cos\tau + \phi(\lambda)Bb\sin^2\tau\,(l_k - s_{c2})\right] \tag{B.29}$$

In order to fit Shuford's equation (B.26), Martin showed that they are identical if,

$$\phi(\lambda) = \frac{\lambda}{1+\lambda} = \frac{1}{1+A} \tag{B.30}$$

$$\frac{\rho\pi}{2}\left(f(\beta)s_{c1}\tan\tau\right)^2 = \frac{\rho\pi b^2}{4}(1 - \sin\beta) \tag{B.31}$$

$$\phi(\lambda)B = C_{D,c}\cos^2\tau\cos\beta \tag{B.32}$$

$$l_k - s_{c2} = \lambda b \tag{B.33}$$

By substitution of equations (B.30) to (B.33) into equation (B.29) and non-dimensionalising,

$$F_{DS} = \frac{\lambda}{1+\lambda}\frac{\pi}{2}\sin\tau\cos\tau(1 - \sin\beta) + C_{D,c}\lambda\sin^2\tau\cos^2\tau\cos\beta \tag{B.34}$$

Also, from equation (A.24),

$$\int_0^{l_k}\mu ds = \frac{\rho\pi}{2}\left(f(\beta)s_{c1}\tan\tau\right)^2\left(l_k - \frac{2}{3}s_{c1}\right) + \frac{\rho}{2}Bb\tan\tau\frac{(l_k - s_{c2})^2}{2} \tag{B.35}$$

so, with the aid of equations (B.30) through to (B.33) and equation (B.35) into equation (B.21), the non-dimensional steady state hydrodynamic moment is,

$$\begin{aligned} M_{DS} = {} & \frac{\lambda}{1+\lambda}\frac{\pi}{2}\sin\tau\cos\tau(1 - \sin\beta)(\lambda_k - \tfrac{2}{3}\lambda_{c_1} - \lambda_g) \\ & + C_{D,c}\lambda\sin^2\tau\cos^2\tau\cos\beta\left(\frac{\lambda}{2} - \lambda_g\right) \end{aligned} \tag{B.36}$$

where,

$$\lambda_{c1} = \frac{s_{c1}}{b} \tag{B.37}$$

$$\lambda_{c2} = \frac{s_{c2}}{b} \tag{B.38}$$

$$\lambda_{g} = \frac{l_{g}}{b} \tag{B.39}$$

$$\lambda_{k} = \frac{l_{k}}{b} \tag{B.40}$$

B.1.1.3 Determination of λ_{c1}, λ_{c2}, λ_k

Wagner found that the effective depth of an impacting V-bottom, before chine immersion, is greater by a factor of $\pi/2$ to the depth relative to the calm water free surface. This is because of wave rise on impact.

The equivalent semi-circular section that represents μ_a is defined by an effective radius, c, such that,

$$c = \frac{\pi}{2} s \frac{\tan\tau}{\tan\beta} \tag{B.41}$$

Combined with equation (B.27) for $0 < s < s_{c1}$ gives,

$$\mu_a = \rho \frac{\pi}{2} c^2 \left[\left(1 - \frac{2\beta}{\pi}\right)^2 \frac{\tan^2\beta}{\beta^2} \right] \qquad \text{for} \quad s \leq s_{c1} \tag{B.42}$$

Shuford found that the term in brackets was better at representing the data if it was replaced by $(1 - \sin\beta)$. Substituting into equation (B.42) and equating to equation (B.31) produces the following expression for c,

$$c = \sqrt{2}.(b/2) \qquad \text{for} \quad s = s_{c1} \tag{B.43}$$

Substituting back into equation (B.41) gives,

$$s_{c1} = \frac{\sqrt{2}\tan\beta}{\pi \ \tan\tau} b = \lambda_{c1} b \tag{B.44}$$

Now from extensive photographic evidence obtained by Brown (1971), the mean wetted length to beam ratio can be written as,

$$\lambda = 0.5(\lambda_k + \lambda_c) + 0.03 \tag{B.45}$$

where λ_c, the ratio of wetted length of chine to beam, is,

$$\lambda_c = \lambda_k - (0.57 + 0.001\beta)\left(\frac{\tan\beta}{2\tan\tau} - 0.006\beta\right) \tag{B.46}$$

provided $\lambda_c > 1.0$. The last term in equation (B.45) is due to stagnation line curvature. Since $\lambda_k = \lambda + \lambda_{c2}$ then

$$\lambda_{c2} = 0.5\,(0.57 + 0.001\beta)\left(\frac{\tan\beta}{2\tan\tau} - 0.006\beta\right) - 0.03 \tag{B.47}$$

So all added mass distribution ranges are defined by equations (B.44), (B.46) and (B.47).

B.1.2 Buoyancy Force and Moment

With a high speed craft, there is a phenomenon where the pressure at the transom corner reaches atmospheric pressure and as a result the transom runs dry. This usually only occurs over a speed coefficient, C_V, greater than 0.5. In this case the usually vertically acting buoyancy force is considered to act normal to the keel.

The non-dimensional steady state buoyancy force can be written as,

$$F_{BS} = \frac{\kappa\lambda^2 \sin\tau}{C_V^2} \tag{B.48}$$

where κ is an empirical correction factor to take into account the ventilation effect on the static pressure. Hsu (1967) proposed a value of 0.7 but a value of $\kappa = 0.624$ was found by Brown (1971) to agree better with data.

Assuming that the buoyancy force acts one third of the wetted length from the transom corner, the steady state buoyancy moment can be written as,

$$M_{BS} = F_{BS}\left(\frac{\lambda}{3} - \lambda_g\right) \tag{B.49}$$

B.1.3 Skin Friction

Skin friction is considered to act tangential to the keel and midway between the keel and chine line.

Savtsky (1964) gives it as a function of mean wetted area,

$$F_{FS} = \frac{\lambda C_f}{\cos\beta} \tag{B.50}$$

where C_f is defined as the ITTC value, $C_f = 0.075/(\ln(Rn) - 2)$

The steady state skin friction moment is,

$$M_{FS} = -F_{FS}(\lambda_v - \frac{\tan\beta}{4}) \tag{B.51}$$

B.1.4 Towing and Aerodynamic Forces

The towing and aerodynamic forces are considered to act in a direction parallel to the steady state part of the straight line motion.

The tow force, T_S, is set equal to the drag or sum horizontal component of all the steady state forces. The aerodynamic force, F_{WS}, acting against the tow carriage was measured and non-dimensionalised to give,

$$F'_{WS} = 0.0032$$

The moments about the centre of gravity for tow force and wind force respectively are,

$$M'_{TS} = -T'_S f(k_1, e_1) \tag{B.52}$$

$$M'_{WS} = F'_{WS} f(k_2, e_2) \tag{B.53}$$

where,

$f(k_n, e_n) = (\lambda_{kn} - \lambda_v)\cos\tau + (\lambda_{en} - \lambda_g)\sin\tau$

$\lambda_{k1}, \lambda_{e1}$ = non-dimensional coordinates of the towpoint to transom corner

$\lambda_{k2}, \lambda_{e2}$ = coordinates of the resultant wind force

λ_v = perpendicular distance from the keel to the CG

B.2 Solution of Steady State Forces for Equilibrium

Substitution of equations (B.34), (B.48) and (B.50) into equation (B.3) gives the steady state lift equation,

$$\begin{aligned} W = -Z_S &= \frac{\lambda}{1+\lambda}\frac{\pi}{2}\sin\tau\cos^2\tau(1-\sin\beta) + C_{D,c}\sin^2\tau\cos^3\tau\cos\beta \\ &+\frac{0.624\lambda^2\sin\tau\cos\tau}{C_v^2} - \frac{\lambda C_f}{\cos\beta}\sin\tau \end{aligned} \tag{B.54}$$

which gives, as a cubic equation in λ,

$$D\lambda^3 + (C+D+E)\lambda^2 + (B+C-E-W)\lambda - W = 0 \tag{B.55}$$

where,

$$\begin{aligned} B &= \frac{\lambda}{1+\lambda}\frac{\pi}{2}\sin\tau\cos^2\tau(1-\sin\beta) \\ C &= C_{D,c}\sin^2\tau\cos^3\tau\cos\beta \\ D &= \frac{0.624\sin\tau\cos\tau}{C_v^2} \\ E &= -\frac{C_f\sin\tau}{\cos\beta} \end{aligned}$$

Substitution of equations (B.36), (B.49), (B.51), (B.52) and (B.53) into equation (B.5) gives the overall steady state moment equation,

$$\begin{aligned} M_S &= \frac{\lambda}{1+\lambda}\frac{\pi}{4}\sin 2\tau(1-\sin\beta)(\lambda + h(\tau) - \lambda_g) + C_{D,c}\frac{\lambda}{4}(\sin 2\tau)^2\cos\beta(\frac{\lambda}{2} - \lambda_g) \\ &+\frac{0.624\lambda^2(\frac{\lambda}{3} - \lambda_g)\sin\tau}{C_v^2} - \frac{\lambda(\lambda_v - \frac{\tan\beta}{4})C_f}{\cos\beta} \\ &+(Z_s\tan\tau - \frac{\lambda C_f}{\cos\tau\cos\beta} - F_{WS})f(k_1,e_1) + F_{WS}f(k_2,e_2) \\ &= 0 \end{aligned} \tag{B.56}$$

where,

$$h(\tau) = \lambda_{c2} - \frac{2}{3}\lambda_{c1}$$

Now for a given value of trim angle, τ, we have three solutions for mean wetted length-to-beam ratio, λ, from the cubic equation (B.55). Each of these pairs of λ and τ must be substituted into equation (B.56), for successive values of τ, until $M_S = 0$. When this is satisfied, the trim angle and mean wetted length for the steady state equilibrium are found.

B.3 Stability Derivatives

The stability derivatives are needed to determine the craft's response to force and moment perturbations. The velocity and acceleration stability derivatives are derived from the linearised dynamic normal force and moment perturbations in surge, heave and pitch, namely ΔF_D and ΔM_D.

Resolving ΔF_D vertically and non-dimensionalising (by dividing by $1/2\rho b^2 U^2$),

$$\begin{aligned} \Delta Z_D &= -2F_{DS}\cos\tau\left(u+\dot{z}\cos\tau+\frac{\dot{\theta}\lambda_g}{\sin\tau}\right) \\ &\quad -\phi(\lambda)\left\{\left(\dot{u}\sin\tau\cos\tau+\ddot{z}\cos^2\tau\right)\int_0^{\lambda_k}\mu ds+\ddot{\theta}\int_0^{\lambda_k}\mu(a-s)ds\right\} \end{aligned} \tag{B.57}$$

and resolving ΔF_D horizontally and non-dimensionalising,

$$\Delta X'_D = \Delta Z'_D \tan\tau \tag{B.58}$$

it is possible to derive the stability derivatives such that,

$$X_{\dot{u}} = Z_{\dot{u}}\tan\tau \tag{B.59}$$
$$X_u = Z_u\tan\tau \tag{B.60}$$
$$X_{\ddot{z}} = Z_{\ddot{z}}\tan\tau \tag{B.61}$$
$$X_{\dot{z}} = Z_{\dot{z}}\tan\tau \tag{B.62}$$
$$X_{\ddot{\theta}} = Z_{\ddot{\theta}}\tan\tau \tag{B.63}$$
$$X_{\dot{\theta}} = Z_{\dot{\theta}}\tan\tau \tag{B.64}$$

$$Z_{\dot{u}} = -\phi(\lambda)\sin\tau\cos\tau\int\mu ds \tag{B.65}$$
$$Z_u = -2\phi(\lambda)\mu_s\sin\tau\cos^2\tau \tag{B.66}$$
$$Z_{\ddot{z}} = -\phi(\lambda)\cos^2\tau\int\mu ds \tag{B.67}$$
$$Z_{\dot{z}} = -2\phi(\lambda)\mu_s\cos^3\tau \tag{B.68}$$
$$Z_{\ddot{\theta}} = -\phi(\lambda)\int\mu(a-s)ds \tag{B.69}$$
$$Z_{\dot{\theta}} = -2\phi(\lambda)\mu_s\lambda_g\cos^2\tau \tag{B.70}$$

The stability derivatives from the moment equation (B.22), are obtained in the same manner as,

$$M_{\ddot{u}} = \phi(\lambda)\sin\tau\int\mu(a-s)ds \tag{B.71}$$

$$M_{u} = 2\phi(\lambda)\sin\tau\cos\tau\left(\int\mu ds-\lambda_g\mu_s\right) \tag{B.72}$$

$$M_{\ddot{z}} = \phi(\lambda)\cos\tau\int\mu(a-s)ds \tag{B.73}$$

$$M_{\dot{z}} = 2\phi(\lambda)\cos^2\tau\left(\int\mu ds-\lambda_g\mu_s\right) \tag{B.74}$$

$$M_{\ddot{\theta}} = -\phi(\lambda)\int\mu(a-s)^2ds \tag{B.75}$$

$$M_{\dot{\theta}} = -2\phi(\lambda)\cos\tau\left(\mu_s\lambda_g^2+\int\mu(a-s)ds\right) \tag{B.76}$$

The remaining stability derivatives are the static stability derivatives and can be readily obtained from equations (B.54) and (B.56). Since for a given deadrise, these equations are functions only of λ and τ, it can be written that,

$$Z_z = \frac{\partial Z}{\partial z} = \frac{\partial Z_s}{\partial\lambda}\frac{\partial\lambda}{\partial z} \tag{B.77}$$

$$X_z = \frac{\partial X}{\partial z} = \frac{\partial X_s}{\partial\lambda}\frac{\partial\lambda}{\partial x} \tag{B.78}$$

$$M_z = \frac{\partial M}{\partial z} = \frac{\partial M_s}{\partial\lambda}\frac{\partial\lambda}{\partial z} \tag{B.79}$$

$$Z_\theta = \frac{\partial Z}{\partial\theta} = \frac{\partial Z_s}{\partial\tau}+\frac{\partial Z_s}{\partial\lambda}\frac{\partial\lambda}{\partial\tau} \tag{B.80}$$

$$X_\theta = \frac{\partial X}{\partial\theta} = \frac{\partial X_s}{\partial\tau}+\frac{\partial X_s}{\partial\lambda}\frac{\partial\lambda}{\partial\tau} \tag{B.81}$$

$$M_\theta = \frac{\partial M}{\partial\theta} = \frac{\partial M_s}{\partial\tau}+\frac{\partial M_s}{\partial\lambda}\frac{\partial\lambda}{\partial\tau} \tag{B.82}$$

where,

$$\begin{aligned}
\frac{\partial Z_s}{\partial \lambda} &= -G\sin\tau\left(\frac{\cos\tau}{1+\lambda}\right)^2 - H\sin^2\tau\cos^3\tau - 2J\sin\tau\cos\tau\lambda + C_f\frac{\sin\tau}{\cos\beta} && \text{(B.83)}\\
\frac{\partial Z_s}{\partial \tau} &= -G\frac{\lambda}{1+\lambda}\left(\cos^3\tau - 2\sin^2\tau\cos\tau\right) - H\lambda\left(2\sin\tau\cos^4\tau - 3\sin^3\tau\cos^2\tau\right)\\
&\quad -2J\lambda^2\cos 2\tau + C_f\lambda\frac{\cos\tau}{\cos\beta} && \text{(B.84)}\\
\frac{\partial X_s}{\partial \lambda} &= \frac{\partial Z_s}{\partial \lambda}\tan\tau + \frac{\partial F_{FS}}{\partial \lambda}\frac{1}{\cos\tau} \approx \frac{\partial Z_s}{\partial \lambda}\tan\tau && \text{(B.85)}\\
\frac{\partial X_s}{\partial \tau} &= \frac{\partial Z_s}{\partial \tau}\tan\tau + \frac{Z_s}{\cos^2\tau} + \frac{F_{FS}\tan\tau}{\cos\tau} \approx \frac{\partial Z_s}{\partial \tau}\tan\tau + \frac{Z_s}{\cos^2\tau} && \text{(B.86)}\\
\frac{\partial M_s}{\partial \lambda} &= G\sin\tau\cos\tau\left[\left(\frac{1}{1+\lambda}\right)^2(\lambda + h(\tau) - \lambda_g) + \frac{\lambda}{1+\lambda}\right]\\
&\quad +H\sin^2\tau\cos^2\tau\,(\lambda - \lambda_g) + J\sin\tau\lambda\,(\lambda - 2\lambda_g)\\
&\quad +\frac{C_f}{\cos\beta}\left(\frac{\tan\beta}{4} - \lambda_v\right) + \left(\frac{\partial Z_s}{\partial \lambda}\tan\tau - \frac{C_f}{\cos\tau\cos\beta}\right) f(k_1, e_1) && \text{(B.87)}
\end{aligned}$$

$$\begin{aligned}
\frac{\partial M_s}{\partial \tau} &= G\frac{\lambda}{1+\lambda}\left[\cos 2\tau\,(\lambda + h(\tau) - \lambda_g) + (0.157 - 0.00025\beta)\frac{\tan\beta}{\tan\tau}\right]\\
&\quad +H\lambda\left(\frac{\lambda}{2} - \lambda_g\right)\sin 2\tau\cos 2\tau + J\lambda^2\left(\frac{\lambda}{3} - \lambda_g\right)\cos\tau\\
&\quad +\left(\frac{\partial Z_s}{\partial \tau}\tan\tau + \frac{Z_s}{\cos^2\tau} - \frac{C_f\lambda\tan\tau}{\cos\tau\cos\beta}\right) f(k_1, e_1)\\
&\quad -\left(Z_s\tan\tau - \frac{C_f\lambda}{\cos\tau\cos\beta} - F_{WS}\right) g(k_1, e_1) - F_{WS}\,g(k_2, e_2) && \text{(B.88)}
\end{aligned}$$

where,

$$g(k_n, e_n) = (\lambda_{kn} - \lambda_v)\sin\tau - (\lambda_{en} - \lambda_g)\cos\tau$$

$$\begin{aligned}
G &= \frac{\pi(1-\sin\beta)}{2} && \text{(B.89)}\\
H &= C_{D,c}\cos\beta && \text{(B.90)}\\
J &= \frac{0.624}{C_V^2} && \text{(B.91)}
\end{aligned}$$

Also

$$\begin{aligned}
\frac{\partial \lambda}{\partial z} &= \frac{1}{\sin\tau} && \text{(B.92)}\\
\frac{\partial \lambda}{\partial \tau} &= -\left(\frac{\lambda_k - \lambda_g}{\tan\tau} + \lambda_v\right) + (0.57 + 0.001\beta)\frac{\tan\beta}{4\sin^2\tau} && \text{(B.93)}
\end{aligned}$$

B.4 Hydrodynamic Normal Force and Moment in Waves

The method for deriving the hydrodynamic normal force and moment has already been discussed in section B.1.1.1 which leads to,

$$F_D = \phi(\lambda)\left[\int_0^{l_k} \dot{\zeta}\frac{d\mu}{dt}ds + \int_0^{l_k} \mu\frac{d\dot{\zeta}}{dt}ds\right] \tag{B.94}$$

for the hydrodunamic normal force and,

$$M_D = \phi(\lambda)\int_0^{l_k} (a-s)\frac{d}{dt}\left(\mu\dot{\zeta}\right) ds \tag{B.95}$$

for the hydrodynamic moment. In calm water, the derivatives for ζ are given (equations (B.13) and (B.14)). However, in waves there will be an added component, ζ_w, so that,

$$\zeta = s\tan\tau + \zeta_w \tag{B.96}$$

and,

$$\begin{aligned} \dot{\zeta} &= U\sin\tau + \dot{\zeta}_w && \text{(B.97)} \\ \ddot{\zeta} &= \ddot{\zeta}_w && \text{(B.98)} \end{aligned}$$

since,

$$\frac{\partial s}{\partial x} = -\cos\tau$$

Now the sectional distribution of added mass must allow for the variation in draught due to wave elevation so that equation (B.27) becomes,

$$\mu_a = \begin{cases} \frac{\rho\pi}{2}f(\beta)^2(s\tan\tau+\zeta_w)^2 & 0 < s \leq s_{c1} \\ \frac{\rho\pi}{2}f(\beta)^2(s_{c1}\tan\tau+\zeta_w)^2 & s_{c1} < s \leq l_k \\ \frac{\rho}{2}Bb\tan\tau(s-s_{c2}) & s_{c2} < s \leq l_k \end{cases} \tag{B.99}$$

Substitution of equations (B.99), (B.98) and (B.96) into (B.9) and discarding second order terms in the wave disturbance gives,

$$F_D = F_1 + F_2 + F_3 + F_4 + F_5 \tag{B.100}$$

where,

$$F_1 = \phi(\lambda)\rho\pi f(\beta)^2 U^2 \sin^2\tau \int_0^{s_{c1}} (s\tan\tau + \zeta_w)\, ds \quad \text{(B.101)}$$

$$F_2 = 2\phi(\lambda)\rho\pi f(\beta)^2 U \sin\tau \tan\tau \int_0^{s_{c1}} s\dot{\zeta}_w ds \quad \text{(B.102)}$$

$$F_3 = \phi(\lambda) Bb\rho U \sin\tau \int_{s_{c2}}^{l_k} \dot{\zeta}_w ds \quad \text{(B.103)}$$

$$F_4 = \phi(\lambda) Bb\frac{\rho}{2} U^2 \sin^2\tau \int_{s_{c2}}^{l_k} ds \quad \text{(B.104)}$$

$$F_5 = \phi(\lambda) \int_0^{l_k} \mu\ddot{\zeta}_w ds \quad \text{(B.105)}$$

By multiplying each of these forces by a moment arm $(a-s)$, the hydrodynamic moment about the centre of gravity is,

$$M_D = M_1 + M_2 + M_3 + M_4 + M_5 \quad \text{(B.106)}$$

where,

$$M_1 = \phi(\lambda)\rho\pi f(\beta)^2 U^2 \sin^2\tau \int_0^{s_{c1}} (s\tan\tau + \zeta_w)(a-s) ds \quad \text{(B.107)}$$

$$M_2 = 2\phi(\lambda)\rho\pi f(\beta)^2 U \sin\tau \tan\tau \int_0^{s_{c1}} s(a-s)\dot{\zeta}_w ds \quad \text{(B.108)}$$

$$M_3 = \phi(\lambda) Bb\rho U \sin\tau \int_{s_{c2}}^{l_k} (a-s)\dot{\zeta}_w ds \quad \text{(B.109)}$$

$$M_4 = \phi(\lambda) Bb\frac{\rho}{2} U^2 \sin^2\tau \int_{s_{c2}}^{l_k} (a-s) ds \quad \text{(B.110)}$$

$$M_5 = \phi(\lambda) \int_0^{l_k} (a-s)\mu\ddot{\zeta}_w ds \quad \text{(B.111)}$$

$$\text{(B.112)}$$

B.4.1 Relative Fluid Displacement, Velocity and Acceleration

To determine the hydrodynamic force and moment equations, expressions are required for the contribution to section immersion from the waves, ζ_w, and its derivatives.

Let ϕ_w represent the velocity potential of a deep water wave such that,

$$\phi_w = ihce^{-kz}.e^{ik[x\cos\beta_h + y\sin\beta_h + (U\cos\beta_h - c)t]} \quad \text{(B.113)}$$

where,

β_h = angle of wave crests from boat x-axis;
$\beta_h = 0$ and π in head and following seas respectively
h = wave amplitude, waveheight/2
c = wave celerity
k = $2\pi/L_w$wavenumber
L_w = wavelength
t = time

In head and following seas only, ϕ_w reduces to,

$$\phi_w = ihce^{-kz}.e^{\mp ik[x+(U\pm c)t]} \tag{B.114}$$

The upper sign refers to head seas and the lower to following seas.

Encounter frequency, ω_e, is,

$$\omega_e = k\,(U \pm c) \tag{B.115}$$

The wave elevation $\eta(x,t)$ is,

$$\eta(x,t) = \frac{1}{g}\left(\frac{d\,(\phi_w)}{dt}\right)_{z=0} = he^{\mp i(kx+\omega_e t)} \tag{B.116}$$

since $c^2 = g/k$.

The horizontal and vertical components of the orbital velocity are given respectively by,

$$v_w = -\frac{\partial\,(\phi_w)}{\partial x} = \mp\omega he^{-kz}e^{\mp i(kx+\omega_e t)} \tag{B.117}$$

$$w_w = -\frac{\partial\,(\phi_w)}{\partial z} = i\omega he^{-kz}e^{\mp i(kx+\omega_e t)} \tag{B.118}$$

where the circular frequency of the orbital motion is $\omega = kc$. Taking the sum of the vertical components of wave orbital velocity,

$$\dot{\zeta}_w = -v_w \sin\tau - w_w \cos\tau \tag{B.119}$$

$$\Rightarrow \quad \dot{\zeta}_w = -i\omega he^{-kz}e^{\mp(kx-\tau+\omega_e t)} \tag{B.120}$$

The contibution to immersion from the wave can now be written as,

$$\zeta_w = \eta e^{\pm i\tau} \tag{B.121}$$

Using equation (B.7) and differentiating equation (B.120),

$$\ddot{\zeta}_w = -\omega^2 h e^{-kz} e^{\mp i(kx-\tau+\omega_e t)} \tag{B.122}$$

B.5 Normal Force and Moment Due to Ambient Pressure

The force due to local pressure effects, namely buoyancy and wave perturbation pressure can be written as,

$$F_p = \int_0^{l_k} \rho \left[gz + \frac{d(\phi_w)}{dt} \right] ds \tag{B.123}$$

The first term is due to buoyancy and can be evaluated from equation (B.48). The second term is from the wave perturbation pressure and can be evaluated from equation (B.114).

Assuming that the buoyancy force acts one-third of the mean wetted length forward of the transom corner gives good agreement with experimental data (Brown 1971). The moment can therefore be written as,

$$M_p = \int_0^{l_k} \rho \left[gz + \frac{d(\phi_w)}{dt} \right] \left(\frac{l_k}{3} - l_g \right) ds \tag{B.124}$$

B.6 Wave Excitation Force and Moment

From equations (B.2), the wave excitation force can now be represented by the sum of the separate force contributions, namely equations (B.105) and (B.123) such that,

$$(Z)_w e^{\mp i\omega_e t} = F_D + F_P - F_{BS} - F_{DS} \tag{B.125}$$

F_{BS} and F_{DS} are subtracted because of the interest only in the motions about the steady-state equilibrium condition.

Likewise, the wave excitation moment can be written as

$$(M)_w e^{\mp i\omega_e t} = M_D + M_P - M_{BS} - M_{DS} \tag{B.126}$$

B.7 Solution of the Equations of Motion

The equations of motion can now be solved. The solution to equations (B.2) is a steady state simple harmonic motion in the perturbations.

Let,

$$z = z_0 e^{\mp i\omega_e t} \tag{B.127}$$

$$\theta = \theta_0 e^{\mp i\omega_e t} \tag{B.128}$$

Substituting the above equations and their derivatives into equations (B.2) gives,

$$\begin{gathered} \left[(Z_{\ddot{z}} - m)\,\omega_e^2 - Z_z \pm iZ_{\dot{z}}\omega_e\right] z_0 + \left[Z_{\ddot{\theta}}\omega_e^2 - Z_\theta \pm iZ_{\dot{\theta}}\omega_e\right]\theta_0 = (Z)_w \\ \left[M_{\ddot{z}}\omega_e^2 - M_z \pm iM_{\dot{z}}\omega_e\right] z_0 + \left[(M_{\ddot{\theta}} - I_y)\,\omega_e^2 - M_\theta \pm iM_{\dot{\theta}}\omega_e\right]\theta_0 = (M)_w \end{gathered} \tag{B.129}$$

The surge equation has been omitted because of its insignificance, but the inclusion can be readily done. Surge has been shown by a number of authors and experimenters, e.g. Fridsma (1969) to be insignificant; the difference between "constant-velocity" tests and "constant-thrust" tests being negligible.

The solutions to equations (B.129) give the complex amplitude of the boat motions,

$$z_0 = z_R + iz_I = |z_o|\, e^{i\alpha_z} \tag{B.130}$$

$$\theta_0 = \theta_R + i\theta_I = |\theta_o|\, e^{i\alpha_\theta} \tag{B.131}$$

Subscripts R and I refer to real and imaginary parts.

The displacement amplitudes and phase angles are given as,

$$|z_o| = \sqrt{z_R^2 + z_I^2} \qquad \alpha_z = \tan^{-1}\left(\frac{z_I}{z_R}\right) \tag{B.132}$$

$$|\theta_o| = \sqrt{\theta_R^2 + \theta_I^2} \qquad \alpha_z = \tan^{-1}\left(\frac{\theta_I}{\theta_R}\right) \tag{B.133}$$

Nomenclature

a	value of s at transverse plane through boat centre of gravity (CG)
B	Bobyleff's function of deadrise
b	beam of boat
$C_{D,c}$	cross flow drag coefficient
C_f	hydrodynamic friction coefficient
C_{lb}	boat lift coefficient non-dimensionalised by beam, $2C_Delta/C_V^2$
C_V	speed coefficient, $U/\sqrt{gb}$
C_Δ	load coefficient, $\Delta/\rho g b^3$
C_λ	modified version of wavenumber
$C_{\lambda R}$	value of C_λ at resonant encounter frequency
c	wave celerity
F_{BS}	steady-state buoyancy force (equal to F_B in figure (A.8))
F_D	dynamic part of hydrodynamic normal force on hull
F_{DS}	steady state part of F_D (equal to R in figure (A.8))
F_{FS}	frictional force parrallel to keel (equal to F_D in figure (A.8))
$(F_h)_w$	normal force due to wave elevation
$(F_p)_w$	force on hull due to perturbation pressure from wave
$(F_1)_w$	normal force due to slope of wave
$(F_2)_w$	normal force due to wave orbital velocity
$(F_5)_w$	normal force due to wave orbital acceleration
$f(\beta)$	deadrise function of Wagner
g	acceleration due to gravity
H	wave height, $2h$
h	wave amplitude
I_y	pitch moment of inertia about CG
k	wavenumber, $2\pi/L_w$
k_o	modified wavenumber
k_y	radius of gyration
LCG	distance from transom to longitudinal CG, measured parallel to keel
L_w	wavelength
l	overall length of boat (m)

l_g	*LCG*
l_k	length of wetted portion of keel
l_m	mean wetted length of hull
M	hydrodynamic pitch moment relative to CG
M_{BS}	steady-state pitch moment due to buoyancy
M_D	dynamic part of hydrodynamic pitch moment
M_{DS}	steady state part of M_D
M_S	total steady state pitch moment
M_z, M_θ, M_u, etc	partial derivative of pitch moment with respect to motion variables z, θ, u etc, respectively
$(M_h)_w$	pitching moment due to wave elevation
$(M_1)_w$	pitching moment due to wave slope
$(M_2)_w$	pitching moment due to wave orbital velocity
$(M_5)_w$	pitching moment due to wave orbital accn
RAO	response amplitude operator
s	coordinate measured along keel from foremost immersed station of keel
s_c1	see equation (A.37)
s_c2	see equation (A.40)
t	time
U	steady reference speed of boat, ms-1
u, $\dot{u}$, $\ddot{u}$	perturbation in surge displacement, velocity and accelaration
V_k	steady reference speed of boat, knots
W	boat weight
X	hydrodynamic force component in direction of positive x
X_D	dynamic part of hydrodynamic X-force
X_S	steady state part of X
X_u, X_z, X_θ, etc	partial derivative of pitch moment with respect to motion variables u, z, θ, etc, respectively
x	horizontal coordinate in direction of U
x_b	horizontal distance from CG to formost immersed point on keel, where s=0
x_{c1}	$s_{c1}/\cos\tau$
x_d	see equation ( )
Z	hydrodynamic force component in direction of postive z
Z_D	dynamic part of hydrodynamic Z-force
Z_S	steady state part of Z
Z_z, Z_θ, Z_u, etc	partial derivative of pitch moment with respect to motion variables z, θ, u etc, respectively
z	vertical coordinate, postive down; perturbation in heave at CG
$\lvert Z'_o \rvert$	non-dimensional amplitude of vertical displacement of CG from steady calm water position

α_x, α_z, α_θ	phase angle of surge, heave and pitch motion, respectively, with respect to wave height
β	deadrise angle
β_h	wave heading angle
Δ	boat weight in kg
$\dot{\zeta}$, $\ddot{\zeta}$	components, normal to keel, of relative velocity and acceleration, respectively
θ	pitch angle perturbation, positive bow up
$\lvert\theta_o\rvert$	amplitude of boat pitch angle perturbation from steady, calm water trim angle, in radians
λ	mean wetted length to beam ratio
λ_c	length of wetted chine to beam ratio
λ_{c1}	non-dimensional value of s_{c1}, s_{c1}/b
λ_{c2}	non-dimensional value of s_{c2}, s_{c2}/b
λ_g	non-dimensional value of LCG, LCG/b
λ_k	non-dimensional value of l_k, l_k/b
μ	total sectional added mass
μ_a	contribution to sectional added mass
μ_s	sectional added mass at the transom
ν	kinematic viscosity of water
ξ	boat damping ratio
ρ	density of water
σ	stability root
σ_I	imaginary part of σ
σ_R	real part of σ
τ	steady state trim angle measured from keel line to calm water free surface at reference speed U (equal to θ in figure (A.8))
τ_c	calculated value of τ
τ_w	average wave slope near bow
$\phi(\lambda)$	three-dimensional or aspect ratio correction factor
ω	circular frequency of waves
ω_e	circular encounter frequency with waves

Appendix C

Added Mass and Damping Coefficient

C.1 Introduction

The accurate solution of the governing equations of motion are very much dependent on the accurate evaluation of the hydrodynamic coefficients. The hydrodynamic coefficients themselves require the evaluation of the added mass terms.

As a body oscillates within or on a fluid, the fluid velocities adjacent to the body changes. The additional force required to accelerate this fluid is obtained by consideration of an appropriate increase in apparent mass of the body, added mass. For a ship-shape section oscillating in the free surface, it is a quantity that is dependent on the wetted surface area and the frequency at which it oscillates (Ursell 1949).

The sectional damping coefficient is a measure of the section's ability to dissipate energy. As the section oscillates in the free surface, waves are generated that radiate outwards, the amplitude of these generated waves in comparison with the amplitude of the heaving motion determine the value of sectional damping.

In linear frequency domain analyses where oscillations are typically small, the added mass and damping coefficients can be considered to be independent of time. For planing hulls undergoing large motions in waves this is obviously an over simplification. The wetted surface area is constantly changing and as a result the solution of the equations of motion need to be solved in a time-domain fashion.

C.2 Multi-parameter Conformal Mapping, $N > 2$

Ship-shape sectional added mass and damping coefficient are derived from the known hydrodynamic coefficients of a semi-circular section of unit radius oscillating in a fluid at infinite depth. Lewis (1929) mapped the semi-circular section into a ship section by the use of a conformal transformation:

$$\begin{aligned} z &= x + iy \\ &= a\left(\zeta + a_1\zeta^{-1} + a_3\zeta^{-3}\right) \end{aligned}$$

where $\zeta = ie^{-i\theta}$ describes the semi-circle which is mapped into the ship section described by the co-ordinates (x, y) in the z-plane and a is a scale factor having the dimension of length. The coefficients a_1 and a_3 are constants which must be determined for a given section. The family of forms produced by this transformation are commonly called 'Lewis forms'. This is effectively a 2-parameter transformation since the section is defined by two coefficients, as a result the Lewis forms, whilst convenient to apply, limited in application to those of more simple shape.

Typically, added mass for planing craft is evaluated using a Lewis method (Payne 1988), thereby neglecting the influence of the free surface and treating the hull section to be oscillating at an infinite frequency. This is not necessarily inappropriate provided that on treatment of the planing hull in waves, the underwater section is not complex in shape and the encounter frequency of the waves is high. But what if these assumptions cannot be made?

Bishop et al (1978) provide a concise summary and comprehensive reference list of the development of conformal transformation theory. They also demonstrate a multi-parameter technique that provides added mass and damping coefficients for more complex hull forms, which will be briefly described later. The benefits of applying this multi- parameter method is that discontinuities possibly associated with planing hull underwater shape, such as spray rails and stepped hull forms, can be included in the evaluation of hydrodynamic coefficients which may also be frequency dependent.

C.3 Lewis Added Mass Approximation, $N = 2$

From Bishop and Price(1974), consider an infinitely long circular cylinder of diameter B moving in a direction perpendicular to its axis in an infinite, incompressible, inviscid liquid of density ρ which is at rest at infinity. Let the velocity of the cylinder at any instant be U, so that the kinetic energy per unit length is $mU^2/2$. Now as the cylinder moves it displaces liquid particles such that they are moved "astern". The liquid thus acquires kinetic energy that at any instant in time, per unit length, is given as $\rho\pi B^2U^2/8$. Thus the total kinetic energy per unit length of the cylinder is given by:

$$\frac{(m + m_a)U^2}{2} = \frac{mU^2}{2} + \frac{\rho\pi B^2U^2}{8} \tag{C.1}$$

where

m = mass per unit length of cylinder

m_a = mass of displaced liquid from unit length of cylinder.

In order to determine the magnitude of an external force F acting on the cylinder in the direction of U, and assuming no change in potential energy, we can write:

$$FU = d(mU^2/2 + maU^2/2)/dt \tag{C.2}$$

$$\text{so that } F = (m + m_a)U$$

The kinetic energy method for a moving cylinder can now be compared to the potential flow method around an accelerating cylinder such that the two coefficients C_v and C_h for a ship floating at a free surface can be found, where

$$C_{m,h} = \frac{\text{(added mass per unit length of body in 2D flow)}}{\text{(added mass per unit length of comparable cylinder)}} \tag{C.3}$$

and C_m is the coefficient for vertical motions (symmetric motions of heave, surge and pitch) C_h is the coefficient for horizontal motions (asymmetric motions of sway, roll and yaw)

hence

$$\begin{aligned} C_m &= m_a/(\pi\rho B^2/8) \\ C_h &= m_{ah}/(\pi\rho T^2/2) \end{aligned}$$

where B = sectional beam, T = sectional draught and m_{ah} is added mass in the horizontal plane.

Lewis assumed that the flow around a circular cylinder floating half immersed in the water surface is identical to that around a deeply submerged cylinder. By conformal transformation of an infinitely long ship section half submerged in an infinite depth fluid, oscillating at high frequency, to that of a deeply submerged cylinder of unit radius, he could determine the added mass. The conformal transformation used is:

$$\kappa = \xi + i\nu = \eta + a_1/\eta + a_3/\eta^3 \tag{C.4}$$

where $\eta = e^{i\theta}$ describes the cross section of the original half immersed circular cylinder of unit radius which is in effect mapped onto the ship shaped equivalent section described by the co-ordinates (ξ, ν). The coefficients a_1 and a_3 depend on the geometry of the section. [A more general conformal transformation leads to the Tasai-Porter close fit method and is given by:

$$\kappa = \sum a_{2p-1}.\eta^{-(2p-1)}$$

where the values of a_{2p-1} are the transformation variables and $a_{-1} = 1$. For the Lewis method $N = 2$, in the Tasai-Porter method N is varied to give the appropriate accuracy.]

Substitution of $\eta = e^{\imath\beta} = \cos\beta + \imath\sin\theta$ leads to

$$\begin{aligned}
\kappa &= e^{\imath\beta} + a_1 e^{-\imath\beta} + a_3 e^{-3\imath\beta} \\
&= \cos\beta + \imath\sin\beta + a_1\cos\beta - \imath a_1\sin\beta + a_3\cos 3\beta - a_3\sin 3\beta \\
\text{hence} \quad \kappa &= \xi + \imath\nu = (1 + a_1)\cos\beta + a_3\cos 3\beta + \imath[(1 - a_1)\sin\beta - a_3\sin 3\beta] \\
\text{therefore} \quad x &= (1 + a_1)\cos\beta + a_3\cos 3\beta \\
\text{and} \quad \nu &= (1 - a_1)\sin\beta - a_3\sin 3\beta
\end{aligned}$$

Now we know that when $\beta = 0$, $\xi = B/2$ and $\nu = 0$ and $\beta = \pi/2$, $\xi = 0$ and $\nu = 0$ therefore $B/2 = 1 + a_1 + a_3$ and $T = 1 - a_1 + a_3$.

The coefficients a_1 and a_3 are related to the sectional area coefficient σ_s and beam-to-draught ratio λ_s of a ship section such that

$$\begin{aligned}
\sigma_s &= A_x/(BT) = \pi(1 - a_1^2 - 3a_3^2)/4[(1 + a_3)^2 - a_1^2] \\
\lambda_s &= B/T = 2(1 + a_1 + a_3)/(1 - a_1 + a_3)
\end{aligned}$$

Solving these equations simultaneously leads to solutions for a_1 and a_3 such that:

$$a_1 = \left(\frac{E-1}{E+1}\right)(1+a_3)$$

and

$$a_3 = \frac{-C_1+3+\sqrt{9-2C_1}}{C_1}$$

where $E = B/2T$, $(B = 2b)$

and

$$C_1 = \left(3+\frac{4A_x}{\pi BT}\right)+\left(1-\frac{4A_x}{\pi BT}\right)\left(\frac{E-1}{E+1}\right)^2$$

A_x is the sectional area and is given by $2\int_0^{\pi/2}\xi d\nu = \pi/2.(1-a_1^2-3a_3^2)$.

At high frequencies, the potential flow solution for added mass reaches an asymptotic value so, from Bishop and Price (1974), the added mass of a symmetrical sectional hull shape in vertical oscillatory motion given by:

$$m_a = \frac{\pi\rho}{2}\left(1+2a_1+\sum_{p-0}^{N}(2p-1)(a_{2p-1})^2\right)$$

where, for Lewis forms, $N = 2$.

Hence we have

$$C_m = \frac{m_a}{\pi\rho B^2/8} = \frac{[(1+a_1)^2+3a_3^2]}{(1+a_1+a_3)^2} \tag{C.5}$$

Equation (C.5) describes the added mass coefficient from a 2-parameter conformal mapping, valid for infinite encounter frequency. Payne (1995) simplifies this expression for wedge forms into a dependency upon the deadrise angle, β.

$$C_m = (1-\frac{\beta}{2\pi})^2 \tag{C.6}$$

The applicabiity of this is shown in figure (A.154) where it is clear that increasing the deadrise angle increases the accuracy of equation (C.6).

C.4 Frequency Dependency of the Hydrodynamic Coefficients

Figures (A.150) and (A.151) show typical plots of the variation of added mass and damping with frequency, whence it can be seen that the evaluation of the coefficients is very much dependent on the frequency when the frequency of oscillation is a small finite value. As the frequency of oscillation increases, an asymptote is reached for both the added mass and damping values.

High speed planing theory typically makes the assumption that the added mass and damping coefficients can be taken at their asymptotic value, i.e. where the frequency of craft oscillation is infinitely high. At first hand, this may seem to be a reasonable assumption since the high speed problem involves large forcing encounter frequencies and this approach reduces the complexity of evaluating the hydrodynamic coefficients. However, there is a considerable range of frequencies, associated with low speed planing or low encounter frequency, where this assumption will lead to the under or over prediction of the added mass and damping terms, which in turn can be expected to have a significant effect on the accuracy of the final solution.

Troesch (1992) carried out a series of experimental tests whereby the hydrodynamic coefficients were evaluated for various frequencies and amplitudes of motion in pure heave or pure pitch. A 20° deadrise form was tested with $L_{\mathrm{wet}}/B = 3, 4$ and $C_V = 1.5, 2.0, 2.5$. The results showed that the hydrodynamic coefficients are relatively amplitude independent especially in heave, for $C_V < 2.5$ and small amplitude perturbations, $z/B < 0.12$ and $\theta < 2.2^\circ$. However, the added mass coefficients, and to a lesser extent, the damping coefficients, are frequency dependent for low to moderate speed planing conditions.

In order to demonstrate the effect of frequency and amplitude dependency on the hydrodynamic coefficients, NoLiPCraMPwas run under pure heave and pure pitch tests with constant restoring force coefficients and the frequency dependent terms neglected. The craft tested were not the same as Troesch's craft[1] but a qualitative comparison could still be reached. Figures (A.83) to (A.86) show the non-dimensional values of the hydrodynamic coefficients against non-dimensional amplitude or frequency. For the low planing speed of $C_V = 1.33$, the coefficients are amplitude independent with significant dependency for very high speed planing, $C_V = 4.00$. This reflects Troesch's results and at the higher planing speed demonstrates the significant non-linear characteristics of the coefficients. The frequency dependency graphs though show poor agreement with the results of Troesch, but this is as expected since the program is considering the added mass and damping terms to be frequency independent. The consequence of this

---

[1] Fridsma's configuration H and J with $C_V = 1.33, 4.00$, $L/B = 5$, $\beta = 10^\circ$

is to show the importance and validity of modelling the frequency dependency in the hydrodynamic coefficients, especially for lower planing speeds; an approach that has not been commonly used in planing theory.

The inclusion of frequency dependence in a time-simulation is, however, computationally expensive. The added mass is dependent on the instantaneous underwater shape of the hull so a method for reducing the problem is presented forthwith. Firstly, the added mass for each defined section is calculated for a range of frequencies and drafts using a six-point conformal mapping technique. A quadratic spline is then fitted to the values of added mass and damping for each frequency value. Linear interpolation can be used for frequencies in-between. The coefficients of the quadratics are then the only required information for the evaluation of instantaneous added mass.

Appendix D

Added Resistance

Vossers (1961) and Hanaoka et al. (1963) suggested that the added resistance in waves for a vessel heaving and pitching may consist of three components:

1. A resistance force, resulting from interference between incident waves and waves generated by the ship when heaving and pitching. This component would be the same as the so-called drifting force.
2. A component which would be equivalent to the damping force associated with forced heaving and pitching in calm water, for example, under the excitation of some external mechanism such as an oscillator.
3. An added resistance due to wave reflection against the ship - commonly called the diffraction effect.

These are all inter-related and interactive which makes division into three measurable areas very difficult. Although the waves produced by the separate force components can be superimposed, the actual force components themselves cannot because of their relation to the square of the wave height.

These three categories help the understanding of the mechanisms for added resistance and measurements and special experimental techniques, such as forced oscillation, have shown that, in general, the drifting force would make the largest contribution to the added resistance whereas diffraction effects would be the least significant.

Havelock (1945) formulated an equation for the added resistance in regular waves as a function of heave amplitude, z_a, and pitch amplitude θ_a, as follows:

$$R_{aw} = -\frac{k}{2}(F_a z_a \sin\epsilon_{ZF} + M_a\theta_a \sin\epsilon_{\theta M}) \tag{D.1}$$

where k is the wave number, F_a and M_a are the exciting force and moment amplitudes, and ϵ_{ZF} and $\epsilon_{\theta M}$ are the phase angles between the exciting function and the response for heave and pitch, respectively.

More commonly the above equation is shown as

$$R_{aw} = \frac{\omega_e^3}{2g}(N_z z_a^2 + N_\theta \theta_a^2) \tag{D.2}$$

where ω_e is the wave-encounter frequency and N_z and N_θ are the damping coefficients for heave and pitch respectively.

The lack of coupling in these equations between heave and pitch does not remove the fundamental concept shown by these equations. Gerritsma and Beukelman (1972) and Hanaoka et al. (1963) discussed these equations pointing out that the source of added resistance is the phase relationship between the ship motions and the forcing functions. A phase lag can only exist when there are non zero damping terms in the equations of motion. The energy loss associated with the damping is related to the work done in keeping the ship motions in a constant phase relationship with the forcing functions. This energy is supplied by the ship and is dissipated in the form of fluid friction and radiation of the waves produced by the ship oscillation. These 'damping waves', indirectly generated by the damping characteristics of the ship, contain the major portion of the wave energy dissipated by the ship. If we can compute the energy stored in these radiated damping waves then we can evaluate the added resistance.

Analytical considerations tell us the nature of added resistance in waves:

1. Added resistance is proportional to the square of the wave height.
2. Added resistance in a seaway is independent of calm-water resistance.
3. Added resistance depends upon the craft motions and their phase relationship to the wave field.

In general it can be assumed that the maximum wave resistance will occur around the point of maximum relative motion (heave and pitch resonance) because of the dependency of added resistance on the square of relative motions. Strom-Tejsen et al. (1973) also pointed out that because of the direct heave and pitch relationship, the hull characteristics that lead to poor motion response behaviour will also produce a large added resistance.

The added resistance has been shown to be related to the energy flux radiated away from the craft to the water. Little of this energy is consumed in viscous effects since viscous damping is shown to be insignificant compared to hydrodynamic damping. Objectively it can be assumed that added resistance is therefore a non-viscous phenomenon, almost exclusively determined by inertial and wave effects. Model testing can then be Froude-scaled up to full scale. The ship added resistance can be evaluated by using the product of the model resistance and scale ratio cubed.

Added resistance in irregular waves can be determined by applying the principle of superposition to equation (D.1). This assumes that the added resistance is proportional to the square of the wave height and that Froude Law dynamic scaling is carried out. In regular wave cases it is necessary to justify the application of the wave height squared assumption and the principle of superposition. Strom-Tejsen et al. (1973) give a good history to the validity of applying these assumptions with the result being that "..the linear relationship between added resistance and wave height square, at constant speed and wave length, can be considered a very good approximation for practical purposes." and the principle of superposition "...was valid as long as the added resistance could be considered a purely second-order function of wave height.".

Gerritsma and Beukelman (1972) looked at the added resistance of a ship in waves as a result of the radiated damping waves created by the motions of a ship relative to the water. They worked on Joosen's variation, equation (D.2), of Havelock's expression for added resistance, equation (D.1). This allowed for forward speed of the ship by including the encounter frequency in their equations.

Gerritsma and Beukelman give the radiated damping energy, P, of the oscillating ship during a period of encounter, T_e, as,

$$P = \int_L \int_0^{T_e} b' V^2 \, dt \, dx \tag{D.3}$$

where V is the sectional impact velocity and the sectional damping coefficient for a ship at speed is,

$$b' = N' - u_0 \frac{dm_a}{dx} \tag{D.4}$$

As V is a harmonic function with amplitude V_a and a frequency equal to the frequency of encounter, ω_e, then,

$$P = \frac{\pi}{\omega_e} \int_L b' V_a^2 \, dx \tag{D.5}$$

Following Maruo (1963), the work done by the towing force, R_{AW}, required to pull the ship through waves is given as,

$$P = R_{AW}(u_0 + c)T_e = R_{AW}\lambda \tag{D.6}$$

where c is wave celerity.

From equation (D.5) and (D.6) it follows that,

$$R_{AW} = \frac{k}{2\omega_e} \int_L b' V_a^2 \, dx \tag{D.7}$$

The theory behind added resistance is mathematically sound such that any errors in added resistance values are more likely to stem from the error in predicting hydrodynamic coefficients than added resistance theory. The added mass and damping which lead to expressions found in Gerritsma-Beukelman's theory for added resistance need to be accurately determined, especially since the vertical relative motions are required to second order. Salvesen (1978) showed the importance and extreme variation in results due to different methods of calculation of the hydrodynamic coefficients. He suggested that as a result of the added resistance being a second order non-linear phenomenon, an accuracy of pitch and heave motions to within 10-15% would give at best an added resistance prediction with 20-30% accuracy.

D.1 Application to Planing Craft

The very notion of operating a planing craft is to develop the highest possible lift:drag ratio, bearing in mind other design criteria. The resistance of a planing craft is considerably less than that experienced by a displacement craft of similar specification. Calm water resistance is usually not larger than 20% of the craft weight, whilst the incremental increase in resistance due to operation in waves is an order lower, around 2% of the craft weight. This means that from a design perspective, added resistance is usually accounted for by tolerance in powering requirements. From a theoretical point of view, inaccuracies in numerical application would be likely to produce uncertain added resistance results. However, the above methodology, namely equation (D.7), is imposed within the program NoLiPCraMPto investigate the prediction of added resistance in waves.

The results of this investigation are presented in figures A.152 and A.153. It is quite obvious that the predicted results are extremely encouraging. The magnitude of the quantities that are being predicted in comparison with the magnitude of the quantities (vertical velocity and damping coefficient) from which they are derived is small and therefore, as mentioned above, extremely sensitive to errors in those values. This does not seem to affect the theoretical agreement with the experiments of Fridsma (1969). However, given the results of figure A.141, which shows obvious discrepancy between two different experimenters results for added resistance, any conclusions as to the comparability between predicted and experimental added resistance must be approached with caution.

Appendix E

Hydrodynamic Coefficients

Listed herein are the hydrodynamic coefficents used in the equations of motion. All second and higher order terms in motion perturbations are neglected. The frequency independent stiffness coefficients related to steady planing in waves c^*_{ij} are identical to c_{ij} except that m_a is replaced by the frequency independent term, m^*_a. $C_{D,c}$ represents damping and crossflow drag.

$$
\begin{aligned}
m_{33} &= M + \cos^2\theta \int_0^L m_a \, dx \\
m_{35} &= -\cos\theta \int_0^L m_a x \, dx \\
m_{53} &= -\cos\theta \int_0^L m_a x \, dx \\
m_{55} &= I + \cos\theta \int_0^L m_a x^2 \, dx \\
n_{33} &= -\cos\theta \int_0^L \dot{m}_a \, dx - 2\rho C_{D,c} \dot{x}_{cg} \cos\theta \sin\theta \int_0^L b \, dx - \dot{x}_{cg} \cos^2\theta m_a \big|_{\text{stern}} \\
&\quad + \dot{x}_{cg} \sin^2\theta m_a \big|_{\text{stern}} + 2\cos^2\theta \int_0^L b\omega_z \, dx + 2\sin\theta\cos\theta\omega_z m_a \big|_{\text{stern}} \\
&\quad - 2\cos\theta\sin\theta \int_0^L \frac{\partial\omega_z}{\partial x} m_a \, dx \\
n_{35} &= -\dot{x}_{cg} \cos\theta \int_0^L m_a \, dx + \int_0^L \dot{m}_a x \, dx + 2\rho C_{D,c} \dot{x}_{cg} \sin\theta \int_0^L bx \, dx \\
&\quad + \dot{x}_{cg} \cos\theta x m_a \big|_{\text{stern}} - \sin\theta \int_0^L m_a \omega_z \, dx - 2 \int_0^L bx\omega_z \, dx + \sin\theta\omega_z x m_a \big|_{\text{stern}} \\
&\quad + \sin\theta \int_0^L \frac{\partial\omega_z}{\partial x} m_a x \, dx \\
n_{53} &= \cos\theta \int_0^L \dot{m}_a x \, dx + 2\rho C_{D,c} \dot{x}_{cg} \cos\theta \sin\theta \int_0^L bx \, dx + \dot{x}_{cg} \cos^2\theta x m_a \big|_{\text{stern}} \\
&\quad - \dot{x}_{cg} \sin^2\theta x m_a \big|_{\text{stern}} + \dot{x}_{cg} \cos^2\theta \int_0^L m_a \, dx - \dot{x}_{cg} \sin^2\theta \int_0^L m_a \, dx \\
&\quad - 2\cos\theta\sin\theta\omega_z x m_a \big|_{\text{stern}} - 2\cos\theta\sin\theta \int_0^L \omega_z m_a \, dx \\
&\quad + 2\cos\theta\sin\theta \int_0^L \frac{\partial\omega_z}{\partial x} m_a x \, dx \\
n_{55} &= -\int_0^L \dot{m}_a x^2 \, dx - 2\rho C_{D,c} \dot{x}_{cg} \sin\theta \int_0^L bx^2 \, dx - \dot{x}_{cg} \cos\theta x^2 m_a \big|_{\text{stern}} \\
&\quad + 2\cos\theta \int_0^L bx\omega_z^2 \, dx - \sin\theta\omega_z x^2 m_a \big|_{\text{stern}} - \sin\theta \int_0^L \frac{\partial\omega_z}{\partial x} m_a x^2 \, dx
\end{aligned}
$$

$$
\begin{aligned}
c_{33} &= 0 \\
c_{35} &= -\dot{x}_{cg}\int_0^L \dot{m}_a\,dx - \dot{x}_{cg}^2\cos\theta x m_a\big|_{\text{stern}} - 2\rho C_{D,c}\dot{x}_{cg}^2\sin\theta\int_0^L b\,dx \\
&\quad +2\rho C_{D,c}\dot{x}_{cg}\cos\theta\int_0^L b\omega_z\,dx - \dot{x}_{cg}\sin\theta\omega_z m_a\big|_{\text{stern}} + \cos\theta\omega_z^2 m_a\big|_{\text{stern}} \\
&\quad -\dot{x}_{cg}\sin\theta\int_0^L \frac{\partial\omega_z}{\partial x}m_a\,dx + 2\cos\theta\int_0^L \frac{\partial\omega_z}{\partial x}\omega_z m_a\,dx \\
c_{53} &= 0 \\
c_{55} &= -\dot{x}_{cg}\int_0^L \dot{m}_a x\,dx + \dot{x}_{cg}^2\cos\theta x m_a\big|_{\text{stern}} + \dot{x}_{cg}^2\cos\theta\int_0^L m_a\,dx \\
&\quad +\rho C_{D,c}\dot{x}_{cg}^2\sin\theta\int_0^L bx\,dx + \dot{x}_{cg}\sin\theta\omega_z x m_a\big|_{\text{stern}} - \cos\theta\omega_z^2 x m_a\big|_{\text{stern}} \\
&\quad +\dot{x}_{cg}\sin\theta\int_0^L m_a\omega_z\,dx - \cos\theta\int_0^L m_a\omega_z^2\,dx + \dot{x}_{cg}\sin\theta\int_0^L \frac{\partial\omega_z}{\partial x}m_a x\,dx \\
&\quad -2\cos\theta\int_0^L \frac{\partial\omega_z}{\partial x}\omega_z m_a x\,dx \\
e_3 &= \cos\theta\int_0^L \frac{\partial\omega_z}{\partial t}m_a\,dx + \cos\theta\int_0^L \dot{m}_a\omega_z\,dx - \cos^2\theta\int_0^L b\omega_z^2\,dx \\
&\quad +\dot{x}_{cg}\cos^2\theta\omega_z m_a\big|_{\text{stern}} + \dot{x}_{cg}\cos\theta\int_0^L \frac{\partial\omega_z}{\partial x}m_a\,dx - \rho g\int_0^L \kappa A\,dx \\
e_5 &= -\cos\theta\int_0^L \frac{\partial\omega_z}{\partial t}m_a x\,dx - \cos\theta\int_0^L \dot{m}_a\omega_z x\,dx + \cos^2\theta\int_0^L b\omega_z^2 x\,dx \\
&\quad -\dot{x}_{cg}\cos^2\theta\omega_z m_a x\big|_{\text{stern}} - \dot{x}_{cg}\cos^2\theta\int_0^L \frac{\partial\omega_z}{\partial x}m_a x\,dx \\
&\quad -2\dot{x}_{cg}\cos\theta\sin\theta\int_0^L bx\omega_z\,dx - \dot{x}_{cg}\cos^2\theta\int_0^L m_a\omega_z\,dx + 2\rho g\int_0^L \kappa A x\,dx
\end{aligned}
$$

References

AKERS, R., HOECKLEY, S., PETERSON, R. AND TROESCH, A. 1999 Predicted vs. measured vertical-plane dynamics of a planing boat. *Proceedings:* FAST'99, Seattle, USA. pp91-105.

BAND, E. 1969 Study of bow impact loads for 100 ton surface effect ship. Technical report. 18008-2. Payne Division of Wyle Labs. December.

BINGHAM, S., KORSEMEYER, F., NEWMAN, J. AND OSBORNE, G. 1993 Time domain analysis for predicting ship motions. *Proceedings:* 6th International Conference on Numerical Ship Hydrodynamics.

BISHOP, R. AND PRICE, W., Eds. 1974 *Probabilistic Theory of Ship Dynamics.* 1 edition. Chapman and Hall, 11 New Fetter Lane, London.

BISHOP, R., PRICE, W. AND TAM, P. 1978 Hydrodynamic coefficients of some heaving cylinders of arbitrary shape. *International Journal for Numerical Methods in Engineering*, **13**, 17–33.

BLAKE, J. 1993 Theoretical predictions of motions of high speed planing craft in waves. Undergraduate Thesis, Department of Ship Science, University of Southampton. July.

BLOUNT, D. AND CODEGA, L. 1995 Dynamic stability of planing hulls. *Proceedings:* 4th Biennial Power Boat Symposium, SNAME.

BRETSCHNEIDER, E. 1952 The generation and decay of wind waves in deep water. Technical report. 37. Transactions of the American Geophysical Union.

BRETSCHNEIDER, E. 1957 Review of practical methods of observing and forecasting ocean waves by means of wave spectra and statistics. Technical report. Transactions of the American Geophysical Union. April.

BROWN, P. 1971 An experimental and theoretical study of planing surfaces with trim flaps. Technical report. R-47. Davidson Laboratory, Stevens Institut of Technology.

CARTWRIGHT, D. AND LONGUET-HIGGINS, M. 1956 The statistical distribution of the maxima of a random function. *Proceedings:* Proceedings of the Royal Society of London: Series A. vol. 237, pp212-232.

CHIU, F.-C. AND FUJINO, M. 1989 Nonlinear prediction of vertical motions and wave loads of high-speed crafts in head sea. *International Shipbuilding Progress*, **36**, 406, 193–232.

CHOU, S.-K., CHIU, F.-C. AND LEE, Y.-J. 1991 Nonlinear motions and whipping loads of high-speed crafts in head sea. *18th Symposium of Naval Hydrodynamics*, 157–170.

CLEMENT, E. AND BLOUNT, D. 1963 Resistance test of systematic series of planing hull forms. *Transactions of SNAME*, **71**, 491–561.

CODEGA, L. AND LEWIS, J. 1987 A case of dynamic instability in a planing hull. *Marine Technology*, **24**, 2.

CUMBERBATCH, E. 1958 Two dimensional planing at high froude number. *Journal of Fluid Mechanics*, **4**, 5, 466–478.

DAVIDSON, K. AND SUAREZ, A. 1949 Tests of 20 related models of v-bottom motor boats - emb series 50. Technical report. R-47. David Taylor Model Basin.

DAY, J. AND HAAG, R. 1952 Planing boat porpoising. Doctoral dissertation, Webb Institute of Naval Architecture, Glen Cove, N.Y. May.

DOCTORS, L. 1974 Representation of planing surface by finite pressure elements. *Proceedings:* 5th Australasian Conference on Hydraulic and Fluid Mechanics. pp480-488.

ERGOROV, I. AND BUNKOV, M. 1978 Performance and seaworthiness of planing hulls. *Sudostraenie, Leningrad.* (in Russian).

FABULA, A. 1957 Ellipse-fitting approximation of two-dimensional normal symmetric impact of rigid bodies on water. *Proceedings:* Proceedings of the 5th Midwestern Conference on Fluid Dynamics. pp299-315.

FALTINSEN, O., Ed. 1990 *Sea Loads on Ships and Offshore Structures.* Cambridge Ocean Technology Series. Cambridge University Press, Cambridge.

FRIDSMA, G. 1969 A systematic study of the rough-water performance of planing boats. Technical report. 1275. Stevens Institute of Technology. November.

FRIDSMA, G. 1971 A systematic study of the rough-water performance of planing boats (irregular waves - part ii). Technical report. SIT-DL-71-1495. Stevens Institute of Technology. March.

GERRITSMA, J. AND BEUKELMAN, W. 1972 Analysis of the resistance increase in waves of a fast cargo ship. *International Shipbuilding Progress*, **19**, 217.

GREEN, A. 1935 The gliding of a flat plate on a stream of infinite depth - part i. *Proceedings:* Cambridge Philosophical Society. Vol. 31, pp589-603.

GREEN, A. 1936a The gliding of a flat plate on a stream of infinite depth - part ii. *Proceedings:* Cambridge Philosophical Society. Vol. 32, pp67-85.

GREEN, A. 1936b Note on the gliding of a flat plate on the surface of a stream. *Proceedings:* Cambridge Philosophical Society. Vol. 32, pp248-252.

GRIGOROPOULOS, G. AND LOUKAKIS, T. 1998 Seakeeping characteristics of a systematic series of fast monohulls. *International Conference on High Speed Craft Motions and Manoeuvrability*, February.

HADLER, J. AND HUBBLE, E. 1974 Resistance characteristics of a systematic series of planing hull forms - series 65. *Society of Naval Architects and Marine Engineers*, May. Chesapeake Section.

HANAOKA, T. E. A. 1963 Researches on seakeeping qualities of ships in japan. *Society of Naval Architects of Japan*, **8**. 60th Anniversary Series, Chapter 5.

HAVELOCK, T. 1945 Notes on the theory of heaving and pitching. *Transactions of RINA*.

HIRANO, S., UCHIDA, S. AND HIMENO, Y. 1974 Pressure measurement on the bottom of prismatic planing hulls. *Aansai Society of Naval Architects*, March, 7–12. Japan.

HOGBEN, N., DUCUNHA, N. AND OLLIVER, G. 1986 Global wave statistics. Technical report. British Maritime Technology.

HOLLING, H. AND HUBBLE, E. 1974 Model resistance data of series 65 hull forms applicable to hydrofoils and planing craft. Technical report. 4121. NSRDC. May.

HSU, C. 1967 On the motions of high speed planing craft. Technical report. 603-1. Hydronautics. May. Laurel, Maryland.

JONES, R. 1946 Properties of low aspect ratio wings at speeds below and above the speed of sound. Technical report. 835. NACA.

KORVIN-KROUKOVSKY, B., SAVITSKY, D. AND LEHMAN, W. 1949 Wetted area and centre of pressure of planing surfaces. Technical report. 360. Stevens Institute of Technology. August.

KRING, D., HUANG, Y., SCLAVOUNOS, P., VADA, T. AND BRAATHEN, A. 1996 Nonlinear ship motions and wave loads by a rankine panel method. *Proceedings:* 21st Symposium on Naval Hydrodynamics.

LAI, C. AND TROESCH, A. 1995 Modeling issues related to the hydrodynamics of three-dimensional steady planing. *Journal of Ship Research*, **39**, 1, March, 1–24.

LAMB, H., Ed. 1932 *Hydrodynamics*. 6th Cambridge University Press, Cambridge.

LATORRE AND TAMIYA 1975 An experimental technique for studying the planing boat spray. *Proceedings:* Proceedings of the 14th International Towing Tank Conference, Ottawa, Canada. vol. 14, pp562-571.

LATORRE, R. 1982 Study of the flow surrounding a prismatic planing model. *International Shipbuilding Progress*, **29**, 289–296.

LATORRE, R. 1983 Study of prismatic planing model spray and resistance components. *Journal of Ship Research*, **27**, 187–196.

LATORRE, R. AND RYAN, S. 1990 Study of the splash angle from a plate at small incidence angle and edge emergence. *Ocean Engineering*, **17**, 3, 315–322.

LEWANDOWSKI, E. 1996 Prediction of the dynamic roll stability of hard-chine planing craft. *Journal of Ship Research*, **40**, 2, June, 144–148.

LEWIS, E., Ed. 1988 *Principles of Naval Architecture.* 2 edition. Vol. 1-3. Society of Naval Architects and Marine Engineers, 601 Pavonia Avenue, Jersey City, NJ.

LEWIS, F. 1929 The inertia of water surrounding a vibrating ship. *Transactions of SNAME*, **27**, 1–20.

LUTOWSKI, R. 1973 A computer program for various performance aspects of planing craft. Doctoral dissertation, Stevens Institute of Technology.

MARTIN, M. 1978a Theoretical determination of porpoising instability of high speed planing boats. *Journal of Ship Research*, **22**, 1, March, 32–53.

MARTIN, M. 1978b Theoretical prediction of motions of high speed planing boats in waves. *Journal of Ship Research*, **22**, 3, September, 140–169.

MARUO, H. 1951 Two dimensional theory of the hydroplane. *Proceedings:* 1st Japan National Congress for Applied Mechanics. pp409-415.

MARUO, H. 1963 Resistance in waves, researches into seakeeping qualities of ships. *Society of Naval Architects of Japan*, **8**. 60th Anniversary Series.

MARUO, H. 1967 High and low aspect ratio approximation of planing surfaces. *Schiffstechnik*, **72**, 3, 57–64.

MUNK, M. 1924 The aerodynamic forces on airship hulls. Technical report. 184. NACA.

NEWMAN, J., Ed. 1977 *Marine Hydrodynamics.* 1 edition. MIT Press, Cambridge, Massachusetts.

NEWMAN, J., Ed. 1978 *Theory of Ship Motions.* Advances in Applied Mechanics, Vol. 18.

OCHI, M. AND HUBBLE, E. 1976 On six-parameter wave spectra. *Proceedings:* 15th Coastal Engineers Conference. ASCE, New York.

PABST, W. 1931 Landing impact of sea planes. Technical report. TM 624. Zeitschrift fur Flugtechnik und Motorluftschiffahart. Verlag von R. Oldenbourg, Munchen und Berlin (Translated in NACA TM 624).

PANCHENKOV, A. AND ZENOVICH, S. 1989 Planing of arbitrary bodies. *4th International Symposium on Practical Design of Ships and Mobile Units.* Bulgaria.

PAYNE, P. 1974 Coupled pitch and heave porpoising instability in hydrodynamic planing. *Ocean Engineering*, **8**, 2, 58–71.

PAYNE, P. 1981 The vertical impact of a wedge on a fluid. *Ocean Engineering*, **8**, 421–436.

PAYNE, P. 1982 The differences between a wing and a planing plate in two-dimensional flow. *Ocean Engineering*, **9**, 5, 441–453.

PAYNE, P. 1984 On the high-speed porpoising stability of a prismatic hull. *Journal of Ship Research*, **28**, 2, June, 77–89.

PAYNE, P., Ed. 1988 *Design of High Speed Boats - Planing.* 1 edition. Vol. 1. Fishergate, 2521 Riva Road, Annapolis, Maryland.

PAYNE, P. 1992 A unification in the added mass theory of planing. *Ocean Engineering*, **19**, 1, 39–55.

PAYNE, P. 1993 The spray sheets produced during vertical wedge impact and steady planing. *Ocean Engineering*, **20**, 3, 247–261.

PAYNE, P. 1994 Recent developments in 'added-mass' planing theory. *Ocean Engineering*, **21**, 3, 257–309.

PAYNE, P. 1995 Contributions to planing theory. *Ocean Engineering*, **22**, 7, 699–729.

PERRING, W. AND GLAUERT, H. 1933 Wetted area and centre of pressure of planing surfaces at very low speed coefficients. Technical report. TR Vol.42. Aeronautical Research Council. September.

PIERSON, J. 1950a The penetration of a fluid surface by a wedge. Technical report. 381. Stevens Institute of Technology. July. IAS Paper FF-3.

PIERSON, J. AND LESHNOVER, S. 1950b A study of the flow, pressures and loads pertaining to prismatic vee-planing surfaces. Technical report. 382. Stevens Institute of Technology. May.

PIERSON, J., DINGHEE, D. AND NEIDINGER, J. 1954 A hydrodynamics study of the chines-dry planing body. Technical report. SIT-DL-54-492. Stevens Institute of Technology, Davidson Laboratory. May.

PIERSON, J. 1961 Models of random seas based on the langrangian equations of motion. *Proceedings:* College of Engineering, Research Division. NYU.

PIERSON, W. AND MOSKOWITZ, L. 1964 A proposed spectral form for fully developed wind seas based on the similarity theory of s.a.kitaigorodskii. *Journal of Geophysical Research*, **69**.

RICE, S. 1945 Mathematical analysis of random noise. Technical report. 23–24. Bell System Technical Journal.

ROSEN, A. AND GARME, K. 1999 Slamming studies on high-speed planing craft through full-scale trials and simulations. *Proceedings:* FAST'99, Seattle, USA. pp683-697.

SALVESEN, N. 1978 Added resistance of ships in waves. *Journal of Hydronautics*, **12**, 1, March, 24–34.

SALVESEN, N., TUCK, E. AND FALTINSEN, O. 1971 Ship motions and sea loads. *Society of Naval Architects and Marine Engineers*, 250–287.

SAMBRAUS, A. 1938 Planing surface tests at large froude numbers - airfoil comparison. Technical report. TM 1097. NACA. February.

SAVITSKY, D. 1964 Hydrodynamic design of planing hulls. *Marine Technology*, October, 71–95.

SAVITSKY, D. 1995 Overview of planing hull developments. *Proceedings:* Proceedings of the Intersociety High Performance Marine Vehicles Conference.

SAVITSKY, D. AND BRESLIN, J. 1958 On the main spray generated by planing surfaces. Technical report. 678. Steven's Institute of Technology.

SAVITSKY, D. AND NEIDINGER, J. 1954 Wetted area and centre of pressure of planing surfaces at very low speed coefficients. Technical report. 493. Steven's Institute of Technology. July.

SCHNITZER, E. 1953 Theory and procedure for determining loads and motions in chine-immersed hydrodynamic impacts of prismatic bodies. Technical report. TM 1152. NACA. supercedes NACA TN 2813.

SCORPIO, S., BECK, R. AND KORSEMEYER, F. 1996 Nonlinear water wave computations using a multipole accelerated, desingularised method. *Proceedings:* 21st Symposium on Naval Hydrodynamics.

SEDOV, L. 1937 Two dimensional problems of gliding on the surface of a heavy fluid. *Transactions of the Conference on the Theory of Wave Resistance.* Moscow, USSR.

SEDOV, L. 1939 Scale effect and optimum relations for sea surface planing. Technical report. TM 1097. NACA. February. Translated February 1947 in TM 1097 (Report No. 439 of the Central Aero-Hydrodynamical Institute, Moscow, 1939).

SEDOV, L., Ed. 1965 *Two-Dimensional Problems in Hydrodynamics and Aerodynamics.* 1 edition. John Wiley and Sons. Trans. from Russian Edition of 'Ploskie Zadachi Gidridinamiki i Aerodinamiki', 1950.

SHEN, Y. AND OGILVIE, T. 1972 Non-linear hydrodynamic theory for finite span planing surfaces. *Journal of Ship Research*, **16**, 3–20.

SHOEMAKER, J. 1934 Tanks tests of flat and vee-bottom planing surfaces. Technical report. TN 509. NACA. November.

SHUFORD, C. 1954 A review of planing theory and experiment with a theoretical study of pure-planing lift of rectangular flat plates. Technical report. 3233. NACA.

SHUFORD, C. 1958 A theoretical and experimental study of planing surfaces including effects of cross-section and planform. Technical report. 1355. NACA.

SOTTORF, W. 1929 Experiments with planing surfaces. *Werft-Reederei-Hafen*, November, 425–432. Translated by NACA, March 1932.

SOTTORF, W. 1932 Experiments with planing surfaces. Technical report. TM 661. NACA.

SPIEGEL, M., Ed. 1964 *Theory and Problems of Complex Variables.* 1 edition. McGraw-Hill.

SQUIRE, H. 1957 The motion of a simple wedge along the water surface. *Proceedings:* Proceedings of the Royal Society of London: Series A. Vol.243 pp48-64.

ST DENIS, M. 1980 On the statistical description of seaways of moderate severity. *Proceedings:* SNAME STAR Symposium.

STROM-TEJSEN, J., YEH, H. AND MORAN, D. 1973 Added resistance in waves. *Society of Naval Architects and Marine Engineers*, November, 109–143.

TAYLOR, J. 1930 Hydrodynamical inertia coefficients. *Philosophical Magazine*, 161–183.

TONG, J. 1989 A finite element approach to planing problem. Doctoral dissertation, University of Southampton, Highfield, Southampton, UK.

TROESCH, A. 1992 On the hydrodynamics of vertically oscillating planing hulls. *Journal of Ship Research*, **36**, 4, December, 317–331.

TUCK, E. 1975 Low aspect ratio flat ship theory. *Journal of Hydronautics*, **9**, 1, 3–12.

TULIN, M. 1957 The theory of slender surfaces planing at high speeds. *Schiffstechnik*, **4**, 21, 125–133.

URSELL, F. 1949 On the heaving motion of a circulr cylinder in the surface of a fluid. *Quarterly Journal of Mechanics and Applied Mathematics*, **2**, 218–231.

VON KARMAN, T. 1929 The impact of seplane floats during landing. Technical report. TN-321. NACA.

VOSSERS, G. 1961 Fundamentals of the behaviour of ships in waves. *Publication No. 151a of the Netherlands Ship Model Basin.*

WAGNER, H. 1932 Uber stoss und gleitvorgange an der obeflachen von flussigkeiten. *Z.A.M.M.*, **12**, 193–215.

WANG, D. AND RISPIN, P. 1971 Three dimensional planing at high froude number. *Journal of Ship Research*, September, 221–230.

WANG, L.-W. 1985 A study on motions of high speed planing boats with controllable flaps in regular waves. *International Shipbuilding Progress*, **32**, 365, October, 6–23.

WELLICOME, J. AND JAHANGEER, Y. 1978 Representation of three dimensional planing surface by finite pressure elements. *Proceedings:* RINA. April. pp53-70.

WU, M.-K. AND MOAN, T. 1996 Linear and nonlinear hydroelastic analysis of high-speed vessels. *Journal of Ship Research*, **40**, 2, June, 149–163.

XU, L. AND TROESCH, A. 1999 A study on hydrodynamics of asymemetric planing surfaces. *Proceedings:* FAST'99, Seattle, USA. pp471-481.

YIM, B. 1971 Investigation of gravity and ventilation effects in water entry of thin foils. *Proceedings:* International Union of Theoretical and Applied Mechanics Symposium. Leningrad, USSR pp471-489.

ZARNICK, E. 1978 A non-linear mathematical model of motions of a planing boat in regular waves. Technical report. DTNSRDC-78/032. David Taylor Naval Ship Research and Development Center.

ZARNICK, E. 1979 A non-linear mathematical model of motions of a planing boat in irregular waves. Technical report. DTNSRDC/SPD-0867-01. David Taylor Naval Ship Research and Development Center.

ZHAO, R. AND FALTINSEN, O. 1992 Water entry of two dimensional bodies. *Journal of Fluid Mechanics*, 593–612.

ZHAO, R., FALTINSEN, O. AND HASLUM, H. 1997 A simplified non-linear analysis of a high-speed craft in calm water. *Proceedings:* FAST'97, Sydney, Australia. pp431-438.